THE UNIVERSITY
of EDINBURGH

Single Data Set Detection for Multistatic Doppler Radar

Bogomil Shtarkalev

A thesis submitted for the degree of Doctor of Philosophy.

The University of Edinburgh.

- May 2015 -

Abstract

The aim of this thesis is to develop and analyse single data set (SDS) detection algorithms that can utilise the advantages of widely-spaced (statistical) multiple-input multiple-output (MIMO) radar to increase their accuracy and performance. The algorithms make use of the observations obtained from multiple space-time adaptive processing (STAP) receivers and focus on covariance estimation and inversion to perform target detection.

One of the main interferers for a Doppler radar has always been the radar's own signal being reflected off the surroundings. The reflections of the transmitted waveforms from the ground and other stationary or slowly-moving objects in the background generate observations that can potentially raise false alarms. This creates the problem of searching for a target in both additive white Gaussian noise (AWGN) and highly-correlated (coloured) interference. Traditional STAP deals with the problem by using target-free training data to study this environment and build its characteristic covariance matrix. The data usually comes from range gates neighbouring the cell under test (CUT). In non-homogeneous or non-stationary environments, however, this training data may not reflect the statistics of the CUT accurately, which justifies the need to develop SDS methods for radar detection. The maximum likelihood estimation detector (MLED) and the generalised maximum likelihood estimation detector (GMLED) are two reduced-rank STAP algorithms that eliminate the need for training data when mapping the statistics of the background interference. The work in this thesis is largely based on these two algorithms.

The first work derives the optimal maximum likelihood (ML) solution to the target detection problem when the MLED and GMLED are used in a multistatic radar scenario. This application assumes that the spatio-temporal Doppler frequencies produces in the individual bistatic STAP pairs of the MIMO system are ideally synchronised. Therefore the focus is on providing the multistatic outcome to the target detection problem. It is shown that the derived MIMO detectors possess the desirable constant false alarm rate (CFAR) property. Gaussian approximations to the statistics of the multistatic MLED and GMLED are derived in order to provide a more in-depth analysis of the algorithms. The viability of the theoretical models and their approximations are tested against a numerical simulation of the systems.

The second work focuses on the synchronisation of the spatio-temporal Doppler frequency data from the individual bistatic STAP pairs in the multistatic MLED scenario. It expands the idea to a form that could be implemented in a practical radar scenario. To reduce the information shared between the bistatic STAP channels, a data compression method is proposed that extracts the significant contributions of the MLED likelihood function before transmission. To perform the inter-channel synchronisation, the Doppler frequency data is projected into the space of potential target velocities where the multistatic likelihood is formed. Based on the expected structure of the velocity likelihood in the presence of a target, a modification to the multistatic MLED is proposed. It is demonstrated through numerical simulations that the proposed modified algorithm performs better than the basic multistatic MLED while having the benefit of reducing the data exchange in the MIMO radar system.

Declaration of originality

I hereby declare that the research recorded in this thesis and the thesis itself was composed and originated entirely by myself in the School of Engineering at the University of Edinburgh.

Bogomil Shtarkalev

May 2015

Acknowledgements

This thesis is the result of years of hard work, patience, and persistence. Fortunately, I did not walk this road alone. Here is a list of the people that have aided me in one way or another.

- Prof. Bernard (Bernie) Mulgrew, my supervisor, without whom none of this would have been possible. I would like to extend my gratitude for his continuous guidance, his time and patience, and his support and belief in my work over the years.
- The Institute for Digital Communications (IDCOM) in the University of Edinburgh for the financial support. Without the funding generously provided to me by the Institute, this work would never have seen the light of day.
- My parents for everything they have and still are doing for me. It is due to their sacrifices and hard work that I stand where I am today. Every step of the way they have supported me without reservations and have ensured that I have the best options that would allow me to progress forward in life. This work is as much of their achievement as it is mine.
- My family for always believing in me and helping me. Their support has been invaluable throughout the years, and I know that I will always be able to rely on them for anything.
- My friends in the office for their infinitesimal contributions in making this an infinitely more enjoyable experience. I would like to thank the Party Corner, Nik, Harald, Stefcho, and Dobro, for the good times we've shared not only in Room 2.01 but also on that (in)famous balcony. I'd also like to thank the Other Guys, Chunli, Sinan, and Rodrigo, for the countless hours of heated debating on topics far and wide in the AGB coffee room.
- Edinburgh University Kendo Club (EUKC) and Edinburgh Kendo Club (EKC) for helping me maintain my sanity throughout the years of my PhD. Kendo has helped me develop not only physically but also emotionally and mentally. The friends I have made in EUKC have allowed me to maintain a connection with the world outside of Engineering ("The Normal World"), where things are always twice as good instead of 3dB better.
- Steve Bishop Sensei, whose teachings have had a profound impact on me both inside and outside the dojo. A special thanks to Andy, the best sempai one can ask for, and Håkon, my Kendo brother, for being amazing friends and for always pushing me to get better.

Contents

Declaration of originality . . . iii
Acknowledgements . . . iv
Contents . . . v
List of figures . . . vii
List of tables . . . ix
List of abbreviations . . . x
Nomenclature . . . xiii

1 Introduction **1**
1.1 Motivation . . . 2
1.2 Contributions and outline . . . 4

2 Single data set detection in space-time adaptive processing **6**
2.1 Introduction . . . 6
2.2 Space-time adaptive processing signal model . . . 7
2.3 Traditional covariance-based two data set detectors . . . 17
2.4 Covariance-based single data set detection . . . 20
2.5 Multiple-input multiple-output radar . . . 23
2.6 Radar ambiguity limitations . . . 25
2.7 Problem formulation . . . 27
2.8 Summary . . . 30

3 The multistatic maximum likelihood and generalised maximum likelihood estimation detectors **31**
3.1 Introduction . . . 31
3.2 Background . . . 32
3.3 Derivation of the multistatic MLED . . . 33
3.4 Derivation of the multistatic GMLED . . . 37
3.5 Analysis . . . 40
3.5.1 Statistical properties of the multistatic MLED . . . 41
3.5.2 Gaussian approximation of the multistatic MLED . . . 43
3.5.3 Statistical properties of the multistatic GMLED . . . 48
3.5.4 Log-normal approximation of the multistatic GMLED . . . 50
3.6 Simulations . . . 55
3.7 Summary . . . 62

4 Multistatic maximum likelihood estimation detector: data compression and velocity space target detection **63**
4.1 Introduction . . . 63
4.2 Subspace compression for the MLED Doppler likelihood . . . 63
4.3 Velocity synchronisation of detection likelihood . . . 67
4.4 Modified MLED . . . 70
4.5 Analysis . . . 73

4.5.1 Statistical properties of the modified multistatic MLED 74
4.5.2 Probability density, detection and false alarm probability 75
4.5.3 Performance effects of the scaling parameter κ 77
4.6 Simulations 80
4.7 Summary 85

5 Practical limitations on growing multiple-input multiple-output radar networks 87
5.1 Introduction 87
5.2 Infinite Gaussian pulse train autoambiguity 88
5.3 Finite Gaussian pulse train autoambiguity 91
5.4 Waveform cross-ambiguity in multiple access MIMO 93
5.5 Ambiguity volume ratio in multiple access MIMO 94
5.5.1 Volume ratio in an TDMA scenario 94
5.5.2 Volume ratio in an FDMA scenario 97
5.5.3 Fejér kernel Gaussian approximation 98
5.6 Simulations 99
5.7 Summary 103

6 Conclusion 104
6.1 Summary 105
6.2 Possible directions for future work 106

A Derivation of the bistatic MLED and GMLED statistics 108
A.1 Derivation of the bistatic MLED statistics 108
A.2 Derivation of the bistatic GMLED statistics 111

B Lindeberg's condition 113
B.1 Proof of Lindeberg's condition for the multistatic MLED approximation 113
B.2 Proof of Lindeberg's condition for the multistatic GMLED approximation . . . 114

C Original publications 117

References 142

List of figures

2.1 Geometric parameters in a bistatic radar setup with a mobile transmitter and ground-based receive ULA . . . 9
2.2 STAP observations datacube in a CPI . . . 11
2.3 Sources of STAP clutter returns in a multistatic configuration . . . 12
2.4 Spatio-temporal spectrum of clutter and jamming returns at a single receiver in a bistatic STAP range gate . . . 13
2.5 Extracting iid snapshots by passing a sliding window over the STAP range gate observations . . . 15
2.6 Relationship between the spatio-temporal steering vectors in the iid snapshots obtained from the STAP range gate observations . . . 16
2.7 Range gates for secondary training data in STAP TDS detectors . . . 19
2.8 An example multistatic radar setup with 3 mobile transmitters and 3 receive ULAs . . . 28

3.1 Probability density function of the multistatic MLED detection variable K=20, M=N=10, SNR=−26dB . . . 46
3.2 Probability density function of the multistatic MLED detection variable K=60, M=N=20, SNR=−36dB . . . 46
3.3 Probability density function of the multistatic GMLED detection variable K=20, M=N=10, SNR=−26dB . . . 53
3.4 Probability density function of the multistatic GMLED detection variable K=60, M=N=20, SNR=−36dB . . . 53
3.5 Radar setup of randomly-placed 10 mobile transmitters and 10 receiver ULAs . 56
3.6 Radar setup of randomly-placed 20 mobile transmitters and 20 receiver ULAs . 56
3.7 Probability of Detection vs SNR of the multistatic MLED and GMLED detectors for $P_{fa} = 0.02$, $K = 20$, $M = N = 10$ . . . 59
3.8 Probability of Detection vs SNR of the multistatic MLED and GMLED detectors for $P_{fa} = 0.02$, $K = 60$, $M = N = 10$ . . . 59
3.9 Probability of Detection vs SNR of the multistatic MLED and GMLED detectors for $P_{fa} = 0.02$, $K = 20$, $M = N = 20$ . . . 60
3.10 Probability of Detection vs SNR of the multistatic MLED and GMLED detectors for $P_{fa} = 0.02$, $K = 60$, $M = N = 20$ . . . 60

4.1 Likelihood function of the standard bistatic MLED and proposed subspace compression, K=60, SNR= − 30dB . . . 67
4.2 Likelihood function of the standard bistatic MLED in velocity space, K=60, SNR= − 30dB, $\boldsymbol{v}$= $[25, -25]$m/s . . . 69
4.3 Likelihood function of the multistatic MLED in velocity space K=60, SNR=10dB, $\boldsymbol{v}$= $[25, -25]$m/s . . . 71
4.4 Probability density function of the modified multistatic MLED detection variable, K=60, M=N=3, SNR=−30dB, κ=$6\sigma_M$ . . . 78

4.5 Probability of detection of the modified multistatic MLED detection variable K=60, M=N=3, SNR=−30dB, P_{fa}=0.02 79
4.6 Probability density function of the modified multistatic MLED detection variable, K=60, M=N=3, SNR=−30dB, optimal value of κ=0.04 79
4.7 ROC curve of multistatic MLED and the proposed modified MLED K=20, SNR=−30dB 82
4.8 ROC curve of multistatic MLED and the proposed modified MLED K=20, SNR=−25dB 82
4.9 ROC curve of multistatic MLED and the proposed modified MLED K=60, SNR=−30dB 83
4.10 ROC curve of multistatic MLED and the proposed modified MLED K=60, SNR=−25dB 83
4.11 Probability of detection of compressed multistatic MLED vs compression ratio K=20, P_{fa}=0.02 84

5.1 Autoambiguity of a 100-pulse delta train waveform 89
5.2 Autoambiguity of a 1000-pulse GPT waveform 90
5.3 Autoambiguity of a 5-pulse waveform at t=0 with Gaussian approximation to the Fejér kernel 100
5.4 Volume ratio of cross-to-auto-ambiguity in a rectangular region A for FDMA-orthogonal radar waveforms of K_T pulses 101
5.5 Volume ratio of cross-to-auto-ambiguity in a rectangular region A for TDMA-orthogonal radar waveforms of K_T pulses 102

List of tables

2.1 Fixed radar scenario parameters 29
2.2 Physical implementation of the multistatic radar detection procedure 30

3.1 Guide to MLED pdf simulations labelling and terminology 45
3.2 Guide to GMLED pdf simulations labelling and terminology 52

4.1 Subspace compression 66
4.2 Modified multistatic MLED procedure 73

List of abbreviations

1-D one-dimensional

2-D two-dimensional

3-D three-dimensional

AMF adaptive matched filter

APES amplitude and phase estimation

AWGN additive white Gaussian noise

CDMA code division multiple access

CFAR constant false alarm rate

CLT central limit theorem

CPI coherent pulse interval

CUT cell under test

D-space Doppler frequency space

DOF degrees of freedom

FDMA frequency division multiple access

GP Gaussian pulse

GPT Gaussian pulse train

GCM general clutter model

GLRT generalised likelihood ratio test

GMLED generalised maximum likelihood estimation detector

ICM intrinsic clutter motion

iid independent and identically distributed

KASSPER knowledge-aided sensor signal processing and expert reasoning

MCARM multi-channel airborne radar measurement

MF matched filter

MIMO multiple-input multiple-output

MISO multiple-input single-output

ML maximum likelihood

MLED maximum likelihood estimation detector

NP Neyman-Pearson

pdf probability density function

pmf probability mass function

PRI pulse repetition interval

RAD range-angle-Doppler

RCS radar cross-section

ROC receiver operating characteristics

SPCM spatial covariance matrix

SDS single data set

SMI sample matrix inversion

SNR signal-to-noise ratio

SP subspace projection

STAP space-time adaptive processing

TDMA time division multiple access

TDS two data set

ULA uniform linear array

v-space velocity space

Nomenclature

$\otimes$	Kronecker product
$\odot$	Hadamard product
$*$	linear convolution
$(\cdot)_{m,n}$	bistatic channel formed by the m^{th} transmitter and n^{th} receiver
$(\cdot)^*$	complex conjugate operator
$(\cdot)^H$	Hermitian operator (complex conjugate transpose)
$(\cdot)^T$	transpose operator
$(\cdot)^{-1}$	inverse operator
$\lvert\cdot\rvert^2$	modulus of a scalar or Euclidean norm of a vector
$\lvert\cdot\rvert$	determinant operator
$\partial(\cdot)$	partial derivative operator
$\text{col}_k(\cdot)$	k^{th} column of a matrix
$E[\cdot]$	expectation of a random variable or vector
$\text{etr}(\cdot)$	exponential of the trace of a matrix
$\exp(\cdot)$	exponential of a number
$\log(\cdot)$	natural logarithm of a number
$\text{Tr}(\cdot)$	matrix trace
$\text{var}(\cdot)$	variance of a random variable or vector
$\mathbf{0}$	zero vector
$\mathbb{0}$	set of elements that are all equal to zero
α	complex amplitude of the reflected waveform from a moving target
$\widehat{\alpha}$	ML estimate of complex amplitude of the reflected radar waveform
$\mathbb{\alpha}$	set of complex amplitudes of the reflected MIMO radar waveforms
$\alpha(t, f)$	Woodward's narrowband radar waveform ambiguity function
$B(x, y)$	beta function
$\delta(x)$	continuous Dirac delta function
ϵ	positive constant used in the proof of Lindeber'g condition
ε	threshold for adding contributions to the compressed MLED likelihood
γ	detection threshold

$\widehat{\gamma}$	detection threshold of modified MLED
γ_c	temporal autocorrelation values of clutter with ICM
$\mathbf{\Gamma}$	covariance matrix of clutter fluctuations due to ICM
ζ	random variable associated with the bistatic GMLED
η	random variable associated with $1 + \boldsymbol{g}^H \boldsymbol{Q}^{-1} \boldsymbol{g}$
θ_{rx}	angle between the target and the normal to a receiver ULA
θ_{tx}	angle between the target and a radar transmitter
κ	weight of the likelihood contribution in the modified multistatic MLED
κ_c	spectral standard deviation of clutter with ICM
λ	non-centrality parameter of an F distribution
$\widetilde{\lambda}$	non-centrality parameter first-order ML estimator
λ_o	radar operating wavelength
μ_a	mean associated with the Gaussian approximation to the Fejér kernel
μ_G	mean of GMLED detection random variable
μ_M	mean of MLED detection random variable
μ_x	mean associated with the Gaussian approximation to the Fejér kernel
ν	GMLED detection threshold
ξ	random variable associated with the proposed additional term to the MLED
ρ	SNR of reflected radar waveform observed in interference
σ	standard deviation of a Gaussian random variable
σ_c^2	power of clutter returns observed in the system
σ_G	standard deviation of GMLED detection random variable
σ_M	standard deviation of MLED detection random variable
σ_v	velocity standard deviation of clutter with ICM
σ_w^2	power of AWGN observed in the system
σ_x	standard deviation of the Gaussian approximation to the Fejér kernel
$\chi(t, f)$	radar cross-ambiguity function between two waveforms
$\mathbb{C}$	set of all complex numbers
$\mathbb{R}$	set of all real numbers
$\mathbb{R}_{\mathbb{s}}$	set of STAP interference covariance matrices from a certain geolocation
$\mathbb{X}$	set of STAP observation matrices from a certain geolocation
$\mathbb{Z}$	set of all whole numbers
$\sim\mathcal{C}\chi_K^2$	complex chi-squared distribution with K DOF

$\sim\mathcal{B}(n,p)$	n-trial binomial distribution with success rate p
$\sim\mathcal{CN}_k$	k-variate complex normal distribution
$\sim\mathcal{C}W_k(K)$	k-variate complex Wishart distribution, K DOF and identity scaling matrix
$\sim\mathcal{N}$	normal distribution
$\sim\ln\mathcal{N}$	log-normal distribution
A	region of radar ambiguity space centred around the origin
$\boldsymbol{A}$	matrix linked with the numerator distribution of the MLED and GMLED
$\boldsymbol{a}$	spatial steering vector of a clutter source in the GCM
a	parameter related to the width of a single GP waveform
$\boldsymbol{B}$	matrix linked with the denominator distribution of the MLED and GMLED
$\boldsymbol{b}$	temporal steering vector of a clutter source in the GCM
B_W	spectrum of a single GP radar waveform
$C(A)$	area of a given region A in the radar waveform ambiguity space
d	spacing between receiver ULA's elements
$\boldsymbol{e}$	the first elementary vector $[1,0,\ldots,0]^T$
f_Δ	frequency separation between two radar FDMA waveforms
f_b	frequency bound on the rectangular region A of ambiguity space
f_d	temporal (Doppler) frequency of incoming STAP target signal
f_s	spatial frequency of incoming STAP target signal
f_{T_G}	pdf associated with the GMLED detection variable
f_{T_M}	pdf associated with the MLED detection variable
$\widehat{f}_{T_M}$	pdf associated with the modified MLED detection variable
$\boldsymbol{g}$	coherent sample mean in reduced-rank STAP
$\boldsymbol{H}$	projection matrix to the orthogonal subspace of the target steering vector
$\boldsymbol{H}_c$	subspace of the clutter steering vectors
$\boldsymbol{h}_a$	APES filter
H_0	absence of target hypothesis for the origin of radar observations
H_1	presence of target hypothesis for the origin of radar observations
$\boldsymbol{I}$	identity matrix
$\boldsymbol{k}$	Doppler response of a bistatic radar pair to moving target
K	number of uncorrelated temporal observations in CUT
K_t	number of training data snapshots in TDS algorithms
K_T	number of radar pulses per CPI

L	degrees of freedom
M	number of transmitters in MIMO radar setup
$\boldsymbol{M}^0$	ML sample covariance estimate of STAP snapshots in the absence of target
$\boldsymbol{M}^\alpha$	ML sample covariance estimate of STAP snapshots in the presence of target
$\boldsymbol{n}_c$	clutter in standard STAP observation vector from a range gate
$\boldsymbol{n}_w$	AWGN in standard STAP observation vector from a range gate
N	number of receiver ULAs in MIMO radar setup
N_a	size of discretised angle search space that each receiver ULA scans
N_c	number if independent clutter sources per bistatic iso-range
N_d	size of discretised D-space that each receiver iterates through
N_r	number of range gates in radar system
N_v	size of discretised v-space that each receiver iterates through
$\boldsymbol{N}$	combined noise and clutter matrix in rearranged STAP observations
$\boldsymbol{N}_c$	clutter matrix in rearranged STAP observations
$\boldsymbol{N}_w$	AWGN matrix in rearranged STAP observations
p	success rate of proposed additional term to the multistatic MLED
P	number of spatial observations in each temporal snapshot in CUT
$\boldsymbol{P}_\perp$	projection matrix to the subspace orthogonal to the one spanned by clutter
P_d	probability of detection
$\widehat{P}_d$	probability of detection of modified MLED
P_{fa}	probability of false alarm
$\widehat{P}_{fa}$	probability of false alarm of modified MLED
P_T	number of listening elements per receiver ULA
$\boldsymbol{Q}$	SDS SPCM estimate from the APES filter
$Q(x)$	Q-function associated with the tail probability of a standard Gaussian
$\boldsymbol{R}$	SPCM of iid clutter and noise in the STAP snapshots
$\widehat{\boldsymbol{R}}$	sample estimate to the SPCM of STAP snapshots
$\boldsymbol{R}_c$	full spatio-temporal covariance matrix of STAP clutter
$\boldsymbol{R}_s$	SPCM of iid clutter in the STAP snapshots
$\boldsymbol{s}$	spatial steering vector of rearranged STAP target observations
$\widetilde{\boldsymbol{s}}$	whitened rotated spatial steering vector of rearranged STAP observations
$\boldsymbol{s}_s$	spatial steering vector of STAP target signal
$\boldsymbol{s}_t$	temporal steering vector of STAP target signal

T	radar transmit waveform PRI
t_Δ	time separation between two radar TDMA waveforms
t_b	time axis bound on the rectangular region A of ambiguity space
T_M	MLED detection variable
$\boldsymbol{T}_M$	MLED likelihood function for all normalised Doppler frequencies
$\widetilde{\boldsymbol{T}}_M$	compressed subspace of MLED likelihood function
T_G	GMLED detection variable
T_W	time duration of a transmitted radar waveform in one CPI
$\boldsymbol{U}$	unitary matrix
$u(t)$	continuous radar waveform for Doppler detection
$V(A)$	volume of the radar ambiguity function in a given region A
V_0	volume of the radar ambiguity function at the origin (0,0)
V_{M0}	volume of the M-waveform MIMO ambiguity function at the origin (0,0)
$\boldsymbol{v}$	velocity of target in 2-D
$\boldsymbol{v}_t$	velocity of radar transmitter in 2-D
v_x	velocity of target in the x-dimension
v_y	velocity of target in the y-dimension
$\boldsymbol{x}$	standard STAP observation vector from a range gate
$\boldsymbol{X}$	rearranged STAP observation matrix from a range gate
$\widetilde{\boldsymbol{X}}$	whitened and rotated rearranged STAP observations from a range gate
$\boldsymbol{Z}$	training data matrix for TDS detection STAP algorithms

Chapter 1
Introduction

The invention of modern radar has been largely credited to Robert Watson-Watt in 1935 [1]. It played an instrumental part in deciding the outcome of World War II and has seen numerous applications since then. While the main interest in radar has always been due to its military uses, commercial air travel has also become dependent on it. Other important applications include weather forecast, astronomy, road traffic control, naval detection and ranging, geology, remote sensing and mapping, medical imaging, etc.

Radar has seen a lot of improvements throughout the decades since its creation. A lot of these improvements can be attributed to the hardware advances that have become available over the past few decades: from continuous waveform to pulse-Doppler radar [2,3], from monostatic to bistatic [4] and multiple-input multiple-output (MIMO) applications [5], etc. These allow for improved detection methods to be implemented through the physical radar setup.

Another area where radar performance has seen a lot of improvement is the signal processing of the observation data collected by the physical installation. With the high computational power available nowadays [6], better target detection algorithms are being developed. The ability to quickly process high quantities of data has lead to the development of detection methods like space-time adaptive processing (STAP) [7] that would have been impossible to implement in the past.

This thesis focuses on the signal processing improvements to radar performance, but makes use of the physical advances provided by widely-spaced (multistatic) MIMO setups that can be implemented nowadays. A number of MIMO algorithms have been developed in the framework of STAP that improve the target detection process in a practical radar scenario. While traditional detectors use a secondary data set for training and a primary data set for operation, the focus in this thesis will be exclusively on single data set (SDS) detection methods that operate blindly and without any sources of prior knowledge on the background interference.

1.1 Motivation

This thesis proposes a potential way of combining multiple concepts in radar research that are currently considered to be the state-of-the-art. The two main such principles are MIMO and SDS detection. While STAP for radar detection may not be considered novel, it has become practical only recently due to the advances in the available real-time computational power for digital signal processing [6].

As all operations reliant on radiowave transmission, radar detection suffers from background noise and interference. In radar, the main interference source is the reflection of the transmitted signal from objects or surfaces other than the actual target. If strong enough, these reflections give rise to the detection of false alarms - signals classified as returns from moving airborne targets that don't actually exist [3, 8]. The problem is challenging because this type of interference is coloured and is not necessarily stationary or homogeneous. To deal with clutter, a target detection algorithm needs to be able to estimate its characteristics and suppress it from the incoming observations. Most traditional algorithms are based on estimating and inverting the covariance matrix of the clutter observed in a particular transmission [9, 10]. This can whiten the process and thus make it easier to average out [11]. Other more recent algorithms use different methods to estimate and project the clutter subspace from the target one [12–14]. In both cases this involves some prior knowledge of the clutter attained before the primary observations are tested. Covariance estimation methods in particular require a secondary set of training observations to estimate the statistics of the clutter [9, 10]. This training set must be target-free and homogeneous with respect to the clutter statistics in the primary observations. In most cases a radar installation will search a certain range for potential targets; it is assumed that outside the investigated range, referred to as the cell under test (CUT), the data coming from other distances to the radar is target-free. Thus, if the clutter statistics of ranges outside the CUT is homogeneous, it can directly provide the samples necessary to perform covariance estimation and inversion.

In some scenarios the data coming from ranges outside the CUT cannot be used for covariance estimation. A rapidly-changing environment or a diverse physical background can result in inhomogeneous statistics of the clutter coming from locations that are otherwise relatively close [15]. In other cases the observed area is target-rich, so obtaining enough target-free samples to characterise and suppress the interference is not possible [16]. This justifies the need to develop SDS detection algorithms that perform both interference estimation and target detection

on the same primary data set and require no training samples [12, 13, 17–21]. These algorithms offer more flexibility than traditional target detectors since they can operate under a wider range of conditions and environments. Even if a reliable training data set can be obtained, SDS detection algorithms can still be used to further enhance the performance of the existing methods [19]. This thesis builds upon the work of the previously developed maximum likelihood estimation detector (MLED) and generalised maximum likelihood estimation detector (GMLED) algorithms for SDS clutter covariance estimation and target detection [17–21].

The other major focus of this thesis is multistatic radar. The application of the principles of MIMO in the field of radar research has gained a significant popularity in the past decade. The main reason for this interest comes from the improvements in processing power and data transmission that have enabled the practical implementation of multistatic radar [22–24]. MIMO is the natural direction of improvement when the benefits of developing new mono/bistatic radar detection algorithms become incremental. It offers an overall increase in performance that constitutes higher accuracy of target localisation, higher detection rate under a certain false alarm probability, increased spatial and angular diversity, increased resolution [25–41]. Moreover, widely-spaced MIMO radar is one of the potential countermeasures to stealth technology [42, 43] which provides significant motivation for research on the topic.

Multistatic radar offers great benefits to target detection, but it also vastly increases the complexity of the problems that have to be solved in its practical implementation. In addition to all the challenges in designing a mono/bistatic system, data exchange and synchronisation must be taken into account. When the radar elements are widely-separated, sharing their observations and their results to produce one target detection decision can involve lengthy transmissions. Before fusing this information, it has to be synchronised to reflect the different locations and parameters associated with the individual units in the network [44]. Multistatic radar is also associated with more complex issues in the field of waveform design, orthogonality, and ambiguity [45–47]. It is also important to analyse and characterise the performance of a MIMO system with respect to the number of elements it is composed of. When a radar installation consists of multiple units, physical cost can become a significant issue [24]; thus the benefits and drawbacks of every additional transmitter or receiver added to a multistatic radar setup must be carefully evaluated in the design stage.

This thesis offers solutions to most of the practical problems associated with the implementation of a multistatic SDS detection algorithm. It outlines the overall process of designing the detector

and using it in a physical MIMO radar setup.

1.2 Contributions and outline

This thesis involves a series of contributions that can all be combined to form an outline of the practical implementation of a multistatic SDS detector based on clutter covariance estimation and inversion. The rest of the thesis is outlined as follows.

Chapter 2 contains the background materials on which the work in this thesis is built. It introduces the basic principles of STAP for radar detection. A historical overview of the existing target detection methods and the progression to MIMO radar and SDS detection is also given. The challenges associated with the ambiguity function in MIMO radar involving orthogonal waveforms is introduced. The signal model, the physical radar parameters, the assumptions undertaken, and the general outline of the detection procedure developed in this thesis can also be found in this chapter.

Chapter 3 is devoted to the derivation of the multistatic MLED and GMLED detection algorithms. It assumes ideal transmission and data synchronisation between the radar nodes and focuses on the maximum likelihood (ML) combination of the results from the individual bistatic transmit-receive pairs. A Gaussian approximation to the statistics of the multistatic detectors is proposed in order to facilitate the simple and easy analysis of the the performance of the MIMO system. This enables the most suitable cost-to-performance ratio for a specific scenario to be calculated at the design stage. Appendix B contains a mathematical proof of some of the concepts needed to facilitate the Gaussian approximation developed in Chapter 3. It involves an investigation into Lindeberg's generalised version of the central limit theorem (CLT) for convergence of independent and non-identically distributed random variables to a Gaussian random variable.

Chapter 4 proposes solutions to some of the major challenges associated with the practical implementation of the multistatic MLED algorithm. A pre-transmission data compression method is described that would reduce the amount of information that the radar network will have to exchange to reach a detection decision. A solution to the issue of synchronising the information from the individual radar nodes is proposed that involves a likelihood projection from frequency to velocity space. Based on the suggested methods, a modification to the multistatic MLED algorithm is proposed that combines the soft and hard decisions coming from the dif-

ferent bistatic pairs in the MIMO radar setup. It is shown that the new algorithm provides a slightly better performance than the standard one while requiring less information exchange in the radar network.

Chapter 5 deals with the practical issue of waveform orthogonality experienced by growing MIMO radar networks and the restrictions that it imposes on the resulting ambiguity function. It proposes a frequency and/or time orthogonality solution that circumvents the inherent reduction of the area of ambiguity space that can be kept clear of sidelobes in the multistatic scenario. An example is investigated that involves a waveform consisting of multiple Gaussian-shaped pulses. It is shown that frequency orthogonality between the different waveforms in the MIMO system relaxes the ambiguity bound developed for waveforms orthogonal in fast-time.

Chapter 6 summarises the work done in this thesis. It contains a discussion on the potential directions where future research can be conducted based on the ideas developed here.

Chapter 2
Single data set detection in space-time adaptive processing

2.1 Introduction

Target detection methods have seen some vast improvements since the invention of radar in 1935 [1]. These advances have come both in the form of better hardware and signal processing algorithms for estimation and detection. The traditional rotating analogue antenna is slowly being replaced by a digitally-steered uniform linear array (ULA) [48]. This gave rise to the development of STAP for moving target detection [11]. In theory STAP could provide improved target detection rate and better clutter mitigation. However, at the time of its introduction the concept was impractical; it is a computationally-heavy signal processing method that was impossible to implement in real time due to hardware limitations [49]. In the past few decades Moore's Law [6] has been diligently observed, and the available computational power for signal processing has been vastly increased. As a result, STAP has become one of the most widely-researched method for moving target detection through radar [7]. A brief introduction to the principle of operation of STAP is provided in Section 2.2. The target and clutter signal models that are used in this thesis are described there as well.

Most STAP target detection algorithms are based on covariance estimation of the underlying background clutter and interference processes [15, 50–52]. The statistical estimations are usually reliant on the assumption that a target-free training data set of observations is available to build a sample covariance matrix and perform sample matrix inversion (SMI) [9, 10]. Because these algorithm perform detection on a primary set of observations while using a secondary set of training data for clutter estimation, this work will refer to them as two data set (TDS) detection methods. Some of the fundamental covariance-based traditional detectors are described in Section 2.3.

For more than a decade TDS algorithms have been the norm in radar detection. While robust and relatively reliable, their need for target-free training data with statistics that match that of

the background clutter and interference cannot always be met and is ultimately considered a shortcoming. This gave rise to the idea of SDS detection that performs both the estimation and detection on the same set of observations. Some SDS algorithms are based on covariance estimation [17–21] while others use subspace projection methods to isolate and suppress clutter from the observations [12–14]. Some examples relevant to the work in this thesis will be shown in detail in Section 2.4.

As the available real-time processing power has increased significantly in the past decade, MIMO radar has become a very popular research topic [25–41]. One application of MIMO is naturally covered in part by STAP since the receiver consists of multiple elements. A STAP implementation with an ULA transmitter is an example of a coherent closely-spaced MIMO radar setup [25–28]. Statistical widely-spaced (multistatic) radar has also attracted a lot of interest due to the spatial diversity that it provides in the target detection problem [28–41]. As this thesis will focus mainly on multistatic Doppler radar, Section 2.5 will provide some more details on the recent advances in this research area.

One of the limitations imposed on MIMO radar is the reduction of the region in the ambiguity function that is clear of sidelobes as the radar network grows larger [45, 46]. This problem arises in the scenario where multiple orthogonal waveforms are transmitted in a system and has to be considered in a practical MIMO implementation. Section 2.6 provides a short description and the mathematical framework in which the ambiguity problem is posed.

The general problem solved in this thesis is described in Section 2.7. The multistatic signal model and some of the physical radar parameters used in the simulated scenarios are discussed there. An overview of the physical implementation of the target detection solutions derived in this thesis is given.

2.2 Space-time adaptive processing signal model

STAP is a concept in radar detection that was first introduced in 1973 [11]; it has attracted significant attention in recent years due to the increased computational power available for real-time signal processing [7, 15, 17–21, 49–56]. The STAP receiver consists of multiple listening elements that are closely-spaced together. They don't have to be arranged in any special configuration, although this thesis will focus on ULAs of P_T elements each for simplicity and consistency. The focus in this thesis is on pulse-Doppler radar that transmits K_T pulses in

one coherent pulse interval (CPI); the Doppler shifts between the reflected pulses are used to perform target detection and ranging. STAP is an adaptive detection method that simultaneously processes the spatial P_T pulse returns observed by the individual ULA elements and the temporal K_T returns observed by the receiver from consecutive pulses.

The incoming STAP target data is characterised by the spatial steering vector $\boldsymbol{s}_s(f_s)$ and the temporal steering vector $\boldsymbol{s}_t(f_d)$. Assuming a ULA receiver and a constant target velocity, both of these vectors take a Vandermonde form and depend on the spatial and temporal frequencies of the target f_s and f_d respectively.

$$\boldsymbol{s}_s(f_s) = \left[1,\ e^{j2\pi f_s},\ \ldots\ ,\ e^{j2\pi(P_T-1)f_s}\right]^T \tag{2.1}$$

$$\boldsymbol{s}_t(f_d) = \left[1,\ e^{j2\pi f_d},\ \ldots\ ,\ e^{j2\pi(K_T-1)f_d}\right]^T \tag{2.2}$$

The superscript $(\cdot)^T$ indicates the transpose operator. The spatial steering vector characterises the response of the receiver ULA to a signal coming at an angle θ_{rx} (Figure 2.1) to the normal of the array. The corresponding spatial frequency is thus shown in [4]

$$f_s = \frac{d}{\lambda_o}\sin\theta_{rx} \tag{2.3}$$

where d is the spacing between the ULA's elements, and λ_o is the radar operating wavelength. For convenience, the spacing will be chosen as half the wavelength of the incoming radar signal so that

$$f_s = \frac{1}{2}\sin\theta_{rx} \tag{2.4}$$

Note that in this work two-dimensional (2-D) motion and position are assumed for all targets and radar elements. This is a simplification done for convenience in order to demonstrate the concepts developed in the thesis [12, 33–35, 44, 57, 58]. A short discussion of the assumption and the procedure to address the more practical scenario of three-dimensional (3-D) motion is found in [44], where the 2-D simplification is achieved by fixing the altitude searched for a potential target. The work can therefore be extended to a real scenario by accounting for the altitude (or the elevation angle in a polar coordinate system) between different elements in addition to the azimuth. If the altitude is discretised, the algorithms developed in this thesis would be executed for each value in the parameter search space in addition to the other spatio-temporal searches already performed. This would result in a higher computational complexity when deployed in a real 3-D search scenario.

In a bistatic STAP scenario the transmit antenna and the receiver ULA are individual elements with different locations [8, pp.655-664]. Let the target velocity vector $\boldsymbol{v}$ in 2-D space be split into its x-y-dimension individual Cartesian components

$$\boldsymbol{v} = [v_x,\ v_y]^T \tag{2.5}$$

Assuming the radar elements are stationary, the temporal (Doppler) frequency f_d is the normalised Doppler frequency shift that consecutive pulses in a CPI experience due to the movement of the target. If the angle between the target and the transmitter is θ_{tx} (Figure 2.1), the bistatic Doppler frequency is described in [12]

$$f_d = \frac{v_x T}{\lambda_o}(\cos\theta_{tx} + \cos\theta_{rx}) + \frac{v_y T}{\lambda_o}(\sin\theta_{tx} + \sin\theta_{rx}) \tag{2.6}$$

where T is the pulse repetition interval (PRI) of the radar's transmit waveform.

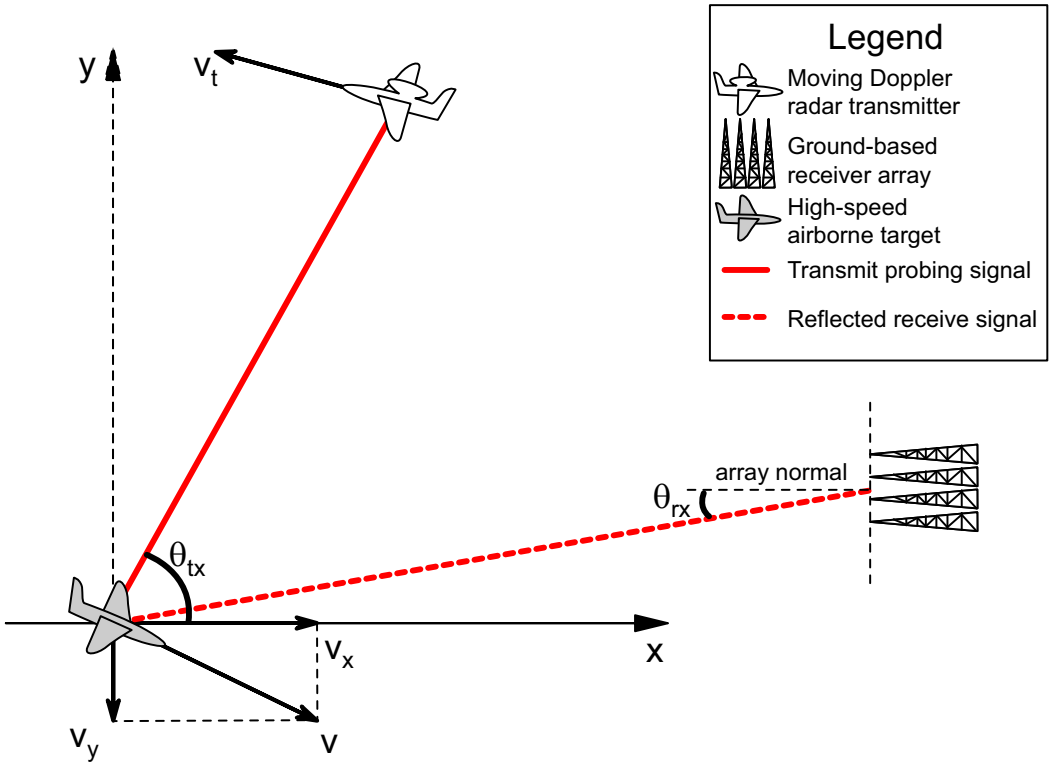

Figure 2.1: *Geometric parameters in a bistatic radar setup with a mobile transmitter and ground-based receive ULA*

This work investigates clutter returns that arise in the case of a mobile radar installation. There-

fore, the velocity of the radar elements also influences the Doppler frequency shift in the observation signal. As the frequency shift is dependent on the relative motion between the radar installation and the target, it will be assumed for simplicity that the receiver ULA is stationary, and only the transmitter is mobile. If the receiver is moving at a constant velocity, its physical location can be fixed as a reference point for the velocity-position coordinate system; the target and transmitter relative velocities to the system can thus be used, degenerating to the static receiver case investigated here. A new parameter can be defined from (2.6)

$$\boldsymbol{k} = \frac{T}{\lambda_o} \begin{bmatrix} \cos\theta_{tx} + \cos\theta_{rx} \\ \sin\theta_{tx} + \sin\theta_{rx} \end{bmatrix} \tag{2.7}$$

that represents the Doppler response of a bistatic radar pair of a transmitter and a receiver to the relative motion of a target with a certain velocity $\boldsymbol{v}$. If the 2-D velocity of the transmitter is $\boldsymbol{v}_t$, the normalised bistatic Doppler frequency shift that is observed at the receiver is

$$f_d = (\boldsymbol{v} - \boldsymbol{v}_t)^T \boldsymbol{k} \tag{2.8}$$

In STAP, a CPI is associated with a 3-D set of observations and is sometimes referred to as a datacube. The standard form of the STAP datacube is shown in Figure 2.2. The receiver divides the PRI into N_r consecutive delays at which it listens for target waveform returns. This dimension is known as fast-time, and the delay of receiving a target signal determines the distance to the target. Thus the N_r fast-time observations are referred to as range gates. Each range gate consists of the temporal returns from the expected K_T pulses referred to as slow-time observations as well as the P_T spatial observations at the individual ULA elements.

Signal processing in STAP is performed on a single range gate at a time. The range gate contains $\mathbb{C}^{P_T \times K_T}$ samples: the K_T temporal observations from the P_T elements of each ULA are arranged as the columns of the range gate data matrix. The standard STAP signal model from a single range gate stacks the spatial snapshots on top of each other to produce the observation vector $\boldsymbol{x} \in \mathbb{C}^{K_T P_T \times 1}$ (Figure 2.2). If the clutter is represented by the vector $\boldsymbol{n}_c$ and the noise by $\boldsymbol{n}_w$, both of the same size as $\boldsymbol{x}$, then the STAP observation model is described in [49, pp.12-17]

$$\boldsymbol{x} = \alpha \boldsymbol{s}_s(f_s) \otimes \boldsymbol{s}_t(f_d) + \boldsymbol{n}_c + \boldsymbol{n}_w \tag{2.9}$$

where α is the complex amplitude of the reflected target signal seen at the receiver, and $\otimes$

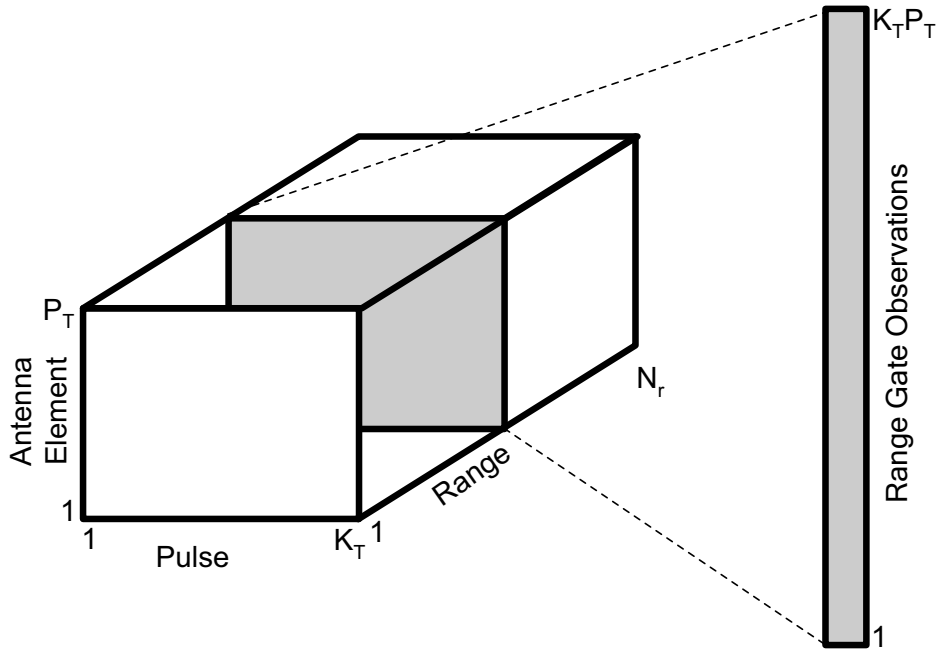

Figure 2.2: *STAP observations datacube in a CPI*

signifies the Kronecker product operator. Additional terms can be added to (2.9) to account for other forms of interference and jamming, but these will not be of interest to the work conducted in this thesis.

Figure 2.3 shows an example physical configuration of two STAP bistatic paths. The transmitter and target are airborne, while the receiver ULAs are ground-based. The range gate that contains the target signal in each bistatic pair also contains clutter returns from any reflectors with bistatic ranges equal to that of the target. These generally lie on a 3-D ellipsoid with the transmitter and receiver positioned at its foci [4]. The ground clutter returns on which this thesis focuses thus come from the iso-range contours where the ground plane slices the ellipsoid. If perfectly flat ground is assumed, these contours are standard 2-D ellipses (Figure 2.3). In monostatic radar the ellipses degenerate to circles.

An example of the spectral returns from the clutter in an iso-range that contains a target is shown in Figure 2.4. To simulate a continuous spatio-temporal clutter spectrum, a large number of ground patches are generated that are evenly-spaced along the elliptical iso-range contour for one of the bistatic pairs of Figure 2.3. The respective spatio-temporal frequencies of the patches are plotted in Figure 2.4. Half of the clutter spectrum originates from the receiver ULA frontal direction, while the other half represents the backlobe returns. An example of a

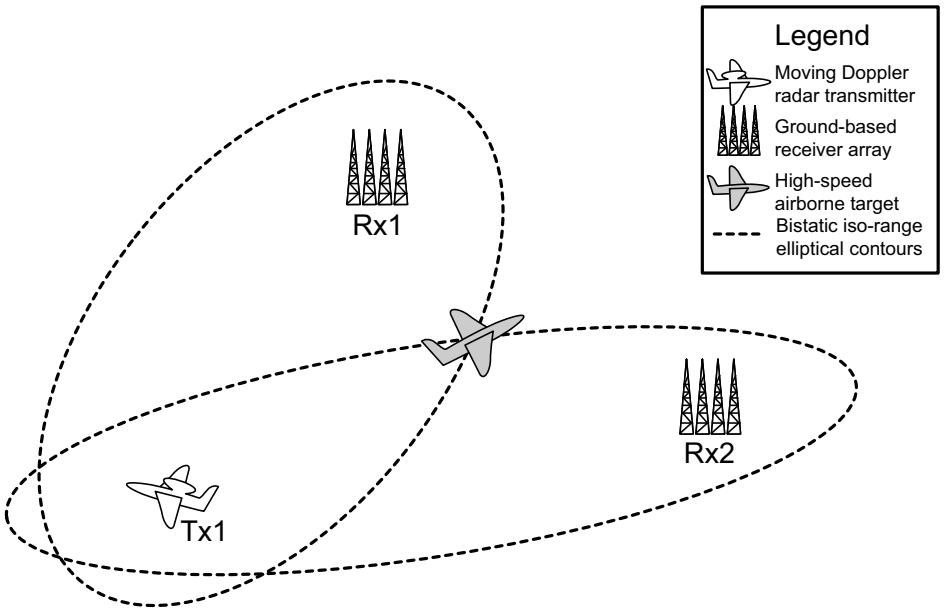

Figure 2.3: *Sources of STAP clutter returns in a multistatic configuration*

jamming signal is also included in the spectrum. Jammers typically come from one direction and aim to interfere with a large portion of the frequency spectrum. Thus they are wideband in their Doppler and narrowband in their spatial frequency [49, p.3]. Figure 2.4 demonstrates the main advantage of STAP and the principle it utilises to enhance target detection. If the target signal is outside of the clutter ridge, it is possible through different detection approaches to reject the clutter while preserving the useful signal. This essentially leads to target detection in an environment where the effective signal-to-noise ratio (SNR) is drastically increased.

The signal models used in this thesis for the observed STAP interference sources are described as follows. The clutter in the system is assumed to be zero-mean complex coloured Gaussian (2.10) with power σ_c^2 and covariance matrix $\boldsymbol{R}_c$; the noise is considered zero-mean complex additive white Gaussian noise (AWGN) with power σ_w^2 (2.11).

$$\boldsymbol{n}_c \sim \mathcal{CN}_{K_T P_T}(\mathbf{0}, \sigma_c^2 \boldsymbol{R}_c) \tag{2.10}$$

$$\boldsymbol{n}_w \sim \mathcal{CN}_{K_T P_T}(\mathbf{0}, \sigma_w^2 \boldsymbol{I}) \tag{2.11}$$

The vector $\mathbf{0}$ represents the zero vector, and $\boldsymbol{I}$ is the identity matrix, both of relevant size to the equation. The normalised covariance matrix of STAP clutter is discussed in detail with the introduction of the general clutter model (GCM) in [49, pp.20-24]. The GCM approximates the continuous field of clutter depicted in Figure 2.3 with a large number of N_c evenly-

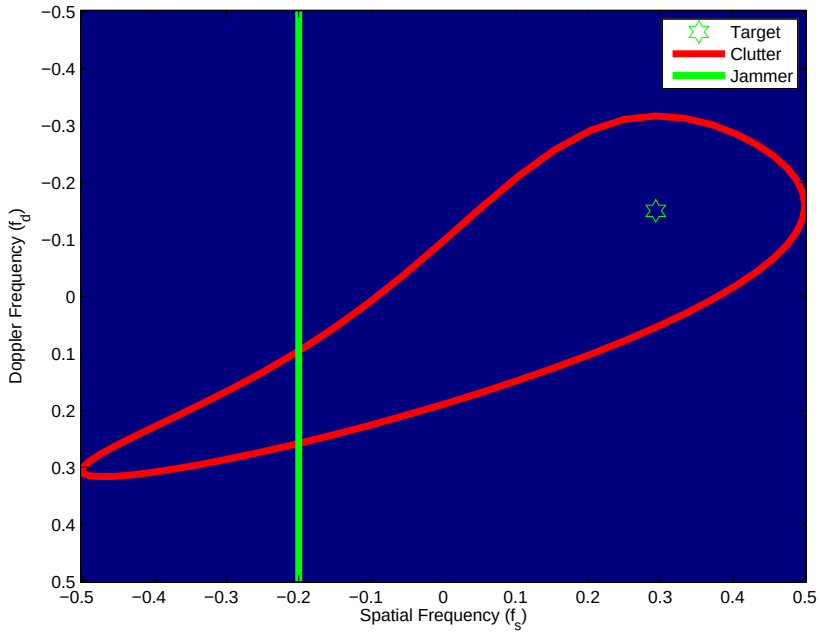

Figure 2.4: *Spatio-temporal spectrum of clutter and jamming returns at a single receiver in a bistatic STAP range gate*

distributed (in azimuth) clutter sources in each bistatic iso-range. It also accounts for intrinsic clutter motion (ICM) which causes slight fluctuations in the clutter statistics between consecutive pulses in a CPI. The autocorrelation of these temporal fluctuations at a time difference m takes the following Gaussian form [49, p.45]

$$\gamma_c(m) = \exp\left\{-\frac{\kappa_c^2 T^2}{2} m^2\right\} \tag{2.12}$$

where κ_c is the spectral standard deviation of clutter normally expressed in terms of the velocity standard deviation

$$\sigma_v = \frac{\lambda_o \kappa_c}{4\pi} \tag{2.13}$$

Typical measured values for the velocity standard deviation in different environments and under different weather conditions can be found in textbooks (e.g. [3, pp.2.25-2.27]). The autocorrelation values (2.12) are arranged in the autocorrelation matrix $\mathbf{\Gamma}$ for the temporal clutter fluctuations

$$\mathbf{\Gamma} = \text{Toeplitz}\left(\gamma_c(0),\ \ldots\ , \gamma_c(K_T - 1)\right) \tag{2.14}$$

The GCM for the STAP clutter covariance matrix with ICM is the combination of all the space-

time contributions coming from the N_c independent clutter patches. Assuming that there are no range ambiguities in the radar scenario, the covariance matrix normalised in power takes the following form [49, pp.23-24]

$$\boldsymbol{R}_c = \sum_{k=1}^{N_c} \left(\boldsymbol{\Gamma}_k \odot \boldsymbol{b}_k \boldsymbol{b}_k^H \right) \otimes \boldsymbol{a}_k \boldsymbol{a}_k^H \tag{2.15}$$

where $\odot$ represents the Hadamard product operator, and the superscript $(\cdot)^H$ signifies the Hermitian transpose. Similar to a moving target, each clutter patch has a spatial steering vector $\boldsymbol{a}_k$ and a temporal steering vector $\boldsymbol{b}_k$. They take the same Vandermonde form as (2.1) and (2.2) where each patch is associated with its own spatial and temporal frequency. These parameters arise from the relative motion between the ground and the bistatic transmitter-receiver pair and can be obtained from (2.4) and (2.8). The dependencies are omitted in the formulas for convenience.

The signal model used throughout this thesis is based on extracting K independent and identically distributed (iid) spatio-temporal snapshots of size P from the STAP observation data. One method for obtaining a set of snapshots that fulfils this criterion is through passing a sliding window over the STAP observations (2.9) from the CUT [14, 19, 21]. A graphical representation of the procedure is provided in Figure 2.5. The samples inside each window form a spatio-temporal local low-dimensional snapshot from the observation data. This windowed data is then vectorised, and the K different vectors are arranged as the columns of the newly-formed observation matrix $\boldsymbol{X}$. If the sliding window approach cannot be applied to a specific setting, multiple iid samples of the full CUT can be used as the K temporal snapshots, and the problem reduces to the one discussed in this thesis.

The observation matrix $\boldsymbol{X}$ thus contains K iid columns, each column representing a snapshot of size P. The matrix thus takes the following form

$$\boldsymbol{X} = \alpha \boldsymbol{s}\boldsymbol{t}^T + \boldsymbol{N}_c + \boldsymbol{N}_w \tag{2.16}$$

The terms $\boldsymbol{N}_c$ and $\boldsymbol{N}_w$ contain in their columns the iid snapshots of the clutter and the AWGN respectively. The process of obtaining the spatial steering vector $\boldsymbol{s}$ and the temporal steering vector $\boldsymbol{t}$ associated with the target signal in the matrix $\boldsymbol{X}$ is depicted in Figure 2.6. The spatial steering vector $\boldsymbol{s}$ is no longer simply linked to the receiver ULA characteristics but rather describes the template of the rearranged target signal in each of the K snapshots of (2.16). Each

extracted spatio-temporal window of observations is associated with its own spatial and temporal steering vectors that are partitions of the ones associated with the full STAP range gate. Their Kronecker product gives the template $\boldsymbol{s}$ of the snapshot, which is now dependent on both the spatial frequency f_s and the temporal frequency f_d.

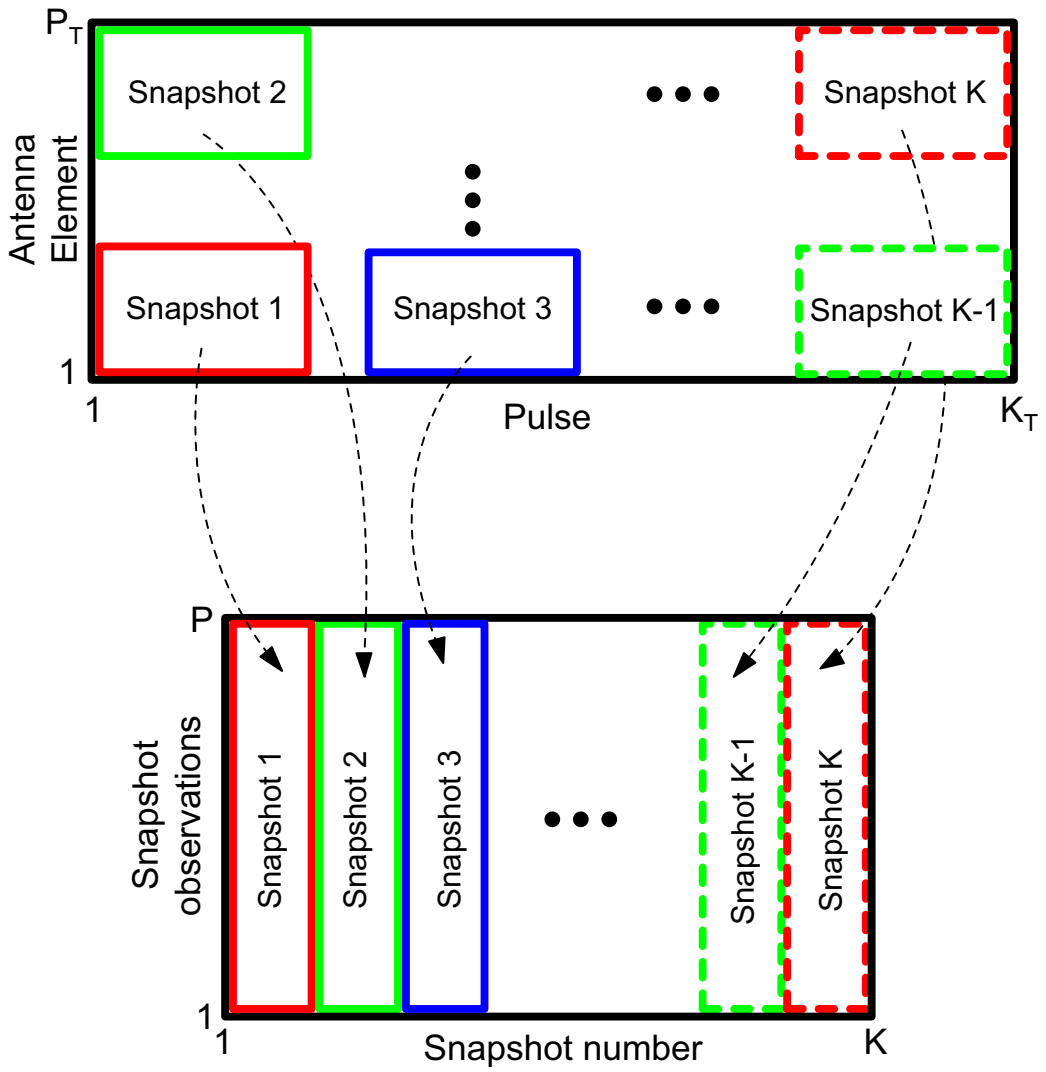

Figure 2.5: *Extracting iid snapshots by passing a sliding window over the STAP range gate observations*

The temporal steering vector $\boldsymbol{t}$ represents the phase relations between the different snapshots. Each window of data is related to the other ones by a phase shift. This phase shift usually depends on both the spatial frequency f_s and the temporal frequency f_d. The spatio-temporal shifts form the snapshot relation, and thus the temporal steering vector $\boldsymbol{t}$. The dependence

of both s and t on the spatial and temporal frequency is omitted in the representations and derivations in this thesis for convenience.

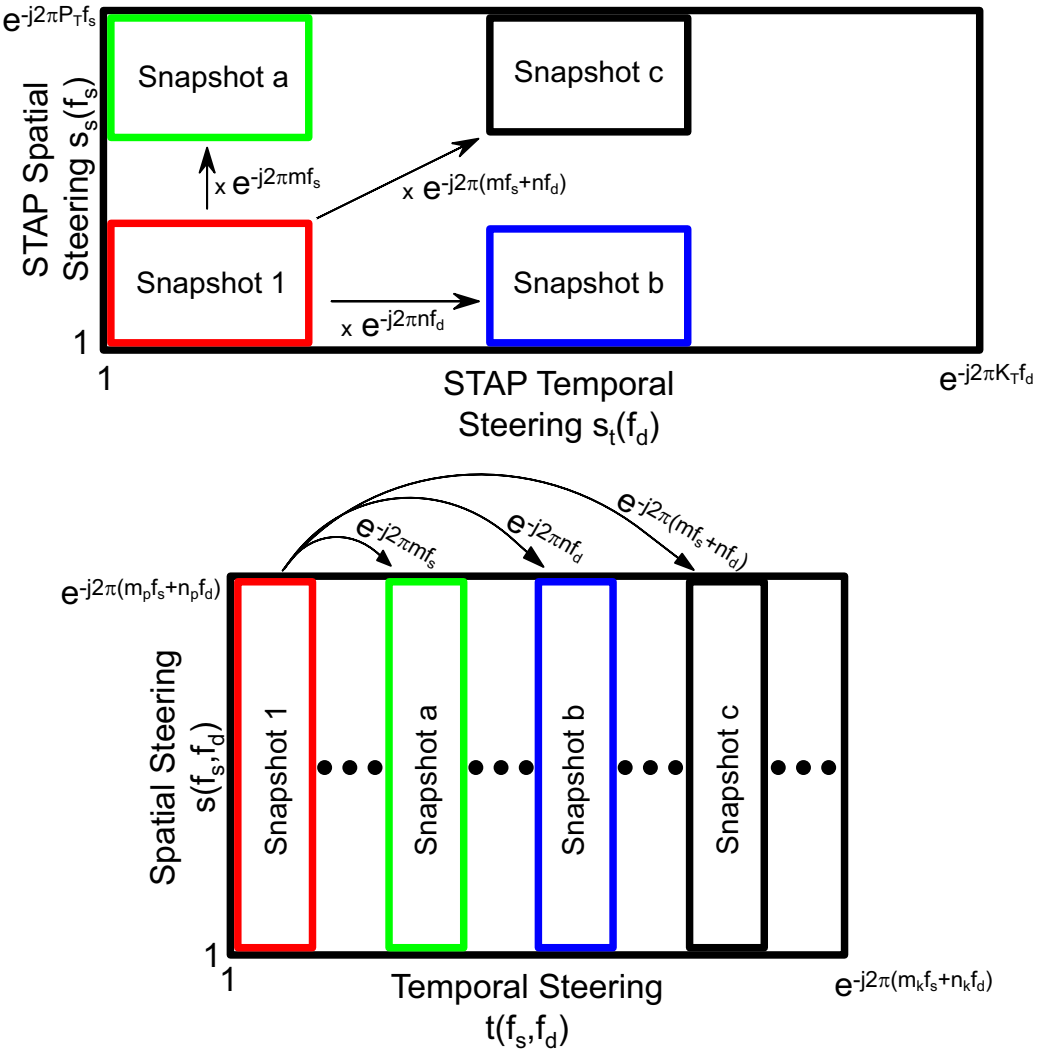

Figure 2.6: *Relationship between the spatio-temporal steering vectors in the iid snapshots obtained from the STAP range gate observations*

If the iid observation snapshots represented by the columns of (2.16) all come from one range gate, the signal model can be seen as a form of reduced-dimension STAP [49, pp.81-93]. If $\mathrm{col}_k(\cdot)$ signifies the k^{th} column of a matrix, then the clutter and noise in each temporally-iid snapshot has the following spatial distribution

$$\mathrm{col}_k(\boldsymbol{N}_c) \sim \mathcal{CN}_P(\boldsymbol{0}, \sigma_c^2 \boldsymbol{R}_s) \tag{2.17}$$

$$\mathrm{col}_k(\boldsymbol{N}_w) \sim \mathcal{CN}_P(\boldsymbol{0}, \sigma_w^2 \boldsymbol{I}) \tag{2.18}$$

where $\boldsymbol{R}_s$ will be referred to as the spatial covariance matrix (SPCM) of the STAP clutter with respect to the adopted model (2.16). The work in this thesis will focus on spatially-adaptive methods for estimating the reduced-rank covariance matrix $\boldsymbol{R}_s$ that is usually much smaller than the full STAP clutter covariance matrix $\boldsymbol{R}_c$.

2.3 Traditional covariance-based two data set detectors

A radar detection algorithm receives a data set of observations and must decide whether a target is present in these observations. From a signal processing standpoint this translates to selecting one of two hypotheses for the model from which the incoming samples originate: H_0 when the data consists of noise and clutter, or H_1 when a target signal is present as well. With the adopted observation signal model (2.16), the two hypotheses are expressed as

$$\begin{aligned} H_0 &: \boldsymbol{X} = \boldsymbol{N}_c + \boldsymbol{N}_w \\ H_1 &: \boldsymbol{X} = \alpha \boldsymbol{s}\boldsymbol{t}^T + \boldsymbol{N}_c + \boldsymbol{N}_w \end{aligned} \tag{2.19}$$

In conventional STAP, the detector is applied to the single snapshot that encompasses the whole range gate (2.9). In the model (2.19) the detection process is performed on the individual snapshots $\text{col}_k(\boldsymbol{X})$ and then the results are combined in the post-detection stage. Since the clutter and noise are independent in each of the $\text{col}_k(\boldsymbol{X})$ by design, the snapshots can be combined before the detection process. The latter is a much more cost-efficient approach and will be assumed in this thesis.

Define the reduced-rank STAP coherent sample mean vector that combines the iid snapshots in the pre-detection phase as

$$\boldsymbol{g} = \frac{1}{K}\boldsymbol{X}\boldsymbol{t}^* \tag{2.20}$$

where the superscript $(\cdot)^*$ indicates the complex conjugate operator. The normalising constant here assumes that the Euclidean norm $|\cdot|^2$ of the temporal steering vector is

$$|\boldsymbol{t}|^2 = K \tag{2.21}$$

which will be used in the derivations throughout this thesis. In (2.20) the target signals in the STAP snapshots are aligned and added coherently, while the temporally-uncorrelated clutter and interference add incoherently.

Traditional target detection algorithms are based on estimating the covariance matrix of the background interference processes and inverting that matrix to whiten and reduce the corruption of the target signal. Let the total SPCM for the noise and clutter in the assumed STAP model be

$$\boldsymbol{R} = \sigma_c^2 \boldsymbol{R}_s + \sigma_w^2 \boldsymbol{I} \tag{2.22}$$

The optimal covariance-based target detector is the matched filter (MF) detector developed in [11]

$$\frac{|\boldsymbol{s}^H \boldsymbol{R}^{-1} \boldsymbol{g}|^2}{\boldsymbol{s}^H \boldsymbol{R}^{-1} \boldsymbol{s}} \underset{H_0}{\overset{H_1}{\gtrless}} \gamma \tag{2.23}$$

where γ is the detection threshold for selecting one of the two hypotheses. In the derivation the MF has been normalised to exhibit the constant false alarm rate (CFAR) property which makes the false alarm rate of a detector independent from the power and structure of the background noise and interference. This is very desirable since the threshold γ can be fixed at the design stage to provide a certain false alarm rate, and the detection probability would vary depending on the SNR in the system.

While optimal in the ML sense, the MF is impractical as it requires knowledge of the clairvoyant covariance matrix $\boldsymbol{R}$. In practical scenarios the matrix is usually estimated from the data, a method known as sample matrix inversion (SMI). Most traditional covariance-based detectors assume the availability of K_t target-free training data snapshots of the background noise and interference. If these snapshots are arranged as the columns of the training data matrix $\boldsymbol{Z}$, an ML estimate to the interference spatial covariance matrix (SPCM) can be constructed.

$$\widehat{\boldsymbol{R}} = \frac{1}{K_t} \boldsymbol{Z} \boldsymbol{Z}^H \tag{2.24}$$

The training data in $\boldsymbol{Z}$ usually comes from range gates neighbouring the CUT [9, 10]. If the interference is homogeneous across range and the distribution of targets in the search area is relatively sparse, the statistics of the secondary data is likely to reflect that of the clutter in the primary observations. As this is not universally the case, different methods that aid the selection of the viable training data have been proposed. If the shape and structure of the surrounding terrain is available, a knowledge-aided selection process for the range gates containing homogeneous clutter can be implemented [59]. In general a non-homogeneity detector [60] can be added to STAP in order to discard training data that does not conform to the statistics of the clutter in the CUT. Figure 2.7 depicts graphically the general sources of secondary data in the

STAP datacube. They are usually taken outside a range region around the CUT isolated by guard gates to prevent angle-Doppler spreading of the target signal into the training data.

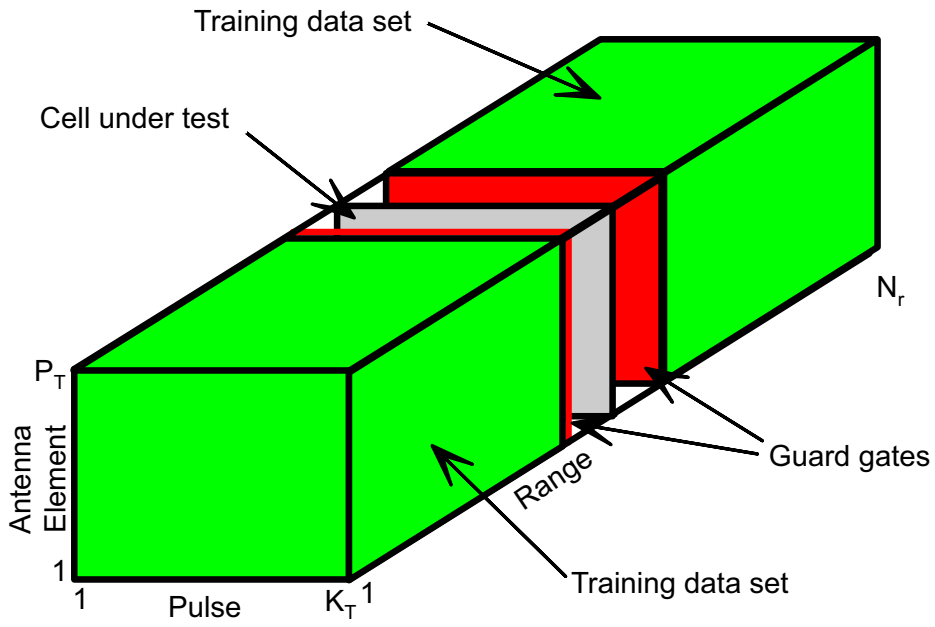

Figure 2.7: *Range gates for secondary training data in STAP TDS detectors*

Due to the requirement of two sets of observations, the algorithms discussed here are referred to as two data set (TDS) detectors. One of the most well-known such detector is the adaptive matched filter (AMF) proposed in [10]. It is a direct derivation from the MF detector in (2.23) where the clairvoyant SPCM $\boldsymbol{R}$ has been replaced by its ML estimate from (2.24).

$$\frac{|\boldsymbol{s}^H \widehat{\boldsymbol{R}}^{-1} \boldsymbol{g}|^2}{\boldsymbol{s}^H \widehat{\boldsymbol{R}}^{-1} \boldsymbol{s}} \underset{H_0}{\overset{H_1}{\gtrless}} \gamma \tag{2.25}$$

The AMF is a relatively simple test in terms of computational power, effectively requiring the inversion of one matrix constructed from the training data set. It preserves the CFAR property of its source algorithm.

Similar to the AMF is Kelly's generalised likelihood ratio test (GLRT) detector proposed in [9].

$$\frac{|\boldsymbol{s}^H \widehat{\boldsymbol{R}}^{-1} \boldsymbol{g}|^2}{\boldsymbol{s}^H \widehat{\boldsymbol{R}}^{-1} \boldsymbol{s} \left(K_t + \boldsymbol{g}^H \widehat{\boldsymbol{R}}^{-1} \boldsymbol{g} \right)} \underset{H_0}{\overset{H_1}{\gtrless}} \gamma \tag{2.26}$$

In the derivation of the GLRT the covariance matrix $\boldsymbol{R}$ is treated as an unknown random parameter and is included in the maximisation process, while in the AMF it is simply replaced by

its ML estimate. Moreover the GLRT includes the observations from the primary data set as well which is reflected in the additional scaling parameter in the denominator of (2.26). Thus it provides a slightly better estimate and is more robust to small variations in statistics between the CUT and its neighbouring range gates [9].

2.4 Covariance-based single data set detection

The AMF and the GLRT described in Section 2.3 have been used predominately in target detection for decades after their introduction; however, they both suffer from one drawback - the need for training data. The training data traditionally comes from range gates neighbouring the CUT outside of a chosen guard region (Figure 2.7). However, the statistics of the interference across different ranges may not always be the same. Some environments are prone to producing non-stationary or non-homogeneous clutter returns. In addition, a target-rich scenario will make it more difficult to select range gates that contain only interference. Such challenges could significantly degrade the performance of TDS algorithms such as the AMF and the GLRT. This justifies the need for reliable SDS algorithms to be developed that perform both detection and estimation on the primary observation data set and require no training samples. It is clear from Figure 2.7 that a SDS detector will have a lot less data than traditional TDS detectors to perform clutter estimation and cancellation since all processing is done only on the CUT. However, irrespective of the background conditions and the environment, SDS detection eliminates the issue of clutter homogeneity and range-stationarity since all information comes from the same range and time.

SDS covariance estimation has been discussed in detail in the development of the amplitude and phase estimation (APES) filter in [61]. The problem solved by APES can easily be transferred to the STAP framework. It is the spatial filter $\boldsymbol{h}_a$ that minimises the Euclidean distance between a given temporally-iid data set $\boldsymbol{X}$ and a phasor of known structure $\boldsymbol{t}$ and unknown complex amplitude α.

$$\min_{\boldsymbol{h}_a,\alpha} \left(\boldsymbol{h}_a^H \boldsymbol{X} - \alpha \boldsymbol{t}^T\right) \left(\boldsymbol{h}_a^H \boldsymbol{X} - \alpha \boldsymbol{t}^T\right)^H \quad \text{s.t.} \quad \boldsymbol{h}_a^H \boldsymbol{s} = 1 \tag{2.27}$$

The variables in (2.27) and the ones in the STAP model adopted in this thesis (2.16) are the same since the problems can be made practically identical. The APES filter forms the ML

estimate of the complex amplitude of the phasor $\boldsymbol{t}$ inside the observation signal.

$$\widehat{\alpha} = \frac{\boldsymbol{s}^H \boldsymbol{Q}^{-1} \boldsymbol{g}}{\boldsymbol{s}^H \boldsymbol{Q}^{-1} \boldsymbol{s}} \tag{2.28}$$

The matrix $\boldsymbol{Q}$ is defined as

$$\boldsymbol{Q} = \frac{1}{K} \boldsymbol{X} \boldsymbol{X}^H - \boldsymbol{g}\boldsymbol{g}^H \tag{2.29}$$

and is a sample estimate to the covariance of the leftover signal in the observations $\boldsymbol{X}$ once the complex phasor $\boldsymbol{t}$ is removed from them. It characterises the statistics of the estimation error of the APES filter.

In the radar detection problem a search over a range of normalised Doppler frequencies is performed. If a moving target is present in the search space, the phasor $\boldsymbol{t}$ will match the slow-time pulses of the reflected radar waveform at the target Doppler frequency. Once the amplitude of this phasor is estimated and it is projected out of the observation signal $\boldsymbol{X}$, the remaining components provide a natural estimate to the noise and clutter in the received samples. Therefore the APES filter can be directly applied to the radar detection problem to produce the matrix $\boldsymbol{Q}$ as the SDS estimate to the interference covariance matrix. The MLED algorithm utilising this application is proposed in [17] (for a detailed analysis see [18]); it performs both covariance estimation and detection on the same primary observation data set.

$$\frac{|\boldsymbol{s}^H \boldsymbol{Q}^{-1} \boldsymbol{g}|^2}{\boldsymbol{s}^H \boldsymbol{Q}^{-1} \boldsymbol{s}} \underset{H_0}{\overset{H_1}{\gtrless}} \gamma \tag{2.30}$$

It is clear that the MLED has the same structure as the AMF detector. It is normalised in the same manner to achieve the CFAR property. Similar to the MLED, the GMLED [18, 19] is defined as

$$\frac{|\boldsymbol{s}^H \boldsymbol{Q}^{-1} \boldsymbol{g}|^2}{\boldsymbol{s}^H \boldsymbol{Q}^{-1} \boldsymbol{s} \left(1 + \boldsymbol{g}^H \boldsymbol{Q}^{-1} \boldsymbol{g}\right)} \underset{H_0}{\overset{H_1}{\gtrless}} \gamma \tag{2.31}$$

where the structural similarity to Kelly's GLRT is evident. In both the MLED and the GMLED the SPCM estimate comes from the primary data set. Thus only the data from the CUT is used. This removes the inherent limitations of TDS algorithms when dealing with environments that are inhomogeneous or non-stationary outside of one CPI. Performance is also greatly enhanced in a target-rich environment where no target-free secondary data can be obtained. The implementation of the discussed SDS detectors when the limitation of one target per range gate still holds is trivial. If this assumption is violated, an itterative approach of finding multiple target in the same primary data set can be undertaken, and the MLED and GMLED can still be

applied.

Despite the benefits of SDS, in a homogeneous environment it would be wasteful to discard the observations from range gates neighbouring the CUT as they still hold valuable information about the background interference statistics. Using those samples alongside the primary observations can increase the accuracy of the estimate to the SPCM. The idea of combining the SDS and TDS covariance estimators has been described in [19] where a hybrid target detector is proposed. While the AMF and the GLRT perform estimation on the training data and detection on the primary, the proposed hybrid approaches include both observation sets in the estimation process by applying the APES filter approach.

Alternative ways to perform SDS detection that are not based on covariance estimation have been developed in the past. One major such area of research investigates subspace projection (SP) approaches to detection. With some additional prior knowledge of the clutter structure and location in Doppler, its subspace can be isolated and projected out of the STAP observations [12, 14]. In the bistatic case the detector takes a form similar to the AMF and the MLED

$$\frac{|\boldsymbol{s}^H \boldsymbol{P}_\perp \boldsymbol{g}|^2}{\boldsymbol{s}^H \boldsymbol{P}_\perp \boldsymbol{s}} \underset{H_0}{\overset{H_1}{\gtrless}} \gamma \tag{2.32}$$

where $\boldsymbol{P}_\perp$ is described in [12] and signifies the matrix that projects to the subspace orthogonal to the one spanned by the clutter in the system

$$\boldsymbol{P}_\perp = \boldsymbol{I} - \boldsymbol{H}_c \left(\boldsymbol{H}_c^H \boldsymbol{H}_c\right)^{-1} \boldsymbol{H}_c^H \tag{2.33}$$

where $\boldsymbol{H}_c$ is the matrix whose columns describe the clutter subspace. Taking the familiar form that is normalised to exhibit the CFAR property, the SP detector requires no SMI and is thus computationally much simpler than the covariance methods described above. However, the detector (2.32) requires prior knowledge of the frequency subspace where clutter may be located. An enhancement to the approach is described in [13] that adaptively estimates the order of the clutter subspace in the observations, although a set of frequencies in the spectrum where the interference may occur is still required. An SP approach that incorporates the SDS covariance estimation of the MLED has been proposed in [20, 21]. The formulation is practically identical to (2.32). The difference is that no prior knowledge of the clutter subspace location is required in this method. Instead the subspace is obtained through the eigencanceller approach [62] from the SDS estimate $\boldsymbol{Q}$ of the SPCM.

2.5 Multiple-input multiple-output radar

MIMO radar is a research topic that has gained an increasing popularity over the past decade. The advantages of using multiple transmitters and receivers are numerous: higher accuracy of target localisation, higher detection rate under a certain false alarm probability, increased spatial and angular diversity, increased resolution [27–34, 63]. It is a natural way of boosting performance once the theoretical limits of the effectiveness that monostatic or bistatic radars can achieve have been approached. Clearly the physical cost of a MIMO installation is higher than traditional radar. However, the real limiting factor to its practical implementation is the complexity of the required time synchronisation and logistics in a widely-spaced installation [34]. As the number of transmitters and receivers in a given scenario increases, so does the data that must be processed, propagated, temporally-aligned, and combined to produce the final detection result. As discussed in [33, 34], employing a distributed detection algorithm instead of a centralised one drastically reduces this complexity but does not completely solve the issue.

Two different types of MIMO radar implementations can be identified depending on the relative location between receivers: coherent and statistical. The former aims to maximise the coherent processing gain between the multiple transmit signals at the receiver side. Examples of this are beamforming and STAP discussed in Section 2.2. The receiver is a closely-spaced array that allows for direction estimation of the incoming target signal as well as electronic steering to be performed [27, 28]. In statistical MIMO radar detection, the angular diversity of different incoherent snapshots of the target is utilised [28–34]. The transmitters and the receivers are widely-spaced so that they obtain multiple independent reflections coming from a moving object. This alleviates the problem of target scintillations that can result in fast fading of the reflected signal in the order of 10-25 dB [2, 64]. Through the usage of multiple statistically-independent snapshots of the target, the average SNR in the system remains relatively constant, which makes the detection process more reliable. With the implementation and advances in stealth technology for airborne targets, multistatic radar can potentially be deployed as a countermeasure [42]. One of the principles of stealth is the scattering of transmitted scanning waveform in directions where a radar receiver is unlikely to be. This is usually done by minimising the radar cross-section (RCS) of the target through its shape and structure. Statistical MIMO radar is more likely to pick up a transmitted waveform that is scattered by a stealthed target, thus increasing the chances for detection [43].

It is possible to utilise the benefits of both closely-spaced and widely-spaced MIMO radar in the

same system. In [28] a setup is considered where the transmitters are sufficiently-separated in position to provide angular diversity of detection; the receiving elements are part of a standard ULA that performs coherent detection. The receiver ULA is thus treated as a single unit, and the arrangement is described as multiple-input single-output (MISO). In [44] a similar concept is explored with multiple widely-separated transmitters and receive ULAs. A detailed description of the physical process of combining the results from the different transmit-receive pairs in a fixed earth-centred Cartesian coordinate system is included. The example depicted in Figure 2.3 of this thesis describes a similar hypothetical scenario with one transmitter and two receivers. In the same MIMO radar scenario where each receiver is a standard ULA that performs STAP detection, the multistatic AMF filter is derived in [65–67].

$$\sum_{m,n} \frac{|\boldsymbol{s}_{m,n}^H \widehat{\boldsymbol{R}}_{m,n}^{-1} \boldsymbol{g}_{m,n}|^2}{\boldsymbol{s}_{m,n}^H \widehat{\boldsymbol{R}}_{m,n}^{-1} \boldsymbol{s}_{m,n}} \underset{H_0}{\overset{H_1}{\gtrless}} \gamma \tag{2.34}$$

The subscript $(\cdot)_{m,n}$ is used to signify that a certain parameter or variable is associated with the bistatic pair formed by the m^{th} transmitter and the n^{th} receive ULA. Note that the parameter γ written without a subscript will always refer to the total decision threshold in a MIMO detection scenario. Because the radar elements are widely-separated, it is assumed that the clutter observations at the receivers are independent for the different transmit waveforms. This explains why (2.34) is a linear combination of the individual bistatic AMF results that are obtained in the radar scenario. In a similar manner and under the same assumptions [65–67] derive the multistatic extension to Kelly's GLRT detector.

$$\prod_{m,n} \frac{K_t + \boldsymbol{g}_{m,n}^H \widehat{\boldsymbol{R}}_{m,n}^{-1} \boldsymbol{g}_{m,n}}{K_t + \boldsymbol{g}_{m,n}^H \widehat{\boldsymbol{R}}_{m,n}^{-1} \boldsymbol{g}_{m,n} - \dfrac{|\boldsymbol{s}_{m,n}^H \widehat{\boldsymbol{R}}_{m,n}^{-1} \boldsymbol{g}_{m,n}|^2}{\boldsymbol{s}_{m,n}^H \widehat{\boldsymbol{R}}_{m,n}^{-1} \boldsymbol{s}_{m,n}}} \underset{H_0}{\overset{H_1}{\gtrless}} \gamma \tag{2.35}$$

Each individual term in the product (2.35) is practically equivalent to the original GLRT from (2.26) as a threshold ratio detector. Thus the multistatic result is once again separable into its bistatic components. This is in line with the assumption that the interference in the transmit-receive radar pairs is independent.

2.6 Radar ambiguity limitations

Many algorithms have been proposed in the past that in theory provide very promising performance gains for larger MIMO radar networks [27, 30, 44, 56, 65–67]. It has been shown in theory [45] and practice [46] that these algorithms often ignore the limiting factor of the MIMO ambiguity function. These effects can degrade the performance of a radar setup that uses a number of orthogonal waveforms in fast time. In a MIMO scenario, the maximum area in the ambiguity function that can be cleared of sidelobes gets proportionally smaller as the number of such waveforms increases [45, 46]. That lowers the effective SNR which in turn degrades the overall detection performance. A short overview of the problem will be given here.

Woodward's ambiguity function of a continuous narrowband signal $u(t)$ is defined as [68–70]

$$\alpha(t,f) = \int_{-\infty}^{\infty} u\left(\tau - \frac{1}{2}t\right) u^*\left(\tau + \frac{1}{2}t\right) e^{-j2\pi f\tau} d\tau \tag{2.36}$$

The ambiguity function is a measure of the distortion that a reflected radar pulse $u(t)$ experiences in both time and frequency (due to a Doppler shift) when passed through the receiver filter matched to the pulse's shape [71]. Any such distortion outside of the immediate region of the ambiguity space origin (0,0) reduces the radar performance in a practical scenario since all reflections at that Doppler and/or delay will experience the distortion. At $f{=}0$ the integral (2.36) reduces to the standard time-domain autocorrelation function of the pulse $u(t)$. A derivation of the theoretical limitations on this factor for mono/bistatic radar can be found in [72]. The analysis is performed for an arbitrary region A around the ambiguity space origin that satisfies two criteria: A is convex, and A is symmetric around the origin. Let $C(A)$ signify the area if the region A, and $V(A)$ the volume of the ambiguity in that region. The ambiguity bound derived in [72] takes the following form

$$V(A) \geq \frac{1}{4} C(A) V_0 \tag{2.37}$$

where V_0 is the volume of the ambiguity at the origin (0,0). It is evident from (2.37) that if the region A expands beyond an area of 4, then the ambiguity in that region will contain volume outside of the one concentrated around the origin. This is a universal limitation that any radar system will have despite the chosen waveform used for target detection.

The theoretical limitations (2.37) imposed by the ambiguity function have been extended to a MIMO scenario in [45, 46]. Consider a radar system with M transmitters, each of them associated with their own unique waveform $u_j(t)$. The M different waveforms are considered orthogonal in fast time. The cross-ambiguity between two waveforms $u_j(t)$ and $u_k(t)$ is defined as a direct extension of (2.36)

$$\chi_{jk}(t,f) = \int_{-\infty}^{\infty} u_j\left(\tau - \frac{1}{2}t\right) u_k^*\left(\tau + \frac{1}{2}t\right) e^{-j2\pi f\tau} d\tau \tag{2.38}$$

Different definitions of the MIMO ambiguity function exist. The one proposed in [45, 46] and adopted here is represented by the sum of the Euclidean norms of all auto- and cross-ambiguities of the M orthogonal waveforms in the radar system.

$$|\chi_M(t,f)|^2 = \sum_{j=1}^{M}\sum_{k=1}^{M} |\chi_{jk}(t,f)|^2 \tag{2.39}$$

It has been derived in [45] and demonstrated in a practical scenario in [46] that the bound on the volume of the ambiguity function $V_M(A)$ in a region A for a MIMO scenario of M orthogonal waveforms is the following

$$V_M(A) \geq \frac{1}{4} C(A) M V_{M0} \tag{2.40}$$

where V_{M0} is the MIMO ambiguity volume around the origin (0,0). A comparison between (2.37) and (2.40) indicates that the area of the region A that can be completely clear of sidelobes is M times smaller in the MIMO scenario compared to the mono/bistatic case.

In a practical scenario, ideal waveform orthogonality cannot be achieved. Although the term orthogonal waveforms is used, it almost always implies that the signals have low cross-correlation between them. Different strategies for achieving this exist that are based on some of the basic principles of communications for shared medium networks [73]: frequency division multiple access (FDMA), time division multiple access (TDMA), and code division multiple access (CDMA). In radar design, CDMA waveforms come from a set of codes that are orthogonal in fast time and share the same resources in time and frequency [74]. At the receiver side a bank of matched filters is implemented to identify and isolate the signals coming from the different transmitters. These waveforms suffer from the limitation imposed by the MIMO ambiguity bound on the region clear of sidelobes (2.40). As the radar network size increases,

the drawbacks from this limitation also increase, which imposes diminishing returns on the performance of large MIMO installations.

This MIMO ambiguity issue could be avoided if the multiple waveforms in the radar scenario occupy different time slots (as in TDMA) or frequency regions (as in FDMA) [47]. However, the cost in terms of delay or spectrum that is required for operation grows linearly with the number of transmitters. A discussion on the multistatic ambiguity function of an FDMA or TDMA waveform radar system is provided in Chapter 5. This thesis will assume that the practical implementation of the proposed multistatic algorithms involves a frequency orthogonality between the different waveforms used for target detection.

2.7 Problem formulation

Consider a MIMO radar setup with M single-element transmitters and N receiver ULAs. In this thesis an ULA is treated as a single unit, and the term MIMO will be strictly reserved for a scenario where more than one array is present to receive the reflections of the transmitted waveforms. All of the radar elements are widely-separated in space, and thus the scenario focuses on multistatic statistical detection. Geolocations and motion are assumed to occur in a 2-D plane. All transmitters are moving at constant velocities, while all receivers are stationary. It is assumed that all elements in the radar installation know of each other's relative position and velocity at all times through a reliable system of data exchange. A single moving target of unknown location and velocity is in the area scanned by the MIMO radar installation. It is always assumed to be in the far-field region for all listening elements. Thus the point-source model for the target is used. The waveforms coming from each transmitter are assumed to be ideally separable at the receiver side. The signals are also narrowband, so the propagation time across each receiver ULA is negligible. An example mock scenario of 3 transmitters and 3 receivers is depicted in Figure 2.8.

The observation model from (2.16) is adapted to the multistatic scenario. Each STAP range gate has been windowed and rearranged into the observation matrix $\boldsymbol{X}_{m,n}$ of size $P \times K$

$$\boldsymbol{X}_{m,n} = \alpha_{m,n} \boldsymbol{s}_{m,n} \boldsymbol{t}_{m,n}^{T} + \boldsymbol{N}_{m,n} \tag{2.41}$$

where $\boldsymbol{N}_{m,n}$ is the combined term for all clutter and noise in the transmit-receive pair $(\cdot)_{m,n}$.

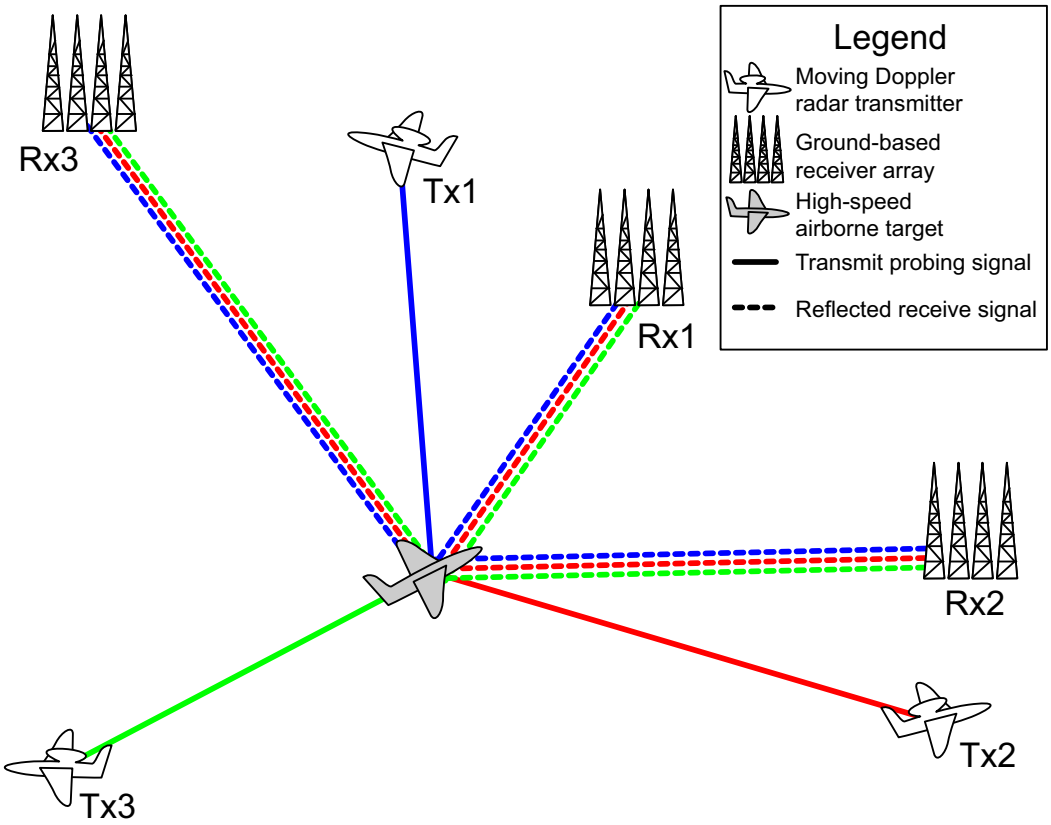

Figure 2.8: *An example multistatic radar setup with 3 mobile transmitters and 3 receive ULAs*

The arrangement is such that the columns of each of the matrices $\boldsymbol{N}_{m,n}$ are assumed to be iid. Each transmit-receive pair in the MIMO system forms a standard bistatic path that will be referred to as "channel" in this thesis. The clutter and noise across the different channels are assumed to be independent but do not have to be identically distributed. Clutter returns are generated through the GCM described in [49] with a certain intrinsic clutter motion (ICM) corresponding to a wooded hills area [3]. This setup was chosen without loss of generality since it naturally provides lower temporal correlation between slow-time pulses; this allows for more efficient simulations to be conducted since the number of temporal observations K_t to produce a certain number K of iid snapshots is kept relatively low. The noise is always spatio-temporal AWGN with power 20 dB below that of clutter. Some parameters related to the operation of the radar installations as well as the target and clutter models will remain fixed throughout this thesis. They are listed in Table 2.1 for convenience. Most physical operation characteristics are selected to directly reflect the ones used in [12] so that an unbiased comparison between the algorithms could be made. While this does not necessarily reflect a realistic choice of pa-

rameters (e.g. the selected velocity is equivalent to 130km/h, which is too slow for an airborne target), the selection is done without loss of generality and does not influence the validity or the performance of the algorithms derived in this thesis.

Parameter	**Value**	**Description**
λ_o	0.3 m	carrier frequency
σ_v	0.2 m/s	clutter velocity standard deviation
σ_w^2	20 dB below σ_c^2	AWGN power
d	0.15 m	ULA element spacing
N_c	1000	clutter contributing patches
P	10	spatial dimension of observations
T	2 ms	PRI
v_x	25 m/s	target velocity in x-direction
v_y	-25 m/s	target velocity in y-direction

Table 2.1: *Fixed radar scenario parameters*

Given the setup described here, this thesis will focus on implementing SDS sample matrix inversion (SMI)-based solutions to the multistatic radar detection problem

$$\begin{aligned} H_0 &: \mathbb{X} = \{\boldsymbol{X}_{m,n} | \boldsymbol{X}_{m,n} = \boldsymbol{N}_{m,n}, m = 1 \ldots M, n = 1 \ldots N\} \\ H_1 &: \mathbb{X} = \{\boldsymbol{X}_{m,n} | \boldsymbol{X}_{m,n} = \alpha_{m,n} \boldsymbol{s}_{m,n} \boldsymbol{t}_{m,n}^T + \boldsymbol{N}_{m,n}, m = 1 \ldots M, n = 1 \ldots N\} \end{aligned} \tag{2.42}$$

where $\mathbb{X} = \{\boldsymbol{X}_{m,n} | m = 1 \ldots M, n = 1 \ldots N\}$ is the notation for the set of all observation matrices $\boldsymbol{X}_{m,n}$ in a multistatic scenario that correspond to the same physical point in space.

The physical implementations of the multistatic threshold detection solutions proposed in this work all follow the same framework similar to the one described in [44]. The procedure is given in Table 2.2.

For a radar receiver the natural physical search space is range-angle-Doppler (RAD). Here the translation into x-y-Doppler space is performed after the bistatic search in each channel since it is much easier to synchronise and fuse the multistatic results given a common Cartesian coordinate system. For each grid space in the physical search area, a bistatic radar pair forms the detection likelihood function with respect to all N_d normalised Doppler frequencies which the algorithm probes for a moving target. Once the likelihoods are transmitted throughout the radar network, the corresponding Doppler likelihoods in each x-y coordinate of the search space can be synchronised and compounded to produce the multistatic likelihood function for that physical patch in the grid. The multistatic threshold detection process is then performed in

Require: Set up the radar parameters
Require: Set up an earth-centred Cartesian coordinate system shared by all radar elements
Require: Set up a normalised Doppler search space of size N_d
Require: Set up an angle search space of size N_a
Require: Set up a range search space of size N_r
  for all bistatic channels $(\cdot)_{m,n}$ **do**
    for ranges between 1 and N_r **do**
      for angles between 1 and N_a **do**
        for Doppler frequencies between 1 and N_d **do**
          Run bistatic detector.
        end for
        Translate point in angle-Doppler space to Cartesian coordinate in x-y space.
        Form detection likelihood function for all Doppler frequencies.
      end for
    end for
    Obtain transmitter velocities and positions
    Synchronise and exchange Doppler likelihoods for all x-y grids
    Synchronise Doppler frequencies from individual bistatic likelihoods
  end for
  Combine bistatic results into multistatic likelihood
  return Multistatic threshold detection decision

Table 2.2 Physical implementation of the multistatic radar detection procedure

order to produce the final decision.

2.8 Summary

This chapter provides a brief overview of the concepts on which the work in this thesis is built. An overview of STAP radar detection and the relevant target and interference signal models is included in Section 2.2. Some of the traditional TDS detectors are provided in Section 2.3. These methods and their shortcomings give rise to the development of the SDS detectors described in Section 2.4 on which a large portion of the work in this thesis is based. Section 2.5 provides a brief overview of MIMO radar. Section 2.6 discusses the practical limitations imposed on MIMO radar by the waveform ambiguity function. The problem investigated in this thesis along with the assumptions made in the formulation are described in Section 2.7.

Chapter 3
The multistatic maximum likelihood and generalised maximum likelihood estimation detectors

3.1 Introduction

This chapter provides an in-depth derivation of the multistatic MLED/GMLED solution [56,75] to the radar detection problem posed in Section 2.7. The algorithms presented here form the core of the detection process described in Table 2.2 inside the innermost iteration loop of the target search sequence. Thus, the focus is on the multistatic fusion of the results instead of the RAD synchronisation between the different channels. It is assumed that such synchronisation is in place and that it is ideal; thus, when the MIMO radar system illuminates an airborne target the ranges, the spatial frequencies $f_{s\{m,n\}}$, and the Doppler frequencies $f_{d\{m,n\}}$ of that target are all precisely-known parameters. This condition will be relaxed in Chapter 4.

The statistical properties of the multistatic MLED/GMLED are derived and analysed, and it is shown that both target detection schemes possess the CFAR property. The usual challenges associated with the theoretical analysis of mono/bistatic STAP detectors (e.g. [17, 18, 20, 76, 77]) are compounded in the multistatic scenario. Even when the individual bistatic channels are mutually independent, MIMO detectors are typically summations or products of bistatic detectors (e.g. [12,14,66,67]). While expression for the probability of false alarm and detection are available for bistatic radar, it is unlikely that the corresponding multistatic solutions exist in closed form [14,65,66]. Thus, a methodology is proposed at the end of this chapter for deriving approximate expressions for probability of false alarm and detection for widely-spaced MIMO systems. The methodology is illustrated in detail for the proposed SDS algorithms. The key to obtaining the approximations is the application of the CLT, or more precisely Lindeberg's condition [78, p.307], to the summation of bistatic detectors. This approximation enables the link between the algorithm parameters and the probabilities of detection and false alarm to be made.

This chapter closely follows the original work published in [75]. The rest of the chapter is structured as follows. Section 3.2 provides a mathematical background on the distribution of the bistatic MLED and GMLED observations. Section 3.3 and Section 3.4 contain the first contribution of the chapter and provide the derivations of the multistatic MLED and GMLED respectively. Section 3.5 contains the second contribution in the form of the statistical analysis of the algorithms and proposes the CLT approximation for relatively large radar networks. Section 3.6 demonstrates the performance of the proposed detectors and the viability of the derived approximations to their statistics through a number of numerical simulations. Section 3.7 contains a summary of the work presented in this chapter.

3.2 Background

Consider a single bistatic channel from the multistatic observation signal model (2.41). The vectors $\boldsymbol{s}_{m,n}$ and $\boldsymbol{t}_{m,n}$ correspond to the described bistatic spactial and temporal steering vectors in Section 2.2. The clutter and noise in each column of the channel-specific observation matrix $\boldsymbol{X}_{m,n}$ is assumed to be iid and complex multivariate Gaussian. The probability density function (pdf) of the k^{th} column of $\boldsymbol{X}_{m,n}$ conditioned on the amplitude of the reflected probing signal $\alpha_{m,n}$ is thus described by the (p-dimensional) multivariate Gaussian distribution [18, p.121]

$$f(\text{col}_k(\boldsymbol{X})|\alpha) = \frac{1}{\pi^P|\boldsymbol{R}|}\exp\left\{-(\text{col}_k(\boldsymbol{X}) - \alpha\boldsymbol{s}\boldsymbol{t}(k))^H\boldsymbol{R}^{-1}(\text{col}_k(\boldsymbol{X}) - \alpha\boldsymbol{s}\boldsymbol{t}(k))\right\} \tag{3.1}$$

where the channel-specific subscripts $(\cdot)_{m,n}$ have been omitted in (3.1) as it focuses on a single channel. Thus the spatial and temporal steering vectors $\boldsymbol{s}$ and $\boldsymbol{t}$ are equivalent to $\boldsymbol{s}_{m,n}$ and $\boldsymbol{t}_{m,n}$ from the observations model (2.41), and $\boldsymbol{t}(k)$ signifies the k^{th} element of the vector $\boldsymbol{t}$. The notation $|\cdot|$ is used here to signify the determinant of a matrix, and $\exp(\cdot)$ is the exponential of a number. The interference in the different snapshots $\text{col}_k(\boldsymbol{X})$ has been assumed to be iid by construction; thus the pdf of the full observation matrix $\boldsymbol{X}$ conditioned on the amplitude α is

given by the product of the pdfs (3.1) of the individual snapshots [18, p.121]

$$\begin{aligned} f(\boldsymbol{X}|\alpha) &= \prod_{k=1}^{K} f(\mathrm{col}_k(\boldsymbol{X})|\alpha) \\ &= \left(\frac{1}{\pi^P|\boldsymbol{R}|}\right)^K \exp\left\{-\sum_{k=1}^{K}(\mathrm{col}_k(\boldsymbol{X}) - \alpha\boldsymbol{st}(k))^H \boldsymbol{R}^{-1}(\mathrm{col}_k(\boldsymbol{X}) - \alpha\boldsymbol{st}(k))\right\} \\ &= \left(\frac{1}{\pi^P|\boldsymbol{R}|}\right)^K \mathrm{etr}\left\{-\boldsymbol{R}^{-1}(\mathrm{col}_k(\boldsymbol{X}) - \alpha\boldsymbol{st}(k))(\mathrm{col}_k(\boldsymbol{X}) - \alpha\boldsymbol{st}(k))^H\right\} \\ &= \left(\frac{1}{\pi^P|\boldsymbol{R}|}\right)^K \mathrm{etr}\left\{-\boldsymbol{R}^{-1}\boldsymbol{M}^\alpha\right\} \end{aligned} \tag{3.2}$$

Here etr$(\cdot)$ is the exponential of the trace of a matrix; the trace itself will be defined as Tr$(\cdot)$. The following identity

$$\boldsymbol{v}^H\boldsymbol{M}\boldsymbol{v} = Tr(\boldsymbol{M}\boldsymbol{v}\boldsymbol{v}^H) \tag{3.3}$$

which stems from the basic properties of the trace and valid for any matrix $\boldsymbol{M}$ and vector $\boldsymbol{v}$ is applied in (3.2) and will be used throughout the derivations in this chapter. In addition, in the last line of (3.2) the following matrix is defined

$$\boldsymbol{M}^\alpha = \sum_{k=1}^{K}(\mathrm{col}_k(\boldsymbol{X}) - \alpha\boldsymbol{st}(k))(\mathrm{col}_k(\boldsymbol{X}) - \alpha\boldsymbol{st}(k))^H \tag{3.4}$$

which is the ML sample estimate of the snapshot covariance matrix up to a power normalising constant K.

3.3 Derivation of the multistatic MLED

An in-depth derivation of the multistatic MLED algorithm described in [56, 75] is given in this section. The resulting detector is similar to the multistatic AMF presented in [65–67] but does not use independent training data sets for covariance estimation and SMI. The derivation directly follows the background presented in the previous section. From this point onward a full multistatic system is considered, and thus the channel-specific subscripts $(\cdot)_{m,n}$ will be used in the equations where relevant. It is assumed that the covariance matrices of the background interference $\boldsymbol{R}_{m,n}$ are known for the time being in order to derive the optimal multistatic detector. In a multistatic scenario with sufficient separation between antennas, the background clutter and noise processes $\boldsymbol{N}_{m,n}$ are uncorrelated to one another. Let $\mathbb{\alpha}=\{\alpha_{m,n}|m=1\ldots M, n=1\ldots N\}$

denote the set of all the complex amplitudes $\alpha_{m,n}$ across the channels of the multistatic radar. The joint pdf of the set of observations $\mathbb{X}$ given the set of amplitudes $\mathbb{\alpha}$ can be represented by the product of the individual pdfs given in (3.2) because all target and interference signals from the different channels are assumed uncorrelated. With M transmitters and N receivers the joint multistatic pdf takes the following form

$$\begin{aligned} f(\mathbb{X}|\mathbb{\alpha}) &= \prod_{m,n} f(\boldsymbol{X}_{m,n}|\alpha_{m,n}) \\ &= \left(\frac{1}{\pi^{MNP} \prod\limits_{m,n} |\boldsymbol{R}_{m,n}|} \right)^{K} \text{etr} \left\{ -\sum_{m,n} \boldsymbol{R}_{m,n}^{-1} \boldsymbol{M}_{m,n}^{\alpha} \right\} \end{aligned} \tag{3.5}$$

Let $\mathbb{\alpha}=\mathbb{0}$ signify the case when every element of the set $\mathbb{\alpha}$ is equal to zero. This reflects the situation when no target is present in the search area of the radar installation, and the observations picked up by each receiver consist purely of clutter and noise. Therefore, the joint pdf of the set of observation signals $\mathbb{X}$ under the null hypothesis from (2.42) is given by

$$\begin{aligned} f_0(\mathbb{X}) &= f(\mathbb{X}|\mathbb{\alpha} = \mathbb{0}) \\ &= \left(\frac{1}{\pi^{MNP} \prod\limits_{m,n} |\boldsymbol{R}_{m,n}|} \right)^{K} \text{etr} \left\{ -\sum_{m,n} \boldsymbol{R}_{m,n}^{-1} \boldsymbol{M}_{m,n}^{0} \right\} \end{aligned} \tag{3.6}$$

where

$$\boldsymbol{M}_{m,n}^{0} = \sum_{k=1}^{K} \text{col}_k(\boldsymbol{X}_{m,n}) \text{col}_k(\boldsymbol{X}_{m,n})^H \tag{3.7}$$

represents the ML sample estimate of the STAP snapshot covariance similar to (3.4) when no target signal is present in the observations. Under hypothesis H_1 from (2.42), the joint pdf $f_1(\mathbb{X})$ is simply given by $f(\mathbb{X}|\mathbb{\alpha})$ from equation (3.5). To obtain the ML estimate of the unknown parameters in the set $\mathbb{\alpha}$, the natural logarithm $\log(\cdot)$ of (3.5) is taken to transform the product of exponentials into a summation. The partial derivative $\partial(\cdot)$ of the expression with respect to each unknown complex amplitude $\alpha_{p,q}^{*}$ is then individually formed; the expression is

solved for zero to find the maximum of the likelihood function of the specific channel $(\cdot)_{p,q}$

$$\begin{aligned}\frac{\partial}{\partial \alpha_{p,q}^*}\log\left(f(\mathbb{X}|\mathbb{\alpha})\right) &= \frac{\partial}{\partial \alpha_{p,q}^*}\text{Tr}\left\{-\sum_{m,n}\boldsymbol{R}_{m,n}^{-1}\boldsymbol{M}_{m,n}^{\alpha}\right\} \\ &= \frac{\partial}{\partial \alpha_{p,q}^*}\text{Tr}\left\{-\boldsymbol{R}_{p,q}^{-1}\boldsymbol{M}_{p,q}^{\alpha}\right\} \\ &= \sum_{k=1}^{K}\boldsymbol{s}_{p,q}^H\boldsymbol{t}_{p,q}^*(k)\boldsymbol{R}_{p,q}^{-1}\left(\text{col}_k(\boldsymbol{X}_{p,q}) - \alpha_{p,q}\boldsymbol{s}_{p,q}\boldsymbol{t}_{p,q}(k)\right) \\ &= \boldsymbol{s}_{p,q}^H\boldsymbol{R}_{p,q}^{-1}\sum_{k=1}^{K}\text{col}_k(\boldsymbol{X}_{p,q})\boldsymbol{t}_{p,q}^*(k) - \alpha_{p,q}K\boldsymbol{s}_{p,q}^H\boldsymbol{R}_{p,q}^{-1}\boldsymbol{s}_{p,q} \\ &= K\boldsymbol{s}_{p,q}^H\boldsymbol{R}_{p,q}^{-1}\boldsymbol{g}_{p,q} - K\alpha_{p,q}\boldsymbol{s}_{p,q}^H\boldsymbol{R}_{p,q}^{-1}\boldsymbol{s}_{p,q} \end{aligned} \tag{3.8}$$

Some trivial steps in the derivation of (3.8) have been omitted. Equation (3.3) has been used to transition from the trace to the summation term, and the 2-norm (2.21) of the temporal steering vector has been replaced. Clearly under the logarithm the problem becomes linearly separable and thus the sum over all the bistatic channels has vanished. The complex amplitude estimate is only dependent on the parameters of its own channel; thus the solution when the derivative (3.8) is zero is identical to the bistatic one presented in [18] for all channels $(\cdot)_{m,n}$

$$\widehat{\alpha}_{m,n} = \frac{\boldsymbol{s}_{m,n}^H\boldsymbol{R}_{m,n}^{-1}\boldsymbol{g}_{m,n}}{\boldsymbol{s}_{m,n}^H\boldsymbol{R}_{m,n}^{-1}\boldsymbol{s}_{m,n}} \tag{3.9}$$

Note that (3.9) is also identical to the amplitude estimate of the APES filter derived in [61]. The Neyman-Pearson (NP) lemma [79] states that the optimal threshold detector is formed by the ratio of the likelihood functions under the two hypotheses (3.5) and (3.6).

$$\begin{aligned}\frac{\max\limits_{\mathbb{\alpha}} f_1}{f_0} &= \frac{\text{etr}\left\{-\sum\limits_{m,n}\boldsymbol{R}_{m,n}^{-1}\boldsymbol{M}_{m,n}^{\widehat{\alpha}}\right\}}{\text{etr}\left\{-\sum\limits_{m,n}\boldsymbol{R}_{m,n}^{-1}\boldsymbol{M}_{m,n}^{0}\right\}} \\ &= \text{etr}\left\{-\sum_{m,n}\boldsymbol{R}_{m,n}^{-1}\left(\boldsymbol{M}_{m,n}^{\widehat{\alpha}} - \boldsymbol{M}_{m,n}^{0}\right)\right\} \end{aligned} \tag{3.10}$$

The likelihood under the hypothesis H_1 has been maximised by plugging in the estimates for the amplitudes $\alpha_{m,n}$ from (3.9). Thus the matrix

$$\boldsymbol{M}_{m,n}^{\widehat{\alpha}} = \sum_{k=1}^{K} (\mathrm{col}_k(\boldsymbol{X}_{m,n}) - \widehat{\alpha}_{m,n}\boldsymbol{s}_{m,n}\boldsymbol{t}_{m,n}(k))(\mathrm{col}_k(\boldsymbol{X}_{m,n}) - \widehat{\alpha}_{m,n}\boldsymbol{s}_{m,n}\boldsymbol{t}_{m,n}(k))^H \quad (3.11)$$

has been used in (3.10), which is the sample covariance from (3.4) with the ML amplitudes plugged in. The relationship between $\boldsymbol{M}_{m,n}^{\widehat{\alpha}}$ and $\boldsymbol{M}_{m,n}^{0}$ becomes evident when the former is expanded as

$$\boldsymbol{M}_{m,n}^{\widehat{\alpha}} = \boldsymbol{M}_{m,n}^{0} - K\widehat{\alpha}_{m,n}^{*}\boldsymbol{g}_{m,n}\boldsymbol{s}_{m,n}^{H} - K\widehat{\alpha}_{m,n}\boldsymbol{s}_{m,n}\boldsymbol{g}_{m,n}^{H} + K|\widehat{\alpha}_{m,n}|^2\boldsymbol{s}_{m,n}\boldsymbol{s}_{m,n}^{H} \quad (3.12)$$

Plugging the relation (3.12) in (3.10), the NP ratio becomes

$$\frac{\max_{\mathbb{\alpha}} f_1}{f_0} = \mathrm{etr}\left\{ K\sum_{m,n} \boldsymbol{R}_{m,n}^{-1}\left(\widehat{\alpha}_{m,n}^{*}\boldsymbol{g}_{m,n}\boldsymbol{s}_{m,n}^{H} + \widehat{\alpha}_{m,n}\boldsymbol{s}_{m,n}\boldsymbol{g}_{m,n}^{H} - |\widehat{\alpha}_{m,n}|^2\boldsymbol{s}_{m,n}\boldsymbol{s}_{m,n}^{H}\right)^H \right\} \quad (3.13)$$

Since the logarithm is a linear operator, applying it to (3.13) does not change the detection capabilities of the NP ratio. Using the identity (3.3) to remove the trace from the equation, the natural logarithm of the ratio becomes

$$\log\frac{\max_{\mathbb{\alpha}} f_1}{f_0} = K\sum_{m,n}\left(\widehat{\alpha}_{m,n}^{*}\boldsymbol{s}_{m,n}^{H}\boldsymbol{R}_{m,n}^{-1}\boldsymbol{g}_{m,n} + \widehat{\alpha}_{m,n}\boldsymbol{g}_{m,n}^{H}\boldsymbol{R}_{m,n}^{-1}\boldsymbol{s}_{m,n} - |\widehat{\alpha}_{m,n}|^2\boldsymbol{s}_{m,n}^{H}\boldsymbol{R}_{m,n}^{-1}\boldsymbol{s}_{m,n}\right) \quad (3.14)$$

If the ML estimates (3.9) are plugged into (3.14), the multistatic threshold detector for the case when the covariance matrices of the background noise and interference $\boldsymbol{R}_{m,n}$ for all different channels are known.

$$\sum_{m,n}\frac{|\boldsymbol{s}_{m,n}^{H}\boldsymbol{R}_{m,n}^{-1}\boldsymbol{g}_{m,n}|^2}{\boldsymbol{s}_{m,n}^{H}\boldsymbol{R}_{m,n}^{-1}\boldsymbol{s}_{m,n}} \underset{H_0}{\overset{H_1}{\gtrless}} \gamma \quad (3.15)$$

The normalising K-factor here has been absorbed in the total decision threshold γ. Note that (3.15) is essentially the multistatic extension to the MF given in (2.23) under the assumption that all the bistatic channels in the radar scenario are independent. The multistatic MLED threshold detector is obtained when the unknown clairvoyant matrices $\boldsymbol{R}_{m,n}$ are replaced by the SDS sample matrices $\boldsymbol{Q}_{m,n}$ in (2.29) coming from the APES filter.

$$\sum_{m,n}\frac{|\boldsymbol{s}_{m,n}^{H}\boldsymbol{Q}_{m,n}^{-1}\boldsymbol{g}_{m,n}|^2}{\boldsymbol{s}_{m,n}^{H}\boldsymbol{Q}_{m,n}^{-1}\boldsymbol{s}_{m,n}} \underset{H_0}{\overset{H_1}{\gtrless}} \gamma \quad (3.16)$$

The ML SDS solution (3.16) to the MIMO case investigated in this work is a summation of the individual single-channel solutions (2.30) for each path $(\cdot)_{m,n}$ in the system. The linear separability of the multistatic detector in the sum of the bistatic ones is in accordance with the prior assumption that the individual transmit-receive channels are independent.

3.4 Derivation of the multistatic GMLED

In this section the multistatic GMLED threshold test algorithm for SDS detection is derived. The derivation is a more in-depth extension of [56, 75]. The resulting detector is similar to the multistatic GLRT presented in [65–67] but does not require independent training data sets. While in the derivation of the MLED the covariance matrices of the noise and interference signals $\boldsymbol{R}_{m,n}$ were assumed to be known, in the GMLED they are unknown parameters from the start. The expression for the pdf of each individual observation signal set $\boldsymbol{X}_{m,n}$, now conditional on both the amplitude $\alpha_{m,n}$ and covariance matrix $\boldsymbol{R}_{m,n}$, is identical to the respective MLED case (3.2) derived in Section 3.2.

$$f(\boldsymbol{X}_{m,n}|\alpha_{m,n}, \boldsymbol{R}_{m,n}) = \left(\frac{1}{\pi^P|\boldsymbol{R}_{m,n}|}\right)^K \text{etr}\left\{-\boldsymbol{R}_{m,n}^{-1}\boldsymbol{M}_{m,n}^{\alpha}\right\} \tag{3.17}$$

Therefore, the joint pdf of the multistatic observations also remains the same as (3.5), this time conditional on the set of unknown covariance matrices $\mathbb{R}_{\mathbb{s}}=\{\boldsymbol{R}_{m,n}|m=1\ldots M, n=1\ldots N\}$.

$$f(\mathbb{X}|\mathbb{\alpha}, \mathbb{R}_{\mathbb{s}}) = \left(\frac{1}{\pi^{MNP}\prod\limits_{m,n}|\boldsymbol{R}_{m,n}|}\right)^K \text{etr}\left\{-\sum_{m,n}\boldsymbol{R}_{m,n}^{-1}\boldsymbol{M}_{m,n}^{\alpha}\right\} \tag{3.18}$$

This is also the expression that provides the relevant likelihood function under the H_1 hypothesis from (2.42). Under the alternative hypothesis, the likelihood function, now conditional on the parameter set $\mathbb{R}_{\mathbb{s}}$, is given by

$$f(\mathbb{X}|\mathbb{\alpha}=\mathbb{0}, \mathbb{R}_{\mathbb{s}}) = \left(\frac{1}{\pi^{MNP}\prod\limits_{m,n}|\boldsymbol{R}_{m,n}|}\right)^K \text{etr}\left\{-\sum_{m,n}\boldsymbol{R}_{m,n}^{-1}\boldsymbol{M}_{m,n}^{0}\right\} \tag{3.19}$$

The logarithm of (3.19) is taken, similar to the maximisation approach in Section 3.3 of this chapter, before taking the derivative and solving it for zero. Since the unknown in this case is a matrix, the Jacobian of the natural logarithm of (3.19) is examined in a particular channel of

interest $(\cdot)_{p,q}$:

$$\begin{aligned}\frac{\partial}{\partial \boldsymbol{R}_{p,q}}\log\left(f_0(\mathbb{X}|\mathbb{R}_{\mathbb{s}})\right) &= \frac{\partial}{\partial \boldsymbol{R}_{p,q}}\left\{-K\log\left\{\pi^{MNP}\prod_{m,n}|\boldsymbol{R}_{m,n}|\right\} - \text{Tr}\left\{\sum_{m,n}\boldsymbol{R}_{m,n}^{-1}\boldsymbol{M}_{m,n}^{0}\right\}\right\} \\ &= \frac{\partial}{\partial \boldsymbol{R}_{p,q}}\left\{-K\sum_{m,n}\log\left\{|\boldsymbol{R}_{m,n}|\right\} - \sum_{m,n}\text{Tr}\left\{\boldsymbol{R}_{m,n}^{-1}\boldsymbol{M}_{m,n}^{0}\right\}\right\} \\ &= \frac{\partial}{\partial \boldsymbol{R}_{p,q}}\left\{-K\log\left\{|\boldsymbol{R}_{p,q}|\right\} - \text{Tr}\left\{\boldsymbol{R}_{p,q}^{-1}\boldsymbol{M}_{p,q}^{0}\right\}\right\} \end{aligned} \tag{3.20}$$

It is clear from the last line of (3.20) that the problem has become linearly separable in the logarithm once again. To obtain the ML, a few useful properties of the Jacobian are taken from literature [80, pp.193-203] and used to follow up on the derivation

$$\frac{\partial \log|\boldsymbol{R}_{p,q}|}{\partial \boldsymbol{R}_{p,q}} = \boldsymbol{R}_{p,q}^{-1} \tag{3.21}$$

$$\frac{\partial \text{Tr}\left\{\boldsymbol{R}_{p,q}^{-1}\boldsymbol{M}_{p,q}^{0}\right\}}{\partial \boldsymbol{R}_{p,q}} = -\boldsymbol{R}_{p,q}^{-1}\boldsymbol{M}_{p,q}^{0}\boldsymbol{R}_{p,q}^{-1} \tag{3.22}$$

where a few Hermitian transpose operators have been omitted since both $\boldsymbol{R}_{p,q}$ and $\boldsymbol{M}_{p,q}^{0}$ are self-adjoint. Plugging in (3.21) and (3.22) into (3.20) and solving for zero, the ML estimate of the unknown covariance matrix for all individual channels $(\cdot)_{m,n}$ is formed [81]

$$\widehat{\boldsymbol{R}}_{m,n} = \frac{1}{K}\boldsymbol{M}_{m,n}^{0} \tag{3.23}$$

The maximised likelihood function under the hypothesis H_0 for the multistatic GMLED detector is thus obtained after plugging in (3.23) into the likelihood (3.19)

$$\max_{\mathbb{R}_{\mathbb{s}}} f_0(\mathbb{X}) = \left(\frac{1}{(Ke\pi)^{MNP}\prod_{m,n}|\boldsymbol{M}_{m,n}^{0}|}\right)^{K} \tag{3.24}$$

The process of deriving the ML under the alternative hypothesis H_1 is identical to the one for H_0. The solution for the covariance matrices $\boldsymbol{R}_{m,n}$ takes the more general form

$$\widehat{\boldsymbol{R}}_{m,n} = \frac{1}{K}\boldsymbol{M}_{m,n}^{\alpha} \tag{3.25}$$

which now depends on the unknown amplitudes $\alpha_{m,n}$. Note that when no target is present, (3.25) reduces to (3.23) since the amplitudes are all zero. When the solutions (3.25) are plugged

into (3.18), the maximised likelihood expression for the multistatic GMLED is obtained

$$\max_{\mathbb{R}_s} f_1(\mathbb{X}|\mathbb{\alpha}) = \left(\frac{1}{(Ke\pi)^{MNP} \prod\limits_{m,n} |\boldsymbol{M}^{\alpha}_{m,n}|} \right)^K \tag{3.26}$$

To maximise the likelihood (3.26) with respect to the unknown complex amplitudes $\alpha_{m,n}$, once again it is useful to render the expression linearly separable through taking the natural logarithm before forming the partial derivatives.

$$\begin{aligned} \frac{\partial}{\partial \alpha_{p,q}} \log f_1(\mathbb{X}|\mathbb{\alpha}) &= -K \frac{\partial}{\partial \alpha^*_{p,q}} \log \left\{ (Ke\pi)^{MNP} \prod_{m,n} |\boldsymbol{M}^{\alpha}_{m,n}| \right\} \\ &= -K \frac{\partial}{\partial \alpha^*_{p,q}} \sum_{m,n} \log \left\{ |\boldsymbol{M}^{\alpha}_{m,n}| \right\} \\ &= -K \frac{\partial}{\partial \alpha^*_{p,q}} \log \left\{ |\boldsymbol{M}^{\alpha}_{p,q}| \right\} \end{aligned} \tag{3.27}$$

To obtain a more suitable expression for the determinants, first equation (3.12) should be modified to take the following form

$$\begin{aligned} \boldsymbol{M}^{\alpha}_{p,q} &= \boldsymbol{M}^{0}_{p,q} - K\alpha^*_{p,q} \boldsymbol{g}_{p,q} \boldsymbol{s}^H_{p,q} - K\alpha_{p,q} \boldsymbol{s}_{p,q} \boldsymbol{g}^H_{p,q} + K|\alpha_{p,q}|^2 \boldsymbol{s}_{p,q} \boldsymbol{s}^H_{p,q} \\ &= K\boldsymbol{Q}_{p,q} + K\boldsymbol{g}_{p,q} \boldsymbol{g}^H_{p,q} - K\alpha^*_{p,q} \boldsymbol{g}_{p,q} \boldsymbol{s}^H_{p,q} - K\alpha_{p,q} \boldsymbol{s}_{p,q} \boldsymbol{g}^H_{p,q} + K|\alpha_{p,q}|^2 \boldsymbol{s}_{p,q} \boldsymbol{s}^H_{p,q} \\ &= K\boldsymbol{Q}_{p,q} + K \left(\boldsymbol{g}_{p,q} - \alpha_{p,q} \boldsymbol{s}_{p,q} \right) \left(\boldsymbol{g}_{p,q} - \alpha_{p,q} \boldsymbol{s}_{p,q} \right)^H \end{aligned} \tag{3.28}$$

where the fact that $\boldsymbol{M}^0_{p,q} = \boldsymbol{X}_{p,q} \boldsymbol{X}^H_{p,q}$ from (3.7) has been utilised. Using the generalisation of Sylvester's identity for matrix determinants [82] it can be shown that, following from (3.28)

$$|\boldsymbol{M}^{\alpha}_{p,q}| = K^P |\boldsymbol{Q}_{p,q}| \left(1 + \left(\boldsymbol{g}_{p,q} - \alpha_{p,q} \boldsymbol{s}_{p,q} \right)^H \boldsymbol{Q}^{-1}_{p,q} \left(\boldsymbol{g}_{p,q} - \alpha_{p,q} \boldsymbol{s}_{p,q} \right) \right) \tag{3.29}$$

Plugging (3.29) back into (3.27), the likelihood maximisation process can be completed

$$\begin{aligned} \frac{\partial}{\partial \alpha^*_{p,q}} \log f_1(\mathbb{X}|\mathbb{\alpha}) &= -K \frac{\partial}{\partial \alpha^*_{p,q}} \log \left(1 + \left(\boldsymbol{g}_{p,q} - \alpha_{p,q} \boldsymbol{s}_{p,q} \right)^H \boldsymbol{Q}^{-1}_{p,q} \left(\boldsymbol{g}_{p,q} - \alpha_{p,q} \boldsymbol{s}_{p,q} \right) \right) \\ &= \frac{-K \boldsymbol{s}^H_{p,q} \boldsymbol{Q}^{-1}_{p,q} \left(\boldsymbol{g}_{p,q} - \alpha_{p,q} \boldsymbol{s}_{p,q} \right)}{1 + \left(\boldsymbol{g}_{p,q} - \alpha_{p,q} \boldsymbol{s}_{p,q} \right)^H \boldsymbol{Q}^{-1}_{p,q} \left(\boldsymbol{g}_{p,q} - \alpha_{p,q} \boldsymbol{s}_{p,q} \right)} \end{aligned} \tag{3.30}$$

When the numerator of (3.30) is solved for zero, the estimates to the unknown amplitudes $\alpha_{m,n}$ in all channels $(\cdot)_{m,n}$ are obtained. This solution will not be made explicit here since it is

identical to (3.9) derived for the multistatic MLED in Section 3.3. When these estimates are plugged back into (3.29), the minimum of the determinant $|\boldsymbol{M}_{m,n}^{\alpha}|$ is obtained

$$\min_{\alpha_{m,n}} |\boldsymbol{M}_{m,n}^{\alpha}| = K^P |\boldsymbol{Q}_{m,n}| \left(1 + \boldsymbol{g}_{m,n}^H \boldsymbol{Q}_{m,n}^{-1} \boldsymbol{g}_{m,n} - \frac{|\boldsymbol{s}_{m,n}^H \boldsymbol{Q}_{m,n}^{-1} \boldsymbol{g}_{m,n}|^2}{\boldsymbol{s}_{m,n}^H \boldsymbol{Q}_{m,n}^{-1} \boldsymbol{s}_{m,n}} \right) \tag{3.31}$$

From (3.29), the determinant of the matrix $\boldsymbol{M}_{m,n}^{0}$ for the hypothesis H_0 can also be expressed in a similar manner by simply putting $\alpha_{m,n}$ to zero.

$$|\boldsymbol{M}_{m,n}^{0}| = K^P |\boldsymbol{Q}_{m,n}| \left(1 + \boldsymbol{g}_{m,n}^H \boldsymbol{Q}_{m,n}^{-1} \boldsymbol{g}_{m,n} \right) \tag{3.32}$$

Forming the ratio of the maximised likelihoods (3.26) and (3.24) in accordance with the NP criterion, the multistatic threshold detector expression can be obtained

$$\frac{\max\limits_{\alpha, \mathbb{R}_{\mathtt{s}}} f_1}{\max\limits_{\mathbb{R}_{\mathtt{s}}} f_0} = \left(\frac{\prod\limits_{m,n} |\boldsymbol{M}_{m,n}^{0}|}{\prod\limits_{m,n} \min\limits_{\alpha_{m,n}} |\boldsymbol{M}_{m,n}^{\alpha}|} \right)^K \tag{3.33}$$

Plugging in the relevant expressions for the determinants (3.31) and (3.32) into (3.33) and taking the K^{th} root of the likelihood ratio, the expression for the multistatic GMLED is obtained

$$\prod_{m,n} \frac{1 + \boldsymbol{g}_{m,n}^H \boldsymbol{Q}_{m,n}^{-1} \boldsymbol{g}_{m,n}}{1 + \boldsymbol{g}_{m,n}^H \boldsymbol{Q}_{m,n}^{-1} \boldsymbol{g}_{m,n} - \dfrac{|\boldsymbol{s}_{m,n}^H \boldsymbol{Q}_{m,n}^{-1} \boldsymbol{g}_{m,n}|^2}{\boldsymbol{s}_{m,n}^H \boldsymbol{Q}_{m,n}^{-1} \boldsymbol{s}_{m,n}}} \underset{H_0}{\overset{H_1}{\gtrless}} \nu \tag{3.34}$$

If the equation for the standard GMLED detector (2.31) is reworked it becomes evident that the multistatic version (3.34) is a product of the bistatic solutions for each path $(\cdot)_{m,n}$ in the system. The property is somewhat similar to the relation between the bistatic and multistatic MLED and comes as no surprise. Because the radar waveforms are orthogonal, and the interference in the different channels is assumed to be independent, the detector is once again linearly separable.

3.5 Analysis

This section provides a statistical analysis of the derived multistatic versions of the MLED and GMLED algorithms. A brief discussion on the theoretical forms of the resulting MIMO detector distributions is included. Based on this discussion and some of the existing analysis of similar multistatic detectors [65–67], it can be concluded that a closed-form expression for the

pdfs of the MLED and GMLED extensions derived here may be impractical to compute or may not even exist. To obtain an expression for the probability of false alarm P_{fa} and the probability of detection P_d, the CLT is employed to obtain a Gaussian approximation to both threshold detectors' pdfs for a large number $M \times N$ of bistatic channels. These approximations are useful in the design and implementation of the proposed multistatic SDS methods; they provide a quick and computationally inexpensive way of predicting the performance of a practical MIMO radar installation.

3.5.1 Statistical properties of the multistatic MLED

The statistical properties of the bistatic MLED detector are described in [18, pp.63-65] and are also derived in Appendix A.1 for convenience. The detection test for a single bistatic channel shown in (2.30) is equivalent to the following combination of random variables

$$\frac{\zeta_{m,n}}{L\eta_{m,n}} \underset{H_0}{\overset{H_1}{\gtrless}} \gamma_{m,n} \tag{3.35}$$

The variable L signifies the degrees of freedom (DOF) available to the detector for performing clutter cancellation. For the SDS detectors examined in this work the value is equal to

$$L = K - P \tag{3.36}$$

Note that the DOF (3.36) in this case are one less than in the case of the traditional TDS algorithms like the AMF and the GLRT [9, 10]. This has been explored in detail in [19] where it has been shown that the lost degree goes into estimating the complex amplitude $\alpha_{m,n}$ in a bistatic channel.

The random variables $\zeta_{m,n}$ and $\eta_{m,n}$ that compose the MLED statistics (3.35) are mutually independent. The variable $\eta_{m,n}$ follows the type I beta distribution with $L+1$ and $P-1$ DOF. The variable $\zeta_{m,n}$ is distributed according to the non-central F distribution with 2 and $2L$ DOF and a non-centrality parameter $\lambda_{m,n}$ given by

$$\lambda_{m,n} = 2KP\eta_{m,n}\rho_{m,n} \tag{3.37}$$

The variable $\rho_{m,n}$ signifies the SNR per observed temporal snapshot in the adopted signal

model (2.41). Its value is derived in [18, p.17] as

$$\rho_{m,n} = \frac{1}{P}|\alpha_{m,n}|^2 \boldsymbol{s}_{m,n}^H \boldsymbol{R}_{m,n}^{-1} \boldsymbol{s}_{m,n} \tag{3.38}$$

where once again the norm of the temporal steering vector has been assumed to be K (2.21). In the case where no target is present in the set of observations $\boldsymbol{X}_{m,n}$, the non-centrality parameter $\lambda_{m,n}$ becomes zero, and the random variable $\zeta_{m,n}$ assumes the standard F distribution with 2 and $2L$ DOF. Using (3.16), the multistatic MLED test statistics are distributed as

$$\sum_{m,n} \frac{\zeta_{m,n}}{L\eta_{m,n}} \underset{H_0}{\overset{H_1}{\gtrless}} \gamma \tag{3.39}$$

The test statistics consist of a sum of random terms shown in [17, 18] to be independent of the underlying noise and interference. The covariance matrix of the clutter and noise $\boldsymbol{R}_{m,n}$ for a certain bistatic channel has no influence on either of the random variables in the test statistics (3.35) under the H_0 hypothesis. Under the H_1 hypothesis the matrix only plays a role in determining the value of the operational SNR of the system (3.38). Naturally, it is the SNR that determines performance. The same argument applies to the statistics of the multistatic sum (3.39). It is independent of any of the clutter and noise matrices $\boldsymbol{R}_{m,n}$. Therefore the inherent CFAR property of the bistatic MLED is preserved in the multistatic extension of the algorithm.

Due to the complex nature of the random variables involved, obtaining a closed form expression for the pdf of the multistatic MLED would be difficult and impractical. Similar conclusions have been reached in [65–67] where analogical TDS MIMO algorithms for target detection have been proposed. None of the mentioned works offer a theoretical closed-form solution for the detection and false alarm probabilities of the multistatic AMF.

In the bistatic case [18, pp.62-64], the approach is to assume that the random variable $\eta_{m,n}$ is known, which leads to the detection variable having the non-central F distribution. This pdf can then be integrated to obtain an expression for the probability of detection and the probability of false alarm.

$$P_d(\gamma_{m,n}) = \int_0^1 \left(\int_{L\eta_{m,n}\gamma_{m,n}}^{\infty} f_\zeta(\zeta_{m,n}) d\zeta \right) f_\eta(\eta_{m,n}) d\eta_{m,n} \tag{3.40}$$

The approach from (3.40) cannot be extended to the multistatic sum of random variables (3.39). The marginalisation of the beta-distributed random variables $\eta_{m,n}$ is no longer trivial because they cannot be isolated from the sum of the ratios in (3.39). Moreover, even if the variables

$\eta_{m,n}$ are assumed to be known, the resulting statistics become a sum of $M \times N$ independent non-identically and non-centrally F-distributed random variables. The pdf of such random variable has no known closed form formulation which makes analysis of the proposed multistatic algorithm difficult.

In the case that the sum (3.39) consists of a sufficiently large number of terms, it can be approximated by a Gaussian distribution through the application of the CLT. This enables the derivation of approximate and relatively accurate expressions for the probability of false alarm $P_{fa}(\gamma)$ and the probability of detection $P_d(\gamma)$ for a given detection threshold γ. The proposed Gaussian approximation to the multistatic MLED statistics is derived in Section 3.5.2.

3.5.2 Gaussian approximation of the multistatic MLED

The multistatic MLED threshold detector consists of a sum of $M \times N$ independent random terms as shown in (3.39). The CLT dictates that the statistics of the decision variable with mean μ_M and variance σ_M^2 can be closely approximated by a Gaussian distribution $\mathcal{N}(\mu_M, \sigma_M^2)$ provided that $M \times N$ is sufficiently large [66]. Because the terms are not identically distributed, Lindeberg's condition [78, p.307] has to be satisfied which is shown in Appendix B.1. Let the mean and variance of the bistatic MLED detectors in each of the individual channels $(\cdot)_{m,n}$ distributed as (3.35) be defined as

$$\mu_{M(m,n)} = E\left[\frac{\zeta_{m,n}}{L\eta_{m,n}}\right] \tag{3.41}$$

$$\sigma^2_{M(m,n)} = \text{var}\left(\frac{\zeta_{m,n}}{L\eta_{m,n}}\right) \tag{3.42}$$

Here $E[\cdot]$ signifies the expectation and var$(\cdot)$ the variance of the random variable or vector. The multistatic detector is the sum of the $M \times N$ independent random variables in those channels. This fact, combined with the linearity of the expectation operator, leads to the conclusion that all the moments of the multistatic MLED random variable (3.39) are the sum of the same moments in the individual bistatic channels $(\cdot)_{m,n}$. Therefore the mean μ_M and variance σ_M^2 of the total MIMO MLED are given by the linear combinations

$$\mu_M = \sum_{m,n} \mu_{M(m,n)} \tag{3.43}$$

$$\sigma_M^2 = \sum_{m,n} \sigma^2_{M(m,n)} \tag{3.44}$$

Because the pairs of random variables $\zeta_{m,n}$ and $\eta_{m,n}$ are independent, the central moments of their ratios factorise in the following manner [83]

$$\mu_{M(m,n)} = \frac{1}{L} E\left[\zeta_{m,n}\right] E\left[\frac{1}{\eta_{m,n}}\right] \tag{3.45}$$

$$\sigma^2_{M(m,n)} = \frac{1}{L^2} E\left[\zeta^2_{m,n}\right] E\left[\left(\frac{1}{\eta_{m,n}}\right)^2\right] - \frac{1}{L^2} E\left[\zeta_{m,n}\right]^2 E\left[\frac{1}{\eta_{m,n}}\right]^2 \tag{3.46}$$

Provided that $L>2$, which should always be the case in practice so that the clutter covariance estimation is reliable, the first two central moments of the F-distributed random variable $\zeta_{m,n}$ are given in statistics literature [84, p.221]

$$E\left[\zeta_{m,n}\right] = \frac{L}{2}\frac{2+\lambda_{m,n}}{L-1} \tag{3.47}$$

$$\text{var}(\zeta_{m,n}) = \frac{L^2}{4}\frac{(2+\lambda_{m,n})^2 + 4(1+\lambda_{m,n})(L-1)}{(L-1)^2(L-2)} \tag{3.48}$$

The expectation of $\eta^{-1}_{m,n}$ is obtained by solving the integral with respect to the reciprocal beta-distributed random variable with $L+1$ and $P-1$ DOF

$$\begin{aligned} E\left[\frac{1}{\eta_{m,n}}\right] &= \int_0^1 \frac{1}{\eta_{m,n}} f_\eta(\eta_{m,n}) d\eta_{m,n} \\ &= \int_0^1 \frac{\eta_{m,n}^{L-1}(1-\eta_{m,n})^{P-2}}{B(L+1,P-1)} d\eta_{m,n} \\ &= \frac{B(L,P-1)}{B(L+1,P-1)} \\ &= \frac{K-1}{L} \end{aligned} \tag{3.49}$$

where $B(x,y)$ is the beta function. Similarly the second central moment of $\eta^{-1}_{m,n}$ can be obtained by solving the second moment integral and subtracting the squared first moment

$$\begin{aligned} \text{var}\left(\frac{1}{\eta_{m,n}}\right) &= E\left[\left(\frac{1}{\eta_{m,n}}\right)^2\right] - E\left[\frac{1}{\eta_{m,n}}\right]^2 \\ &= \int_0^1 \frac{\eta_{m,n}^{L-2}(1-\eta_{m,n})^{P-2}}{B(L+1,P-1)} - \frac{K-1}{L} \\ &= \frac{B(L-1,P-1)}{B(L+1,P-1)} - \frac{K-1}{L} \\ &= \frac{(K-1)(P-1)}{L^2(L-1)} \end{aligned} \tag{3.50}$$

Using the fact that $E\left[(\cdot)^2\right]$ =var$(\cdot)$+$E\left[\cdot\right]^2$, (3.47), (3.48), (3.49), and (3.50) can be plugged in (3.45) and (3.46) to obtain an expression for the mean and variance of the random variable that signifies the bistatic MLED threshold detector

$$\mu_{M(m,n)} = \frac{K-1}{2L}\frac{2+\widetilde{\lambda}_{m,n}}{L-1} \tag{3.51}$$

$$\sigma^2_{M(m,n)} = \frac{(K-1)(K+P-2)(2+\widetilde{\lambda}_{m,n})^2}{4L^2(L-1)^2(L-2)} + \frac{(K-1)(K-2)(1+\widetilde{\lambda}_{m,n})}{L(L-1)^2(L-2)} \tag{3.52}$$

The non-centrality parameters $\lambda_{m,n}$ are themselves of random nature since they are dependent on $\eta_{m,n}$. In the case of the multistatic MLED it is easy to marginalise them out of the equations for the mean (3.51) and variance (3.52) to produce a closed-form solution. However, in the case of the multistatic GMLED approximation that is described in Section 3.5.4 the marginalisation process is not trivial. Therefore, for consistency, a first-order approximation to $\lambda_{m,n}$ is done for both algorithms where they are replaced by their expected values $\widetilde{\lambda}_{m,n}$ given by [85, p.11]

$$\begin{aligned}\widetilde{\lambda}_{m,n} &= E\left[2KP\rho_{m,n}\eta_{m,n}\right] \\ &= 2P(L+1)\rho_{m,n}\end{aligned} \tag{3.53}$$

It should be noted that (3.53) is an additional approximation that is performed for convenience. The CLT holds without replacing the variables $\lambda_{m,n}$ with their first order estimates proposed here. In the case of the multistatic MLED, it has been determined numerically that using the first-order estimator (3.53) instead of taking the standard marginalisation approach makes little difference to the final results.

Label	**Relevant equations**	**Description**
Simulated	(3.16)	Monte Carlo simulation of the multistatic MLED detector, histogram approximation to pdf
Theoretical	(3.39)	Monte Carlo simulation of random variables composing the theoretical distribution of the multistatic MLED, histogram approximation to pdf
Approximation	(3.51) (3.52) (3.56) (3.57)	Gaussian approximation to the multistatic MLED, normal pdf with relevant parameters (3.51) (3.52)

Table 3.1: *Guide to MLED pdf simulations labelling and terminology*

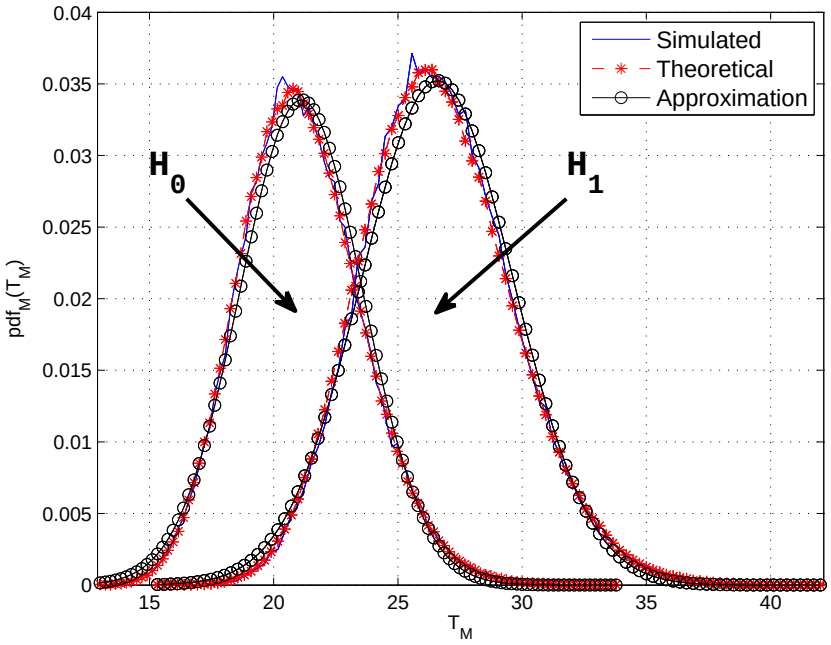

Figure 3.1: *Probability density function of the multistatic MLED detection variable* K=20, M=N=10, SNR=$-26dB$

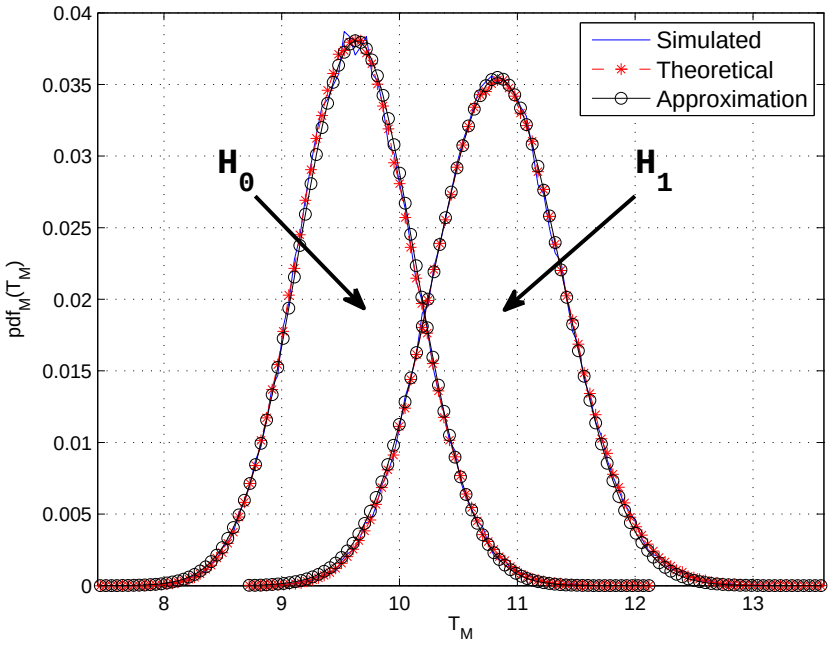

Figure 3.2: *Probability density function of the multistatic MLED detection variable* K=60, M=N=20, SNR=$-36dB$

Figure 3.1 and Figure 3.2 depict the pdfs of the multistatic MLED detection variable and its Gaussian approximation. Three sets of results are provided in the graphs, "simulated," "theoretical," and "approximation." A short description of the labeling is summarised in Table 3.1 along with the relevant equations. A more detailed explanation is given in the Simulations section (Section 3.6) of this chapter. Figure 3.1 shows the respective pdfs for a network of 10 transmitters and 10 receivers which observes K=20 temporal iid snapshots per range gate. Since there are a total of 100 bistatic channels in the multistatic scenario, it is expected that the Gaussian approximation model will have a reasonable convergence to the actual pdf of the MLED random variable. The values of the SNR for the simulations under the H_1 hypothesis are chosen so that the H_0 and H_1 pdfs are relatively close to each other. It was also aimed that Figure 3.1 and Figure 3.2 look relatively similar to each other for ease of comparison. This is done for convenience of the visual representation and without loss of generality. The simulated and theoretical results are obtained from the histogram approximation to the pdf. A million sample points were generated for each run and placed in 100 histogram bins in order to produce relatively smooth pdf curves.

In the second set of pdf simulations shown in Figure 3.2, a larger radar network of 20 transmitters and receivers is simulated. A larger number K=60 of temporal snapshots is also used. The number of terms that take part in the process of applying the CLT has now risen from 100 to 400, which evidently reduces the error of approximation. The approximating Gaussian pdfs now better match the distribution of the multistatic detection variable. Since the resulting simulated and theoretical pdfs are now produced by a convolution of 400 terms, all central moments above the second are negligible.

To obtain the probability of false alarm P_{fa} for a given threshold γ, it is noted that in the absence of target the multistatic MLED threshold detector is approximately distributed as $\mathcal{N}(\mu_{M0}, \sigma^2_{M0})$ where the two relevant moments of the approximation follow directly from (3.51) and (3.52)

$$\mu_{M0} = \sum_{m,n} \mu_{m,n}(\widetilde{\lambda}_{m,n} = 0) \tag{3.54}$$

$$\sigma^2_{M0} = \sum_{m,n} \sigma^2_{m,n}(\widetilde{\lambda}_{m,n} = 0) \tag{3.55}$$

Therefore the false alarm probability P_{fa} of the multistatic MLED for a given detection thresh-

old γ is approximately

$$P_{fa}(\gamma) \approx Q\left(\frac{\gamma - \mu_{M0}}{\sigma_{M0}}\right) \tag{3.56}$$

where $Q(x)$ is the Q-function associated with the tail probability $Pr[X>x]$ of the standard Gaussian distribution. The probability of detection P_d is obtained in the case where a target is present in the observations. The multistatic MLED detector variable is then approximately distributed as $\mathcal{N}(\mu_{M1}, \sigma^2_{M1})$, where μ_{M1} and σ^2_{M1} are the same sums as (3.43) and (3.44) respectively with the $\widetilde{\lambda}_{m,n}$ parameters given by (3.53). Thus the probability of detection for the given decision threshold γ is approximately

$$P_d(\gamma) \approx Q\left(\frac{\gamma - \mu_{M1}}{\sigma_{M1}}\right) \tag{3.57}$$

Note that the Gaussian approximation to the multistatic MLED proposed here can be easily extended to the multistatic AMF proposed in [65] and [67]. The approach is the same as the one presented in this work and thus the results provided here are valid for the TDS algorithm with a slight modification of the added degree of freedom.

3.5.3 Statistical properties of the multistatic GMLED

The analysis of the GMLED in [18, pp.54-63] has been performed for the threshold detector expressed in the form given in (2.31). If expressed in this manner, the statistics of the bistatic GMLED are distributed as

$$\frac{\zeta_{m,n}}{L} \underset{H_0}{\overset{H_1}{\gtrless}} \tau_{m,n} \tag{3.58}$$

where $\zeta_{m,n}$ is the same F-distributed random variable from the MLED statistics with the same non-centrality parameter and DOF, and $\tau = \gamma/(1-\gamma)$. The derivation of this expression has been provided in Appendix A.2 of this thesis for convenience. The multistatic expression (3.34) requires the return of the bistatic GMLED likelihood ratio to its original form given by

$$\frac{1}{1 - \dfrac{|\boldsymbol{s}^H_{m,n}\boldsymbol{Q}^{-1}_{m,n}\boldsymbol{g}_{m,n}|^2}{\boldsymbol{s}^H_{m,n}\boldsymbol{Q}^{-1}_{m,n}\boldsymbol{s}_{m,n}(1+\boldsymbol{g}^H_{m,n}\boldsymbol{Q}^{-1}_{m,n}\boldsymbol{g}_{m,n})}} \underset{H_0}{\overset{H_1}{\gtrless}} \nu_{m,n} \tag{3.59}$$

where

$$\nu_{m,n} = \frac{1}{1-\gamma_{m,n}} \tag{3.60}$$

is the relation between the transformations of the threshold in the bistatic case. It can be easily shown that the relation between the two manipulated thresholds $\nu_{m,n}$ and $\tau_{m,n}$ is the following

$$\nu_{m,n} = \tau_{m,n} + 1 \tag{3.61}$$

Therefore, the statistical equivalence of the left-hand side of (3.59) takes the following simplified form

$$\frac{\zeta_{m,n}}{L} + 1 \underset{H_0}{\overset{H_1}{\gtrless}} \nu_{m,n} \tag{3.62}$$

The multistatic GMLED threshold detector in (3.34) consists of the product of its bistatic components. It is therefore distributed as

$$\prod_{m,n} \left(\frac{\zeta_{m,n}}{L} + 1 \right) \underset{H_0}{\overset{H_1}{\gtrless}} \nu \tag{3.63}$$

The test statistics thus consist of a product of random terms that were shown in [18, p.61] to be independent of the underlying noise and clutter distributions. Is is evident that the covariance matrices of the clutter $\boldsymbol{R}_{m,n}$ do not directly influence the test statistics (3.63) apart from determining the operational SNR. Therefore, the multistatic GMLED threshold detector is, in turn, independent of the statistics of the noise, preserving the CFAR property in the MIMO extension of the algorithm.

Similar to the multistatic MLED detector, its generalised extension is difficult to analyse in the statistical sense. A closed-form solution for the probability of false alarm of the MIMO GLRT has been proposed in [86]. However, the approach cannot be taken when the non-centrality parameters $\lambda_{m,n}$ are introduced and the probability of detection has to be derived instead. Therefore, deriving a Gaussian approximation to the multistatic GMLED similar to the one presented in Section 3.5.2 for the MLED can once again provide a useful guideline to the overall performance of the algorithm. Section 3.5.4 proposes such an approximation to the multistatic detector statistics (3.63) given that a large number of terms take part in the product. As a result it is possible to derive approximate expressions for the probability of false alarm $P_{fa}(\nu)$ and the probability of detection $P_d(\nu)$ for a given detection threshold ν.

3.5.4 Log-normal approximation of the multistatic GMLED

The multistatic GMLED threshold detector consists of a product of $M \times N$ random terms as shown in (3.63). It would be convenient to take the logarithm of this product to transform it into a sum of random variables.

$$\log\left\{\prod_{m,n}\left(\frac{\zeta_{m,n}}{L}+1\right)\right\} = \sum_{m,n}\log\left(\frac{\zeta_{m,n}}{L}+1\right) \underset{H_0}{\overset{H_1}{\gtrless}} \log\nu \tag{3.64}$$

The CLT dictates that the statistics of the logarithm of the decision variable given in (3.64) can be closely approximated by a Gaussian distribution $\mathcal{N}(\mu_G, \sigma_G^2)$ provided that the number of signal paths $M \times N$ in the system is sufficiently large [66]. Once again the random variables in the sum are not identically distributed so a proof of the validity of Lindeberg's condition for the detector is given in Appendix B.2. Because the exponential of a normally-distributed random variable follows the log-normal distribution with the same parameters, it can be concluded that in a large network the multistatic GMLED pdf can be approximated by $\ln\mathcal{N}(\mu_G, \sigma_G^2)$. To obtain expressions for the parameters of this distribution, the first two moments of the multistatic GMLED random variable have to be obtained. The expectation of the individual terms in the product (3.34) can be obtained from (3.62) by using the expectation of an F-distributed random variable given in (3.47) and the linearity of the expectation operator.

$$E\left[\frac{\zeta_{m,n}}{L}+1\right] = \frac{2L+\lambda_{m,n}}{2(L-1)} \tag{3.65}$$

Because it is assumed that the random variables coming from the different channels $(\cdot)_{m,n}$ are independent, all the (non-central) moments of their product will factorise into the product of their individual (non-central) moments. Therefore, the first moment of the multistatic GMLED random variable is given by

$$E\left[\prod_{m,n}\left(\frac{\zeta_{m,n}}{L}+1\right)\right] = \prod_{m,n}\frac{2L+\lambda_{m,n}}{2(L-1)} \tag{3.66}$$

The second moment of the individual product terms (3.62) is obtained from the variance of the F-distributed random variable given in (3.48) and the derived first moment (3.65).

$$E\left[\left(\frac{\zeta_{m,n}}{L}+1\right)^2\right] = \frac{(\lambda_{m,n}+2L)^2-4L}{4(L-1)(L-2)} \tag{3.67}$$

The second moment of the multistatic GMLED detection variable is the product of the second moments of the statistically independent individual terms from the different channels $(\cdot)_{m,n}$.

$$E\left[\prod_{m,n}\left(\frac{\zeta_{m,n}}{L}+1\right)^2\right]=\prod_{m,n}\frac{(\lambda_{m,n}+2L)^2-4L}{4(L-1)(L-2)} \tag{3.68}$$

From the statistics literature, the first and second moments of a random variable following the log-normal distribution $\ln\mathcal{N}(\mu_G,\sigma_G^2)$ with parameters μ_G and σ_G^2 are given by [85, p.8]

$$E\left[\ln\mathcal{N}(\mu_G,\sigma_G^2)\right]=e^{\mu_G+\sigma_G^2/2} \tag{3.69}$$

$$E\left[\left(\ln\mathcal{N}(\mu_G,\sigma_G^2)\right)^2\right]=e^{2\mu_G+2\sigma_G^2} \tag{3.70}$$

The derived expectations (3.66) and (3.68) and the parametric expressions (3.69) and (3.70) form a system of two equations.

$$\mu_G+\frac{\sigma_G^2}{2}=\sum_{m,n}\log\left(\frac{2L+\lambda_{m,n}}{2(L-1)}\right) \tag{3.71}$$

$$2\mu_G+2\sigma_G^2=\sum_{m,n}\log\left(\frac{(\lambda_{m,n}+2L)^2-4L}{4(L-1)(L-2)}\right) \tag{3.72}$$

Solving the system (3.71), (3.72) for the parameters μ_G and σ_G^2 results in

$$\mu_G=\frac{1}{2}\sum_{m,n}\log\left(\frac{(\widetilde{\lambda}_{m,n}+2L)^4(L-2)}{4((\widetilde{\lambda}_{m,n}+2L)^2-4L)(L-1)^3}\right) \tag{3.73}$$

$$\sigma_G^2=\sum_{m,n}\log\left(\frac{((\widetilde{\lambda}_{m,n}+2L)^2-4L)(L-1)}{(\widetilde{\lambda}_{m,n}+2L)^2(L-2)}\right) \tag{3.74}$$

where once again the random variables $\lambda_{m,n}$ have been replaced with their expected values $\widetilde{\lambda}_{m,n}$ given by (3.53). In the absence of target the threshold detector is distributed as $\ln\mathcal{N}(\mu_{G0},\sigma_{G0}^2)$ where μ_{G0} and σ_{G0}^2 no longer need to be approximated. Their exact values can be computed due to the fact that for $\lambda_{m,n}$=0 the non-central F distribution becomes a standard F distribution with 2 and $2L$ DOF. The pdf of the distribution takes the following closed-form simple form that can be easily integrated.

$$f_\zeta(\zeta_{m,n})=\frac{1}{\left(1+\dfrac{\zeta_{m,n}}{L}\right)^{L+1}} \tag{3.75}$$

Thus, the integral expression for the first and second central moments of the logarithm of the bistatic GMLED random variable becomes solvable and yields the following results for the exact statistical parameters of the multistatic GMLED log-normal approximation

$$\mu_{G0} = \frac{MN}{L} \tag{3.76}$$

$$\sigma^2_{G0} = \frac{MN}{L^2} \tag{3.77}$$

Label	**Relevant equations**	**Description**
Simulated	(3.34)	Monte Carlo simulation of the logarithm of the multistatic GMLED detector, histogram approximation to pdf
Theoretical	(3.63)	Monte Carlo simulation of random variables composing the theoretical distribution of the logarithm of the multistatic GMLED, histogram approximation to pdf
Approximation	(3.73) (3.74) (3.78) (3.79)	Gaussian approximation to the logarithm of the multistatic GMLED, normal pdf with relevant parameters (3.73) (3.74)

Table 3.2: *Guide to GMLED pdf simulations labelling and terminology*

Figure 3.3 and Figure 3.4 depict the pdfs of the logarithm of the GMLED and the appropriate Gaussian approximations to the detection variables. The simulation labeling is consistent with the one used in Section 3.5.2 and is provided for convenience along with the relevant equations in Table 3.2. Figure 3.3 shows the respective pdfs for a smaller 10-transmitters and 10-receivers network. The number of temporal iid snapshots observed by the system is K=20 per range gate. The values of the SNR for the simulations under the H_1 hypothesis are the same as in the MLED pdf analysis in Section 3.5.2. The simulated and theoretical results are obtained from the histogram approximation to the pdf. A million sample points were generated for each run and placed in 100 histogram bins in order to produce relatively smooth pdf curves.

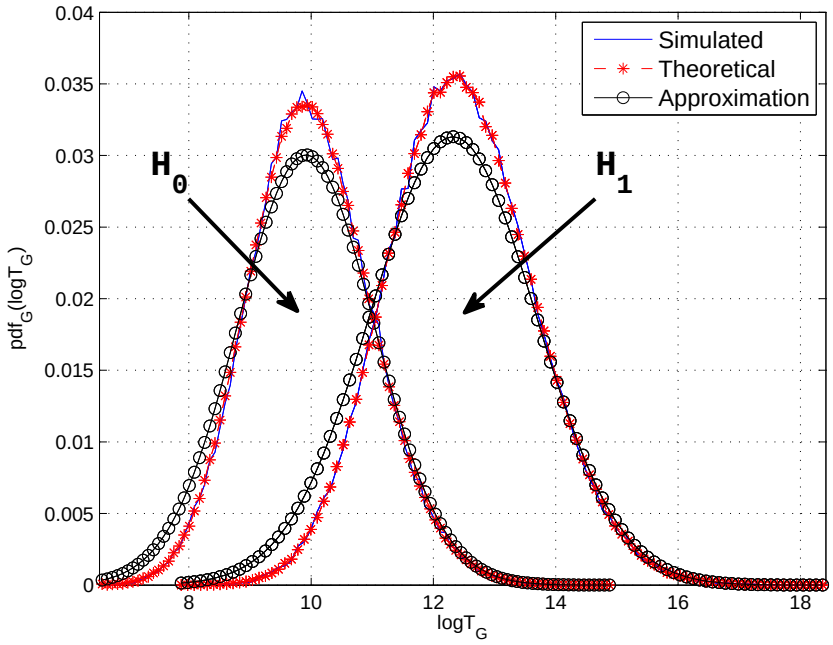

Figure 3.3: *Probability density function of the multistatic GMLED detection variable* K=20, M=N=10, SNR=$-26dB$

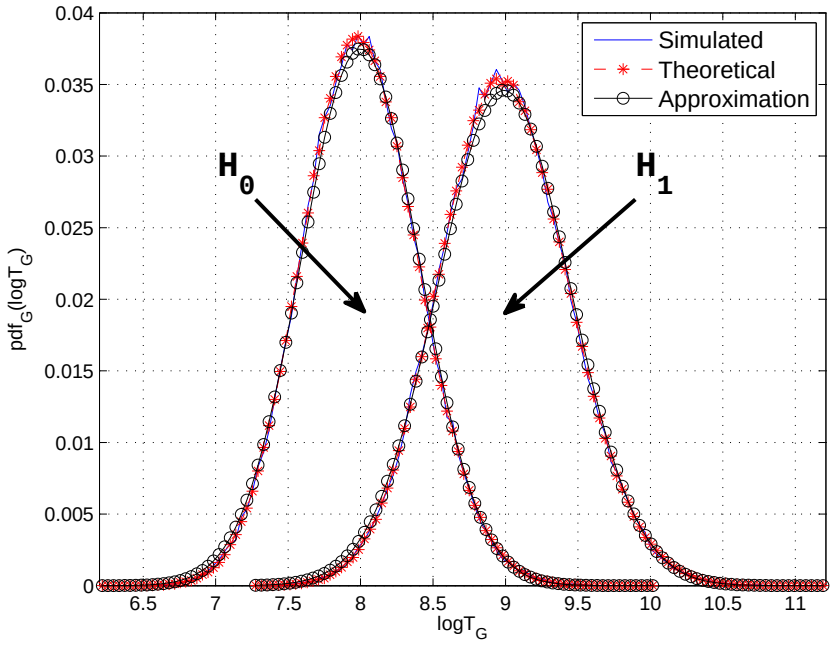

Figure 3.4: *Probability density function of the multistatic GMLED detection variable* K=60, M=N=20, SNR=$-36dB$

The results demonstrate a relatively good match between the simulated and theoretical pdfs. However, the mismatch between approximating Gaussians and the Monte Carlo simulated histograms observed for the MLED are even more pronounced here. The theoretical and simulated distributions evidently differ from the approximating ones not only in skewness but also in excess kurtosis. The approximating error is not large but it is likely to have a slight influence on the process of estimating the probability of detection and false alarm.

In the second set of pdf simulations shown in Figure 3.4, a larger radar network of 20 transmitters and 20 receivers has been used. A larger number K=60 of temporal iid snapshots is also used. Similar conclusions can be drawn for the GMLED pdfs shown here as the ones for the MLED. The resulting distributions consist of 400 convolutions of independent but not identically distributed components. Thus the approximating Gaussian pdf now better matches the distribution of the multistatic GMLED detection variable. Once again this is linked to the fact that all central moments above the second are negligible for a larger number of convolved terms.

The probability of false alarm of the multistatic GMLED for a certain threshold ν follows from the log-normal approximation

$$P_{fa}(\nu) \approx Q\left(\frac{\log \nu - \mu_{G0}}{\sigma_{G0}}\right) \tag{3.78}$$

When a target is present the detector statistics are distributed as $\ln \mathcal{N}(\mu_{G1}, \sigma_{G1}^2)$ where μ_{G1} and σ_{G1}^2 are given by (3.73) and (3.74) respectively. The probability of detection is thus

$$P_d(\nu) \approx Q\left(\frac{\log \nu - \mu_{G1}}{\sigma_{G1}}\right) \tag{3.79}$$

Note that the log-normal approximation to the multistatic GMLED proposed here can be easily extended to the multistatic GLRT proposed in [65, 67]. The approach is the same as the one presented in this work and thus the results provided here are valid for the TDS algorithm with a slight modification of the added degree of freedom.

3.6 Simulations

This section contains the simulations of the multistatic MLED and GMLED derived in the chapter as well as the proposed Gaussian approximations to their statistics. Similar to Section 3.5.2 and Section 3.5.4, in all the conducted simulations, three data sets are presented for the purpose of analysing the performance of the derived detectors: "simulated," "theoretical," and "approximation." A short summary of these terms and the associated relevant equations is provided in Table 3.1 for the MLED and Table 3.2 for the GMLED.

The results labelled as "simulated" are related to the multistatic MLED and GMLED threshold detectors derived in Section 3.3 and Section 3.4. This set of data involves simulating an actual multistatic radar network similar to the toy example depicted in Figure 2.3 of Chapter 2 with a much larger number of transmit-receive pairs. A Monte Carlo simulation of a million runs of the MLED (3.16) and the GMLED (3.34) is then used to obtain the results.

The results labelled as "theoretical" are related to the theoretical model for the distribution of the multistatic MLED and GMLED threshold detectors derived in Section 3.5.1 and Section 3.5.3. The challenge here is that a closed-form expression for the pdf of the test statistics of the two SDS detectors was never obtained. However, the viability of the combinations of random variables that describe the distributions of the MLED and GMLED can still be tested. The theoretical simulation results provided here are obtained through drawing samples from the random variables (3.39) and (3.63) in a second set of Monte Carlo simulations. These results are useful not only because they confirm the viability of the derived detection statistics components, but also because they utilise the approximation of the non-centrality parameters $\lambda_{m,n}$ proposed in equation (3.53). The set of theoretical simulations purposefully uses $\widetilde{\lambda}_{m,n}$ instead of numerically simulating the values of $\lambda_{m,n}$ in order to show the viability of the proposed first-order approximation.

The results labelled as "approximation" are related to the normal and log-normal approximations to the multistatic MLED and GMLED derived in Section 3.5.2 and Section 3.5.4. The parameters of the approximating Gaussian distributions (3.51), (3.52), (3.73) and (3.74) have been calculated and used throughout this set of simulations. The derived approximate probabilities of detection and false alarm (3.56), (3.57), (3.78) and (3.79) have been obtained, and the results have been compared to the numerical ones.

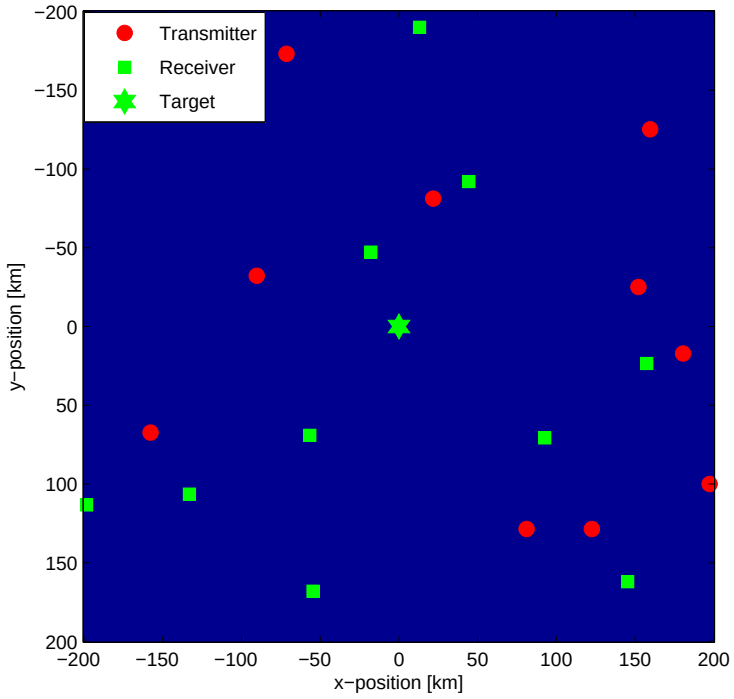

Figure 3.5: *Radar setup of randomly-placed 10 mobile transmitters and 10 receiver ULAs*

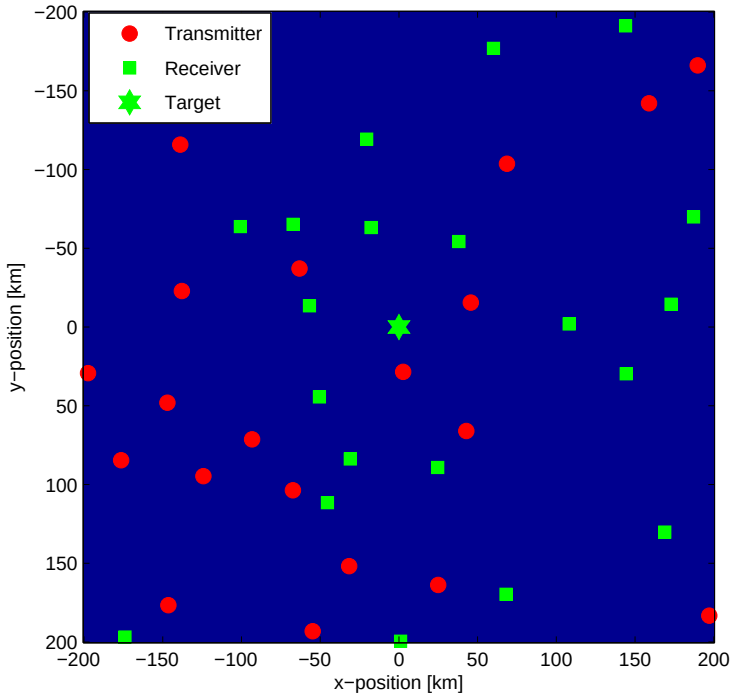

Figure 3.6: *Radar setup of randomly-placed 20 mobile transmitters and 20 receiver ULAs*

A basic multistatic radar scenario has been created in order to produce the numerical simulations. Two network sizes have been considered for the simulations: a smaller setup of 10 transmitters and 10 receivers (Figure 3.5), and a larger one of 20 transmitters and 20 receivers (Figure 3.6). The radar components have been placed at randomly-chosen locations around an existing airborne target. The minimum distance between any two radar components is 20km, and the search area is a 2-D square with a side of 400km. The target is in the centre of the Cartesian coordinate system.

Most of the operational parameters of the transmitted pilots are the same as the ones in [12]. The values that remain unchanged throughout all sets of simulations are provided for convenience in Table 2.1 of Section 2.7. The amplitudes of the returned pilots $\alpha_{m,n}$ are random and drawn from a standard zero-mean complex normal distribution $\mathcal{CN}(0,1)$. The size of the observation snapshots remains constant P=10, but simulations involving a different number of iid snapshots K=20 and K=60 have been conducted.

The clutter in the radar scenario is generated in accordance with the GCM [49, pp.20-24] described in Section 2.2. Each transmitter and receiver in the radar setup forms an individual bistatic channel. The elliptical iso-range where the target is located in that channel provides N_c=1000 discrete clutter contribution returns that form the clutter covariance matrix. This ensures a relatively good approximation to the continuous clutter ridge observed in a practical radar scenario [49, p.22]. The matrix is then used to colour AWGN of power σ_c^2, which results in a coloured Gaussian clutter model for the interfering ground returns of the transmitted waveforms.

The overall performance of the multistatic threshold detectors presented in this chapter has been simulated. The probability of false alarm in all cases has been fixed to 0.02. As the average SNR that the radar system observes is varied, the resulting probability of detection is investigated. Figure 3.7 shows the obtained results for the smaller network of 10 transmitters and 10 receivers and K=20 observed temporal snapshots. As expected from the SDS results for the bistatic case [18, pp.74-78], the GMLED algorithm performs slightly better than the MLED one for a small K, exhibiting the same probability of detection at approximately 1 dB less SNR. The results show that the simulated detector curves based on (3.16) and (3.34) match the theoretical models describing their statistics shown in (3.39) and (3.63) respectively. Moreover, the fact that the approximation to the $\lambda_{m,n}$ variables was used in the theoretical curves proves the viability and justifies the usage of (3.53). The Gaussian approximations to

the multistatic detectors given in (3.56), (3.57), (3.78) and (3.79) are also close to the simulated and theoretical curves. The small difference comes from the fact that approximation based on the first two moments of the multistatic MLED and GMLED threshold detector random variables is performed. This phenomenon has also been observed in the discussion of the relevant pdfs. Moreover, it should be noted that according to the Berry-Esséen theorem the convergence of sums of non-identically distributed random variables to the CLT is slower than the iid counterparts [87].

Figure 3.8 shows the simulation results for the same radar network with the number of observed temporal snapshots per range gate increased to K=60. It can be seen that both the multistatic MLED and GMLED are significantly affected by the temporal frame size, having the same detection rate at approximately 6 dB lower SNR value. This can be explained by the improvement in the SDS covariance matrix estimate (2.29) through the addition of more data samples. It should be noted that as the temporary frame size increases, the multistatic MLED and GMLED algorithms' performance becomes almost identical. This is evident in the simulations as well and reflects the behaviour of the MLED and GMLED bistatic algorithms presented in [17] and [18]. The difference comes from the fact that the MLED uses the K iid snapshots for covariance estimation, while the GMLED uses additional information from the coherent sample means $\boldsymbol{g}_{m,n}$ for normalisation. As the number of snapshots K grows large, the relative contribution of the additional information to the estimation and detection process becomes insignificant. Similar behaviour is observed in the comparison of the AMF and the GLRT threshold detection algorithms [9, 10].

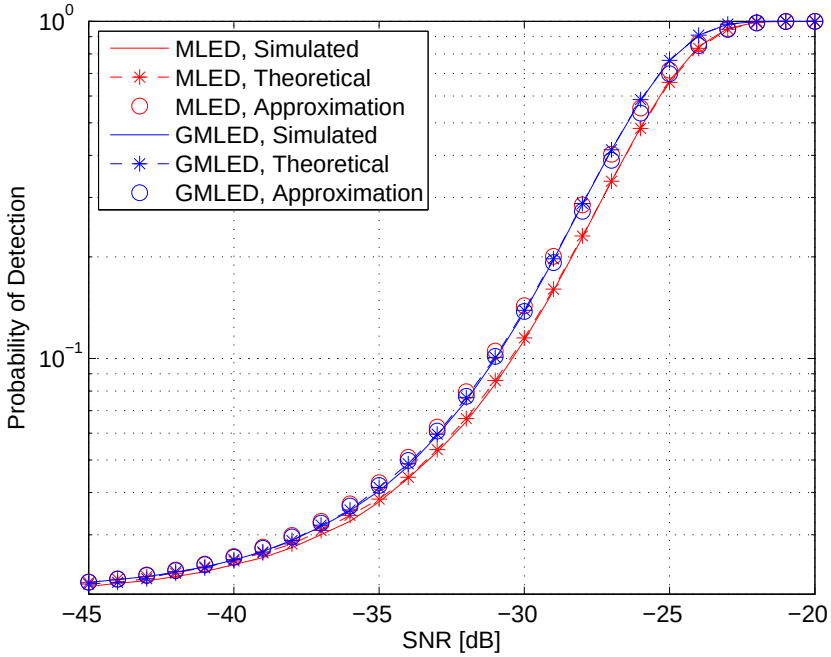

Figure 3.7: *Probability of Detection vs SNR of the multistatic MLED and GMLED detectors for* $P_{fa} = 0.02$, $K = 20$, $M = N = 10$

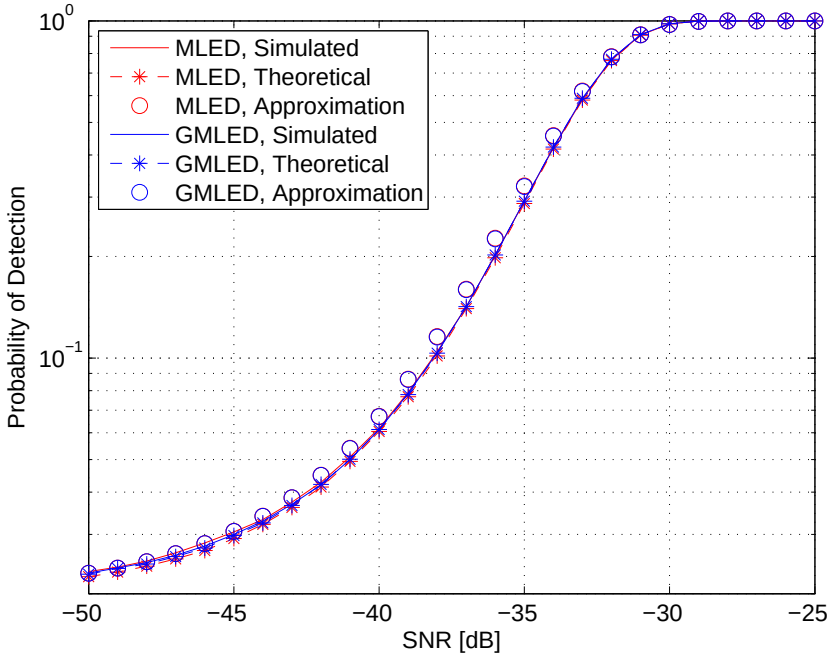

Figure 3.8: *Probability of Detection vs SNR of the multistatic MLED and GMLED detectors for* $P_{fa} = 0.02$, $K = 60$, $M = N = 10$

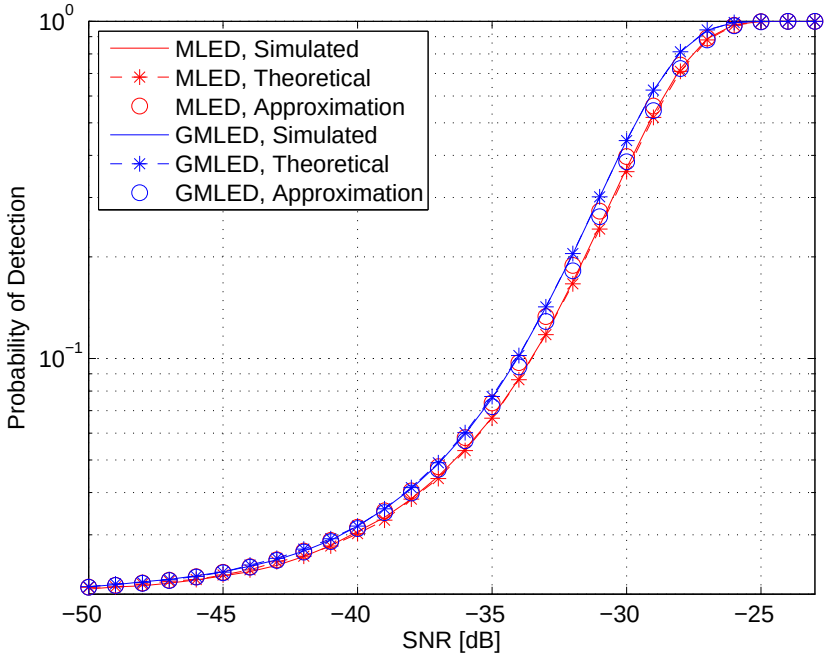

Figure 3.9: *Probability of Detection vs SNR of the multistatic MLED and GMLED detectors for* $P_{fa} = 0.02$, $K = 20$, $M = N = 20$

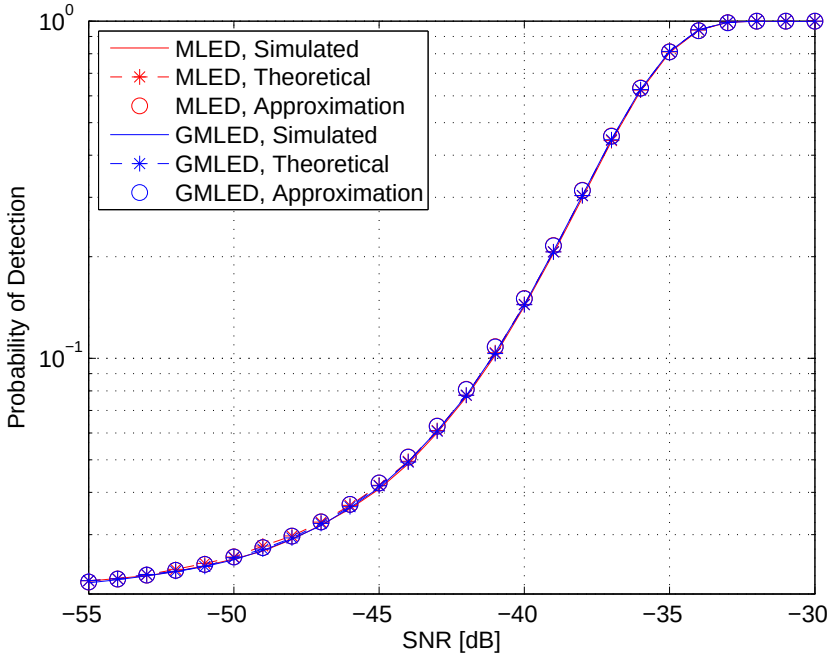

Figure 3.10: *Probability of Detection vs SNR of the multistatic MLED and GMLED detectors for* $P_{fa} = 0.02$, $K = 60$, $M = N = 20$

Figure 3.9 and Figure 3.10 aim to simulate the performance of the larger radar network for 20 and 60 temporal observations respectively. The number of transmitters and receivers now doubles to 20. Compared to Figure 3.7 and Figure 3.8, the curves of the probability of detection shift by a further 3 dB to the left. This reflects the improvement in the performance of the multistatic MLED and GMLED detectors due to the increased spatial diversity in the system. The accuracies of the proposed Gaussian and log-normal approximations to the multistatic MLED and GMLED respectively are also greatly enhanced. This is because the number of terms in the summations (3.39) and (3.64) increases which, according to the CLT, brings the distribution of the sums closer to the Gaussian curve. As more and more pdfs are involved in the convolution to obtain the final distributions of the multistatic variables, the moments higher than second asymptotically converge to zero. In a hypothetical radar network of infinite size this approximation will become exact.

It can be seen in Figure 3.8 and Figure 3.10 that the number of iid temporal snapshots K available for estimation is a very important factor for the performance of the multistatic MLED and GMLED threshold detectors. The way these snapshots are generated from the CUT is described in Section 2.2 where the signal model assumed in this thesis was discussed. This model has been adopted in other STAP applications in the past [14, 19, 21] since it provides a number of benefits. In the presence of K iid snapshots, the analysis and derivation of a target detection algorithm are facilitated or greatly simplified. Previous analysis of a practical radar scenario [55] performed on the MCARM data set [88] demonstrates that the model can be applied on the observations in a single range gate. Similar conclusions can be drawn from the model proposed in [76] where the simulations are performed on the KASSPER data set [89]. If a sufficient number of iid snapshots cannot be drawn from one range gate, the data from concurrent STAP observations from the same range could be used in some cases to provide more samples. The main drawback of the iid model adopted in this thesis is that in a real radar scenario the independence assumption is rarely perfectly satisfied. A discussion of this has been provided in the derivation of the APES algorithm in [61] along with the implications. The term "approximate ML" has been proposed there to describe the APES filter in the case of snapshot correlation. The algorithm still functions as a ML derivation, but suffers a performance loss proportional to the degree of correlation. This drawback applies directly to the multistatic MLED and GMLED threshold detectors derived here. In a scenario where K perfectly iid snapshots cannot be extracted, the temporal correlation will result in an effective reduction of the opreational performance. However, the algorithms will still function and provide a relatively

reliable process of SDS detection in a scenario where secondary data cannot be acquired.

3.7 Summary

In this chapter two SDS multistatic STAP algorithms have been derived for the detection of signals of known template in coloured Gaussian interference. The performance of the algorithms in a MIMO radar target detection scheme has been analysed. It has been shown that the algorithms exhibit the CFAR property. To facilitate the analysis and provide a basic guidance for predicting the detection performance of the proposed algorithms, two simplified Gaussian approximation models for the statistics of the detectors have been proposed. Through these models the theoretical probabilities of detection and false alarm have been derived. The validity of the theoretical models as well as the simplified Gaussian approximations has been verified through numerical simulations. It has been demonstrated that the performance of both algorithms increases as the number of temporal snapshots in the system is also increased. Furthermore, the performance gains of the multistatic detectors over their bistatic counterparts have been shown. With an increased number of bistatic channels both the performance as well as the approximation model get better.

The theory and results in this chapter are valid under the assumption of ideal synchronisation of the Doppler frequencies that a target would produce in the different bistatic channels. That assumption is necessary to derive the optimal multistatic maximum likelihood detectors in the considered scenario. However, ideal Doppler synchronisation is unlikely to exist in a real target detection scenario. Chapter 4 relaxes this assumption and provides a practical solution to the synchronisation problem in the case of the multistatic MLED algorithm developed here.

Chapter 4
Multistatic maximum likelihood estimation detector: data compression and velocity space target detection

4.1 Introduction

This chapter discusses the practical implementation of the multistatic MLED and proposes the modified multistatic MLED algorithm for enhanced target detection in velocity space. While the multistatic MLED derived in Chapter 3 offers great performance advantages over the existing bistatic detectors, the practicality of its implementation in a real radar scenario may be limited by a number of factors. In a MIMO radar scenario, the amount of data that has to be shared through the network is very significant. This issue is discussed in Section 4.2 where a method for compressing the MLED likelihood function before transmission is proposed to alleviate the problem. Section 4.3 discusses the difficulties that arise in synchronising the corresponding Doppler frequencies from the multiple radar channels. A solution is proposed that projects the channel-specific relative Doppler frequencies upwards into a fixed absolute velocity space where the multistatic likelihood fusion is performed. Section 4.4 explores the structure of the the velocity likelihood function produced by a moving target and proposes a modification to the multistatic MLED detector based on this structure. The modified multistatic MLED utilises prior knowledge to provide enhanced target detection. Section 4.5 provides theoretical analysis of the proposed enhanced algorithm based on the findings in Chapter 3. Section 4.6 demonstrates the performance of the modified MLED through numerical simulations and verifies the theoretical analysis. Section 4.7 contains a brief summary of the work presented in this chapter.

4.2 Subspace compression for the MLED Doppler likelihood

The multistatic solution to the MLED target detection problem shown in (3.16) is optimal in the ML sense under the assumptions made in this thesis. An overall practical implementation of the

detector in a MIMO scenario has been roughly outlined in Table 2.2 of Chapter 2 and is similar to the process proposed in [44]. One of the major challenges of this practical implementation is the amount of data that has to be shared between the multiple receiver elements in the widely-spaced radar setup.

In Chapter 3 it has been assumed that the ranges to target, the spatial frequencies $f_{s\{m,n\}}$, and the Doppler frequencies $f_{d\{m,n\}}$ are known parameters (composing what this thesis will refer to as RAD space), and the focus was on deriving the ML combination of the bistatic solutions in the different channels $(\cdot)_{m,n}$. This represents the outermost loop of the process outlined in Table 2.2. In a practical MIMO scenario, a full search in RAD space has to be performed in all bistatic channels to cover the physical area in range of the radar installation and the potential Doppler frequencies produced by moving airborne targets. The RAD contributions from different channels have to be transmitted through the network, and the results have to be synchronised before being compounded in the multistatic ML target detection decision variable. This section focuses on the data transmission between nodes in the radar network, while Section 4.3 deals with the synchronisation.

In a practical implementation of a multistatic STAP algorithm such as the MLED, the amount of data that has to be shared between the computational nodes in a radar network can become overwhelmingly large; this can limit the possibility of real-time processing and detection. It is natural to assume that the processing of observations in a bistatic radar channel is performed locally by the receiver. The amount of data handled in a CPI is proportional to the number of range gates N_r in the CPI and the number of angles N_a, and Doppler frequencies N_d searched for a target in a specific channel. In a multistatic scenario each of the N receivers locally processes the observations from the M transmitters. This can be done in parallel, and due to the linear nature of the multistatic MLED with respect to its bistatic components, the results can also be fused locally to produce a MISO target detection result. A hard decision can be made based on that result and propagate through the radar network, but to achieve a true distributed ML result, each receiver has to share its complete RAD likelihood estimates either with a central fusion node or with the other $N-1$ computational nodes.

To reduce the amount of data propagated through the MIMO radar network, an adaptive compression of the bistatic MLED Doppler likelihood is proposed here. The method extracts the

subspace of significant components from the N_d-point MLED likelihood given by

$$\boldsymbol{T}_M = [T_M(f_{d1}), \ldots, T_M(f_{dN_d})] \tag{4.1}$$

where $T_M(f_d)$ signifies the detection variable that the standard bistatic MLED algorithm (2.30) produces when probing a certain Doppler frequency f_d for potential targets. References to the channel $(\cdot)_{m,n}$ will be omitted for the time being for simplicity. The normalised Doppler frequencies f_d are selected to be equally distributed and span the whole range from -½ to ½. The subspace extracted from (4.1) denoted as $\widetilde{\boldsymbol{T}}_M$ is sparse and consists only of the significant contributions of $\boldsymbol{T}_M$. This idea has been explored in the field of distributed detection in the past and has often been referred to as "sensor censoring" [90–93]. The definition of significant contributions can be arbitrary and application-specific if additional information about the target and clutter are available; e.g. if a target is known to be moving away from a given bistatic radar pair, the information from half of the Doppler frequencies in the search space can be discarded. If the normalised Doppler frequency of a target is known to be in a certain range, the subspace $\widetilde{\boldsymbol{T}}_M$ can contain only the likelihood contributions from that range. Other existing methods rely on the knowledge of the set or range of frequencies where clutter contributions may occur [12, 13]. Here this knowledge can be used to eliminate these contributions in the process of extracting the relevant subspace $\widetilde{\boldsymbol{T}}_M$ of potential target contributions. Other data compression schemes for detection and localisation perform a similar task by ordering the significant contributions according to their weight before transmission [94, 95]; thus the exchange of data can be stopped once the network reaches a decision. This can easily be adapted to the multistatic radar detection scenario and the compression scheme proposed in this section.

No prior interference or target knowledge is assumed in the current problem; thus here a simple approach of extracting the subspace of local peaks $\widetilde{\boldsymbol{T}}_M$ of the MLED likelihood $\boldsymbol{T}_M$ will be employed for data compression in the pre-transmission stage. A brief description of the process of compression is given in Table 4.1. A small threshold ε is introduced for selecting the local maxima that contribute to the compressed subspace. It helps to remove some of the insignificant components and artefacts from the likelihood function, and it provides direct control over the compression rate at the expense of performance.

The ideal MLED likelihood function in a hypothetical scenario of infinite SNR has a sharp peak at the target's Doppler frequency and is zero elsewhere. As the SNR gets lower, other peaks appear resulting from noise and clutter. This is demonstrated in Figure 4.1 which shows an ex-

for Doppler frequencies f_d between 1 and N_d **do**
  if $\widetilde{\boldsymbol{T}}_M(f_d)$ is a local maximum **then**
    if $\widetilde{\boldsymbol{T}}_M(f_d) > \varepsilon$ **then**
      $\widetilde{\boldsymbol{T}}_M(f_d) = \boldsymbol{T}_M(f_d)$
    end if
  else
    $\widetilde{\boldsymbol{T}}_M(f_d) = 0$
  end if
end for

Table 4.1 Subspace compression

ample likelihood function of the bistatic MLED at a relatively low SNR of -30dB per temporal snapshot with 60 such snapshots in total. The extracted likelihood subspace is also depicted in the figure. The particular SNR and snapshot number have been chosen without loss of generality in order to provide a suitable visual example and demonstrate the concepts discussed in this section; the target contribution is still identifiable but also practically undetectable in a single bistatic scenario due to the higher likelihood peaks produced by the noise and clutter in the channel.

The justification for using the proposed likelihood compression method described in Table 4.1 lies in the linearity of the multistatic MLED detection variable (3.16) with respect to its bistatic components (2.30). Since the former is an unweighed sum of the individual components, the main contributions to the multistatic detection variables will always come from the peaks of the bistatic likelihoods. This is true for a collection of channels that have a relatively uniform SNR. If one or more channels have a very low SNR compared to the others, the subspace compression method may completely discard the contribution from the target Doppler frequency bin, but this is unlikely to influence the overall multistatic threshold detector decision. If one or more channels have a dominantly high SNR compared to the others, it is likely that the extracted likelihood will contain only the subspace of the target Doppler frequency bin which provides an excellent compression rate with no loss of performance.

It is clear that the transmitted signal $\widetilde{\boldsymbol{T}}_M$ is a sparse subset of $\boldsymbol{T}_M$. While this method provides vast reduction in the amount of data that is transmitted between the computational nodes of the radar system, it also degrades the sensitivity of the MLED to mismatches between the actual and the estimated target Doppler frequency. If in a bistatic channel the MLED likelihood function does not peak exactly at the target Doppler, all information from this channel is lost after the compression. The issue can be mitigated by running the received subspace $\widetilde{\boldsymbol{T}}_M$ through a

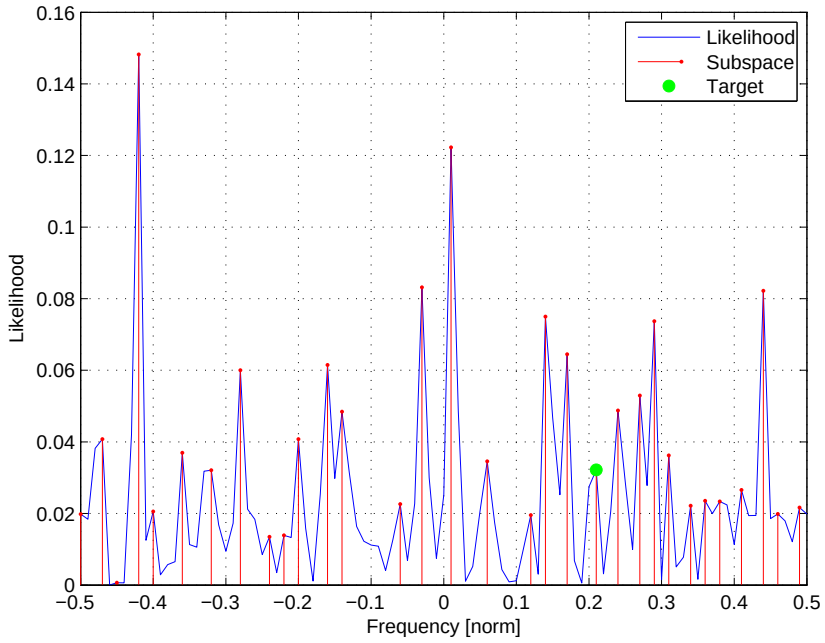

Figure 4.1: *Likelihood function of the standard bistatic MLED and proposed subspace compression,* K=60*,* $SNR = -30dB$

smoothing filter operator. This can be done after the compressed likelihoods have been transmitted throughout the radar network and thus provides no additional data to be exchanged.

4.3 Velocity synchronisation of detection likelihood

One of the major tasks in a practical implementation of the multistatic MLED algorithm is the synchronisation of the data coming from the different bistatic channels before forming the multistatic decision variable. Since the physical implementation of widely-spaced MIMO radar is still relatively underdeveloped, litle literature exists at the moment that specialises on the issues of data exchange and synchonisation. However, extensive work has been done on analysing and solving those problems for general sensor netowors that could be adapted to MIMO radar. For a relatively exhaustive analysis on the transmission, delay, and energy limitations of data exchange and synrhonisation in sensor networks, refer to [40,41,58,93] and references within.

In the considered MIMO radar scenario and developed multistatic algorithms, every channel operates and forms its detection likelihood in its own unique RAD space. The RAD spaces then

have to be aligned in order to properly combine the corresponding likelihoods for the multistatic decision. This can be divided into two distinct steps: synchronising between the different geolocations in the physical search space (range and angle synchronisation) and synchronising the different Doppler frequency bins from the bistatic channels.

A method for geolocation synchronisation has been proposed in [44] and is part of the multistatic radar implementation procedure outlined in Table 2.2 of Chapter 2. Range and angle form the basis of a polar 2-D coordinate system and are the natural parameters that a radar employs to locate a target. To facilitate channel synchronisation, [44] proposes the translation of these two parameters into a standard Earth-Centred Earth-Fixed Cartesian coordinate system. Depending on the range-angle resolution of the radar scenario, the system can be discretised into different physical patches that are individually searched for a target. It is assumed that all the radar elements know of each other's relative positions and velocities. Because the Cartesian coordinates are shared and synchronised in the radar network, combining the results from the same geolocation becomes trivial.

Doppler frequency synchronisation between the different channels is a challenging task due to the non-linear nature of the parameters involved. The generic form of the bistatic Doppler frequency produced by a target is given in (2.8). In a multistatic scenario the Doppler frequency is channel-specific for every transmit-receive pair $(\cdot)_{m,n}$

$$f_{d\{m,n\}} = \boldsymbol{v}^H \boldsymbol{k}_{m,n} - \boldsymbol{v}_{t\{m\}}^H \boldsymbol{k}_{m,n} \tag{4.2}$$

where $\boldsymbol{k}_{m,n}$ is given by (2.7) and is the response of the bistatic channel to a target at a certain geolocation. It is assumed that the radar network can have full knowledge of all bistatic responses $\boldsymbol{k}_{m,n}$ as well as the velocities of the mobile transmitters $\boldsymbol{v}_{t\{m\}}$. However, since the Doppler frequency $f_{d\{m,n\}}$ is not mapped to a unique target velocity $\boldsymbol{v}$, no trivial mapping between the Doppler frequencies of the different channels exists. Thus combination of the detection likelihood variables cannot be directly performed in Doppler space.

This section proposes the transition from Doppler frequency space (D-space) to velocity space (v-space) to facilitate the multistatic MLED likelihood combination of its bistatic components [32–36]. As evident from (4.2), Doppler frequencies are unique to their bistatic channels, but the target velocity is absolute. The transition from D-space to v-space involves the upward projection of the one-dimensional (1-D) variable $f_{d\{m,n\}}$ into the space of the 2-D variable $\boldsymbol{v}$.

The projection can be obtained from transforming (4.2) into the linear equation

$$v_y = \frac{f_{d\{m,n\}} + \boldsymbol{v}_{t\{m\}}^H \boldsymbol{k}_{m,n} - v_x k_{m,n}(1)}{k_{m,n}(2)} \tag{4.3}$$

where the target velocity $\boldsymbol{v}$ is split into its x-y components as shown in (2.5). In practice the velocity map produced by (4.3) will be discrete. Both the v_x and v_y components will consist of N_v possible values. While (4.3) can provide a real-time link between the N_d Doppler frequency bins and the $N_v \times N_v$ velocity bins searched by the system, the mapping can also be pre-computed for the different physical areas searched by the radar system; thus the upward projection of D-space into v-space does not present any major additional burden on the computational nodes. In Figure 4.1 the likelihood function of the bistatic MLED in D-space was shown. Figure 4.2 shows the same likelihood function projected upwards into v-space through the mapping (4.3). The target velocity is in the middle, and the search space is taken as a small region around the target value.

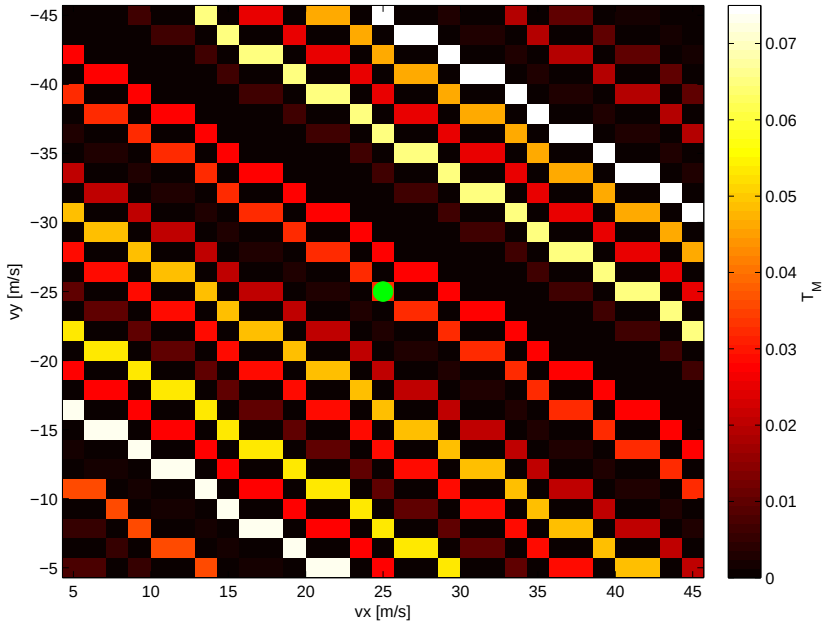

Figure 4.2: *Likelihood function of the standard bistatic MLED in velocity space,* K=60, *SNR*= $-$ 30*dB,* $\boldsymbol{v}$= $[25, -25]$*m/s*

Once the individual bistatic MLED likelihood functions are projected from D-space into v-space, the multistatic combination becomes trivial. This method of translation can be used

in the practical implementation of any other multistatic algorithm based on either covariance estimation [56,65,67], subspace projections [12,13,21], or other models for estimation (e.g. autoregressive [14]). There are other advantages to the method proposed in this section. Velocity estimation has always been an integral part of target radiolocation. In v-space, the multistatic MLED will be able to directly provide an estimate to the velocity if the average SNR of the channels is sufficiently high. Moreover, identifying a target's position and velocity can predict its movement. Usually an additional tracking algorithm is required post-detection to perform this task. If the detection process is done in v-space, the result can aid the tracking algorithm.

The v-space syncronisation method proposed here clearly depends on the accuracy of the target's Doppler and subsequent velocity estimation. Under normal mode of operation this is fulfilled by the fact that the APES filter on which the MLED is based is sharp and accurate at the frequency it estimates [21]. However, the drawback of this precision is the oversampling of the observations required to support such filter sharpness. This issue and some of its potential solutions involving the utilisation of the stop-band APES filter are discussed in [96].

The projection into v-space proposed here can be combined with the proposed likelihood compression model from Section 4.2. This completes all the steps of the multistatic target detection method outlined in Table 2.2 and provides a potential practical implementation guideline for MIMO radar detection. When an airborne target is present, it will produce a distinct likelihood pattern in v-space when the compressed multistatic MLED is used for detection. In Section 4.4 this pattern is examined, and based on the findings an enhancement to the multistatic MLED is proposed that would increase the performance of the algorithm.

4.4 Modified MLED

This section proposes a modification of the multistatic MLED algorithm based on the expected structure of the target velocity likelihood. The idea extends from the general multistatic radar binomial analysis presented in [37] and applies the principle to the multistatic STAP scenario discussed in this thesis. It is assumed that the MLED likelihood function compression proposed in Section 4.2 is employed and that the target signal, if present, always lies in the subspace $\widetilde{\boldsymbol{T}}_M$. As previously discussed, in an ideal environment of infinite SNR (no noise or interference) the D-space likelihood function of the bistatic MLED algorithm consists only of a sharp peak at the correct target Doppler frequency. Thus the compressed likelihood subspace has only

one component. Based on the v-space translation given in (4.3), the ideal bistatic likelihood function is a line that passes through the target velocity. Therefore in a multistatic scenario of ideal channels with infinite SNR, all bistatic contributions will pass through and cross over at the target velocity. Figure 4.3 demonstrates this concept visually in a multistatic 9-channel scenario ($M{=}N{=}3$) with very low noise and clutter returns. The figure shows the combined multistatic MLED detection variable $T_M(\boldsymbol{v})$ for all velocities $\boldsymbol{v}$ in the search space. Each of the 9 lines in the figure represents the Doppler reflection projected into v-space from the moving target in a single bistatic channel of the radar system. All lines pass through the correct target velocity, which is their intersection point.

Since the algorithms in this chapter generate likelihood values in the whole v-space range, the physical space for saving the results becomes a consideration. Thus the number of simulated channels will be kept relatively low. In a practical scenario this issue is alleviated by the fact that computations and storage are distributed and local for each receiver.

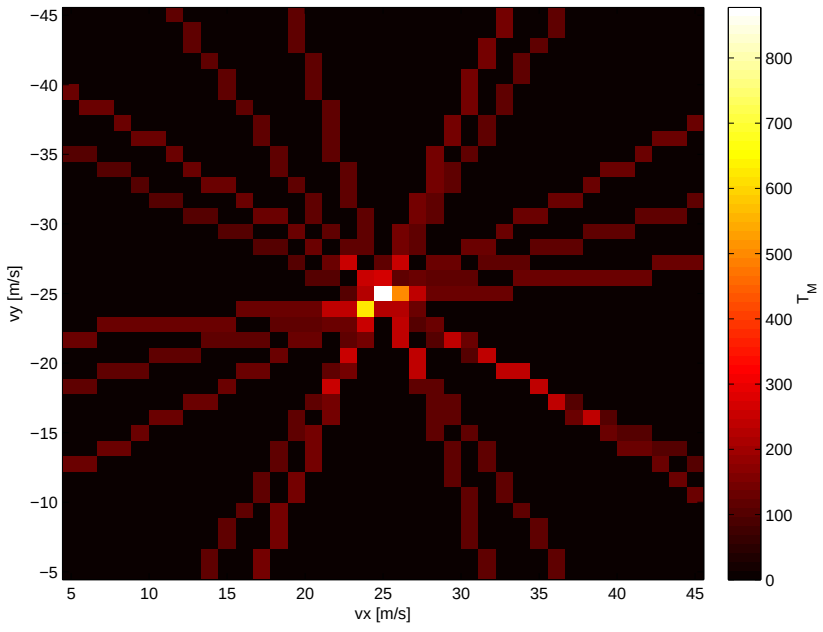

Figure 4.3: *Likelihood function of the multistatic MLED in velocity space* $K{=}60$*,* $SNR{=}10dB$*,* $\boldsymbol{v}{=}[25, -25]m/s$

The structure shown in Figure 4.3 is only characteristic for target returns because the target velocity remains fixed across all channels. The bistatic clutter contributions are considered to be independent, and thus they don't share a common velocity. The only ground patch whose

clutter returns are observed across all channels is the one under the target. However, since the transmitter velocities $\boldsymbol{v}_{t\{m\}}$ are not the same, the relative velocities of the ground patch with respect to the bistatic channels $-\boldsymbol{v}_{t\{m\}}$ also differ. Thus the clutter returns will not produce a well-defined likelihood structure such as the one from the target shown in Figure 4.3.

If the bistatic MLED likelihood is sparse, the knowledge that target and clutter would produce different patterns can be utilised to aid the detection process. The subspace compression method described in Section 4.2 naturally fulfils the sparsity criterion. The subspace $\widetilde{\boldsymbol{T}}_M$ consists of the target component and the components of the strongest clutter returns. The multistatic MLED weighs all contributions according to their likelihood before adding them up in v-space as suggested in Section 4.3.

$$\sum_{m,n} \frac{|\boldsymbol{s}_{m,n}^H(\boldsymbol{v})\boldsymbol{Q}_{m,n}^{-1}(\boldsymbol{v})\boldsymbol{g}_{m,n}(\boldsymbol{v})|^2}{\boldsymbol{s}_{m,n}^H(\boldsymbol{v})\boldsymbol{Q}_{m,n}^{-1}(\boldsymbol{v})\boldsymbol{s}_{m,n}(\boldsymbol{v})} \underset{H_0}{\overset{H_1}{\gtrless}} \gamma \tag{4.4}$$

The likelihood structure discussed here suggests that the number of contributions at a given point can also be used in order to distinguish between a potential target and a strong clutter return. Define the following bistatic likelihood contribution function:

$$\boldsymbol{B}_{M\{m,n\}}\left(f_{d\{m,n\}}\right) := \widetilde{\boldsymbol{T}}_{M\{m,n\}}\left(f_{d\{m,n\}}\right) \underset{0}{\overset{1}{\gtrless}} \varepsilon_{m,n} \tag{4.5}$$

The threshold $\varepsilon_{m,n}$ is used to determine the non-zero components of $\widetilde{\boldsymbol{T}}_{M\{m,n\}}$. By design these components are all larger than $\varepsilon_{m,n}$ as shown in the subspace extraction procedure in Table 4.1. Therefore, $\boldsymbol{B}_{M\{m,n\}}$ is a signal subspace that equally weighs (with a weight of one) all MLED likelihood frequency contributions that are local maxima and surpass a certain threshold. This process is theoretically equivalent to performing threshold detection in each bistatic MLED channel individually before combining the results. Such distributed detectors based on the combination of the individual bistatic hard decisions have been proposed and analysed in the past [37–41].The difference here is that in the detection process, the thresholds $\gamma_{m,n}$ are selected to provide a relatively low probability of false alarm; here the thresholds $\varepsilon_{m,n}$ need to be small enough to prevent the target contribution from being excluded from the analysis in low SNR scenarios.

To successfully perform target detection, it should be assumed that the target is sufficiently far from the clutter ridge in the individual bistatic channels. In that case, provided that the returned power is high enough to surpass the thresholds $\varepsilon_{m,n}$, it can be assumed that the target will

produce a local peak in the MLED likelihood function. Thus the proposed modified multistatic MLED algorithm can be described by the following equation

$$\sum_{m,n} \widetilde{\boldsymbol{T}}_{m,n}(\boldsymbol{v}) + \kappa \sum_{m,n} \boldsymbol{B}_{M\{m,n\}}(\boldsymbol{v}) \underset{H_0}{\overset{H_1}{\gtrless}} \gamma \tag{4.6}$$

where the dependence of the variables on the target velocity $\boldsymbol{v}$ has been included to underline the fact that the detection process is performed in v-space. The second term on the left hand side of (4.6) represents the additional information that exploits the structure of the target signal's likelihood in v-space. It is not a ML term in the direct sense, so it is simply added to the existing detection variable to enhance the algorithm's performance. A constant κ is applied to the likelihood contribution terms $\boldsymbol{B}_{M\{m,n\}}(\boldsymbol{v})$ before adding them to the multistatic decision variable in (4.6). This constant is a positive small weight that ensures that the modified MLED is not dominated by the newly added parameters. This keeps the detector approximately ML.

1.	Run bistatic MLED in all channels to obtain likelihoods $\boldsymbol{T}_{M\{m,n\}}\left(f_{d\{m,n\}}\right)$
2.	Compress likelihoods into subspaces $\widetilde{\boldsymbol{T}}_{M\{m,n\}}\left(f_{d\{m,n\}}\right)$
3.	Share compressed likelihoods across network
4.	Form the sets of subspace contributions $\boldsymbol{B}_{M\{m,n\}}\left(f_{d\{m,n\}}\right)$
5.	Filter and project likelihoods onto v-space
6.	Combine likelihood subspaces $\widetilde{\boldsymbol{T}}_{M\{m,n\}}(\boldsymbol{v})$ with contributions $\kappa\boldsymbol{B}_{M\{m,n\}}(\boldsymbol{v})$
7.	Join bistatic results into multistatic likelihood

Table 4.2: *Modified multistatic MLED procedure*

An overview of the procedure of applying the modified multistatic MLED is given in Table 4.2. Section 4.5 discusses some models and statistical analysis of the proposed modification.

4.5 Analysis

This section provides a statistical analysis of the proposed modified multistatic MLED threshold detector. As mentioned in Section 4.4, the proposed algorithm is not derived as a ML solution but rather a knowledge-based one. However, the modified detector (4.6) is dominated (through the weight κ) by the standard multistatic MLED term (3.16) which is ML. Thus the modification can be labelled as "approximately maximum likelihood," a term first introduced in the derivation of the APES filter [61] on which the original MLED algorithm is based [17]. The statistical properties of the proposed modified algorithm are discussed in Section 4.5.1. The pdf, the false alarm and the detection probabilities are discussed in Section 4.5.2. Section 4.5.3

provides a brief discussion of the influence of the scaling parameter κ on the performance of the proposed modified multistatic MLED.

4.5.1 Statistical properties of the modified multistatic MLED

The statistical analysis of the multistatic MLED is provided in Section 3.5.1. A closed-form solution for the pdf was never reached, but the combination of random variables that make up the statistics of the detector is provided in (3.39). Using this information, the statistics of the additional term in the modified multistatic MLED proposed in this chapter are distributed as

$$\xi = \sum_{m,n} \xi_{m,n} \sim \sum_{m,n} \left(\frac{\zeta_{m,n}}{L\eta_{m,n}} \underset{0}{\overset{1}{\gtrless}} \epsilon_{m,n} \right) \tag{4.7}$$

Each of the channels contributes a 1 or a 0 to the total term (4.7). It is clear that this term is directly derived from the multistatic MLED (3.39) which is a CFAR detector. Thus (4.7) inherits the property of independence from the clutter and noise covariance matrices $\boldsymbol{R}_{m,n}$, which means that the modified multistatic MLED is also CFAR. Therefore, for a given SNR, the probability of each of the individual components of (4.7) to be either 0 or 1 is constant and independent of the background noise and clutter. It can thus be concluded that the individual components of (4.7) follow the Bernoulli distribution, or more generally, the single-trial binomial distribution

$$\xi_{m,n} \sim \mathcal{B}(1, p_{m,n}) \tag{4.8}$$

where $p_{m,n}$ is the channel-specific success rate of the ε-thresholded compressed likelihood being a 1. It may be desirable to design the system such that the success rate in each channel is the same. This idea was first discussed in [37] where an extensive analysis of multistatic binomial detection can be found. The assumption that the channel SNR is constant was made in [37]. Here this assumption will be relaxed. A constant channel-specific success rate p will be achieved through scaling the selection thresholds $\varepsilon_{m,n}$ with the SNR $\rho_{m,n}$ in each channel. Thus the total additional term ξ is the sum of $M \times N$ iid Bernoulli distributed variables, which is equivalent to the binomial distribution

$$\begin{aligned} H_0 &: \xi \sim \mathcal{B}(MN, p_0) \\ H_1 &: \xi \sim \mathcal{B}(MN, p_1) \end{aligned} \tag{4.9}$$

where the success rate p_0 under hypothesis H_0 can never surpass the rate p_1 under the alternative hypothesis by design. The amended multistatic MLED is then distributed as the following combination of random variables

$$\sum_{m,n} \frac{\zeta_{m,n}}{L\eta_{m,n}} + \kappa\xi \underset{H_0}{\overset{H_1}{\gtrless}} \widehat{\gamma} \tag{4.10}$$

where $\widehat{\gamma}$ is the threshold associated with the modified multistatic detector. This is a linear combination of the distributions of the standard multistatic MLED and a scaled version of the multistatic binomial detector [37].

4.5.2 Probability density, detection and false alarm probability

The statistics of the modified multistatic MLED (4.10) consist of the sum of the multistatic MLED random variable and the newly-added binomial term. As such, the latter is discrete and has the following probability mass function (pmf)

$$Pr(q|M,N,p) = \binom{MN}{q} p^q (1-p)^{MN-q} \tag{4.11}$$

which can be represented by the continuous pdf

$$\mathcal{B}(x,MN,p) = \sum_{q=0}^{MN} \binom{MN}{q} p^q (1-p)^{MN-q} \delta(x-q) \tag{4.12}$$

through the use of the continuous Dirac delta function $\delta(x)$. Scaling (4.12) by the coefficient κ can be done through the standard transformation of random variable

$$\begin{aligned} \mathcal{B}(\kappa x,MN,p) &= \frac{1}{\kappa} \sum_{q=0}^{MN} b(q,MN,p)\delta\left(\frac{x}{\kappa} - q\right) \\ &= \sum_{q=0}^{MN} b(q,MN,p)\delta\left(x - \kappa q\right) \end{aligned} \tag{4.13}$$

where the scaling factor in front of (4.13) disappears because the Dirac delta is a homogeneous and even function of degree -1, giving it the property [97, p.24]

$$\delta\left(\kappa x\right) = \frac{\delta\left(x\right)}{|\kappa|} \tag{4.14}$$

The values of the binomial distribution (4.13) are the combined $\varepsilon_{m,n}$-thresholded values of the channel-specific MLED random variables $T_{M\{m,n\}}$. Therefore the newly added parameter distributed as ξ is jointly conditional on the MLED detection variable and the thresholds $\varepsilon_{m,n}$. The individual channel-specific components of ξ are formed in a process that is no different than standard threshold detection, thus the success rate parameters in (4.9) are simply given by

$$p_0 = P_{fa\{m,n\}}(\varepsilon_{m,n}) \tag{4.15}$$

$$p_1 = P_{d\{m,n\}}(\varepsilon_{m,n}) \tag{4.16}$$

where $P_{fa\{m,n\}}$ and $P_{d\{m,n\}}$ here represent the standard bistatic MLED false alarm and detection probabilities derived in [18, pp.62-64]. Previously it was assumed that each threshold $\epsilon_{m,n}$ is adaptively scaled to its respective channel SNR so that the binomial success rates (4.15) and (4.16) remain constant across the different channels. This greatly simplifies the analysis and allows for a certain value of p_0 to be chosen during the design stage of the detection algorithm implementation. Since p_0 is now fixed, the value of p_1 can be obtained through the detection-false alarm relation of the standard bistatic MLED explored in the results of [18, pp.74-79]. When the success rates p_0 and p_1 are fixed, the dependence of the added binomial parameter ξ on the MLED random variables $T_{M\{m,n\}}$ is relaxed, i.e. they become conditionally independent given p [98].

Let the pdf of the standard multistatic MLED be labelled as $f_{T_M}(x)$. It is described by the sum of random ratios of the F-distributed $\zeta_{m,n}$ and the beta-distributed $\eta_{m,n}$ featured in (4.10). Because this sum is conditionally independent from the additional scaled binomial distributed as $\kappa\xi$, the pdf of the modified multistatic MLED labelled here as $\widehat{f}_{T_M}(x)$ is given by

$$\begin{aligned}
\widehat{f}_{T_M}(x) &= f_{T_M}(x) * \mathcal{B}(\kappa x, MN, p) \\
&= f_{T_M}(x) * \sum_{q=0}^{MN} b(q, MN, p)\delta\left(x - \kappa q\right) \\
&= \sum_{q=0}^{MN} b(q, MN, p) f_{T_M}\left(x - \kappa q\right)
\end{aligned} \tag{4.17}$$

where $*$ is the symbol used to denote linear convolution. The pdf of the modified multistatic MLED algorithm consists of the summation of copies of the pdf of the standard multistatic MLED shifted at the locations κq and scaled by the standard binomial pmf coefficients $b(q, MN, p)$ given by (4.11). To obtain the detection and false alarm of the newly proposed

modified algorithm, the linearity of the integral operator is exploited in the following probability measure given a detection threshold $\widehat{\gamma}$

$$\begin{aligned}\int_{\widehat{\gamma}}^{\infty} \widehat{f}_{T_M}(x)dx &= \int_{\widehat{\gamma}}^{\infty} \sum_{q=0}^{MN} b(q, MN, p) f_{T_M}\left(x - \kappa q\right) dx \\ &= \sum_{q=0}^{MN} b(q, MN, p) \int_{\widehat{\gamma}}^{\infty} f_{T_M}\left(x - \kappa q\right) dx \\ &= \sum_{q=0}^{MN} b(q, MN, p) \int_{\widehat{\gamma}-\kappa q}^{\infty} f_{T_M}(x)dx \end{aligned} \tag{4.18}$$

The integrals on the left and right hand side of (4.18) can directly give the relation between the probability of false alarm and detection of the standard multistatic MLED labelled as P_{fa} and P_d and the ones of the proposed modified algorithm labelled as $\widehat{P}_{fa}$ and $\widehat{P}_d$.

$$\widehat{P}_{fa}(\widehat{\gamma}) = \sum_{q=0}^{MN} b(q, MN, p_0) P_{fa}\left(\widehat{\gamma} - \kappa q\right) \tag{4.19}$$

$$\widehat{P}_d(\widehat{\gamma}) = \sum_{q=0}^{MN} b(q, MN, p_1) P_d\left(\widehat{\gamma} - \kappa q\right) \tag{4.20}$$

While not explicitly stated, it is clear that both the probability of false alarm (4.19) and detection (4.20) are dependent on the value of the scaling parameter κ. A brief discussion on the relation is provided in Section 4.5.3.

4.5.3 Performance effects of the scaling parameter κ

It is clear that the value of the scaling parameter κ plays a very important role on the performance of the modified multistatic MLED proposed here. It controls the degree of influence that the additional binomial term has on the detection algorithm. As expected, for κ=0 the probability of false alarm (4.19) and the probability of detection (4.20) reduce to those of the standard multistatic MLED. If the value of κ becomes large, the modified MLED becomes dominated by the binomial detector and its performance is comparable to the one discussed in [37]. The binomial detector is based on the combination of hard decisions from multiple radar channels, while the multistatic MLED is the ML combination of the respective soft decisions. As such, the isolated performance of the former is expected to be worse than that of the latter, a concept that is widely applied in communications and decoding [73]. This claim cannot be verified the-

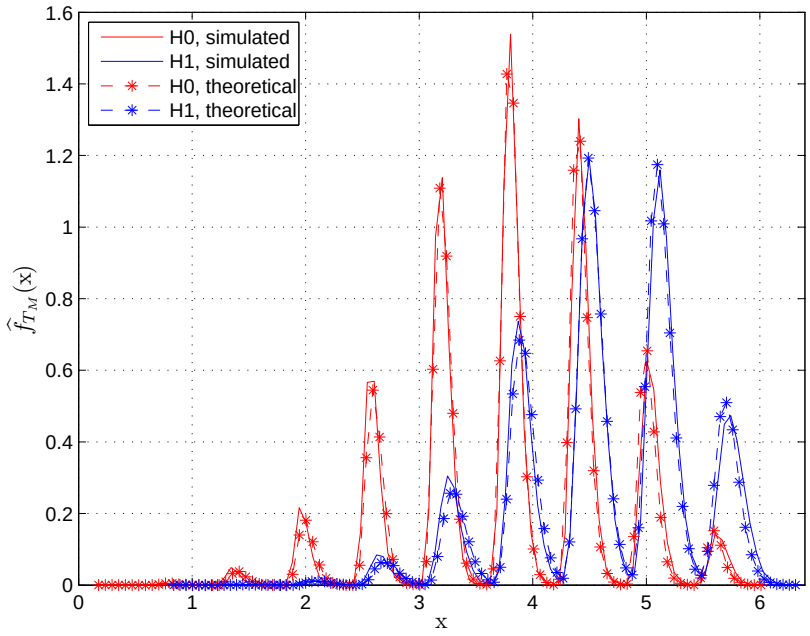

Figure 4.4: *Probability density function of the modified multistatic MLED detection variable,* K=60, M=N=3, SNR=-30*dB*, κ=$6\sigma_M$

oretically since closed-form expressions for the false alarm and detection probabilities of the multistatic MLED are not available. However, a comparison between the numerical results [37] associated with the binomial detector and the results for a multistatic radar network of the same size presented in Chapter 3 of this thesis confirms the expectations.

The standard deviation of the multistatic MLED (3.44) (3.52) (3.55) derived in the approximations from Section 3.5.2 could serve as an indicator of the expected influence of a large value of κ on the modified algorithm. Since the multistatic MLED can roughly be described by a Gaussian pdf (Section 3.5.2), most of its weight is within 3 standard deviations σ_M of its mean. Thus a κ of $6\sigma_M$ provides an almost ideal separation between the different components of the modified multistatic pdf (4.17). Figure 4.4 shows the pdf for a multistatic scenario of 3 transmitters and 3 receivers and an arbitrarily chosen SNR of -30 dB. The labelling of the different data sets follows the one described in Table 3.1 and 3.2. The shape of the pdf demonstrates that for this value of κ the performance of the multistatic detection algorithm is dominated by the scaled binomial term $\kappa\xi$. Thus, if the modified multistatic MLED does offer an enhanced performance as expected, this should come for a value of κ that roughly lies somewhere between 0 and $6\sigma_M$ where neither of the two components of (4.10) is heavily dominating the signal statistics.

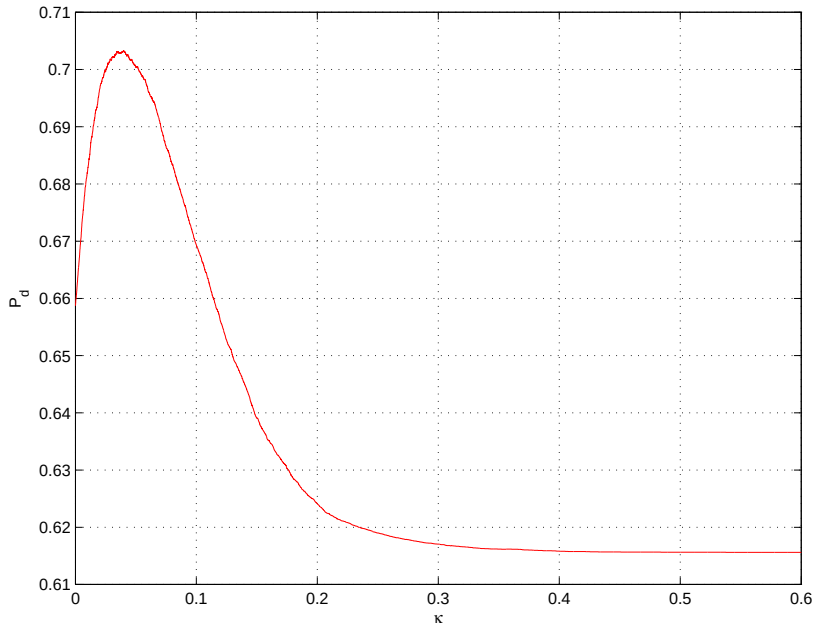

Figure 4.5: *Probability of detection of the modified multistatic MLED detection variable* K=60, M=N=3, SNR=-30*dB*, P_{fa}=0.02

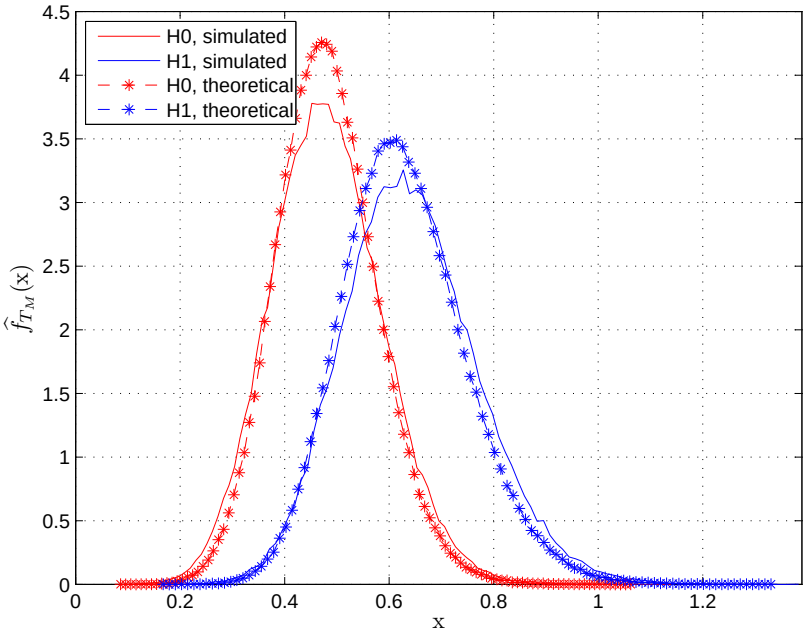

Figure 4.6: *Probability density function of the modified multistatic MLED detection variable,* K=60, M=N=3, SNR=-30*dB, optimal value of* κ=0.04

At this stage deriving an optimal value for κ is difficult because the modified probability of false alarm (4.19) and probability of detection (4.20) involve a sum of terms with no associated closed form expressions. Both probabilities are dependent on the threshold $\widehat{\gamma}$ and the scaling κ, so fixing P_{fa} to obtain the maximum of P_d with respect to κ is not feasible. The two parameters have to be considered jointly. Plugging in the Gaussian approximations (3.56) (3.57) derived in Section 3.5.2 into (4.19) and (4.20) does not alleviate the issue. No trivial method of inverting a sum of Q-functions can be found, and according to Galois theory, a solution in terms of traditional arithmetic may not exist depending on the approximating Gaussian parameters [99, pp.92-105].

Obtaining the value of the scaling parameter κ that maximises the modified probability of detection (4.20) for a fixed probability of false alarm (4.19) can be done numerically. The relationship is depicted in Figure 4.5 for the same radar system as the one used for plotting Figure 4.4 and a fixed probability of false alarm. The simulation is for a fixed set of parameters but describes well the behaviour of the detection probability with respect to κ observed over multiple tests of variable radar characteristics. There are two important observations evident in Figure 4.5: the modified multistatic MLED performs better than its isolated individual components, and there is a value of κ that maximises the performance curve. The numerically-found optimal value of the scaling parameter is used to depict the pdf of the modified multistatic MLED random variable in Figure 4.6. The shape of the distribution is no longer dominated by the scaled binomial term $\kappa\xi$.

4.6 Simulations

This section contains the numerical and theoretical simulations of the modified multistatic MLED detector proposed in this chapter. Two data sets, "simulated" and "theoretical," are depicted in the results; the labelling corresponds to the one described in Table 3.1 and 3.2. A relatively small multistatic radar network similar to the toy example depicted in Figure 2.3 of Chapter 2 is used in the simulations. There are a total of 3 mobile transmitters and 3 stationary ULA receivers placed around a moving airborne target. The number of bistatic channels in this set of simulations is kept low since the algorithm requires significant physical storage space. In a practical scenario this storage space will be distributed between the different receivers and will become less of a problem. The physical radar parameters from Table 2.1 are also employed in this set of simulations.

Unlike in Chapter 3 where only a single Doppler frequency was considered, here the full bistatic likelihood functions of the MLED in D-space is calculated for all Monte Carlo runs of every channel. The range of normalised Doppler frequencies has been divided into N_d=101 equidistant bins that are scanned for potential targets. A compressed subspace from each of the bistatic likelihoods is extracted according to the procedure described in Table 4.1. The values of $\varepsilon_{m,n}$ are chosen to allow local likelihood maxima that are within 99% of the global maximum in order to remove any insignificant contributions caused by thermal noise or other phenomena.

After being shared throughout the radar network, the bistatic likelihoods are passed through a 3-point smoothing Gaussian filter; this reduces the effects of potential frequency mismatches between the target Doppler and the corresponding bin component of the likelihood. The results are then projected into a v-space of N_v=21 equidistant points 0.5m/s apart centred at the correct target velocity. The bistatic likelihoods are then compounded to form the multistatic MLED likelihood in v-space.

The added binomial term associated with the bistatic hard decisions is formed from the unfiltered bistatic MLED likelihoods. The set of binary decisions is then projected from D-space into v-space. In every simulation run the scaling parameter κ that would produce the optimal result is obtained numerically. In practice a table of the optimal values of κ for certain SNR levels and radar parameters could be calculated in advance and used as a reference. The optimal scaling here is applied to the binomial detection likelihoods before adding them to the multistatic MLED results. This forms the modified multistatic MLED likelihood function with subspace compression in v-space.

The receiver operating characteristics (ROC) curves have been plotted for a scenario where K=20 iid temporal snapshots are available in every channel. Figure 4.7 shows the results for an SNR value of -30dB. It is clear from the graph that the detection rate in this scenario is very poor and almost equal to the probability of false alarm. The benefit that the modified MLED provides in this case is insignificant. A better performance is seen on Figure 4.8 where the SNR has been increased to -25dB. The separation between the curves of the original multistatic MLED and its proposed modification can be observed. Figure 4.9 and Figure 4.10 repeat the previous simulations for a scenario of K=60 iid temporal snapshots. Naturally, as more data is available for SDS covariance estimation, the performance of the multistatic MLED becomes better. It must be noted that the advantages of the proposed modified algorithm also become more apparent here, as the detection rate gains can clearly be seen on both graphs.

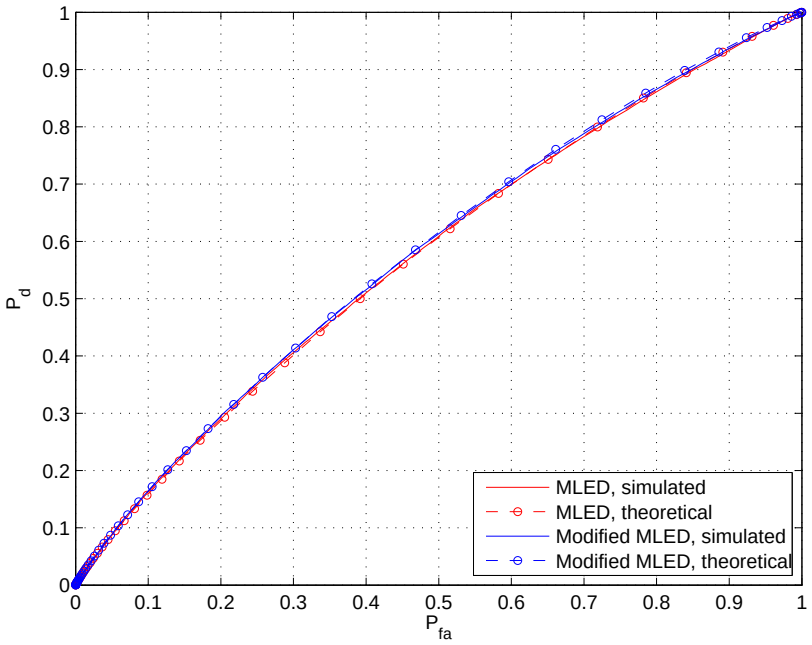

Figure 4.7: *ROC curve of multistatic MLED and the proposed modified MLED* K=20, *SNR*=$-30dB$

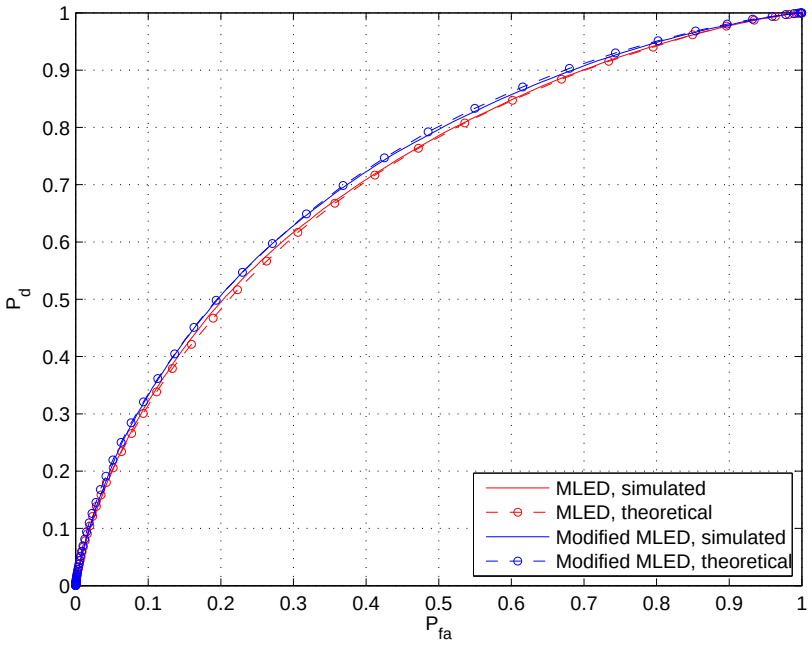

Figure 4.8: *ROC curve of multistatic MLED and the proposed modified MLED* K=20, *SNR*=$-25dB$

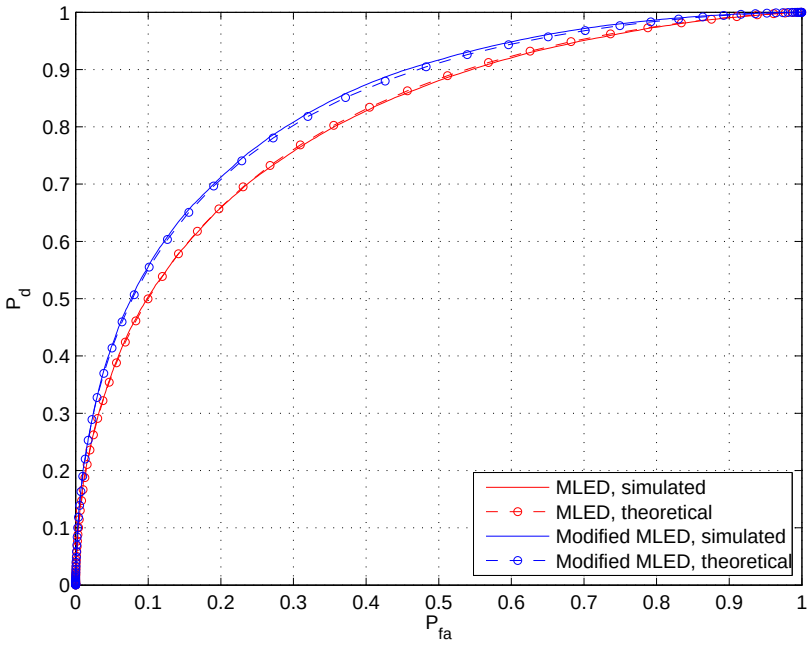

Figure 4.9: *ROC curve of multistatic MLED and the proposed modified MLED* K=60, *SNR*=$-30dB$

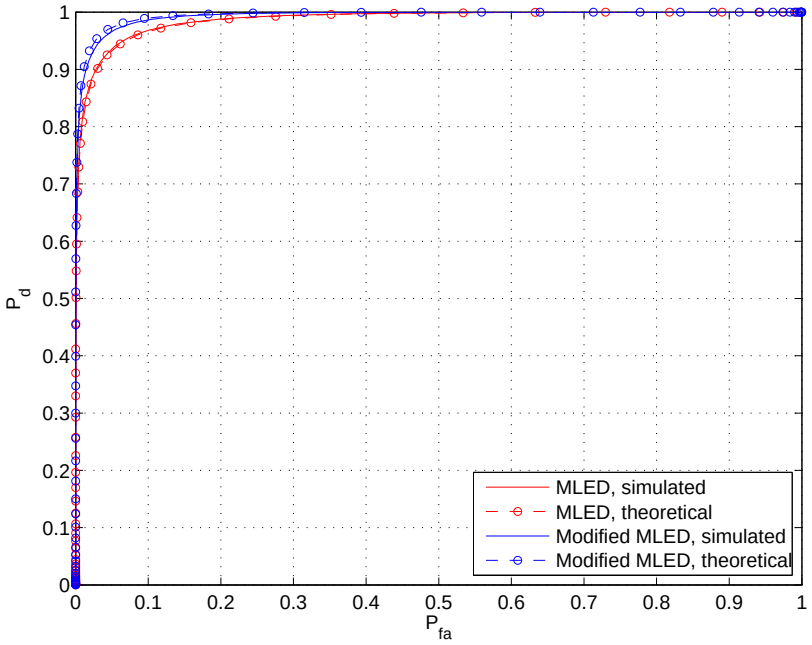

Figure 4.10: *ROC curve of multistatic MLED and the proposed modified MLED* K=60, *SNR*=$-25dB$

The ROC curves shown so far demonstrate the range of viability of the detector proposed in this chapter. The binomial term in the modified MLED represents a combination of scaled hard decisions linked to the performance of the soft-decision standard MLED. In a low SNR scenario the false alarm and detection probabilities of the MLED are very similar. Thus there is almost no difference in the additional binomial term under the H_0 and H_1 detection hypotheses, and as a result the success rates p_0 and p_1 are almost the same. This simply offsets the false alarm and detection probabilities by the same amount and provides no relative increase in performance in the lower SNR region, as can be observed in Figure 4.7.

In the very high SNR region the detection rate based on the standard MLED is nearly ideal even for a very low probability of false alarm. Thus the multistatic decisions from the MLED and the binomial detector will be nearly identical. Since the performance is already very high, the additional term is of little effect for such very high levels of SNR. The results can be observed in Figure 4.10 where the performance boost of the modified MLED is relatively smaller compared to Figure 4.9. These observations suggest that the algorithm enhancement proposed in this chapter operates best in the mid-to-high SNR region where the detection rate can benefit the most from the difference in structure between the target and the clutter likelihood.

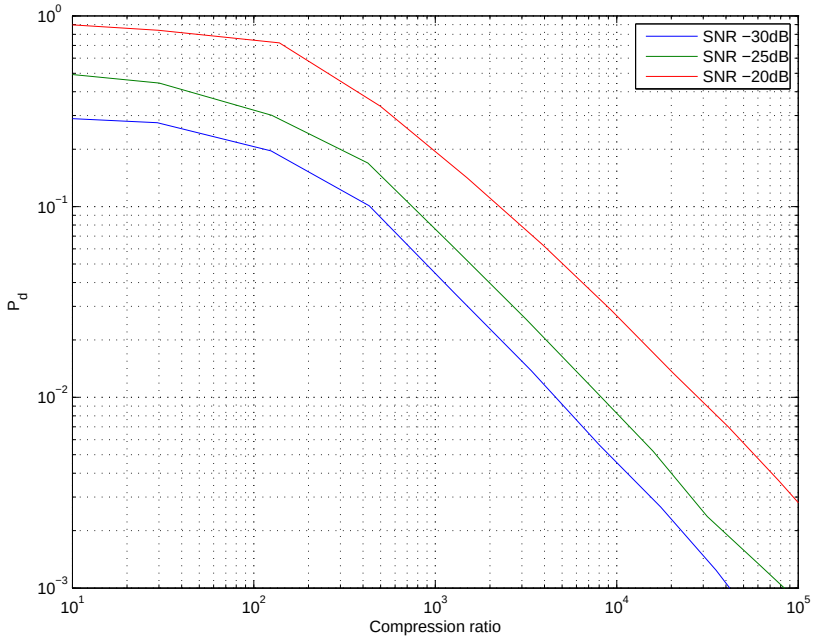

Figure 4.11: *Probability of detection of compressed multistatic MLED vs compression ratio* K=20, P_{fa}=0.02

It must be noted that the benefits of the proposed modified multistatic MLED algorithm, even when minimal, are accompanied by a reduction of the data shared throughout the network based on the compression proposed in Section 4.2. The influence of the level of compression on the algorithm performance has been shown for K=20 in Figure 4.11. The standard form of the compression ratio of algorithms is employed as a measure here [100].

$$\text{Compression Ratio} = \frac{\text{Uncompressed Size}}{\text{Compressed Size}} \tag{4.21}$$

The results are averaged over all Monte Carlo runs for a few SNR levels. The lowest compression ratio is always shown for the thresholds $\varepsilon_{m,n}$ set to 0, which means that all local maxima are included in the compressed subspace. An interesting phenomenon observed in the results is the robustness of the algorithm performance for high SNR with respect to the measure in Figure 4.11. A higher SNR means a higher target likelihood. Therefore, raising the compression ratio (up to a certain point) mainly removes the subspace contributions of the clutter since a lot of them come with a relatively lower likelihood than the target one. That explains the relative flatness at the start of the highest SNR curve plotted in the graph. In a hypothetical scenario of infinite SNR the ideal maximum compression rate can be achieved; the full likelihood function in this scenario can be described by the single point where the target contribution is located.

Clearly from Figure 4.11 there is a tradeoff between the compression ratio and the maximum performance that a system can be expected to achieve. The simulations demonstrate that if the tolerance for the performance loss is set to 10% of the uncompressed one, the maximum compression ratio that the algorithm can support and thus the reduction in the data exchange between receivers is approximately 30 times.

4.7 Summary

This chapter describes the steps necessary to realise the practical implementation of the multistatic MLED threshold detector and proposes an enhanced version of the algorithm. A method for compression of the Doppler detection likelihood function has been proposed and analysed that would greatly reduce the data shared between the computational nodes of the radar network. To synchronise the bistatic contributions coming from the multiple radar channels, the method of projecting the detection likelihood function from the channel-specific D-space into the universal v-space has been suggested. Based on the compressed likelihood structure of

a potential target in v-space, the modified multistatic MLED algorithm has been proposed; it utilises a combination of the soft and hard decisions coming from the different bistatic channels into the multistatic decision variable to provide a better detection rate in the mid-to-high SNR region of operation. It is shown that the newly proposed modified algorithm retains the CFAR property. An analysis of the performance of the enhanced target detector is provided and demonstrated in a series of numerical simulations. It is shown that the enhanced detector performs better than the standard multistatic MLED derived in Chapter 3 in the mid-SNR region. This benefit is obtained in addition to the reduction of the likelihood data exchanged between the different receivers in the radar setup. The simulations also demonstrate the tradeoff between the compression ratio and the system performance. It is shown that compressions of up to 30 times still yield a reasonable detection probability as compared to the uncompressed transmission scenario.

While this chapter has focused on some of the practical issues of implementing and deploying the multistatic MLED threshold detector, the waveforms transmitted in the radar system have still been assumed ideally-orthogonal. This is an unrealistic scenario, and the effects of non-ideal waveform orthogonality can impose some additional limitations on the performance of MIMO radar and its respective MIMO ambiguity function. Chapter 5 addresses this issue by demonstrating that realistic low-correlation waveforms separated in time and/or frequency experience negligible effects in their multistatic ambiguity function as the MIMO system grows.

Chapter 5
Practical limitations on growing multiple-input multiple-output radar networks

5.1 Introduction

This chapter investigates the practical limitations of waveform orthogonality and residual interference experienced by growing MIMO radar networks that have not been considered so far. The main focus is on the overall reduction of the MIMO ambiguity function region that can be clear of sidelobes [45, 46] that is briefly described in Section 2.6. This is a well-known phenomenon that occurs in a scenario where multiple waveforms occupying the same time and bandwidth are designed to be nearly ideally-orthogonal in fast-time.

It will be shown here that in a multistatic radar system the ambiguity function limiting factors can be alleviated if the transmitted waveforms are designed to be orthogonal in time and/or frequency [101]. The concept is identical to FDMA and TDMA in wireless communication [73]. To evaluate the relative interference effects between channels, the ratio of the cross-to-auto-ambiguity function has been proposed as a measure of waveform orthogonality and influence on the performance of the MIMO radar system. It is shown in this chapter that the ratio becomes negligible if the radar pulses are band-limited to sufficiently separated bands. The ambiguity bound then reduces to the familiar mono/bistatic form (2.37) and is independent of the radar network size. The work in this chapter utilises a specific waveform, namely the Gaussian pulse train (GPT), for convenience and ease of analysis. However, the conclusions drawn here can be generalised to a variety of other waveforms that conform to certain requirements specified in the discussion later on in the chapter.

The rest of this chapter is organised as follows. Section 5.2 contains the background derivations of the well-known ambiguity of an infinite train of Dirac delta functions as well as the ambiguity of a single Gaussian pulse (GP). These results are combined to provide the ambiguity of a theoretical GPT waveform of ininite number of pulses. The original work in the chapter

begins at Section 5.3, which contains the more practical derivation of the autoambiguity of a GPT waveform with a finite number of pulses K_T. Section 5.4 defines and derives the respective cross-ambiguity between two finite GPT waveforms that are separated in time and/or frequency. Section 5.5 derives the respective ambiguity volumes as well as their ratio in a given region of interest around the origin. The major contribution of the chapter, which consists of an approximation to that ratio, has been derived in the same section for the practical case of finite GPT waveforms. Section 5.6 provides a numerical simulation that demonstrates the feasibility of the volume ratio approximation as well as demonstrates that the expected values for this ratio are negligible compared to the autoambiguity volumes in the multistatic system. This alleviates the compounding negative effect on the MIMO ambiguity function of a multistatic radar with the addition of more channels in the system. The benefits of the investigated orthogonality methods come at the price of an increased bandwidth or delay in the MIMO radar system. While the derivations are performed for GPTs for convenience, guidelines for extending the approach to a wider variety of waveforms are discussed. This chapter closely follows the work published in [47].

5.2 Infinite Gaussian pulse train autoambiguity

In this section, the autoambiguity of the theoretical GPT waveform that consists of an infinite number of consecutive pulses is derived. An assumption made throughout this whole chapter is that the considered waveforms experience no fast-time delays and small Doppler shifts. If this assumption is not fulfilled, the narrowband form of Woodward's ambiguity function (2.36) is no longer applicable.

To analyse the GPT waveform, a single GP is first considered.

$$u_g(t) = \left(\frac{2a}{\pi}\right)^{\frac{1}{4}} \exp\left\{-at^2\right\} \tag{5.1}$$

where the parameter a is related to the standard deviation σ and thus the width of the GP.

$$a = \frac{1}{2\sigma^2} \tag{5.2}$$

The ambiguity of the GP is a two-dimensional Gaussian function extending in time and fre-

quency [68, 70]

$$\alpha_g(t,f) = \exp\left(-\frac{1}{2}at^2\right)\exp\left(-\frac{\pi^2 f^2}{2a}\right) \tag{5.3}$$

A radar waveform consists of multiple pulses. To obtain the ambiguity function of a GPT, the following property can be used: if two waveforms are convolved in time, their ambiguity functions are also convolved along the time axis [68]. An infinite GPT is the convolution of a GP and a train of Dirac delta functions

$$u_\delta(t) = \sum_{k=-\infty}^{\infty} \delta(t - kT) \tag{5.4}$$

where the spacing between pulses is the radar's PRI, and $k \in \mathbb{Z}$. The ambiguity function of (5.4) takes the well-known "bed of nails" form [68, pp.6-8]

$$\alpha_\delta(t,f) = \sum_n \sum_m \delta(t - nT)\delta\left(f - \frac{m}{T}\right) \tag{5.5}$$

where $m, n \in \mathbb{Z}$. An approximation to this function is shown in Figure 5.1 for a 100-pulse Kronecker delta train waveform.

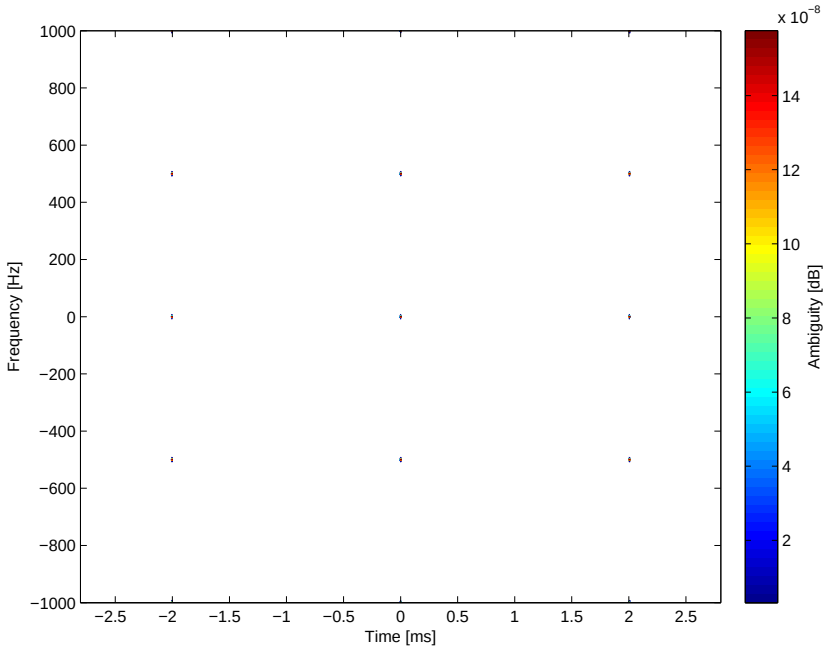

Figure 5.1: *Autoambiguity of a* 100*-pulse delta train waveform*

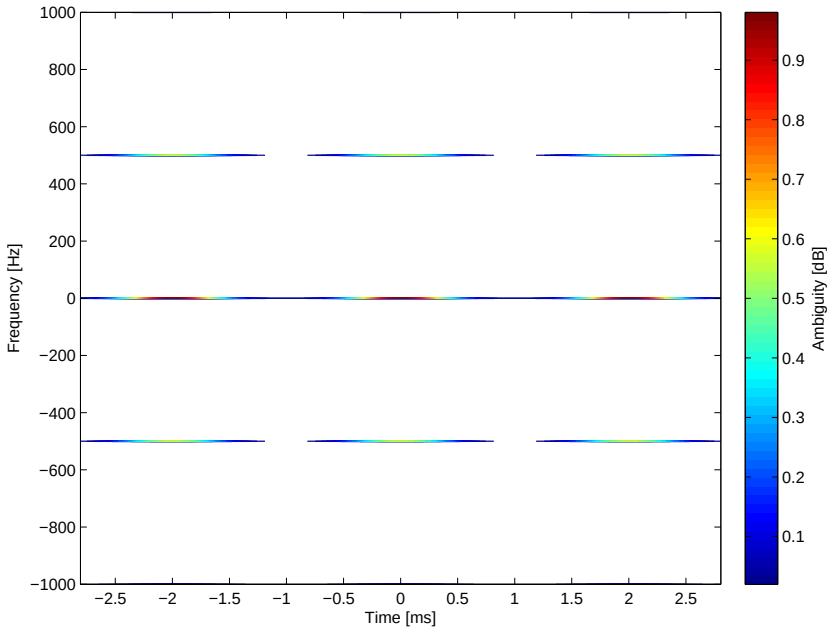

Figure 5.2: *Autoambiguity of a* 1000*-pulse GPT waveform*

The ambiguity function of an infinite GPT will be the convolution of (5.3) and (5.5) along the time axis. The spacing T is equal to the length of each GP, which will be defined here as 6 times its standard deviation σ. Plugging this into (5.2) results in

$$a = \frac{18}{T^2} \tag{5.6}$$

The ambiguity function of the infinite GPT consists of shifted copies of (5.3) in time at $t{=}nT$ sampled along frequency at $f{=}mT^{-1}$.

$$\alpha_{g\delta}(t,f) = \sum_n \exp\left(-\frac{1}{2}a(t-nT)^2\right) \sum_m \exp\left(-\frac{\pi^2 m^2}{2aT^2}\right) \delta\left(f - \frac{m}{T}\right) \tag{5.7}$$

The waveform is reminiscent of a "bed of razors" which take the shape of Gaussian functions along the time axis and are infinitesimally thin along the frequency axis. An approximation to this function is shown in Figure 5.2 for a 1000-pulse GPT waveform.

The derivation of the autoambiguity of the infinite GPT waveform is a necessary step but reflects only a theoretical scenario. In practice a radar waveform will consist of a finite number of pulses. The respective autoambiguity derivation for this case is shown in the following section.

5.3 Finite Gaussian pulse train autoambiguity

A pulse Doppler radar's waveform consists of multiple consecutive pulses. Consider a GPT constructed by transmitting K_T consecutive GPs. This waveform is the time-domain convolution of (5.1) and a train of K_T equally-spaced Dirac delta functions.

$$u_{K_T\delta}(t) = \frac{1}{\sqrt{K_T}} \sum_{k=0}^{K_T-1} \delta(t - kT) \tag{5.8}$$

In order to ensure that the energy of the waveform remains constant (chosen as unity here), a normalising factor is applied to (5.8). The ambiguity function of (5.8) can be calculated through direct evaluation of Woodward's narrowband ambiguity integral given by (2.36). The result is a symmetric sum of Dirac delta functions along the time axis and a sum of exponentials along frequency

$$\alpha_{K_T\delta}(t,f) = \frac{1}{K_T} \sum_{p=-K_T+1}^{0} \delta(t - pT) \sum_{k=0}^{K_T+p-1} e^{-j2\pi fkT} + \frac{1}{K_T} \sum_{p=1}^{K_T-1} \delta(t - pT) \sum_{k=p}^{K_T-1} e^{-j2\pi fkT} \tag{5.9}$$

Define the following function

$$D_n(x) = \frac{\sin(\pi n x)}{\sin(\pi x)} \tag{5.10}$$

which is a special case of the Dirichlet kernel function [102, pp.89-92]. The formula for a geometric series of exponentials can be written in terms of the Dirichlet kernel as

$$\sum_{k=0}^{K_T-1} e^{-j2\pi fkT} = D_{K_T}(fT) e^{-j\pi f(K_T-1)T} \tag{5.11}$$

The normalised square norm of the ambiguity of the finite GPT is obtained after convolving (5.3) and (5.9) along the time axis and through using the geometric series representation (5.11)

$$|\alpha_{K_T g}(t,f)| = \frac{1}{K_T} \sum_{k=-K_T+1}^{K_T-1} \alpha_g(t - kT, f) |D_{K_T-|k|}(fT)| \tag{5.12}$$

As the number of pulses K_T approaches infinity, the Dirichlet kernel (5.10) becomes an arbitrarily close approximation to an infinite Dirac delta train in frequency, and the ambiguity function takes the form (5.7).

The volume of the Eucledian norm of the ambiguity function $\alpha(t, f)$ in an arbitrary region A is

defined as the following integral

$$V(A) = \iint\limits_{A} |\alpha(t,f)|^2 df\, dt \tag{5.13}$$

To obtain the Eucledian norm of the GPT ambiguity, (5.12) is squared, which involves multiple cross-terms on the right hand side of the equation. Here the shape of the terms $\alpha_g(t,f)$ is Gaussian, and the distance T between the different copies of $\alpha_g(t,f)$ along the time axis is chosen as 6σ. Thus the weight of the tail of the Gaussian shape $\alpha_g(t,f)$ outside the chosen width is negligibly small. Since the cross-terms when squaring the right hand side of (5.12) involve multiplications with those tails, they can be neglected. Thus the following approximation for the Eucledian norm of the GPT ambiguity can be made

$$|\alpha_{K_T g}(t,f)|^2 \approx \frac{1}{K_T^2} \sum_{k=-K_T+1}^{K_T-1} |\alpha_g(t-kT,f)|^2 F_{K_T-|k|}(fT) \tag{5.14}$$

Here $F_n(x)$ is the Fejér kernel function [103, pp.17-19] that can be defined as the square of the Dirichlet kernel expressed as (5.10).

$$F_n(x) = \frac{\sin(\pi n x)^2}{\sin(\pi x)^2} \tag{5.15}$$

Using the approximation for the Eucledian norm (5.14), the volume for a GPT in an area A around the origin takes the following form

$$V^{\alpha}_{K_T g}(A) = \frac{1}{K_T^2} \sum_{k} \iint\limits_{A} \alpha_g(t-kT,f)^2 F_{K_T-|k|}(fT) df\, dt \tag{5.16}$$

The limits of the sum in (5.16) have been omitted. Usually the aim is to make the volume as close to the ideal case $V(A)$=V_0 as possible (where V_0 is the volume at the origin), and thus small regions A around the origin are considered. The contribution to such a region will come from no more than the set $k \in \{-1,0,1\}$ in (5.16).

In the next section, the respective cross-ambiguity between two foreign waveforms carried on orthogonal frequencies or received at orthogonal times is derived.

5.4 Waveform cross-ambiguity in multiple access MIMO

Consider the MIMO radar scenario where waveform orthogonality has been ahcieved through time and/or frequency separation in an FDMA/TDMA transmission scheme. Let the main waveform of interest be the single GP $u_g(t)$ given in (5.1). Consider a foreign interfering waveform $u_i(t)$ of the same shape but separated in frequency by an offset f_Δ and in time by t_Δ

$$u_i(t) = \left(\frac{2a}{\pi}\right)^{\frac{1}{4}} e^{-a(t-t_\Delta)^2} e^{-j2\pi f_\Delta t} \tag{5.17}$$

The duration and bandwidth of (5.1) and (5.17) are the same. The cross-ambiguity between the two waveforms can be obtained by plugging their expressions in the integral (2.38). Instead of solving this integral, the shifting properties of Woodward's ambiguity function can be used [68]. The pulse (5.17) can be represented as (5.1) convolved in time with $\delta(t - t_\Delta)$ and in frequency with $\delta(f - f_\Delta)$. This convolution translates to ambiguity space to obtain the following cross-ambiguity between the GP of interest and its interferer

$$\chi_g(t, f) = e^{-j\phi} \exp\left(-\frac{a(t - t_\Delta)^2}{2}\right) \exp\left(-\frac{\pi^2(f - f_\Delta)^2}{2a}\right) \tag{5.18}$$

up to a time-frequency phase term ϕ due to the symmetric form of Woodward's ambiguity integral considered in this thesis. As expected, (5.18) is a shifted version of (5.3) in time and frequency. The phase term disappears when the ambiguity norm is taken into account.

$$|\chi_g(t, f)| = |\alpha_g(t - t_\Delta, f - f_\Delta)| \tag{5.19}$$

For simplicity it is assumed that the different waveforms in the MIMO radar are all of equal length for a CPI and contain K_T pulses each. Following the approach in Section 5.3, the square Euclidean norm of the cross-ambiguity of two GPTs offset in time and frequency is

$$|\chi_{K_T g}(t, f)| = \frac{1}{K_T} \sum_{k=-K_T+1}^{K_T-1} |\chi_g(t - kT, f) D_{K_T-|k|}((f-f_\Delta)T)| \tag{5.20}$$

The approximation to the Eucledian norm in (5.14) based on ignoring the Gaussian tail terms is once again employed to produce the following expression

$$|\chi_{K_T g}(t, f)|^2 \approx \frac{1}{K_T^2} \sum_{k=-K_T+1}^{K_T-1} |\chi_g(t - kT, f)|^2 F_{K_T-|k|}((f-f_\Delta)T) \tag{5.21}$$

The formula for the volume of (5.21) is the same as (5.16) with the area A centred around (t_Δ, f_Δ) instead of $(0,0)$. The Fejér kernel is $1/T$-periodic. Thus most of the volume of (5.21) is contained around the points $(kT-t_\Delta, n/T-f_\Delta)$ where $n\in\mathbb{Z}$ and k is within the limits given in the sums above.

The following section combines the results obtained here and in Section 5.3 in order to define a measure of relative ambiguity interference in a MIMO radar scenario.

5.5 Ambiguity volume ratio in multiple access MIMO

The definition of the MIMO radar ambiguity function (2.39) leads to the bound on the volume that can be clear of sidelobes given in (2.40). It is discussed in [45] that in the ideal case, orthogonal waveform design aims to simultaneously reduce the volume of the cross-ambiguitiesin the region of interest A while maintaining autoambiguities that are concentrated at the origin

$$\iint_A |\alpha_{gg}(t,f)|^2 df dt = V_0 \tag{5.22}$$

$$\iint_A |\chi_{gi}(t,f)|^2 df dt = 0 \tag{5.23}$$

where it is assumed that all channels have the same volume V_0 at (0,0). If both (5.22) and (5.23) can be satisfied at the same time for all channels, then the total MIMO ambiguity function (2.39) would reduce to the sum of the autoambiguities in the system, and the bound would be relaxed to the mono/bistatic one (2.37). While it is shown in [45] that for CDMA orthogonal waveforms that occupy the same time and bandwidth, both (5.22) and (5.23) cannot be simultaneously satisfied, frequency and/or time orthogonality will be evaluated here. The conditions (5.22) and (5.23) will also be relaxed. The proposed measure of relative waveform orthogonality here is the ratio between the cross-to-autoambiguity between any two orthogonal waveforms. As long as this ratio is small, the cross-ambiguity terms can be ignored from the MIMO ambiguity function, and the criterion for relaxing the bound (2.40) is fulfilled.

5.5.1 Volume ratio in an TDMA scenario

The cross-to-auto-ambiguity volume ratio of two foreign GPT waveforms orthogonal in time will be derived in this subsection. This corresponds to a TDMA scenario where each transmitter

is given a unique time slot in which its waveform is transmitted and received throughout the network. Thus time-orthogonality between waveforms is achieved. Since the GPT considered here consists of K_T consecutive GPs spaced at a distance T, the total waveform duration for one CPI is

$$T_W = TK_T \tag{5.24}$$

This time is also the theoretical minimum delay that has to occur between two waveforms at the receiver side in order for them to be considered orthogonal. Therefore it can be assumed that $t_\Delta \geq T_W$. Since the narrowband signal model is adopted, it is assumed that the Doppler shifts between the pulses in the waveform contribute no additional fast-time delay or sigificant frequency shift relative to the carrier.

Consider the volume of the cross-ambiguity of the finite GPT (5.21) around the origin. Since this subsection focuses on TDMA, $f_\Delta{=}0$ here. The cross-ambiguity volume is highest when the foreign waveforms are offset by a multiple of the duration T in time. Theoretically the worst-case scenario that still achieves time orthogonality is $t_\Delta{=}T_W$, since T_W is already a multiple of T (5.24), and since the cross-ambiguity volume (5.21) decays when moving away from the origin.

The volume ratio proposed here as a measure of relative waveform orthogonality is investigated in a small rectangular region A around the origin. Therefore this region satisfies both properties imposed in [72] since it is convex and symmetric about the origin of ambiguity space (0,0).

Because the region A is small, only the $k{=}0$ term contributes significantly to the autoambiguity volume (5.16). To evaluate the cross-ambiguity contribution, note that the volume of the cross-ambiguity can be expressed through the volume of the shifted autoambiguity using the shifting property in (5.19)

$$V^c_{K_T g} hi(A) = \frac{1}{K_T^2} \sum_k \iint\limits_A \alpha_g(t - kT - t_\Delta, f)^2 F_{K_T - |k|}(fT) df dt \tag{5.25}$$

Since the time shift t_Δ is already larger than the limit of the sum in (5.25), only the first term $k{=}{-}K{+}1$ in the sum contributes any significant amount to the volume. The rest of the contributions come from negligibly small Gaussian tails. Thus the volume ratio in the case of TDMA

reduces to

$$V_r = \frac{\int \exp\left(-a(t+(K-1)T-t_\Delta)^2\right) dt}{K^2 \int \exp\left(-at^2\right) dt} \tag{5.26}$$

The integral with respect to frequency has disappeared since it is the same in the numerator and denominator for the assumed frequency offset $f_\Delta{=}0$. The extra scaling parameter is necessary since the peak of the The Fejér kernel (5.15) varies with the kernel order. The result in (5.26) is valid for any region A that satisfies the properties imposed in [72]. To obtain a practical value and solve the integral, consider a rectangular symmetric region around the origin $\{|t|{\leq}t_b, |f|{\leq}f_b\}$. For $f_b{<}B_W/2$, where B_W is the frequency 6σ width of the GP ambiguity, only the term around $k{=}0$ is considered since the other contributions are negligible Gaussian tail terms. The solution to the volume ratio integral (5.26), dependent on the temporal size t_b of the considered region, for a purely TDMA system is

$$V_r(t_b) = \frac{\operatorname{erf}\left(\sqrt{\frac{a}{2}}\left(t_b+(K-1)T+t_\Delta\right)\right) - \operatorname{erf}\left(-\sqrt{\frac{a}{2}}\left(t_b+(K-1)T-t_\Delta\right)\right)}{2K^2 \operatorname{erf}\left(\sqrt{\frac{a}{2}}t_b\right)} \tag{5.27}$$

Utilising a purely TDMA scheme may not be the most applicable option in a large multistatic radar system. Since the target is usually a fast-moving airborne object, implementing artificial delays between the waveform transmissions in the different bistatic channels can disrupt the ability of the network to obtain multiple independent snapshots of the target at a fixed point in space and time. However, the volume ratio (5.27) derived here can be applied to the analysis and characterisation of non-TDMA systems. Time synchronisation and data fusion is an important and difficult step in the practical implementation of multistatic radar. Each receiver can simultaneosly observe up to M incoming waveforms from the M transmitters in the system. Since the waveforms are observed at an arbitrary and varying delay of t_Δ, the additive effects of this on the MIMO ambiguity can be described by the derived volume ratio (5.27).

The next subsection derives the respective volume ratio of a multistatic radar that employes a purely FDMA transmission scenario.

5.5.2 Volume ratio in an FDMA scenario

The cross-to-auto-ambiguity volume ratio of two foreign GPT waveforms orthogonal in frequency will be derived in this subsection. This corresponds to an FDMA scenario where each transmitter is given a unique frequency band in which its waveform is transmitted and received throughout the network. Thus frequency-orthogonality between waveforms is achieved.

The bandwidth of a GP (5.1) can be obtained through its Fourier transform

$$U_g(f) = \left(\frac{2a}{\pi}\right)^{\frac{1}{4}} \exp\left\{-\frac{f^2\pi^2T^2}{18}\right\} \tag{5.28}$$

If the 6σ width rule is also applied to (5.28), the double-sided width of the spectrum of a GP is

$$B_W = \frac{18}{\pi T} \approx \frac{6}{T} \tag{5.29}$$

This is 6 times the usual rule of thumb for the bandwidth that states $B_W{\approx}1/T$; however, under this assumption, the spectrum of the GP can be considered practically band-limited since the weight of the frequency tails outside the 6σ region are negligible. The width of the spectrum of a GPT will not exceed (5.29) since by design the GPT has a duration longer than a GP.

In an FDMA system the distance between channels will usually be at least equal to the channel width so that no overlap of the bands occurs. Therefore it can be assumed that $f_\Delta{\geq}B_W$. Also it will be assumed that the Doppler shifts of the waveforms are small relative to their bandwidths to eliminate interchannel interference. The 6σ width of the ambiguity $|\alpha_g(f,t)|^2$ in frequency is also B_W. The cross-ambiguity volume is highest when the foreign waveforms are offset by a multiple of the inverse duration $1/T$ in time. The theoretical worst-case scenario for the interfering volume of the cross-ambiguity at the origin that still achieves frequency orthogonality occurs for $f_\Delta{=}6/T$, where also the Fejér kernel peaks.

Since a purely FDMA system is assumed here, there is no time delay between the interfering waveforms, so $t_\Delta{=}0$. Mirroring the derivation in the previous subsection, a small rectangular region A around the ambiguity origin will be considered in this analysis. Since the region A is small, only the $k{=}0$ terms contribute significantly to its volume. The rest of the contributions

come from negligibly small Gaussian tails. Thus the volume ratio reduces to

$$V_r = \frac{\int \exp\left(-\frac{\pi^2(f-f_\Delta)^2}{a}\right) F_{K_T}((f-f_\Delta)T)df}{\int \exp\left(-\frac{\pi^2 f^2}{a}\right) F_{K_T}(fT)df} \tag{5.30}$$

The integral with respect to time has disappeared since it is the same in the numerator and denominator for the assumed time delay $t_\Delta{=}0$. The frequency bounds on the region A will not be defined for the time being. The integration of multiplications of Gaussian and sinusoid functions in (5.30) can only be done numerically. A theoretical result could be obtained if the Fejér kernel is approximated by a Gaussian function. This approximation and the subsequent theoretical form of the volume ratio (5.30) is described in Section 5.5.3.

5.5.3 Fejér kernel Gaussian approximation

The Fejér kernel in (5.15) is a $1/T$-periodic non-negative function. One period of (5.15) centred around the origin is considered in the following analysis. It takes the form of a rapidly decaying oscillation with a mainlobe centred around the origin, and the first zero-crossing occurs at $f{=}\pm 1/n$. Therefore, a rough approximation to the mainlobe of the Fejér kernel can be done with a Gaussian function with a 6σ width of $2/n$. Consider the Fejér kernel from the numerator of the volume ratio (5.30). The function a version of the standard form (5.15) where the argument is scaled by T and shifted by f_Δ. The periodicity of the kernel will be represented in the approximation as an infinite sum over $n{\in}\mathbb{Z}$. The Gaussian approximation to the full periodic Fejér kernel takes the following form

$$\tilde{F}_{K_T}((f-f_\Delta)T) = K_T^2 \sum_n \exp\left(-\frac{9}{2}K_T^2\left(f-f_\Delta-\frac{n}{T}\right)^2 T^2\right) \tag{5.31}$$

Plugging (5.31) in (5.30), the expression inside the integral is a sum of products of two Gaussian functions. The product of two Gaussian functions is also a Gaussian with parameters described in [104]. Therefore, for a given value of n, the resulting mean $\mu_x(n)$ and variance σ_x^2 are given

by the following expressions

$$\mu_x(n) = f_\Delta + \mu_a(n) \tag{5.32}$$

$$\mu_a(n) = 9K_T^2 T\sigma_x^2 n \tag{5.33}$$

$$\sigma_x^2 = \frac{9}{T^2((3K_T)^2+\pi^2)} \tag{5.34}$$

where $\mu_a(n)$ are the means in the denominator of (5.30) associated with the approximation for the autoambiguity case.

Consider a rectangular symmetric region around the origin $\{|t|\leq t_b, |f|\leq f_b\}$. For $t_b<T/2$ only the ambiguity around $k=0$ is considered since the other contributions are negligible Gaussian tail terms. The volume ratio approximation is

$$\begin{aligned}\tilde{V}_r(f_b) &= \frac{\sum_n \int_{-f_b}^{f_b} \exp\left(-\frac{(f-\mu_x(n))^2}{2\sigma_x^2}\right)\exp\left(-\frac{\pi^2\mu_a^2(n)}{a}\right)df}{\sum_n \int_{-f_b}^{f_b} \exp\left(-\frac{(f-\mu_a(n))^2}{2\sigma_x^2}\right)\exp\left(-\frac{\pi^2\mu_a^2(n)}{a}\right)df} \\ &= \frac{\sum_n \exp\left(-\frac{\pi^2\mu_a^2(n)}{a}\right)\left[\operatorname{erf}\left(\frac{f_b+\mu_x(n)}{\sigma_x}\right)-\operatorname{erf}\left(-\frac{f_b-\mu_x(n)}{\sigma_x}\right)\right]}{\sum_n \exp\left(-\frac{\pi^2\mu_a^2(n)}{a}\right)\left[\operatorname{erf}\left(\frac{f_b+\mu_a(n)}{\sigma_x}\right)-\operatorname{erf}\left(-\frac{f_b-\mu_a(n)}{\sigma_x}\right)\right]}\end{aligned} \tag{5.35}$$

where each contributing factor along the frequency axis is scaled accordingly. The sum over the integer n in (5.35) represents the contributions of the different Gaussian shapes along the frequency axis to the volume in the area A. As usually this area of interest is small, only a few of the contributors around $n=0$ are enough to represent the whole sum.

5.6 Simulations

A small MIMO radar system with two orthogonal GPT waveforms has been simulated. Both TDMA and FDMA have been separately considered for the simulations. The PRI (and thus the length of each individual GP) is the same as the value from Table 2.1, T=2ms; the resulting channel bandwidth is approximately B_W=3kHz. The worst-case scenarios of $t_\Delta=2K$ms f_Δ=3kHz is investigated. Figure 5.3 shows the temporal crosssection of a GPT ambiguity

(5.12) at t=0; the result is compared to its approximation (5.14) that ignores the tail term contributions and also features the Gaussian model (5.31) for the Fejér kernel. The fitting described

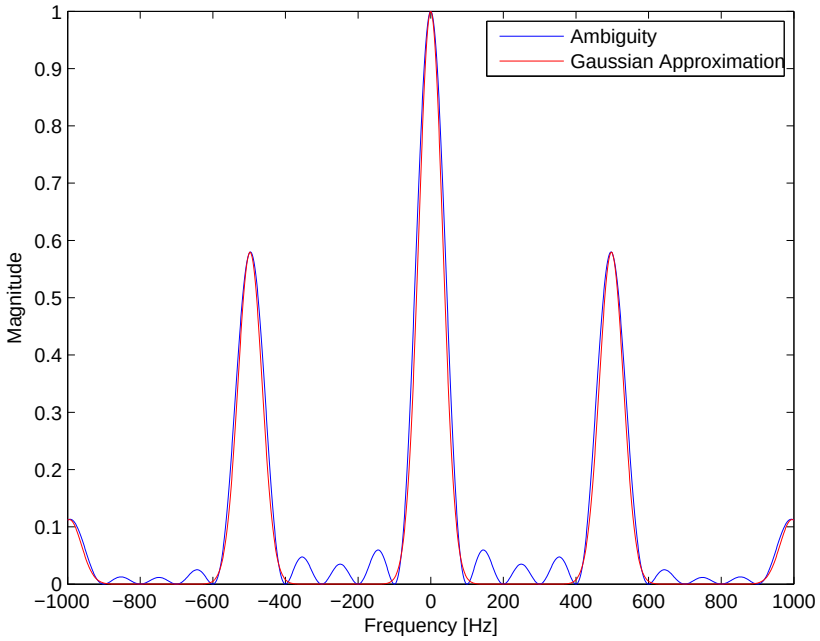

Figure 5.3: *Autoambiguity of a* 5*-pulse waveform at* t=0 *with Gaussian approximation to the Fejér kernel*

in Section 5.5.3 has been done for the periodic mainlobes of the Fejér kernel. All sidelobes outside the mainlobes, however, are ignored by the model. Thus it is expected for the approximate model of the volume ratio (5.35) to also best match the theoretical values around the peaks of the Fejér kernel. This can be seen in the results in Figure 5.4 where the theoretical and numerical volume ratios in the FDMA case are shown for relatively short GPTs of K_T=4 and K_T=40 pulses. The simulated volume ratio in the FDMA scenario (5.30) is calculated through numeric integration in a rectangular area A. The bound on the region along the time axis is t_b=1ms. The bound in frequency f_b is varied along the x-axis of Figure 5.4. As predicted, the theoretical model closely approximates the volume ratio (5.30) around the points n/T where the Fejér kernel peaks. Between the mainlobes the theoretical model underestimates the volume ratio since it ignores the ambiguity sidelobes. The general behaviour of the volume ratio is relatively well predicted through the proposed estimator (5.35) which is very computationally cheap and does not involve numeric integration.

Similar to the FDMA case, the TDMA volume ratio (5.26) is calculated through numeric inte-

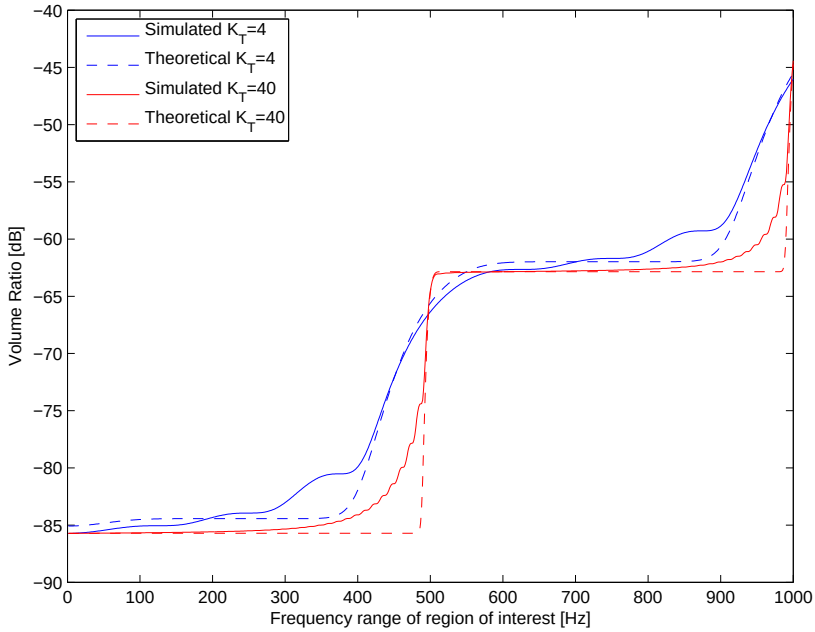

Figure 5.4: *Volume ratio of cross-to-auto-ambiguity in a rectangular region A for FDMA-orthogonal radar waveforms of K_T pulses*

gration in a rectangular area A. The bound on the region along the frequency axis is f_b=1.5kHz. The bound in time t_b is varied along the x-axis of Figure 5.5. The theoretical results in 5.5 come from the direct application of the derived volume ratio (5.26), while the simulated ones come from the numeric integration of the fully-generated autoambiguity (5.12) and cross-ambiguity (5.20) without any approximations performed. The results are almost an exact match since the only difference comes from truncated tails of Gaussian distributions.

The results in Figure 5.4 and Figure 5.5 show that the volume of the cross-ambiguity function in a rectangular region centred at the origin of ambiguity space is at least 40dB lower than the volume of the autoambiguity in the same region. Therefore, in a MIMO system with M FDMA- or TDMA-orthogonal waveforms, the total ambiguity (2.39) can be approximated as strictly the sum of the autoambiguities

$$|\chi_{MN}(t,f)|^2 \approx \sum_{m=1}^{M} |\chi_{mm}(t,f)|^2 \tag{5.36}$$

This reflects the waveform orthogonality achieved through TDMA/FDMA and relaxes the bound on the MIMO ambiguity function given in (2.40) to the original mono/bistatic case

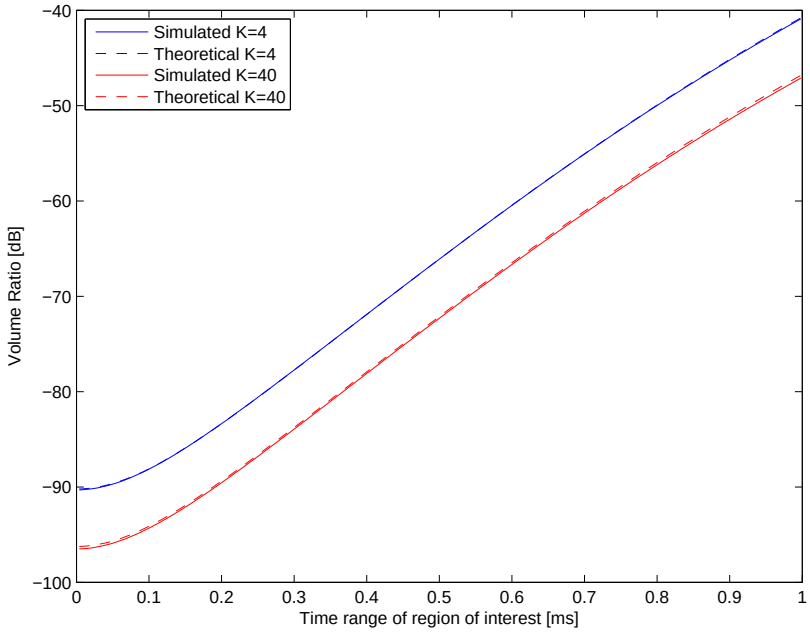

Figure 5.5: *Volume ratio of cross-to-auto-ambiguity in a rectangular region A for TDMA-orthogonal radar waveforms of K_T pulses*

(2.37). The tradeoff is the increased bandwidth and/or of the system used by the additional channels or time slots for transmission. A MIMO system of M FDMA-orthogonal waveforms requires a bandwidth of MB_W. A MIMO system of M TDMA-orthogonal waveforms has a total decision delay of MK_TT. This limits the FDMA- and TDMA-orthogonal waveform design investigated here to radar networks with a relatively small number of transmitters.

The analysis in this chapter is performed on GPTs for convenience. Note that the approximations (5.14) and (5.21) hold for any pulse with ambiguity $\alpha(t, f)$ that can be neglected outside of a region T along the time axis. However, one must ensure the spacing between pulses in (5.8) is also greater than T. If the pulses forming a waveform meet these conditions, the autoambiguity at the origin and around f_Δ as well as the Fejér kernel weights at those points can be used as a rough estimate of the behaviour of the waveform volume ratio. Note that the Gaussian approximation to the Fejér kernel (5.31) is independent of the shape of the transmitted waveforms.

5.7 Summary

This chapter discusses the method of frequency and/or time separation between different waveforms in a multistatic radar to achieve waveform orthogonality and alleviate the well-known ambiguity issue that arises in such a scenario. To aid the discussion, a practical waveform of a finite number of consecutive Gaussian pulses is considered. It is shown that the additional reduction in the ambiguity region that is clear of sidelobes in a multistatic scenario is a result of the cross-ambiguity contributions between waveforms that are assumed to be orthogonal. The cross-to-autoambiguity ratio is introduced as a measure of the relative weight of these contribution. An approximate model is derived for this ratio in the case of GPTs and simulated to demonstrate its feasibility. It is also shown through these simulations that in practice, if the frequency and/or time separation between waveforms is sufficient, the relative cross-ambiguity contributions to the multistatic ambiguity are negligible. While the work focuses on pulses of Gaussian form, a short discussion is provided in the end of the chapter that generalises the results to other pulse shapes that conform to certain conditions.

Chapter 6
Conclusion

This thesis presents a detailed development, analysis, and practical implementation solutions for different SDS detection methods based on covariance estimation in a scenario involving a widely-spaced MIMO radar. The proposed algorithms can operate blindly in any environment that involves coloured Gaussian interference and clutter. No additional knowledge of the clutter spectrum of structure is assumed, and no homogeneous secondary training data is required to perform estimation and detection.

The algorithms developed here are primarily based on the MLED and GMLED bistatic SDS methods. The thesis derives and analyses these algorithms in a multistatic scenario where multiple independent bistatic channels cooperate to detect an airborne target in coloured Gaussian interference. Tools for quick and reliable approximation of the performance of the proposed algorithms are proposed that can estimate the radar network size required to provide a certain desired detection rate. To facilitate the practical implementation of the developed multistatic detectors, a method of compression and synchronisation of the individual bistatic results is proposed prior to their transmission accross the radar network. A method of enhanced detection based on the expected target signal structure is proposed that is directly linked to the compression and synchronisation scheme. In order to minimise interference between the different bistatic channels, frequency orthogonality between the individual probing waveforms in the radar system is used. The work in this thesis demonstrates through a developed theoretical model that this method for achieving orthogonality does not introduce any additional constraints on the multistatic radar ambiguity function.

A more detailed summary of this thesis follows in Section 6.1. It expands on the achievements and contributions of the different chapters of this work. Section 6.2 provides some potential directions for future research that can build upon the contributions of this thesis.

6.1 Summary

Chapter 1 presents a brief introduction to the challenges and improvements that radar has seen throughout the years. This provides the setting and motivation for the problems solved in this thesis. A brief summary of the contributions and outline of the work is given in the end of the chapter.

Chapter 2 contains the background materials upon which the research of this thesis is built. It introduces the concept of STAP used in all algoritms developed throughout the rest of the work. It also provides a mathematical description of the evolution of covariance-based SDS detection algorithms from their related TDS counterparts. The different types of MIMO radar, coherent and widely-spaced, are introduced, and some of the most significant challenges associated with them are discussed. Finally, the problem setting and assumptions made in the thesis are described in the end of the chapter.

Chapter 3 is the first technical chapter of the thesis and presents the first major contribution: the derivation and approximate analysis of the multistatic MLED and GMLED threshold detectors. Ideal data exchange and synchronisation between multiple ideally-orthogonal and statistically independent radar channels is assumed. The optimal (in the ML-sense) fusion of the bistatic MLED and GMLED results from those channels into a multistatic variable is derived. It is demonstrated that this variable has the CFAR property which makes its statistics independent from the background interference structure and power. To facilitate the analysis of the proposed multistatic algorithms, a Gaussian model is developed that reliably approximates their statistical behaviour and performance under given SNR conditions. A number of numerical simulations have been developed in order to demonstrate the viability of the approximation models. The performance gains of adding more channels and iid temporal observation snapshots to the multistatic radar system have also been shown.

Chapter 4 is the second technical chapter of the thesis and provides a number of contributions towards the practical implementation of the proposed multistatic MLED detector. An adaptive subspace compression method for the bistatic likelihood functions of the detection variables in the individual channels is developed. The compression transmits only the significant components from each channel rather than the full Doppler spectrum of decisions, and thus the amount of data exchanged within the radar network is reduced. A method of projecting the MLED likelihood function from D-space into v-space is also proposed. This allows for the

easy synchronisation and fusion of the search spaces of the different bistatic channels into the multistatic result. Based on the subspace compression of the likelihood and the subsequent search space projection, a modified multistatic MLED detection procedure is proposed that exploits the structure of the reflected target signal in v-space. This results in an enhanced algorithm performance for mid-to-high SNR levels. A number of numerical simulations have been conducted that demonstrate the performance increase of the proposed modification over the standard multistatic MLED developed in Chapter 3. It is also shown that through the developed compression scheme, compression ratios of up to 30 times can be achieved while keeping the algorithm performance within 10% of the uncompressed one.

Chapter 5 is the third and final technical chapter of the thesis and develops a theoretical model for the MIMO ambiguity function if frequency orthogonality between the different transmitted waveforms is assumed. It is shown through this theoretical model that if the frequency separation between the waveforms is sufficient, adding more transmitters to the multistatic radar system presents no additional burden to the total ambiguity. Through numerical simulations it has been demonstrated that the cross-ambiguity contributions of additional waveforms are negligible compared to the existing autoambiguities. While the work in the chapter is built around Gaussian pulse train waveforms, the results are extended to other pulse shapes that conform to certain specified requirements.

6.2 Possible directions for future work

The overall derivation and procedure developed in this thesis is relatively exhaustive in terms of the assumptions made and the problem undertaken. However, it may be of interest to relax or alter some of the assumptions and see how that affects the target detection solution. The work in this thesis focuses on coloured Gaussian clutter. The case of non-Gaussian interference is a complex one and comes with its own set of challenges. Deriving the MLED and GMLED as well as their multistatic versions under this assumption can be a direction with significant research potential.

Another potentially important derivation is the multitarget solution for the MLED and GMLED algorithms. In this thesis a single target was assumed to be buried in the background interference. Searching for two targets at the same time involves the ML search and estimation over multiple pairs of spatio-temporal steering vectors. This can be computationally expensive but

adds more flexibility to the algorithms.

There is still potential for additional work on the enhanced detector proposed in Chapter 4. A theoretical or approximate method for selecting the optimal scaling parameter κ can be investigated. It may be worthwhile to attempt to combine the proposed multistatic algorithm with the hybrid SDS-TDS detection procedure from [19]. Before any final conclusions are drawn, it will be interesting to test the performance of the detectors proposed in this thesis on real STAP data collected by multiple radar receiver ULAs.

Appendix A
Derivation of the bistatic MLED and GMLED statistics

This appendix provides the derivation of the statistical distribution of the bistatic MLED and GMLED threshold detectors. The derivations are included here only for convenience and are not original contributions. The original source of the derivations is found in [17], while a much more detailed version is reproduced in [18, pp.55-58].

A.1 Derivation of the bistatic MLED statistics

The original form of the bistatic MLED threshold detector given in eq. (2.30) of Chapter 2 is reproduced here for convenience:

$$\frac{|\boldsymbol{s}^H\boldsymbol{Q}^{-1}\boldsymbol{g}|^2}{\boldsymbol{s}^H\boldsymbol{Q}^{-1}\boldsymbol{s}} \underset{H_0}{\overset{H_1}{\gtrless}} \gamma$$

To facilitate the analysis, a spatial whitening operation is applied to the steering vector and the observation samples of the bistatic MLED to produce the following whitened versions

$$\widetilde{\boldsymbol{s}} = \boldsymbol{R}^{-\frac{1}{2}}\boldsymbol{s} \tag{A.1}$$

$$\widetilde{\boldsymbol{X}} = \boldsymbol{R}^{-\frac{1}{2}}\boldsymbol{X} \tag{A.2}$$

After the whitening process, a unitary transformation is applied that rotates the steering vector into the first elementary vector $\boldsymbol{e}=[1,0,\ldots,0]^T$. The unitary matrix $\boldsymbol{U}$ having $\frac{1}{\sqrt{P}}$ as its first column and the rest of the columns forming an orthonormal basis is used to perform this operation:

$$\boldsymbol{e} = \boldsymbol{U}^H\widetilde{\boldsymbol{s}} \tag{A.3}$$

$$\widetilde{\boldsymbol{X}} = \boldsymbol{U}^H\widetilde{\boldsymbol{X}} \tag{A.4}$$

Note that the unitary transformation does not affect the statistical properties of the random vectors it is applied to. Therefore, in eq. (A.4) the symbol for the random variable after rotation is preserved for convenience since the focus here is on the statistical analysis. The respective whitened and rotated variables $\widetilde{\boldsymbol{g}}$ and $\widetilde{\boldsymbol{Q}}$ have been spatially decorrelated and are distributed as

$$\widetilde{\boldsymbol{g}} \sim \mathcal{N}_P(\alpha \boldsymbol{e}, \boldsymbol{I}) \tag{A.5}$$

$$\widetilde{\boldsymbol{Q}} \sim \mathcal{C}W_P(K-1) \tag{A.6}$$

where $\mathcal{C}W_P(K-1)$ is the complex Wishart distribution with $K-1$ DOF and the identity as the scale matrix. The whitened and rotated quantities can be substituted back into the original MLED threshold detector equation without altering its statistics. The equation takes the following form:

$$\frac{|\boldsymbol{e}^H \widetilde{\boldsymbol{Q}}^{-1} \widetilde{\boldsymbol{g}}|^2}{\boldsymbol{e}^H \widetilde{\boldsymbol{Q}}^{-1} \boldsymbol{e}} \underset{H_0}{\overset{H_1}{\gtrless}} \gamma \tag{A.7}$$

The whitened and rotated matrix $\widetilde{\boldsymbol{X}}$ as well as the variables $\widetilde{\boldsymbol{g}}$ and $\widetilde{\boldsymbol{Q}}$ are now partitioned in the following manner:

$$\widetilde{\boldsymbol{X}} = \begin{bmatrix} \widetilde{\boldsymbol{x}}_A^H \\ \widetilde{\boldsymbol{X}}_B \end{bmatrix} \quad \widetilde{\boldsymbol{g}} = \begin{bmatrix} \widetilde{g}_A \\ \widetilde{\boldsymbol{g}}_B \end{bmatrix} \quad \widetilde{\boldsymbol{Q}} = \begin{bmatrix} \widetilde{q}_{AA} & \widetilde{\boldsymbol{q}}_{BA}^H \\ \widetilde{\boldsymbol{q}}_{BA} & \widetilde{\boldsymbol{Q}}_{BB} \end{bmatrix} \tag{A.8}$$

Define the following $K \times K$ matrix

$$\boldsymbol{H} = \boldsymbol{I} - \boldsymbol{t}^* \boldsymbol{t}^T \tag{A.9}$$

which is clearly idempotent with rank $K-1$. The matrix represents the projection onto a subspace orthogonal to the target's temporal steering vector. Then the partitions from eq. (A.8) can be related to each other through the following equations

$$\widetilde{g}_A = \widetilde{\boldsymbol{x}}_A^H \boldsymbol{t}^* \tag{A.10a}$$

$$\widetilde{\boldsymbol{g}}_B = \widetilde{\boldsymbol{X}}_B^H \boldsymbol{t}^* \tag{A.10b}$$

$$\widetilde{q}_{AA} = \widetilde{\boldsymbol{x}}_A^H \boldsymbol{H} \widetilde{\boldsymbol{x}}_A \tag{A.10c}$$

$$\widetilde{\boldsymbol{q}}_{BA} = \widetilde{\boldsymbol{X}}_B \boldsymbol{H} \widetilde{\boldsymbol{x}}_A \tag{A.10d}$$

$$\widetilde{\boldsymbol{Q}}_{BB} = \widetilde{\boldsymbol{X}}_B \boldsymbol{H} \widetilde{\boldsymbol{X}}_B^H \tag{A.10e}$$

Let the inverse of the matrix $\widetilde{\boldsymbol{Q}}$ be denoted as $\widetilde{\boldsymbol{P}}=\widetilde{\boldsymbol{Q}}^{-1}$. Using the blockwise matrix inversion theorem [105, p.459] the following matrix partitions can be defined

$$\widetilde{p}_{AA} = \left(\widetilde{q}_{AA} - \widetilde{\boldsymbol{q}}_{BA}^{H}\widetilde{\boldsymbol{Q}}_{BB}^{-1}\widetilde{\boldsymbol{q}}_{BA}\right)^{-1} \tag{A.11a}$$

$$\widetilde{\boldsymbol{p}}_{BA} = -\widetilde{p}_{AA}\widetilde{\boldsymbol{q}}_{BA}^{H}\widetilde{\boldsymbol{Q}}_{BB}^{-1} \tag{A.11b}$$

$$\widetilde{\boldsymbol{P}}_{BB} = \widetilde{p}_{AA}\widetilde{q}_{AA}\widetilde{\boldsymbol{Q}}_{BB}^{-1} \tag{A.11c}$$

Since $\boldsymbol{e}$ is the first elementary vector, it is easy to show that the left-hand side of (A.7) is equivalent to

$$\begin{aligned}\frac{|\boldsymbol{e}^{H}\widetilde{\boldsymbol{Q}}^{-1}\widetilde{\boldsymbol{g}}|^{2}}{\boldsymbol{e}^{H}\widetilde{\boldsymbol{Q}}^{-1}\boldsymbol{e}} &= \widetilde{p}_{AA}\left|\widetilde{g}_{A} - \widetilde{\boldsymbol{q}}_{BA}^{H}\widetilde{\boldsymbol{Q}}_{BB}^{-1}\widetilde{\boldsymbol{g}}_{B}\right|^{2} \\ &= \frac{\left|\widetilde{g}_{A} - \widetilde{\boldsymbol{q}}_{BA}^{H}\widetilde{\boldsymbol{Q}}_{BB}^{-1}\widetilde{\boldsymbol{g}}_{B}\right|^{2}}{\widetilde{q}_{AA} - \widetilde{\boldsymbol{q}}_{BA}^{H}\widetilde{\boldsymbol{Q}}_{BB}^{-1}\widetilde{\boldsymbol{q}}_{BA}}\end{aligned} \tag{A.12}$$

Define the following support random variable η through the following expression

$$\eta = \left(1 + \widetilde{\boldsymbol{g}}_{B}^{H}\widetilde{\boldsymbol{Q}}_{BB}^{-1}\widetilde{\boldsymbol{g}}_{B}\right)^{-1} \tag{A.13}$$

Note the fact that

$$\eta^{-1} = \left(\boldsymbol{t}^{*} - \boldsymbol{H}\widetilde{\boldsymbol{X}}_{B}^{H}\widetilde{\boldsymbol{Q}}_{BB}^{-1}\widetilde{\boldsymbol{g}}_{B}\right)^{H}\left(\boldsymbol{t}^{*} - \boldsymbol{H}\widetilde{\boldsymbol{X}}_{B}^{H}\widetilde{\boldsymbol{Q}}_{BB}^{-1}\widetilde{\boldsymbol{g}}_{B}\right) \tag{A.14}$$

Thus the numerator of (A.12) takes the form $\widetilde{\boldsymbol{x}}_{A}^{H}\boldsymbol{A}\widetilde{\boldsymbol{x}}_{A}\eta^{-1}$ where

$$\boldsymbol{A} = \eta\left(\boldsymbol{t}^{*} - \boldsymbol{H}\widetilde{\boldsymbol{X}}_{B}^{H}\widetilde{\boldsymbol{Q}}_{BB}^{-1}\widetilde{\boldsymbol{g}}_{B}\right)\left(\boldsymbol{t}^{*} - \boldsymbol{H}\widetilde{\boldsymbol{X}}_{B}^{H}\widetilde{\boldsymbol{Q}}_{BB}^{-1}\widetilde{\boldsymbol{g}}_{B}\right)^{H} \tag{A.15}$$

Similarly the denominator of the left-hand side of (A.23) can be expressed as

$$\begin{aligned}\widetilde{q}_{AA} - \widetilde{\boldsymbol{q}}_{BA}^{H}\widetilde{\boldsymbol{Q}}_{BB}^{-1}\widetilde{\boldsymbol{q}}_{BA} &= \widetilde{\boldsymbol{x}}_{A}^{H}\left(\boldsymbol{H} - \boldsymbol{H}\widetilde{\boldsymbol{X}}_{B}^{H}\widetilde{\boldsymbol{Q}}_{BB}^{-1}\widetilde{\boldsymbol{X}}_{B}\right)\widetilde{\boldsymbol{x}}_{A} \\ &= \widetilde{\boldsymbol{x}}_{A}^{H}\boldsymbol{B}\widetilde{\boldsymbol{x}}_{A}\end{aligned} \tag{A.16}$$

Thus the equivalent and simplified form of the MLED statistics takes the following form:

$$\frac{\widetilde{\boldsymbol{x}}_{A}^{H}\boldsymbol{A}\widetilde{\boldsymbol{x}}_{A}}{\widetilde{\boldsymbol{x}}_{A}^{H}\boldsymbol{B}\widetilde{\boldsymbol{x}}_{A}} \underset{H_0}{\overset{H_1}{\gtrless}} \gamma\eta \tag{A.17}$$

Because $\boldsymbol{AB}=\boldsymbol{0}$, the numerator and denominator of the left-hand side of (A.17) are statistically independent [105, Theorem 3.4.5]. The matrix $\boldsymbol{A}$ has been normalised to a form that is clearly idempotent and of rank 1. Thus the numerator of the left-hand side of (A.17) has a non-central complex $\sim \mathbb{C}\chi_1^2$ distribution with 1 DOF and a non-centrality parameter $2\lambda=KP\eta\rho$, where ρ is the SNR defined in eq. (3.38). Similarly, $\boldsymbol{B}$ is idempotent of rank $L=K-P$ since $\widetilde{\boldsymbol{g}}_B^H\widetilde{\boldsymbol{Q}}_{BB}^{-1}\widetilde{\boldsymbol{g}}_B$ is of rank $P-1$ [105, Corollary 3.4.8.1] and $\boldsymbol{H}$ is idempotent with rank $K-1$. Thus the denominator of (A.17) has the complex chi-squared distribution with L DOF denoted as $\sim \mathbb{C}\chi_L^2$. Therefore, equivalent distribution of the MLED statistics is the following

$$\frac{\mathcal{C}\chi_1^2}{\mathcal{C}\chi_L^2} \underset{H_0}{\overset{H_1}{\gtrless}} \gamma\eta \tag{A.18}$$

Since the ratio of two independent variables that hold the chi-squared distribution is equivalent to an F-distribution, the equivalent statistics of the bistatic MLED random variable (3.35) used in the thesis follow directly from (A.18).

A.2 Derivation of the bistatic GMLED statistics

The original form of the bistatic GMLED threshold detector given in eq. (2.31) of Chapter 2 is reproduced here for convenience:

$$\frac{|\boldsymbol{s}^H\boldsymbol{Q}^{-1}\boldsymbol{g}|^2}{\boldsymbol{s}^H\boldsymbol{Q}^{-1}\boldsymbol{s}\left(1+\boldsymbol{g}^H\boldsymbol{Q}^{-1}\boldsymbol{g}\right)} \underset{H_0}{\overset{H_1}{\gtrless}} \gamma$$

The analysis steps of the GMLED statistics mirror those of the MLED ones presented in Section A.1 of this appendix. After a whitening operation and a unitary rotation has been performed, the equivalent GMLED threshold detector expression is the following

$$\frac{|\boldsymbol{e}^H\widetilde{\boldsymbol{Q}}^{-1}\widetilde{\boldsymbol{g}}|^2}{\boldsymbol{e}^H\widetilde{\boldsymbol{Q}}^{-1}\boldsymbol{e}} \underset{H_0}{\overset{H_1}{\gtrless}} \gamma\left(1+\widetilde{\boldsymbol{g}}^H\widetilde{\boldsymbol{Q}}^{-1}\widetilde{\boldsymbol{g}}\right) \tag{A.19}$$

The left-hand side expression of (A.19) is the same as the one in (A.7). Thus the analysis remains the same. On the right-hand side of the same equation, the following manipulation can be performed:

$$\widetilde{\boldsymbol{g}}^H\widetilde{\boldsymbol{Q}}^{-1}\widetilde{\boldsymbol{g}} = \widetilde{p}_{AA}\left(\widetilde{g}_A\widetilde{g}_A^* + \widetilde{g}_A\widetilde{\boldsymbol{g}}_B^H\widetilde{\boldsymbol{Q}}_{BB}^{-1}\widetilde{\boldsymbol{q}}_{BA}^H - \widetilde{g}_A^*\widetilde{\boldsymbol{q}}_{BA}^H\widetilde{\boldsymbol{Q}}_{BB}^{-1}\widetilde{\boldsymbol{g}}_B^H\right) - \widetilde{\boldsymbol{g}}_B^H\widetilde{\boldsymbol{P}}_{BB}\widetilde{\boldsymbol{g}}_B \tag{A.20}$$

where the inverse partition relations (A.11) have been substituted in (A.20). Completing the square for the term in the parentheses in (A.20) and once again using the inverse partition relations (A.11) results in the following manipulation:

$$\begin{aligned}&\left(\widetilde{g}_A\widetilde{g}_A^* + \widetilde{g}_A\widetilde{\boldsymbol{g}}_B^H\widetilde{\boldsymbol{Q}}_{BB}^{-1}\widetilde{\boldsymbol{q}}_{BA}^H - \widetilde{g}_A^*\widetilde{\boldsymbol{q}}_{BA}^H\widetilde{\boldsymbol{Q}}_{BB}^{-1}\widetilde{\boldsymbol{g}}_B^H\right)\\ &= \left|\widetilde{g}_A - \widetilde{\boldsymbol{q}}_{BA}^H\widetilde{\boldsymbol{Q}}_{BB}^{-1}\widetilde{\boldsymbol{g}}_B^H\right|^2 - \widetilde{p}_{AA}^{-2}\widetilde{\boldsymbol{g}}_B^H\widetilde{\boldsymbol{p}}_{BA}\widetilde{\boldsymbol{p}}_{BA}^H\widetilde{\boldsymbol{g}}_B\end{aligned} \tag{A.21}$$

The final manipulation that can be peformed through the inverse partition relations (A.11) is the following:

$$\widetilde{\boldsymbol{g}}_B^H\widetilde{\boldsymbol{P}}_{BB}\widetilde{\boldsymbol{g}}_B - \widetilde{p}_{AA}^{-1}\widetilde{\boldsymbol{g}}_B^H\widetilde{\boldsymbol{p}}_{BA}\widetilde{\boldsymbol{p}}_{BA}^H\widetilde{\boldsymbol{g}}_B = \widetilde{\boldsymbol{g}}_B^H\widetilde{\boldsymbol{Q}}_{BB}^{-1}\widetilde{\boldsymbol{g}}_B \tag{A.22}$$

By using (A.12), (A.20), (A.21), and (A.22), the GMLED statistics can be written as

$$\frac{\left|\widetilde{g}_A - \widetilde{\boldsymbol{q}}_{BA}^H\widetilde{\boldsymbol{Q}}_{BB}^{-1}\widetilde{\boldsymbol{g}}_B\right|^2}{\widetilde{q}_{AA} - \widetilde{\boldsymbol{q}}_{BA}^H\widetilde{\boldsymbol{Q}}_{BB}^{-1}\widetilde{\boldsymbol{q}}_{BA}} \underset{H_0}{\overset{H_1}{\gtrless}} \frac{\tau}{\eta} \tag{A.23}$$

where

$$\tau = \frac{\gamma}{1-\gamma} \tag{A.24}$$

Following the analysis of the left-hand side expression of (A.23) shown in Section A.1, the equivalent and simplified form of the GMLED statistics is:

$$\frac{\widetilde{\boldsymbol{x}}_A^H\boldsymbol{A}\widetilde{\boldsymbol{x}}_A}{\widetilde{\boldsymbol{x}}_A^H\boldsymbol{B}\widetilde{\boldsymbol{x}}_A} \underset{H_0}{\overset{H_1}{\gtrless}} \tau \tag{A.25}$$

Thus the bistatic GMLED random variable is distributed as

$$\frac{\mathcal{C}\chi_1^2}{\mathcal{C}\chi_L^2} \underset{H_0}{\overset{H_1}{\gtrless}} \tau \tag{A.26}$$

which is once again equivalent to a non-central F-distribution as used in eq. (3.62) of this thesis.

Appendix B
Lindeberg's condition

B.1 Proof of Lindeberg's condition for the multistatic MLED approximation

In this appendix the following notation will be used to denote the MLED threshold detector in a single bistatic channel $(\cdot)_{m,n}$

$$T_{M(m,n)} = \frac{|\boldsymbol{s}_{m,n}^H \boldsymbol{Q}_{m,n}^{-1} \boldsymbol{g}_{m,n}|^2}{\boldsymbol{s}_{m,n}^H \boldsymbol{Q}_{m,n}^{-1} \boldsymbol{s}_{m,n}} \tag{B.1}$$

The multistatic MLED detection variable consists of the sum of (B.1) across all channels as derived in (3.16). Thus Lindeberg's condition for the CLT takes the following form

$$\lim_{\substack{M\to\infty \\ N\to\infty}} \frac{1}{\sigma_M^2} \sum_{m=1}^{M} \sum_{n=1}^{N} \int_{|T_{M(m,n)}-\mu_{M(m,n)}|>\epsilon\sigma_M} \left(T_{M(m,n)} - \mu_{M(m,n)}\right)^2 f_{T_M}(T_{M(m,n)}) dT_{M(m,n)} = 0 \tag{B.2}$$

where $\mu_{M(m,n)}$ is the channel variable mean given by (3.51) and σ_M^2 is the total MIMO detector variance given by the sum (3.44) of (3.52). The pdf $f_{T_M}(x)$ is associated with the bistatic MLED random variable (3.35). For any constant $\epsilon>0$ Lindeberg's condition (B.2) is sufficient (and necessary in this case according to the Feller-Lévy Condition [106]) to claim that the multistatic MLED random variable (3.39) will converge to a Gaussian distribution as the number of transmit-receive pairs $M\times N$ goes to infinity. Chebyshev's inequality for the variance of the bistatic MLED detector states that

$$P(|T_{M(m,n)} - \mu_{M(m,n)}| \geq \epsilon\sigma_M) \leq \frac{\sigma_{M(m,n)}^2}{\epsilon^2 \sigma_M^2} \tag{B.3}$$

Note that the mean $\mu_{M(m,n)}$ (3.51) and the variance $\sigma_{M(m,n)}^2$ (3.52) both exist and are finite if a realistic system with finite number of independent temporal samples K and spatial samples P is considered. This is due to the assumption that $\lambda_{m,n}$ is finite as well because the SNR $\rho_{m,n}$ will always be limited by the thermal noise in the transmission medium. The term σ_M^2 (3.44)

is the sum of the individual variances $\sigma^2_{M(m,n)}$ (3.52) across all channels. It takes the form of a second degree polynomial with respect to the non-centrality parameters $\lambda_{m,n}$ (or their proposed estimates $\widetilde{\lambda}_{m,n}$) and can thus be written as

$$\sigma^2_M = \sum_{m,n} a_{m,n}\lambda^2_{m,n} + \sum_{m,n} b_{m,n}\lambda_{m,n} + cMN \tag{B.4}$$

where $a_{m,n}, b_{m,n}, c \in \mathbb{R}$ are the arbitraty polynomial coefficients. Since realistically the DOF $L>2$, the coefficient c is positive and the sum in (B.4) diverges to infinity as $M\times N\to\infty$. Therefore, the right hand side of Chebyshev's inequality (B.3) goes to 0 since $\epsilon>0$ is a constant.

$$\lim_{\substack{M\to\infty \\ N\to\infty}} \frac{\sigma^2_{M(m,n)}}{\epsilon^2\sigma^2_M} = 0 \tag{B.5}$$

Therefore the left hand side probability in the inequality is bounded by 0, which translates to

$$\lim_{\substack{M\to\infty \\ N\to\infty}} \int_{|T_{M(m,n)}-\mu_{M(m,n)}|>\epsilon\sigma_M} f_{T_M}(T_{M(m,n)})dT_{M(m,n)} = 0 \tag{B.6}$$

Combined with the fact that the mean $\mu_{M(m,n)}$ is finite, this proves that each term in the sum (B.2) converges to 0 in the limit. Therefore the whole sum converges to 0 and Lindeberg's condition is satisfied, which justifies the Gaussian approximation of the multistatic MLED threshold detector.

B.2 Proof of Lindeberg's condition for the multistatic GMLED approximation

In this appendix the following notation will be used to denote the GMLED threshold detector in a single bistatic channel $(\cdot)_{m,n}$

$$T_{G(m,n)} = \frac{1 + \boldsymbol{g}^H_{m,n}\boldsymbol{Q}^{-1}_{m,n}\boldsymbol{g}_{m,n}}{1 + \boldsymbol{g}^H_{m,n}\boldsymbol{Q}^{-1}_{m,n}\boldsymbol{g}_{m,n} - \dfrac{|\boldsymbol{s}^H_{m,n}\boldsymbol{Q}^{-1}_{m,n}\boldsymbol{g}_{m,n}|^2}{\boldsymbol{s}^H_{m,n}\boldsymbol{Q}^{-1}_{m,n}\boldsymbol{s}_{m,n}}} \tag{B.7}$$

Lindeberg's condition for the multistatic GMLED must be considered in the natural logarithm since the approximation is log-normal.

$$\lim_{\substack{M\to\infty \\ N\to\infty}} \frac{1}{\sigma_G^2} \sum_{m=1}^{M} \sum_{n=1}^{N} \int_{|\log T_{G(m,n)} - \mu_{G(m,n)}| > \epsilon\sigma_G} \left(\log T_{G(m,n)} - \mu_{G(m,n)}\right)^2 f_{\log T_G}(\log T_{G(m,n)}) d\log T_{G(m,n)} = 0 \quad \text{(B.8)}$$

The expectation (3.65) and second moment (3.67) of the bistatic GMLED (B.7) are both finite due to the assumptions that the system parameters K, P, and $\lambda_{m,n}$ are practically finite (see B.1). In this proof the following logarithmic inequality will be used

$$\log x \leq x - 1 \quad \text{(B.9)}$$

which is a basic property valid for any $x{>}0$. From (B.9) an upper bound for the expectation of the logarithm of the bistatic GMLED threshold detector can be obtained

$$E\left[\log T_{G(m,n)}\right] \leq E\left[T_{G(m,n)} - 1\right] \quad \text{(B.10)}$$

where the right hand side of (B.10) is finite. Moreover, due to the nature of the random variables involved, it can be concluded that the expectation in the same equation is bounded from below by the case when the non-centrality parameter of the F-distribution becomes zero, or $\lambda_{m,n}{=}0$

$$\frac{1}{L} \leq E\left[\log T_{G(m,n)}\right] \quad \text{(B.11)}$$

where the left hand side of (B.10) is obtained from the mean (3.76) taken in a single bistatic channel. In a similar manner boundaries for the second moment of the logarithm of the bistatic GMLED threshold detector can be derived:

$$\frac{1}{L^2} \leq E\left[(\log T_{G(m,n)})^2\right] \leq E\left[(T_{G(m,n)} - 1)^2\right] \quad \text{(B.12)}$$

The upper boundary in (B.12) comes from applying the logarithmic property (B.9); the lower boundary is derived from the fact that $E\left[x^2\right] {\geq} E\left[x\right]^2$ where the bound on the variance $\sigma^2_{G(m,n)}$ comes from (3.77). Combining (B.11),(B.10), and (B.12), it can be concluded that the variance of the logarithm of the bistatic GMLED detector is also bounded from below and above by certain finite bounds. The exact values of these bounds are not essential for the current proof

and will therefore not be calculated

$$\sigma_{lb}^2 \leq \sigma_{G(m,n)}^2 \leq \sigma_{ub}^2 \tag{B.13}$$

The bounds in (B.13) are enough to conclude that for any arbitrary constant $\epsilon{>}0$

$$\lim_{\substack{M\to\infty \\ N\to\infty}} \frac{\sigma_{G(m,n)}^2}{\epsilon^2 \sigma_G^2} = 0 \tag{B.14}$$

since the lower bounds on the total multistatic variance σ_G^2 tends to infinity as the number of transmitter-receiver pairs in the system tends to infinity. At this point the Chebyshev bound for the variance of the natural logarithm of the bistatic GMLED

$$P(|\log T_{G(m,n)} - \mu_{G(m,n)}| \geq \epsilon\sigma_M) \leq \frac{\sigma_{G(m,n)}^2}{\epsilon^2 \sigma_G^2} \tag{B.15}$$

becomes zero. This, combined with the fact that $\mu_{G(m,n)}$ is finite, proves the validity of Lindeberg's condition (B.8) for the natural logarithm of the multistatic GMLED.

Appendix C
Original publications

- † B. Shtarkalev and B. Mulgrew, "Multistatic single data set target detection in unknown coloured Gaussian interference," in *Radar Conference (RADAR), 2013 IEEE*, pp. 1–5, 2013.
- † B. Shtarkalev and B. Mulgrew, "Effects of FDMA/TDMA orthogonality on the Gaussian pulse train MIMO ambiguity function," *Signal Processing Letters, IEEE*, vol. 22, pp. 153–157, Feb 2015.
- † B. Shtarkalev and B. Mulgrew, "Multistatic moving target detection in unknown coloured Gaussian interference," *Signal Processing*, vol. 115, no. 0, pp. 130 – 143, 2015.

† Reprinted in this appendix.

Multistatic Single Data Set Target Detection in Unknown Coloured Gaussian Interference

Bogomil Shtarkalev
Institute for Digital Communications
School of Engineering and Electronics
The University of Edinburgh
Edinburgh, EH9 3JL, UK
Email: b.shtarkalev@ed.ac.uk

Bernard Mulgrew
Institute for Digital Communications
School of Engineering and Electronics
The University of Edinburgh
Edinburgh, EH9 3JL, UK
Email: b.mulgrew@ed.ac.uk

***Abstract*—This paper proposes a solution to the problem of searching for a moving airborne target in unknown coloured Gaussian interference. Traditional space-time adaptive processing (STAP) approaches to this problem rely on the existence of a training data set that helps build an estimate to the covariance matrix of the background noise and interference. These algorithms are thus labelled as two data set (TDS). In contrast, the work in this paper focuses on single data set (SDS) STAP detection that forms an estimate to the noise covariance matrix without access to training data and without any assumptions on the shape of the noise spectrum. Two such algorithms for target detection are presented that operate in a multiple-input multiple-output (MIMO) system of widely-spaced transmit and receive antennas. These algorithms are proven to possess the highly desirable constant false alarm rate (CFAR) property. It is shown through simulations that the proposed SDS solutions are comparable in their performance to the existing TDS solutions to the same problem.**

I. Introduction

Moving target detection in unknown correlated Gaussian interference is a problem that has seen a number of improving solutions over the years (see [1]–[8]). Traditional detection algorithms require the aid of a target-free secondary training data set and can thus be classified as two data set (TDS) detectors [1], [2]. In recent years single data set (SDS) algorithms that require no training data have been proposed as improvements over the TDS methods (see [3]–[5]). A different way of enhancing target detection that has gained popularity is the use of multiple-input multiple-output (MIMO) systems [6]. Its advantages are numerous: higher accuracy of target localisation, higher detection rate, increased spatial and angular diversity, increased resolution. Distributed TDS target localisation methods have been proposed that combine the benefits of traditional detectors with the availability of modern MIMO radar systems ([7], [8]). These methods however still suffer from the requirement of a target-free training data set.

In this paper two methods that combine the benefits of widely-spaced MIMO radar systems and SDS moving target detection in unknown coloured Gaussian noise are proposed. The focus of the work is on the space-time adaptive processing (STAP) technique which boosts radar performance when dealing with ground clutter returns [9]. The relations between the proposed multistatic SDS algorithms and the bistatic ones presented in [4], [5] are derived. It is shown that the developed target detectors possess the constant false alarm rate (CFAR) property. The behaviours of the proposed methods is studied through numerical simulations in a scenario involving a mixture of multiple transmit antennas and multiple receive phased arrays. It is shown that the presented SDS algorithms are comparable in performance to the existing multistatic TDS solutions to the same problem [7], [8]. Scenarios involving different numbers of antennas are explored in order to demonstrate the benefits of using a MIMO system.

The rest of this paper is organised as follows. Section II formulates the problem and provides a background on some of the existing target detection schemes. Sections III and IV provide the derivations of the two multistatic radar algorithms proposed in this paper. Section V contains the results of the numerical simulations and a discussion of these results. Section VI presents the conclusions drawn from the work.

II. Background

Consider a MIMO array with M transmitters and N receivers that probe an area for the presence of a moving target. Each receiver is subdivided into P sensors that collect K observation snapshots $\boldsymbol{x}_{m,n,k}, k{=}1\ldots K$. The index $\{m,n\}$ signifies the path between the m^{th} transmitter and the n^{th} receiver. In this work these paths will be referred to as "channels." The observations in each channel are arranged as columns in the matrix $\boldsymbol{X}_{m,n}{\in}\mathbb{C}^{P\times K}$. This work assumes that pulse compression has been performed on the reflected probing waveforms and focuses on slow-time processing. In the context of STAP, the system searches for a reflection of a probing signal with a spatial steering vector $\boldsymbol{s}_{m,n}{\in}\mathbb{C}^{P\times 1}$ and a temporal steering vector $\boldsymbol{t}_{m,n}{\in}\mathbb{C}^{K\times 1}$ in each channel. A detection algorithm will decide between two possible hypotheses for the origin of the observations

$$\begin{aligned} H_0 &: \boldsymbol{X}_{m,n} = \boldsymbol{N}_{m,n} \\ H_1 &: \boldsymbol{X}_{m,n} = \alpha_{m,n}\boldsymbol{s}_{m,n}\boldsymbol{t}_{m,n}^T + \boldsymbol{N}_{m,n} \end{aligned} \tag{1}$$

where $\alpha_{m,n}$ are complex magnitudes. The superscripts T, $*$, and H used throughout this work indicate the transpose, conjugate, and Hermitian transpose operators respectively. The matrix $\boldsymbol{N}_{m,n} \in \mathbb{C}^{P\times K}$ is a combined term for the background

2013 IEEE Radar Conference (RadarCon13)
978-1-4673-5794-4/13/$31.00 ©2013 IEEE

noise and interference. It is assumed to be zero-mean circular Gaussian with independent and identically distributed (iid) columns $\boldsymbol{n}_{m,n,k} \sim \mathcal{CN}_P(\boldsymbol{0}, \boldsymbol{C}_{m,n})$. The optimum STAP CFAR threshold detector derived in [10] is given by

$$\frac{|\boldsymbol{s}_{m,n}^H \boldsymbol{C}_{m,n}^{-1} \boldsymbol{g}_{m,n}|^2}{\boldsymbol{s}_{m,n}^H \boldsymbol{C}_{m,n}^{-1} \boldsymbol{s}_{m,n}} \underset{H_0}{\overset{H_1}{\gtrless}} \gamma_{m,n} \tag{2}$$

and is known as the matched filter (MF). The term $\boldsymbol{g}_{m,n}$ is the STAP coherent sample mean of the observation data

$$\boldsymbol{g}_{m,n} = c\boldsymbol{X}_{m,n}\boldsymbol{t}_{m,n}^* \tag{3}$$

where c is a normalising constant. Usually the noise covariance matrix $\boldsymbol{C}_{m,n}$ is unknown. Traditional detection algorithms use a secondary data set $\boldsymbol{Z}_{m,n}$ with K_t target-free observation vectors to form a sample correlation matrix estimate:

$$\hat{\boldsymbol{C}}_{m,n} = \frac{1}{K_t} \boldsymbol{Z}_{m,n} \boldsymbol{Z}_{m,n}^H \tag{4}$$

Using (4) in (2) to replace the covariance matrix gives the adaptive matched filter (AMF) threshold detector [1]:

$$\frac{|\boldsymbol{s}_{m,n}^H \hat{\boldsymbol{C}}_{m,n}^{-1} \boldsymbol{g}_{m,n}|^2}{\boldsymbol{s}_{m,n}^H \hat{\boldsymbol{C}}_{m,n}^{-1} \boldsymbol{s}_{m,n}} \underset{H_0}{\overset{H_1}{\gtrless}} \gamma_{m,n} \tag{5}$$

A slightly modified version of (5) is the well-known generalised likelihood ratio test (GLRT) derived by Kelly [2]:

$$\frac{|\boldsymbol{s}_{m,n}^H \hat{\boldsymbol{C}}_{m,n}^{-1} \boldsymbol{g}_{m,n}|^2}{\boldsymbol{s}_{m,n}^H \hat{\boldsymbol{C}}_{m,n}^{-1} \boldsymbol{s}_{m,n} \left(1 + \boldsymbol{g}_{m,n}^H \hat{\boldsymbol{C}}_{m,n}^{-1} \boldsymbol{g}_{m,n}\right)} \underset{H_0}{\overset{H_1}{\gtrless}} \gamma_{m,n} \tag{6}$$

Assuming a non-homogeneous or non-stationary environment, the training data $\boldsymbol{Z}_{m,n}$ required by (5) and (6) has to be constantly re-estimated to match the changes in the background interference. This creates a large data overhead and may be difficult in a target-rich environment. These challenges justify the rise in popularity of SDS algorithms that use data only from the primary observations. One of the pioneering algorithms in the field is the direct data domain (D^3) approach adapted to STAP in [3]. The D^3 is a deterministic algorithm that utilises the knowledge of the spatio-temporal steering vectors $\boldsymbol{s}_{m,n}$ and $\boldsymbol{t}_{m,n}$ for a given Doppler frequency f_D to perform target detection in a non-homogeneous environment. Combining the same apriori knowledge of the shape of the STAP received target signal with the idea of approximating the optimal MF has lead to the development of statistical SDS algorithms for target detection and estimation. These approaches can form a sample correlation estimate as (4) only through the observation data set $\boldsymbol{X}_{m,n}$ [4], [5], [11]. Such an estimate was first derived in the development of the amplitude and phase estimation (APES) filter in [12]

$$\boldsymbol{Q}_{m,n} = \frac{1}{K} \boldsymbol{X}_{m,n} \boldsymbol{X}_{m,n}^H - \boldsymbol{g}_{m,n} \boldsymbol{g}_{m,n}^H \tag{7}$$

where $\boldsymbol{g}_{m,n}$ is the same as (3) with $c{=}K^{-1}$. Through the usage of (7), the maximum likelihood estimation detector (MLED) was presented in [4] as the SDS counterpart of the AMF:

$$\frac{|\boldsymbol{s}_{m,n}^H \boldsymbol{Q}_{m,n}^{-1} \boldsymbol{g}_{m,n}|^2}{\boldsymbol{s}_{m,n}^H \boldsymbol{Q}_{m,n}^{-1} \boldsymbol{s}_{m,n}} \underset{H_0}{\overset{H_1}{\gtrless}} \gamma_{m,n} \tag{8}$$

It has been shown in the same reference that (7) is an unbiased estimator of the noise and interference covariance matrix $\boldsymbol{C}_{m,n}$. This explains the evident link between the form of the TDS detector (5) and the SDS one (8). In a similar manner the generalised maximum likelihood estimation detector (GMLED) was derived as the SDS equivalent of (6) [11]:

$$\frac{|\boldsymbol{s}_{m,n}^H \boldsymbol{Q}_{m,n}^{-1} \boldsymbol{g}_{m,n}|^2}{\boldsymbol{s}_{m,n}^H \boldsymbol{Q}_{m,n}^{-1} \boldsymbol{s}_{m,n} \left(1 + \boldsymbol{g}_{m,n}^H \boldsymbol{Q}_{m,n}^{-1} \boldsymbol{g}_{m,n}\right)} \underset{H_0}{\overset{H_1}{\gtrless}} \gamma_{m,n} \tag{9}$$

In addition to requiring no training data, the MLED and GMLED algorithms have the benefit of being able to operate in any environment without prior knowledge on the structure of the background noise and interference. All they require is prior information on the structure of the target signal which in radar detection can easily be extrapolated from the form of the transmitted probing waveform.

III. Multistatic Maximum Likelihood Estimation Detector

In this section the maximum likelihood (ML) multistatic solution to the target detection problem is derived. The resulting algorithm is similar to the one presented in [7] and [8] but does not use training data. The channel-specific probability density function (pdf) of each observed data matrix $\boldsymbol{X}_{m,n}$ conditioned on the complex magnitude of the returned waveform $\alpha_{m,n}$ is given by [5, p.121]

$$f(\boldsymbol{X}_{m,n}|\alpha_{m,n}) = \left(\pi^P |\boldsymbol{C}_{m,n}|\right)^{-K} \text{etr}\left\{\boldsymbol{C}_{m,n}^{-1} \boldsymbol{M}_{m,n}^{\alpha}\right\} \tag{10}$$

where $\boldsymbol{M}_{m,n}^{\alpha}{=}\sum_{k=1}^{K}(\boldsymbol{x}_{m,n,k} - \alpha_{m,n}\boldsymbol{s}_{m,n}\boldsymbol{t}_{m,n}(k))(\boldsymbol{x}_{m,n,k} - \alpha_{m,n}\boldsymbol{s}_{m,n}\boldsymbol{t}_{m,n}(k))^H$. The dependence of the pdf on the incoming Doppler frequency is omitted. This work assumes that the geolocation-Doppler search space is discretised (e.g. [13]) and focuses on the incoming data from a single bin where the presence of a target is tested for. It is also assumed that the covariance matrices of the interference $\boldsymbol{C}_{m,n}$ are known. Furthermore, the probing signals sent from each of the transmit antennas are assumed to be ideally separable at the receiver end, thus eliminating interference between transmitters. This can be achieved by using additional modulation on the transmitted pulses from the different probing antennas or by keeping these pulses orthogonal in the frequency domain. In this work $|\bullet|$ is the determinant, $\text{etr}(\bullet){=}e^{\text{Tr}(\bullet)}$, and $\text{Tr}(\bullet)$ is the trace of the matrix $(\bullet)$. In a MIMO system, assuming that the background noise processes $\boldsymbol{N}_{m,n}$ are uncorrelated to one another, the joint pdf of the complete set of observations $\boldsymbol{X}{=}\{\boldsymbol{X}_{m,n}|m{=}1\ldots M, n{=}1\ldots N\}$ given the set of complex amplitudes $\alpha{=}\{\alpha_{m,n}|m{=}1\ldots M, n{=}1\ldots N\}$ can be represented by the product of the individual pdfs in (10). Let the joint pdf of the observation signals under hypothesis H_0 from (1) be denoted as $f_0(\boldsymbol{X})$ and under H_1 as $f_1(\boldsymbol{X})$. Then

$$f_0(\boldsymbol{X}){=}\left(\pi^{MNP}\prod_{m,n}|\boldsymbol{C}_{m,n}|\right)^{-K}\text{etr}\left\{-\sum_{m,n}\boldsymbol{C}_{m,n}^{-1}\boldsymbol{M}_{m,n}^{0}\right\} \tag{11}$$

$$f_1(\boldsymbol{X}){=}\left(\pi^{MNP}\prod_{m,n}|\boldsymbol{C}_{m,n}|\right)^{-K}\text{etr}\left\{-\sum_{m,n}\boldsymbol{C}_{m,n}^{-1}\boldsymbol{M}_{m,n}^{\alpha}\right\} \tag{12}$$

where $\boldsymbol{M}^0_{m,n}=\sum_{k=1}^{K}\boldsymbol{x}_{m,n,k}\boldsymbol{x}^H_{m,n,k}$. The dependence of (12) on the set α has been omitted for convenience. Equation (12) is linearly separable in the logarithm. Therefore, taking the derivative and minimising with respect to each individual unknown parameter $\alpha_{m,n}$ will produce $M\times N$ ML solutions for the complex amplitudes that are identical to the isolated bistatic case in [4]

$$\hat{\alpha}_{m,n}=\frac{\boldsymbol{s}^H_{m,n}\boldsymbol{C}^{-1}_{m,n}\boldsymbol{g}_{m,n}}{\boldsymbol{s}^H_{m,n}\boldsymbol{C}^{-1}_{m,n}\boldsymbol{s}_{m,n}} \tag{13}$$

This outcome is not unexpected and follows directly from the assumptions made in this work that render the $M\times N$ individual bistatic channels virtually independent. Note that (13) is the amplitude estimate of the APES filter derived in [12]. Forming the ML ratio of (12) and (11), the multistatic MLED threshold detector is derived

$$\frac{\max\limits_{\alpha} f_1(\boldsymbol{X})}{f_0(\boldsymbol{X})}=\text{etr}\left\{-\sum_{m,n}\boldsymbol{C}^{-1}_{m,n}\left(\boldsymbol{M}^{\hat{\alpha}}_{m,n}-\boldsymbol{M}^0_{m,n}\right)\right\} \tag{14}$$

where $\boldsymbol{M}^{\hat{\alpha}}_{m,n}=\sum_{k=1}^{K}(\boldsymbol{x}_{m,n,k}-\hat{\alpha}_{m,n}\boldsymbol{s}_{m,n}\boldsymbol{t}_{m,n}(k))(\boldsymbol{x}_{m,n,k}-\hat{\alpha}_{m,n}\boldsymbol{s}_{m,n}\boldsymbol{t}_{m,n}(k))^H$. The following relation from [5, p. 122]

$$\begin{aligned}\boldsymbol{M}^{\hat{\alpha}}_{m,n}=&\boldsymbol{M}^0_{m,n}-K\boldsymbol{g}_{m,n}\boldsymbol{g}^H_{m,n}\\&+K\left(\boldsymbol{g}_{m,n}-\hat{\alpha}_{m,n}\boldsymbol{s}_{m,n}\right)\left(\boldsymbol{g}_{m,n}-\hat{\alpha}_{m,n}\boldsymbol{s}_{m,n}\right)^H\end{aligned} \tag{15}$$

is plugged in (14). Using the identity $\boldsymbol{v}^H\boldsymbol{M}\boldsymbol{v}=Tr(\boldsymbol{M}\boldsymbol{v}\boldsymbol{v}^H)$ for a vector $\boldsymbol{v}$ and matrix $\boldsymbol{M}$, the ML multistatic threshold detector is obtained for the case when the covariance matrices of the background noise and interference $\boldsymbol{C}_{m,n}$ are known

$$T_{MF}=\sum_{m,n}\frac{|\boldsymbol{s}^H_{m,n}\boldsymbol{C}^{-1}_{m,n}\boldsymbol{g}_{m,n}|^2}{\boldsymbol{s}^H_{m,n}\boldsymbol{C}^{-1}_{m,n}\boldsymbol{s}_{m,n}}\underset{H_0}{\overset{H_1}{\gtrless}}\gamma \tag{16}$$

where γ is the multistatic decision threshold. The T_{MF} in (16) is the multistatic MF detector analogous to the bistatic one in (2). To obtain the multistatic MLED, the covariance matrices $\boldsymbol{C}_{m,n}$ are replaced with their SDS estimates $\boldsymbol{Q}_{m,n}$ from (7)

$$T_{M}=\sum_{m,n}\frac{|\boldsymbol{s}^H_{m,n}\boldsymbol{Q}^{-1}_{m,n}\boldsymbol{g}_{m,n}|^2}{\boldsymbol{s}^H_{m,n}\boldsymbol{Q}^{-1}_{m,n}\boldsymbol{s}_{m,n}}\underset{H_0}{\overset{H_1}{\gtrless}}\gamma \tag{17}$$

Note that the ML SDS solution (17) to the MIMO case investigated in this work is a summation of the individual single-antenna solutions for each path $\{m,n\}$ in the system. The linear separability of the multistatic detector in the sum of the bistatic ones is in accordance with the prior assumption that the individual transmit-receive channels are independent. Because (17) is a sum of $M\times N$ bistatic detectors that have the CFAR property (see [4]), it can be concluded that the multistatic MLED detector also inherits this property. A benefit of the form of the multistatic MLED detector derived here is the fact that each individual receiver can perform target estimation independently of its neighbours. The multistatic estimation is thus asynchronous which reduces the complexity of implementing the algorithm. To make the detection decision, the results from receivers can either be sent to a designated fusion centre, or the decision variable can be transmitted and updated between nodes in a round-robin fashion.

IV. Multistatic Generalised Maximum Likelihood Estimation Detector

In this section the multistatic GMLED algorithm for SDS detection is derived. The resulting solution is similar to the one from [7] and [8] but does not require training data. The pdf expressions for the set of observations $\boldsymbol{X}$ under hypotheses H_0 and H_1 are the same as (11) and (12) respectively. In the GMLED case, however, they are conditional on the set of covariance matrices $\boldsymbol{C}=\{\boldsymbol{C}_{m,n}|m=1\ldots M,n=1\ldots N\}$. These matrices are now considered to be unknown parameters which will be estimated in a ML fashion from the expression of the multistatic variable's pdf. Because these expressions are once again linearly separable (in the logarithm), the ML solution of (11) and (12) with respect to all $\boldsymbol{C}_{m,n}$ parameters is equivalent to the ML solutions for the individual likelihoods in (10). As the bistatic case has been solved in [5, p.122], the maximised multistatic pdfs take the following forms

$$\max_{\boldsymbol{C}} f_0(\boldsymbol{X})=\left((e\pi)^{MNP}\prod_{m,n}|\boldsymbol{M}^0_{m,n}|\right)^{-K} \tag{18}$$

$$\max_{\boldsymbol{C}} f_1(\boldsymbol{X}|\alpha)=\left((e\pi)^{MNP}\prod_{m,n}|\boldsymbol{M}^{\alpha}_{m,n}|\right)^{-K} \tag{19}$$

Noting that once again the conditioned likelihood (19) can be made linearly separable through taking the logarithm, the maximisation of the expression can be achieved when each of the individual terms $|\boldsymbol{M}^{\alpha}_{m,n}|$ is minimised with respect to the unknown complex amplitude $\alpha_{m,n}$. Once again due to the channel independence assumption, the solution is the same as the one provided in the bistatic GMLED derivation [5, p.122]:

$$\begin{aligned}\min_{\alpha_{m,n}}|\boldsymbol{M}^{\alpha}_{m,n}|=|\boldsymbol{Q}_{m,n}|\Bigg(&1+\boldsymbol{g}^H_{m,n}\boldsymbol{Q}^{-1}_{m,n}\boldsymbol{g}_{m,n}\\&-\frac{|\boldsymbol{s}^H_{m,n}\boldsymbol{Q}^{-1}_{m,n}\boldsymbol{g}_{m,n}|^2}{\boldsymbol{s}^H_{m,n}\boldsymbol{Q}^{-1}_{m,n}\boldsymbol{s}_{m,n}}\Bigg)\end{aligned} \tag{20}$$

$$|\boldsymbol{M}^0_{m,n}|=|\boldsymbol{Q}_{m,n}|\left(1+\boldsymbol{g}^H_{m,n}\boldsymbol{Q}^{-1}_{m,n}\boldsymbol{g}_{m,n}\right) \tag{21}$$

Forming the ratio of the maximised likelihood functions (19) and (18), the expression for the multistatic threshold detector can be obtained

$$\frac{\max\limits_{\alpha,\boldsymbol{C}} f_1(\boldsymbol{X})}{\max\limits_{\boldsymbol{C}} f_0(\boldsymbol{X})}=\left(\frac{\prod\limits_{m,n}|\boldsymbol{M}^0_{m,n}|}{\prod\limits_{m,n}\min\limits_{\alpha_{m,n}}|\boldsymbol{M}^{\alpha}_{m,n}|}\right)^K \tag{22}$$

Plugging in the relevant expressions for the determinants (20) and (21) into (22) and forming the K^{th} root of the likelihood ratio, the expression for the multistatic GMLED is obtained

$$T_G=\prod_{m,n}\frac{1+\boldsymbol{g}^H_{m,n}\boldsymbol{Q}^{-1}_{m,n}\boldsymbol{g}_{m,n}}{1+\boldsymbol{g}^H_{m,n}\boldsymbol{Q}^{-1}_{m,n}\boldsymbol{g}_{m,n}-\frac{|\boldsymbol{s}^H_{m,n}\boldsymbol{Q}^{-1}_{m,n}\boldsymbol{g}_{m,n}|^2}{\boldsymbol{s}^H_{m,n}\boldsymbol{Q}^{-1}_{m,n}\boldsymbol{s}_{m,n}}}\underset{H_0}{\overset{H_1}{\gtrless}}\nu \tag{23}$$

where ν is the multistatic decision threshold. The multistatic GMLED (23) is a product of the bistatic solutions for each path $\{m,n\}$ in the system. Each of these bistatic detectors has the CFAR property (see [5, p.61]). Therefore, the multistatic GMLED threshold detector also possesses the CFAR property.

V. Simulation Results

The multistatic MLED and GMLED algorithms were simulated and compared to their existing TDS counterparts, the multistatic AMF and GLRT respectively [7], [8]. As a benchmark, the multistatic MF from (16) was also simulated to provide an upper bound for the performance of the other four MIMO algorithms. Three antenna configurations were simulated: (i) $M{=}N{=}2$ for a small network; (ii) $M{=}N{=}4$ for a medium-sized network; (iii) $M{=}N{=}8$ for a large network. All transmit antennas and receive phased arrays are placed around the target at a random angle. The magnitudes of the returned pilots $\alpha_{m,n}$ are also chosen at random from a complex normal distribution $\mathcal{CN}(0,1)$. The formula for obtaining the Doppler frequencies of the returned pilots in the sense of MIMO radar can be found in [14, p.194]. The size of the receiver phased arrays is $P{=}10$ sensors, which is also the size of the spatial steering vector in the STAP sense. To generate the clutter in each channel, a filter is used to spatially colour the columns of an additive white Gaussian noise (AWGN) term of size $P{\times}K$. The spectrum of the clutter exhibits low-pass behaviour and is roughly shaped in accordance to the realistic model discussed in [14, pp.293-322]. The simulations consist of 10^6 Monte Carlo runs of each system for different signal-to-noise ratio (SNR) values and depict the average probability of detection P_d for each case when the probability of false alarm has been fixed to $P_f{=}10^{-2}$.

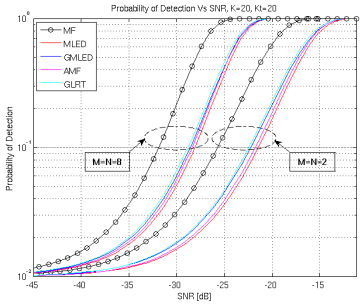

Fig. 1. Probability of Detection vs SNR for $P_f{=}10^{-2}$, $K{=}K_t{=}20$

The results of the first set of simulations are found in fig. 1. The case when $M{=}N{=}4$ has not been shown on the figure for clarity. The performance of the different transmit-receive setups is studied for $K{=}K_t{=}2P$. This case is often considered marginal in terms of the samples available for obtaining a sensible covariance matrix estimate of order P. The estimate, however, is relatively poor. Therefore the fact that the MF greatly outperforms all other algorithms in fig. 1 is anticipated. As described in [5, pp 54-66] for the bistatic SDS detection algorithms, for a low number of temporal samples K the GMLED slightly outperforms the MLED. As K increases, the performance of the two detectors becomes virtually identical. This behaviour can also be observed in the multistatic MLED and GMLED. It can also be seen on fig. 1 that the multistatic MLED and GMLED algorithms perform slightly worse than the multistatic AMF and GLRT respectively. The reason for this is the fact that all threshold detectors intrinsically form an estimate to the system SNR and then compare this number to a predefined decision variable. The TDS algorithms use K_t more observations than the SDS ones, and as a result the SNR estimate of the former is more accurate. In the current simulation the performance of the SDS algorithms is less than $0.5dB$ worse than that of their TDS counterparts which use twice the observations. This proves that the performance of the detection methods developed in this paper is comparable to existing algorithms at the benefit of using less data that is also much easier to obtain.

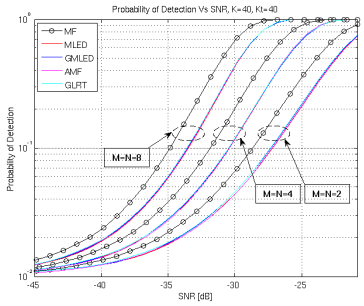

Fig. 2. Probability of Detection vs SNR for $P_f{=}10^{-2}$, $K{=}K_t{=}40$

The results of the second set of simulations are found in fig. 2. The STAP signal time frame as well as the number of training data vectors are increased to $K{=}K_t{=}4P$. This causes an improvement in the covariance matrix estimation in both the SDS (7) and the TDS (4) case. Therefore the curves for the covariance estimation algorithms are much closer to their theoretical MF upper bounds. In addition all detectors on fig. 2 perform better than their counterparts in fig. 1 which further reflects the improvement in performance as the number of observations increases. As expected, the curves for the multistatic MLED and GMLED algorithms become almost identical as K increases. In addition, the difference in performance between the TDS and SDS detectors becomes marginally small in this case. This goes to show that the AMF and GLRT do not use all the observation data that is available to them in an optimal manner. The training data is used solely for covariance estimation, while the primary observations are used for obtaining estimates to the amplitudes of the reflected pilot signals $\hat{\alpha}_{m,n}$. The MLED and GMLED use a single observation data set to do both of these tasks, which proves that the primary K vectors can aid the secondary K_t ones when it comes to TDS covariance estimation. Such

a hybrid SDS/TDS detector has been proposed in [15] in the bistatic case. A more in-depth mathematical discussion on the performance of the bistatic SDS and TDS algorithms for large observation data sets is provided in [5, pp 66] and can be extended to the multistatic case examined in this paper.

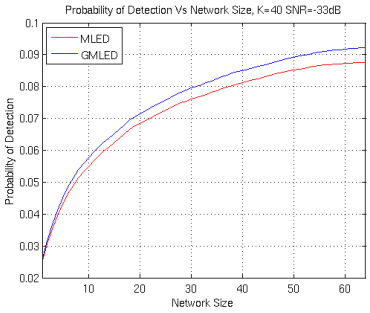

Fig. 3. Probability of Detection vs Network Size for $P_f{=}10^{-2}$, $K{=}40$, SNR$=-33dB$

In addition to the previous analysis, a simulation investigating in more detail the benefits of MIMO radar has been conducted. The results are shown in fig. 3 and depict the performance gain of the detection system as additional antennas are introduced. The network size is represented by the total numbers of independent bistatic channels $M \times N$ between the individual transmitters and receivers. At a fixed SNR of $-33dB$ and probability of false alarm $P_f{=}10^{-2}$, the detection probability of the radar network is shown. The results are averaged over 64 networks with randomly placed transmit-receive pairs. As it can be seen on fig. 3, the performance gains have a roughly logarithmic behaviour with the increased network size. This phenomenon could be explain by the fact that the benefits from the diversity that an additional independent bistatic channel provides are relative to the diversity provided by the number of already existing channels. This result is important in a real-life implementation of the system where a smaller network may be more cost-effective and thus preferred over a larger antenna array. It also shows that choosing the slightly more complex GMLED detection algorithm over the MLED one may be a more desirable solution than adding extra antennas in the system when certain performance is targeted.

VI. Conclusion

In this paper two SDS multistatic STAP algorithms for moving target detection in coloured Gaussian noise have been proposed. The detectors use a ML covariance estimation to optimally combine the results from a number of transmit-receive pairs of devices in a widely-spaced MIMO radar system and decide on the presence of a target. It has been shown that the proposed algorithms possess the highly desirable CFAR property. Numerical simulations have been conducted in order to demonstrate how the choice of the different system parameters influences the operation of the detectors. Furthermore, through these simulations it has been shown that the proposed multistatic SDS algorithms have a comparable performance to the existing multistatic TDS detectors while requiring significantly less observations. The practical difficulty of obtaining target-free training data from the nowadays target-rich environment has also been eliminated.

References

[1] F. Robey, D. Fuhrmann, E. Kelly, and R. Nitzberg, "A CFAR adaptive matched filter detector," *Aerospace and Electronic Systems, IEEE Transactions on*, vol. 28, pp. 208 –216, jan 1992.

[2] E. Kelly, "An adaptive detection algorithm," *Aerospace and Electronic Systems, IEEE Transactions on*, vol. AES-22, pp. 115 –127, march 1986.

[3] R. Adve, T. Hale, and M. Wicks, "Practical joint domain localised adaptive processing in homogeneous and nonhomogeneous environments. 2. nonhomogeneous environments," *Radar, Sonar and Navigation, IEE Proceedings -*, vol. 147, pp. 66 –74, apr 2000.

[4] E. Aboutanios and B. Mulgrew, "A STAP algorithm for radar target detection in heterogeneous environments," in *Statistical Signal Processing, 2005 IEEE/SP 13th Workshop on*, pp. 966–971, July 2005.

[5] C.-H. Lim, *Bistatic Space-Time Adaptive Processing for Ground Moving Target Indication*. PhD thesis, Engineering, The University of Edinburgh, Oct 2006. Available: http://hdl.handle.net/1842/6373.

[6] E. Fishler, A. Haimovich, R. Blum, D. Chizhik, L. Cimini, and R. Valenzuela, "MIMO radar: an idea whose time has come," in *Radar Conference, 2004. Proceedings of the IEEE*, pp. 71 – 78, april 2004.

[7] D. Bruyere and N. Goodman, "Adaptive detection and diversity order in multistatic radar," *Aerospace and Electronic Systems, IEEE Transactions on*, vol. 44, pp. 1615 –1623, oct. 2008.

[8] L. Kong, M. Yang, and B. Zhao, "Adaptive detection for shared-spectrum multistatic radar in gaussian clutter," in *Radar Conference (RADAR), 2012 IEEE*, pp. 0309 –0313, may 2012.

[9] W. Melvin, "A STAP overview," *Aerospace and Electronic Systems Magazine, IEEE*, vol. 19, pp. 19 –35, jan. 2004.

[10] L. Brennan and L. Reed, "Theory of adaptive radar," *Aerospace and Electronic Systems, IEEE Transactions on*, vol. AES-9, pp. 237 –252, march 1973.

[11] C. Lim, E. Aboutanios, and B. Mulgrew, "Training strategies for joint domain localised-space-time adaptive processing in a bistatic environment," *Radar, Sonar and Navigation, IEE Proceedings*, vol. 153, pp. 516 –524, december 2006.

[12] P. Stoica, H. Li, and J. Li, "A new derivation of the APES filter," *Signal Processing Letters, IEEE*, vol. 6, pp. 205–206, Aug 1999.

[13] W. Melvin, R. Hancock, M. Rangaswamy, and J. Parker, "Adaptive distributed radar," in *Radar Conference - Surveillance for a Safer World, 2009. RADAR. International*, pp. 1 –6, oct. 2009.

[14] G. W. Stimson, *Introduction to Airborne Radar*. SciTech Publishing, Inc., second ed., 1998.

[15] E. Aboutanios and B. Mulgrew, "Hybrid detection approach for STAP in heterogeneous clutter," *Aerospace and Electronic Systems, IEEE Transactions on*, vol. 46, pp. 1021 –1033, July 2010.

IEEE SIGNAL PROCESSING LETTERS, VOL. 22, NO. 2, FEBRUARY 2015 153

Effects of FDMA/TDMA Orthogonality on the Gaussian Pulse Train MIMO Ambiguity Function

Bogomil Shtarkalev and Bernard Mulgrew, *Fellow, IEEE*

***Abstract*—As multiple-input multiple-output (MIMO) radar gains popularity, more efficient and better-performing detection algorithms are developed to exploit the benefits of having more transmitters and receivers. Many of these algorithms are based on the assumption that the multiple waveforms used for target scanning are orthogonal to each other in fast time. It has been shown that this assumption can limit the practical detector performance due to the reduction of the area that is clear of sidelobes in the MIMO radar ambiguity function. In this work it is shown that using the same waveform with a different carrier frequency and/or delay across different transmitters ensures relative waveform orthogonality while alleviating the negative effects on the ambiguity function. This is demonstrated in a practical scenario where the probing waveforms consist of Gaussian pulse trains (GPTs) separated in frequency. An approximate theoretical model of the ambiguity is proposed and it is shown that the effects of cross-ambiguity in the MIMO system are negligible compared to the waveform autoambiguities.**

***Index Terms*—Ambiguity function, Gaussian approximation, Gaussian pulse waveforms, MIMO radar.**

I. Introduction

MULTIPLE-INPUT MULTIPLE-OUTPUT (MIMO) radar with widely-separated antennas is a widespread research area that has gained an increasing popularity over the past decade. The advantages of using multiple transmitters and receivers are numerous: higher accuracy of target localisation, higher detection rate, increased spatial and angular diversity, increased resolution [1]–[6]. Many algorithms have been proposed in the past that in theory provide very promising performance gains for larger MIMO radar networks [1]–[6]. It has been shown in theory [7] and practice [8] that these algorithms often ignore the limiting factor of the MIMO ambiguity function. These effects can degrade the performance of a radar setup that uses a number of orthogonal waveforms in fast time. In a MIMO scenario, the maximum area in the ambiguity function that can be cleared of sidelobes gets proportionally smaller as the number of such waveforms increases [7], [8]. That lowers the effective signal-to-interference and noise ratio (SINR) which in turn degrades the overall detection performance.

Manuscript received July 02, 2014; revised August 13, 2014; accepted August 14, 2014. Date of publication August 22, 2014; date of current version September 05, 2014. This work was supported by the Institute for Digital Communications at the University of Edinburgh, Selex ES and EPSRC (EP/J015180/1). The associate editor coordinating the review of this manuscript and approving it for publication was Prof. Qian He.

The authors are with the Institute for Digital Communications, School of Engineering, The University of Edinburgh, Edinburgh EH9 3JL, U.K. (e-mail: B.Shtarkalev@ed.ac.uk; B.Mulgrew@ed.ac.uk).

Color versions of one or more of the figures in this paper are available online at http://ieeexplore.ieee.org.

Digital Object Identifier 10.1109/LSP.2014.2351256

In this work it will be shown that in a widely-spaced MIMO radar system the limiting factors of the ambiguity function can be alleviated if the transmitted waveforms are separated in time and/or frequency. The concept is identical to frequency-division multiple access (FDMA) and time-division multiple access (TDMA) in wireless communication [9]. If the radar pulses are band-limited to sufficiently separated bands, the cross-ambiguity contributions to the total MIMO ambiguity are negligible. The effects have been demonstrated for a Gaussian pulse train (GPT) waveform with no delays and small Doppler shifts. An approximation to the ratio of cross-to-auto-ambiguity has been derived and simulated for the case investigated in this work. The benefits of the proposed methods come at the price of an increased bandwidth or delay in the MIMO radar system. While the derivations are performed for GPTs for convenience, guidelines for extending the approach to a wider variety of waveforms are discussed.

The rest of this paper is organized as follows. Section II provides a description of the ambiguity function and introduces the ambiguity of an infinite GPT. Section III derives the autoambiguity of a finite GPT, and Section IV derives the cross-ambiguity between two FDMA-orthogonal GPTs. In Section V the volume ratio of cross-to-autoambiguity is introduced as a metric for interference between waveforms. A Gaussian approximation to the Fejér kernel is proposed in order to derive a theoretical expression for the volume ratio of the GPT. Section VI demonstrates the viability of the proposed approximation and shows that the cross-ambiguity terms in the MIMO ambiguity function can be effectively ignored.

II. Background

Woodward's ambiguity function of a continuous narrowband signal $u(t)$ is defined as [10], [11]

$$\alpha(t,f) = \int_{-\infty}^{\infty} u\left(\tau - \frac{1}{2}t\right) u^*\left(\tau + \frac{1}{2}t\right) e^{-j2\pi f\tau} d\tau \qquad (1)$$

where the subscript $*$ denotes the complex conjugate. At $f = 0$ the integral (1) reduces to the standard time-domain autocorrelation function of $u(t)$. A waveform with a well-known ambiguity function is the Gaussian pulse (GP)

$$u_g(t) = \left(\frac{2a}{\pi}\right)^{\frac{1}{4}} \exp\left\{-at^2\right\} \qquad (2)$$

where the parameter a is related to the standard deviation σ and thus the width of the GP.

$$a = \frac{1}{2\sigma^2} \qquad (3)$$

The ambiguity of the GP is a two-dimensional Gaussian function extending in time and frequency [10], [11]

$$\alpha_g(t,f) = \exp\left(-\frac{1}{2}at^2\right)\exp\left(-\frac{\pi^2 f^2}{2a}\right) \tag{4}$$

A radar waveform consists of multiple pulses. To obtain the ambiguity function of a GPT, the following property can be used: if two waveforms are convolved in time, their ambiguity functions are convolved in time [10]. An infinite GPT is the convolution of a GP and a train of Dirac delta functions

$$u_\delta(t) = \sum_{k=-\infty}^{\infty} \delta(t - kR) \tag{5}$$

spaced at a distance R. The ambiguity function of (5) takes the well-known "bed of nails" form [10, pp.6-8]

$$\alpha_\delta(t,f) = \sum_n \sum_m \delta(t - nR)\delta(f - m/R) \tag{6}$$

The ambiguity function of an infinite GPT will be the convolution of (4) and (6) along the time axis. The spacing R is equal to the length of each GP, which this work defines as 6 times its standard deviation σ. Plugging this into (3) results in

$$a = \frac{18}{R^2} \tag{7}$$

The ambiguity function of the infinite GPT consists of shifted copies of (4) in time at $t = nR$ sampled along frequency at $f = mR^{-1}$. The waveform is reminiscent of a "bed of razors" which are infinitely long and infinitesimally wide.

III. Finite Gaussian Pulse Train Ambiguity

In a real scenario a radar transmits a finite number of pulses. Consider a GPT of K consecutive GPs. It is the convolution of (2) and a train of K equally-spaced Dirac delta functions.

$$u_{K\delta}(t) = \frac{1}{\sqrt{K}} \sum_{k=0}^{K-1} \delta(t - kR) \tag{8}$$

The normalising constant in (8) ensures that the energy in the waveform remains unity. The ambiguity function of (8) can be calculated through direct evaluation of the integral in (1). The result is a symmetric sum of Dirac delta functions along the time axis and a sum of exponentials along frequency

$$\begin{aligned}\alpha_{K\delta}(t,f) = \frac{1}{K} \sum_{p=-K+1}^{0} \delta(t - pR) \sum_{k=0}^{K+p-1} e^{-j2\pi fkR} \\ + \frac{1}{K} \sum_{p=1}^{K-1} \delta(t - pR) \sum_{k=p}^{K-1} e^{-j2\pi fkR}\end{aligned} \tag{9}$$

To facilitate the analysis, define the following expression

$$D_n(x) = \frac{\sin(\pi nx)}{\sin(\pi x)} \tag{10}$$

which is a special case of the Dirichlet kernel function. The formula for a geometric series of exponentials is

$$\sum_{k=0}^{K-1} e^{-j2\pi fkR} = D_K(fR)e^{-j\pi f(K-1)R} \tag{11}$$

The volume of the ambiguity function in a given area is used as a measure of waveform orthogonality in MIMO radar detection [7]. Thus it can limit the performance of MIMO radar. The normalized ambiguity of the finite GPT is obtained after convolving (4) and (9) in time and through using (11)

$$|\alpha_{Kg}(t,f)| = \frac{1}{K} \sum_{k=-K+1}^{K-1} \alpha_g(t - kR, f)|D_{K-|k|}(fR)| \tag{12}$$

As the number of pulses K approaches infinity, the Dirichlet kernel (10) becomes an arbitrarily close approximation to an infinite Dirac delta train in frequency, and the ambiguity function takes the form described at the end of Section II. The volume of the ambiguity function $\alpha(t,f)$ in a region A is

$$V(A) = \int_A |\alpha(t,f)|^2 df dt \tag{13}$$

Due to the shape of $\alpha_g(t,f)$ and since the distance R is equal to 6σ, the cross-terms when squaring the right hand side of (12) involve Gaussian tails and can be ignored. Thus the following approximation can be made

$$|\alpha_{Kg}(t,f)|^2 \approx \frac{1}{K^2} \sum_{k=-K+1}^{K-1} \alpha_g(t - kR, f)^2 F_{K-|k|}(fR) \tag{14}$$

$F_n(x)$ is the Fejér kernel defined here as (10) squared.

$$F_n(x) = \frac{\sin(\pi nx)^2}{\sin(\pi x)^2} \tag{15}$$

Essentially (14) ignores the tail contributions from neighbouring GPs to the peaks centred around $t = kR$. The volume of the ambiguity of the GPT in an area A around the origin is

$$V^o_{Kg}(A) = \frac{1}{K^2} \sum_k \int_A \alpha_g(t - kR, f)^2 F_{K-|k|}(fR) df dt \tag{16}$$

The limits of the sum in (16) have been omitted. Usually the aim is to make the volume as close to the ideal case $V(A) = \delta(t)\delta(f)$ as possible, and thus small regions A around the origin are considered. The contribution to such a region will come from no more than the set $k \in \{-1, 0, 1\}$ in (16).

IV. Waveform Cross-Ambiguity in a Multiple Access MIMO Scenario

The waveforms in a MIMO radar scenario are usually considered orthogonal and ideally separable [1]–[5]. In reality this is not achievable; however, there are transmission schemes similar to FDMA and TDMA which result in low cross-correlation waveforms. Thus the waveforms are "orthogonal" in frequency or time. Consider the GP (2) and an interferer separated in frequency by an offset f_Δ and in time by t_Δ

$$u_i(t) = \left(\frac{2a}{\pi}\right)^{\frac{1}{4}} e^{-a(t-t_\Delta)^2} e^{-j2\pi f_\Delta t} \tag{17}$$

The duration and bandwidth of (2) and (17) are the same. The cross-ambiguity between the two waveforms is defined as

$$\chi_g(t,f) = \int_{-\infty}^{\infty} u_g\left(\tau - \frac{1}{2}t\right) u_i^*\left(\tau 0 + \frac{1}{2}t\right) e^{-j2\pi f\tau} d\tau \tag{18}$$

One can either solve the integral (18) or use the fact that the pulse (17) is (2) convolved in time with $\delta(t-t_\Delta)$ and in frequency with $\delta(f-f_\Delta)$ to obtain the cross-ambiguity

$$\chi_g(t,f) = e^{-j\phi} \quad \exp\left(-\frac{a(t-t_\Delta)^2}{2}\right) \exp\left(-\frac{\pi^2(f-f_\Delta)^2}{2a}\right) \tag{19}$$

where ϕ is a time-frequency phase term. As expected, (19) is simply a shifted version of (4) in time and frequency.

$$|\chi_g(t,f)| = |\alpha_g(t-t_\Delta, f-f_\Delta)| \tag{20}$$

For simplicity it is assumed that each GPT contains K pulses. Following the approach in Section III, the normalized cross-ambiguity of two GPTs offset in time and frequency is

$$|\chi_{Kg}(t,f)| = \frac{1}{K} \sum_{k=-K+1}^{K-1} |\chi_g(t-kR,f) D_{K-|k|}((f-f_\Delta)R)| \tag{21}$$

The approximation to the squared magnitude is once again

$$|\chi_{Kg}(t,f)|^2 \approx \frac{1}{K^2} \sum_{k=-K+1}^{K-1} |\chi_g(t-kR,f)|^2 F_{K-|k|}((f-f_\Delta)R) \tag{22}$$

The formula for the volume of (22) is the same as (16) with the area A centred around (t_Δ, f_Δ) instead of (0,0). The Fejér kernel is $1/R$-periodic. Thus most of the volume of (22) is contained around the points $(kR-t_\Delta, n/R-f_\Delta)$ where n is an integer and k is within the limits given in the sums above.

V. Ambiguity Volume Ration in a Multiple Access MIMO Scenario

A. Volume Ratio in an FDMA Scenario

The aim of orthogonal waveform design is to reduce the volume of the cross-ambiguity (22) around the origin. The worst-case scenario is when the waveforms are offset by a multiple of R in time and $1/R$ in frequency. The bandwidth of the GP (2) can be obtained through its Fourier transform

$$U_g(f) = \left(\frac{2a}{\pi}\right)^{\frac{1}{4}} \exp\left\{-\frac{f^2\pi^2R^2}{18}\right\} \tag{23}$$

If the 6σ width rule is also applied to (23), the double-sided width of the spectrum of a GP is

$$B_W = \frac{18}{\pi R} \approx \frac{6}{R} \tag{24}$$

This is 6 times the rule of thumb $B_W \approx 1/R$ but renders the spectrum of the GP practically band-limited. Under this assumption, the width of the spectrum of a GPT will not exceed (24). In an FDMA system the channel separation will usually be at least equal to the channel width. Therefore one can assume $f_\Delta \geq B_W$. Also assume that the Doppler shifts of the waveforms are small relative to their bandwidths to eliminate inter-channel interference. The 6σ width of the ambiguity $|\alpha_g(f,t)|^2$ in frequency is also B_W. The worst-case scenario is $f_\Delta = 6/R$, where also the Fejér kernel peaks.

An FDMA system is considered here, but the results can be extended to TDMA. Thus it is assumed that no time delays between waveforms occur ($t_\Delta = 0$). In a MIMO system with M transmitters and N receivers the total ambiguity is defined as the sum of all channel cross- and auto-ambiguities [7], [12]

$$|\chi_{MN}(t,f)|^2 = \sum_{m=1}^{M}\sum_{n=1}^{N} |\chi_{mn}(t,f)|^2 \tag{25}$$

The aim to reduce cross-ambiguities means that (25) can reduce to the sum of autoambiguities. Thus in this work the volume ratio between the cross- and auto-ambiguity of waveforms is introduced as a measure of self-interference in MIMO radar. The volume ratio is investigated in a small rectangular region A around the origin where only the $k=0$ terms contribute significantly. The volume ratio reduces to

$$V_r = \frac{\int \exp\left(-\frac{\pi^2(f-f_\Delta)^2}{a}\right) F_K((f-f_\Delta)R)df}{\int \exp\left(-\frac{\pi^2 f^2}{a}\right) F_K(fR)df} \tag{26}$$

since the integral with respect to time is the same in the numerator and denominator. The integration of multiplications of Gaussian and sinusoid functions in (26) can only be done numerically. A theoretical result could be obtained if the Fejér kernel is approximated by a Gaussian function.

B. Fejér Kernel Gaussian Approximation

The Fejér kernel in (15) is a $1/R$-periodic non-negative function. Consider one period of (15) centred around the origin. It takes the form of a rapidly decaying oscillation where the first zero-crossing is at $f = \pm 1/n$. The mainlobe of the Fejér kernel can thus be approximated by a Gaussian with a $6\sigma_f$ width of $2/n$. Consider the Fejér kernel from (26). The signal is scaled by R and shifted by f_Δ. The periodicity of the kernel will be represented in the approximation as an infinite sum of Gaussian functions. The approximation is therefore

$$\tilde{F}_K((f-f_\Delta)R) = \sum_n K^2 \exp\left(-\frac{9}{2}K^2\left(f-f_\Delta-\frac{n}{R}\right)^2R^2\right) \tag{27}$$

Plugging (27) in (26), the expression inside the integral is a sum of products of two Gaussian functions. Each of these products is Gaussian with mean $\mu_c(n)$ and variance σ_c^2[13]

$$\mu_c(n) = f_\Delta + \mu_p(n) \tag{28}$$

$$\mu_p(n) = 9K^2R\sigma_c^2 n \tag{29}$$

$$\sigma_c^2 = \frac{9}{R^2((3\text{ K})^2+\pi^2)} \tag{30}$$

where $\mu_p(n)$ are the means in the denominator of (26). Consider a rectangular symmetric region around the origin $\{|t| \leq t_b, |f| \leq f_b\}$. For $t_b < R/2$ only the ambiguity around $k=0$ is considered. The volume ratio approximation is shown in

$$\begin{aligned}\tilde{V}_r(f_b) &= \frac{\sum_n \int_{-f_b}^{f_b} \exp\left(-\frac{(f-\mu_c(n))^2}{2\sigma_c^2}\right)\exp\left(-\frac{\pi^2\mu_p^2(n)}{a}\right)df}{\sum_n \int_{-f_b}^{f_b} \exp\left(-\frac{(f-\mu_p(n))^2}{2\sigma_c^2}\right)\exp\left(-\frac{\pi^2\mu_p^2(n)}{a}\right)df} \\ &= \frac{\sum_n \exp\left(-\frac{\pi^2\mu_p^2(n)}{a}\right)\left[\text{erf}\left(\frac{f_b+\mu_c(n)}{\sigma_c}\right)-\text{erf}\left(-\frac{f_b-\mu_c(n)}{\sigma_c}\right)\right]}{\sum_n \exp\left(-\frac{\pi^2\mu_p^2(n)}{a}\right)\left[\text{erf}\left(\frac{f_b+\mu_p(n)}{\sigma_c}\right)-\text{erf}\left(-\frac{f_b-\mu_p(n)}{\sigma_c}\right)\right]}\end{aligned} \tag{31}$$

where each contributing factor along the frequency axis is scaled accordingly. The sum over the integer n in (31) represents the contributions of the different Gaussian shapes along the frequency axis to the volume in the area A. As usually this area of interest is small, only a few of the contributors around $n = 0$ are enough to represent the whole sum.

VI. Simulations

A small MIMO radar system with two FDMA-orthogonal GPT waveforms has been simulated. The length of each individual GP is $R = 2ms$, and the bandwidth is $B_W = 3kHz$. The worst-case scenario of $f_\Delta = 3kHz$ is investigated. Fig. 1 shows an example of a GPT ambiguity (12) at $t = 0$ alongside its approximation (14) with the Gaussian model (27) for the Fejér kernel. Due to the nature of the fitting described in Section V-B, the model predicts the behaviour of the ambiguity well at the mainlobes of the Fejér kernel. All sidelobes outside the mainlobes, however, are ignored by the model. Thus it is expected for the approximate model of the volume ratio (31) to also best match the theoretical values around the peaks of the Fejér kernel. This can be seen in the results in Fig. 2 where the theoretical and actual volume ratios are shown for GPTs of $K = 4$ and $K = 40$ pulses. The simulated volume ratio (26) is calculated through numeric integration in a rectangular area A bounded by $t_b = 1ms$. The bound in frequency f_b is varied along the x-axis in Fig. 2. As predicted, the theoretical model closely approximates the volume ratio (26) around the points n/R where the Fejér kernel peaks. Between the mainlobes the theoretical model underestimates the volume ratio since it ignores the sidelobes. The general behaviour of the volume ratio is relatively well predicted through the proposed estimator (31) which does not involve numeric integration. The results in Fig. 2 show that the volume of the cross-ambiguity function in a rectangular area centred at the origin of the range-Doppler space is at least $40dB$ lower than the volume of the autoambiguity in the same area. Therefore in the system (25) with M transmitters and N receivers, the total ambiguity can be approximated as strictly the sum of the autoambiguities

$$|\chi_{MN}(t,f)|^2 \approx \sum_{m=1}^{M} |\chi_{mm}(t,f)|^2 \tag{32}$$

This reflects the waveform orthogonality achieved through FDMA. The tradeoff is the increased bandwidth of the system used by the additional channels. A MIMO system of M orthogonal waveforms requires a bandwidth of MB_W. This limits the FDMA waveform design to small radar networks.

The analysis in this work is performed on GPTs for convenience. Note that the approximations (14) and (22) hold for any pulse with ambiguity $\alpha(t,f)$ that can be neglected outside of a region R along the time axis. However, one must ensure the spacing between pulses in (8) is also greater than R. If the pulses forming a waveform meet these conditions, the autoambiguity at the origin and around f_Δ as well as the Fejér kernel weights at those points can be used as a rough estimate of the behaviour of the waveform volume ratio. Note that the Gaussian approximation to the Fejér kernel (27) is independent of the shape of the transmitted waveforms.

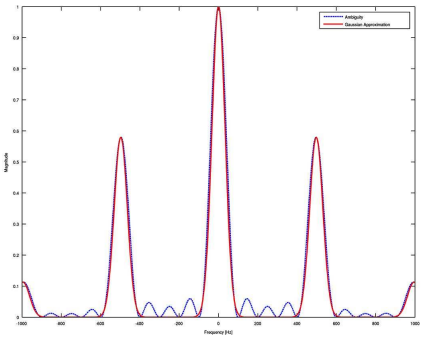

Fig. 1. Autoambiguity of a 5-pulse waveform at $t = 0$ with Gaussian approximation to the Fejér kernel.

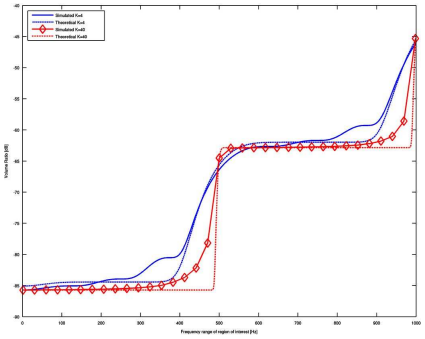

Fig. 2. Volume ratio of cross-ambiguity to autoambiguity in a rectangular region A for FDMA-orthogonal radar waveforms.

VII. Conclusion

In this work the volume of the ambiguity and cross-ambiguity function of GPT waveforms separated in frequency has been analyzed. The waveforms could be but are not limited to pilots in an FDMA MIMO radar scenario where through increase of bandwidth, interference between different transmitters is minimized. A theoretical model for the volume ratio of the cross- and auto-ambiguity functions is proposed that is inexpensive in terms of processing power and can predict the amount of interference between waveforms in the Doppler-range ambiguity space. Through this model it is demonstrated that if channels in an FDMA MIMO radar scenario are sufficiently separated in frequency, virtually no interference between transmitters occurs in the MIMO ambiguity function.

Acknowledgment

The authors would like to thank the associate editor, Prof. Q, He, and the anonymous reviewers for their comments that helped improve the final version of this manuscript.

REFERENCES

[1] E. Fishler, A. Haimovich, R. Blum, D. Chizhik, L. Cimini, and R. Valenzuela, "MIMO radar: An idea whose time has come," in *2004 Proc. IEEE Radar Conference*, Apr. 2004, pp. 71–78.

[2] A. Haimovich, R. Blum, and L. Cimini, "MIMO radar with widely separated antennas," *IEEE Signal Process. Mag.*, vol. 25, no. 1, pp. 116–129, 2008.

[3] W. Melvin, R. Hancock, M. Rangaswamy, and J. Parker, "Adaptive distributed radar," in *2009 RADAR. Int. Radar Conf. Surveillance for a Safer World*, Oct. 2009, pp. 1–6.

[4] D. Bruyere and N. Goodman, "Adaptive detection and diversity order in multistatic radar," *IEEE Trans. Aerosp. Electron. Syst.*, vol. 44, no. 4, pp. 1615–1623, Oct. 2008.

[5] L. Kong, M. Yang, and B. Zhao, "Adaptive detection for shared-spectrum multistatic radar in Gaussian clutter," in *2012 IEEE Radar Conf. (RADAR)*, May 2012, pp. 0309–0313.

[6] B. Shtarkalev and B. Mulgrew, "Multistatic single data set target detection in unknown coloured Gaussian interference," in *2013 IEEE Radar Conf. (RADAR)*, 2013, pp. 1–5.

[7] Y. Abramovich and G. J. Frazer, "Bounds on the volume and height distributions for the MIMO radar ambiguity function," *IEEE Signal Process. Lett.*, vol. 15, pp. 505–508, 2008.

[8] G. Frazer, Y. Abramovich, and B. Johnson, "MIMO radar limitations in clutter," in *2009 IEEE Radar Conference*, 2009, pp. 1–5.

[9] I. Glover and P. Grant, *Digital Communications*, 3rd ed. ed. Upper Saddle River, NJ, USA: Pearson/Prentice-Hall, 2010.

[10] P. M. Woodward, "Radar ambiguity analysis," DTIC Doc. Tech. Rep.,, 1967.

[11] D. Swick, A review of narrowband ambiguity functions DTIC Document, 1970, tech. rep.,.

[12] G. San Antonio, D. Fuhrmann, and F. Robey, "MIMO radar ambiguity functions," *IEEE J. Sel. Topics Signal Process.*, vol. 1, no. 1, pp. 167–177, 2007.

[13] P. A. Bromiley, Products and convolutions of Gaussian distributions Imag. Sci. Biomed. Eng. Div. Med. Sch., Univ. Manchester, Manchester, U.K., Int. Rep. Tina Memo 2003-003, Nov. 2003.

Signal Processing 115 (2015) 130–143

Contents lists available at ScienceDirect

Signal Processing

journal homepage: www.elsevier.com/locate/sigpro

Review

Multistatic moving target detection in unknown coloured Gaussian interference

Bogomil Shtarkalev*, Bernard Mulgrew

Institute for Digital Communications, The University of Edinburgh, Edinburgh EH9 3JL, United Kingdom

ARTICLE INFO

Article history:
Received 8 December 2014
Received in revised form
8 March 2015
Accepted 1 April 2015
Available online 16 April 2015

Keywords:
Doppler radar
Multiple-input multiple-output (MIMO)
Target detection
Reduced-rank space–time adaptive processing (STAP)
Heterogeneous clutter
Gaussian approximation

ABSTRACT

One of the main interferers for a Doppler radar has always been the radar's own signal being reflected off the surroundings. This creates the problem of searching for a target in a coloured noise and interference environment. Traditional space–time adaptive processing (STAP) deals with the problem by using target-free training data to study this environment and build its characteristic covariance matrix. The maximum likelihood estimation detector (MLED) and its generalised counterpart (GMLED) are two reduced-rank STAP algorithms that eliminate the need for training data when mapping the statistics of the background interference. In this work the MLED and GMLED solutions to a multistatic scenario are derived. A hybrid multiple-input multiple-output (MIMO) system where each receiver is a coherent STAP radar has been employed. The focus of the work is the spatial diversity provided by the wide separation of the individual transmitter and receiver platforms. It is proven that this configuration does not affect the constant false alarm rate (CFAR) property of the bistatic radar case. A Gaussian approximation to the statistics of the multistatic algorithms is derived in order to provide a more in-depth analysis. The viability of the theoretical models and their approximations are tested against a numerical simulation.

1. Introduction

Multiple-input multiple-output (MIMO) radar with widely separated antennas has gained an increasing popularity over the past decade. The advantages of using multiple transmitters and receivers are numerous: higher accuracy of target localisation, higher detection rate under a certain false alarm probability, increased spatial and angular diversity, increased resolution [1–8]. All the benefits come at the cost of the additional elements in the system and the higher processing power that is required to obtain and utilise their observations. Apart from deliberate jamming techniques, ground clutter reflections are usually the strongest interferers for Doppler radar. In the MIMO case this is likely to cause an even more significant problem due to the additional probing signals and their reflections present in the system. A well-known limitation of MIMO radar with fast-time orthogonal waveforms is the reduction of the region clear of sidelobes in the total ambiguity function [9,10]. This phenomenon has the potential to degrade the expected theoretical performance of a MIMO detector.

In this paper two single data set (SDS) [11–22,8] MIMO algorithms for target detection in coloured Gaussian clutter are presented. The strength of the algorithms is that they require neither prior knowledge of the spectral support or power of the background interference as in [18] nor access to secondary data as in [23–26] and thus can operate blindly in any environment. Moreover, in a heterogeneous environment there is no secondary data for

* Corresponding author. Tel.: +44 131 6505655.
E-mail addresses: b.shtarkalev@ed.ac.uk (B. Shtarkalev), b.mulgrew@ed.ac.uk (B. Mulgrew).

http://dx.doi.org/10.1016/j.sigpro.2015.04.001
0165-1684/

covariance estimation, thus leaving SDS detection as the only viable option.

Each receiver platform in the proposed algorithms operates coherently using the space–time adaptive processing (STAP) technique which boosts radar performance when dealing with ground clutter returns [27]. However, the main focus of this work is not on the coherent processing at each unit but rather on the cooperation between multiple widely spaced transmitters and STAP receivers as in [5]. Thus the maximum likelihood (ML) estimation and detection of a single target in such a multistatic scenario is derived where the whole radar network reaches a joint detection decision.

The proposed algorithms draw multiple low-rank snapshots from the observations of each STAP range gate. This greatly reduces the computational load associated with estimating and inverting the full STAP interference correlation matrix. Further rank-reduction of the algorithm can be achieved through the subspace projection methods proposed in [21,22].

The main contribution of this paper is the derivation of an approximate model for the statistics of the proposed MIMO detection algorithms. Extensive statistical analysis of the bistatic case has been derived and presented in [14,12,15]. As discussed in [23–26], the challenges associated with the theoretical analysis of mono/bistatic target detectors are compounded in multistatic widely spaced MIMO. Even when the individual bistatic paths (or channels) are mutually independent, it is unlikely that the corresponding general multistatic solutions exist in closed form [23–26,20]. In [24,26] a specific closed-form expression is provided for the pdf of a multistatic detector when no target is present in the system, and thus the multistatic probability of false alarm is derived. However, the corresponding derivation for the pdf and detection probability in the presence of targets is a problem of higher complexity that has not been solved. In this paper a methodology is proposed for deriving approximate expressions for probability of false alarm and detection for widely spaced MIMO systems. The methodology is illustrated in detail for the proposed SDS algorithms and could easily Fbe extended to the theoretical analysis of other multistatic target detectors such as [23–26]. The key to obtaining the approximations is the application of the central limit theorem (CLT), or more precisely Lindeberg's condition [28, p. 307], to the summation of bistatic detectors. This approximation enables the link between the radar operational parameters and the probabilities of detection and false alarm to be made.

The performance of the proposed detectors and the validity of the approximate statistical analysis are tested. It has been shown that the proposed detectors exhibit the highly desirable constant false alarm rate (CFAR) property. The two target detection algorithms have been simulated in a scenario involving a mixture of multiple transmit antennas and multiple receive phased arrays. A number of numerical tests have been performed that validate the approximate statistical analysis of the algorithms proposed in this paper. The advantages of the MIMO system with the increasing number of antennas in terms of detection probabilities are shown in the results.

Section 2 of this paper states the problem and assumptions of this work and provides a brief background on the most widely used target detection schemes currently available. Sections 3 and 4 provide the derivations of the two multistatic SDS radar detection algorithms proposed in this paper. Section 5 contains the statistical analysis of the detectors, the proposed Gaussian approximations. Section 6 contains the results of the numerical simulations and a discussion of these results. Section 7 presents the conclusions drawn from the work.

2. Problem formulation and background

This work focuses on widely separated (multistatic) radar detection, sometimes referred to as statistical MIMO radar. Consider a setup consisting of M transmit antennas and N receive arrays that probe an area for the presence of a moving target. Each array consists of P_T closely spaced elements that can perform coherent processing and STAP detection. However, as coherent processing is not the main focus of this work, each array is considered as a single unit, and the aim is to combine the detection capabilities of multiple widely separated such units. For simplicity and without loss of generality the receivers are assumed to be uniform linear arrays (ULA). Therefore each transmit–receive pair here forms a standard bistatic STAP system; this setup is often referred to as a single-input multiple-output (SIMO) coherent radar [29,30]. The term MIMO here is reserved for a multistatic setup (Fig. 1) and refers to non-coherent processing of a number of widely spaced STAP phased array receivers. Each of the ULA units collects K_T slow-time pulses per STAP range gate. A sliding window over the observation samples is used to produce K snapshots containing independent clutter observations, each one consisting of a total of P spatio-temporal samples (Fig. 2 top). The values of K and P can be arbitrary and chosen to suit a specific radar setup and clutter conditions, e.g. in clutter with heavy correlation, the sliding window can skip over samples and trade available data for estimation accuracy, the window can contain more than once slow-time pulse or only a part of a slow time pulse, etc.

Once obtained from the sliding window, the snapshots are vectorised by stacking their columns on top of each other and labelled as $\boldsymbol{x}_{m,n,k}$, $k=1\ldots K$. The index $\{m,n\}$ signifies the path between the mth transmitter and the nth receiver. Throughout this work these different bistatic paths will be referred to as "channels." Let the observation vectors be arranged as the columns of the observation matrix $\boldsymbol{X}_{m,n}$ (Fig. 2 bottom). If the complex amplitude of the returned signal in a channel is $\alpha_{m,n}$, the signal model for the observations in each individual bistatic STAP channel is the following:

$$\boldsymbol{X}_{m,n}=\alpha_{m,n}\boldsymbol{s}_{m,n}\boldsymbol{t}_{m,n}^{T}+\boldsymbol{N}_{m,n} \tag{1}$$

The superscript T indicates the transpose operator. The vectors $\boldsymbol{s}_{m,n}$ and $\boldsymbol{t}_{m,n}$ will be referred to as the spatial steering and the temporal steering vector respectively, and the matrix $\boldsymbol{N}_{m,n}$ is a combined term for the noise and interference in each channel. The spatial steering vector $\boldsymbol{s}_{m,n}\in\mathbb{C}^{P\times 1}$ is the template that the returned signal produces in each observation snapshot. It depends on the Doppler frequency of the

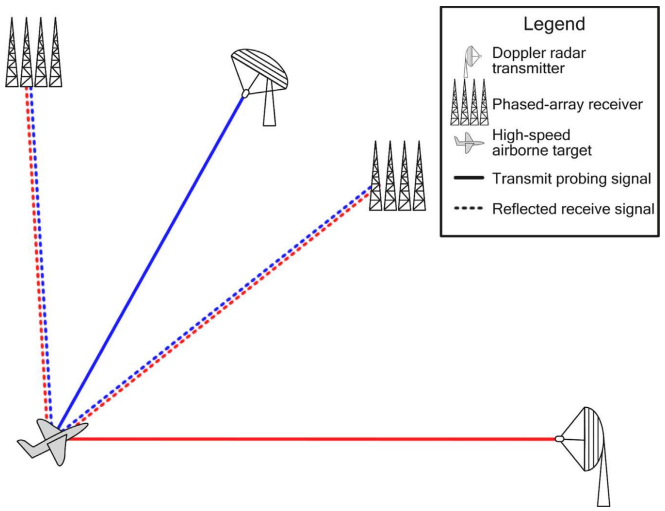

Fig. 1. Example of a 2-transmitter 2-receiver MIMO system.

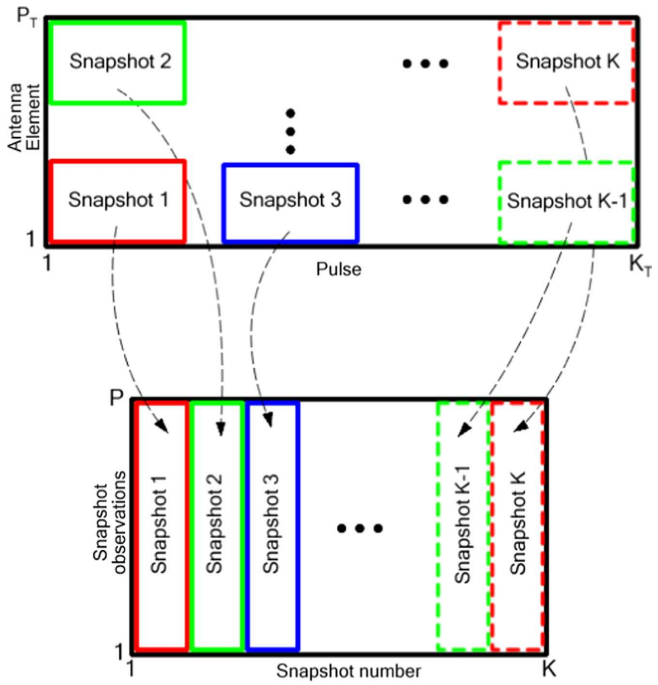

Fig. 2. Extracting snapshots containing iid clutter contributions with a sliding window over the STAP range gate (top) and vectorising them to produce the observation matrix $\boldsymbol{X}_{m,n}$ (bottom).

incoming signal as well as the receiver ULA geometry and orientation. The temporal steering vector $\boldsymbol{t}_{m,n} \in \mathbb{C}^{K\times 1}$ indicates the complex phase relations between the K individual observation snapshots [12–16].

As already mentioned, the observation snapshots in (1) are obtained from windowing and rearranging the STAP samples of the cell under test (CUT) such that their clutter contributions are independent. This can be achieved through the choice of snapshots size P and snapshot number K parameters. It is likely that in reality some residual correlation between snapshot clutter will remain, but this will be neglected for the purpose of derivation in this work. Therefore the columns of the noise and interference matrix are assumed to be independent and identically distributed (iid) complex zero-mean Gaussian $\boldsymbol{n}_{m,n,k} \sim \mathcal{CN}_P(\boldsymbol{0}, \boldsymbol{C}_{m,n})$, each with a different autocorrelation matrix $\boldsymbol{C}_{m,n}$. The interference from channel to channel is also assumed to be independent. Because the snapshots size P is significantly smaller than the total number of observations in the CUT, the STAP signal model used here reduces the size of the correlation matrix that is estimated [31].

In addition to the interference, the pulses coming from the different transmitters in the system are also assumed to be nearly orthogonal to each other (low cross-correlation). A well-documented problem that arises from the simultaneous transmission of M ideal orthogonal waveforms at the same time and on the same bandwidth is the reduction of the clear region in the range-Doppler MIMO ambiguity function by a factor of M [9,10]. At the expense of additional bandwidth or delay, this problem can be alleviated by utilising time division multiple access (TDMA) or a frequency division multiple access (FDMA) methods for providing low cross-correlation between different transmit waveforms. As demonstrated in [32], such schemes result in negligible inter-channel interference between the different waveforms in the multistatic radar scenario. These additional resources are traded for the spatial diversity that MIMO radar provides in target detection. Finally, this paper assumes that the range-Doppler search space has been discretised (e.g. [33]), and the proposed detectors operate on each separate bin of the grid. Thus in the derivations that follow the Doppler frequencies $f^{D}_{m,n}$ and the array spatial response frequencies $f^{sp}_{m,n}$ are assumed to be known as they come from a specific range-Doppler CUT.

For the time being consider the signal model in (1) and only a single channel. Thus the index $\{m,n\}$ will be dropped for convenience for now. A bistatic STAP detection algorithm receives the observations $\boldsymbol{X}$ and decides between two hypotheses for their origin

$$H_0: \boldsymbol{X} = \boldsymbol{N}$$
$$H_1: \boldsymbol{X} = \alpha \boldsymbol{s}\boldsymbol{t}^T + \boldsymbol{N} \tag{2}$$

The optimum STAP pre-detection filter derived in [34] and normalised to exhibit the CFAR property is

$$\boldsymbol{w} = \frac{\boldsymbol{C}^{-1}\boldsymbol{s}}{\boldsymbol{s}^H\boldsymbol{C}^{-1}\boldsymbol{s}} \tag{3}$$

which is also known as the matched filter (MF). The superscript H indicates the Hermitian transpose. In a STAP system this filter is applied to the K individual observation snapshots, and the results are combined in the post-processing phase. A more efficient method is to combine the observations in the pre-detection stage in the case of iid data. The amplitude and phase estimation (APES) filter presented in [35] proposes the STAP coherent sample mean vector for the observation data that can perform this task given the current observation model (1)

$$\boldsymbol{g} = \frac{1}{K}\boldsymbol{X}\boldsymbol{t}^* \tag{4}$$

It is assumed that the 2-norm of the temporal steering vector is $|\boldsymbol{t}|^2 = K$, and the superscript $*$ signifies the complex conjugate operator. Eq. (4) can also be seen as a narrow filtering operation that maximises the response to a certain space–time steering vector $\boldsymbol{t}$. The weighted output $\boldsymbol{w}^H\boldsymbol{g}$ is then used in a power threshold-comparison scheme in order to choose the more viable hypothesis from which the observations originated:

$$\frac{|\boldsymbol{s}^H\boldsymbol{C}^{-1}\boldsymbol{g}|^2}{\boldsymbol{s}^H\boldsymbol{C}^{-1}\boldsymbol{s}} \underset{H_0}{\overset{H_1}{\gtrless}} \gamma \tag{5}$$

Usually the covariance matrix $\boldsymbol{C}$ of the noise and interference is not known. Traditional sample matrix inversion (SMI) detection algorithms have assumed the availability of a secondary data set $\boldsymbol{Z}$ consisting of K_t target-free observation vectors of size $\mathbb{C}^{P\times 1}$ from which the sample covariance matrix estimate can be built:

$$\widehat{\boldsymbol{C}} = \frac{1}{K_t}\boldsymbol{Z}\boldsymbol{Z}^H \tag{6}$$

Using (6) in (3) to replace the covariance matrix gives the adaptive matched filter (AMF) threshold detector [36]:

$$\frac{|\boldsymbol{s}^H\widehat{\boldsymbol{C}}^{-1}\boldsymbol{g}|^2}{\boldsymbol{s}^H\widehat{\boldsymbol{C}}^{-1}\boldsymbol{s}} \underset{H_0}{\overset{H_1}{\gtrless}} \gamma \tag{7}$$

Assuming that the covariance matrix $\boldsymbol{C}$ is unknown from the start and minimising over it in the process, Kelly derived his generalised likelihood ratio test (GLRT) [37]:

$$\frac{|\boldsymbol{s}^H\widehat{\boldsymbol{C}}^{-1}\boldsymbol{g}|^2}{\boldsymbol{s}^H\widehat{\boldsymbol{C}}^{-1}\boldsymbol{s}(1+\boldsymbol{g}^H\widehat{\boldsymbol{C}}^{-1}\boldsymbol{g})} \underset{H_0}{\overset{H_1}{\gtrless}} \gamma \tag{8}$$

Because these algorithms rely on the availability of a secondary training data set, they are commonly known as two-data set (TDS) detectors [37,36]. In recent years SDS detection algorithms have gained an increasing popularity [11–22]. The reason for that is the fact that in a non-homogeneous or non-stationary environment the observation-free training data $\boldsymbol{Z}$ required by traditional algorithms needs to be constantly re-estimated to match the changes in the background noise and interference. This creates a large data overhead, and given the ever-increasing air traffic nowadays, continuously obtaining target-free training observations may become difficult. With an SDS of observations $\boldsymbol{X}$, a system can construct a sample correlation estimate of the data in the same manner as (6):

$$\widehat{\boldsymbol{R}} = \frac{1}{K}\boldsymbol{X}\boldsymbol{X}^H \tag{9}$$

Under H_0 the matrix (9) is an estimate to the central noise covariance matrix $\boldsymbol{C}$ similar to (6), while under H_1 it is a non-central estimate of $\boldsymbol{C}$ offset by the additional contribution $|\alpha|^2\boldsymbol{s}\boldsymbol{s}^H$ from the target. The APES filter [35] shown in (10) can be used to derive an SDS estimate to the central noise

covariance matrix from (9)

$$\boldsymbol{w}^{APES} = \frac{\boldsymbol{Q}^{-1}\boldsymbol{s}}{\boldsymbol{s}^H\boldsymbol{Q}^{-1}\boldsymbol{s}} \tag{10}$$

$$\boldsymbol{Q} = \widehat{\boldsymbol{R}} - \boldsymbol{g}\boldsymbol{g}^H \tag{11}$$

The sample covariance estimate (11) was utilised in the development of the maximum likelihood estimation detector (MLED) in [12], which is the SDS counterpart of the AMF detector:

$$\frac{|\boldsymbol{s}^H\boldsymbol{Q}^{-1}\boldsymbol{g}|^2}{\boldsymbol{s}^H\boldsymbol{Q}^{-1}\boldsymbol{s}} \underset{H_0}{\overset{H_1}{\gtrless}} \gamma \tag{12}$$

The generalised maximum likelihood estimation detector (GMLED) is also derived as the natural SDS counterpart to Kelly's GLRT [14, pp. 54–57, 12,15]:

$$\frac{|\boldsymbol{s}^H\boldsymbol{Q}^{-1}\boldsymbol{g}|^2}{\boldsymbol{s}^H\boldsymbol{Q}^{-1}\boldsymbol{s}(1+\boldsymbol{g}^H\boldsymbol{Q}^{-1}\boldsymbol{g})} \underset{H_0}{\overset{H_1}{\gtrless}} \gamma \tag{13}$$

Both (12) and (13) are SDS threshold detection algorithms that are based on statistical modelling of the noise and interference through covariance estimation. A different algorithm that combines SDS and TDS detection is proposed in [16]. It exploits the benefits of both detection methods but still relies on forming an estimate to the statistics of the background noise and interference. A different approach of dealing with target detection in non-homogeneous environment is presented in [18]. It derives an SDS projection-based MIMO solution to the problem while avoiding the need to do any statistical analysis of the environment. The shortcoming of these methods is that prior information about the structure and spectral range of the clutter has to exist. The MLED and GMLED algorithms operate without any such prior knowledge. A comparison of the hybrid SMI, the TDS SMI, and the projections approaches has been conducted in [38]. The subspace approach has been further developed to incorporate the autoregressive clutter model from [17] in a MIMO projection-based scenario [20].

3. Multistatic maximum likelihood estimation detector

In this section the ML multistatic solution to the target detection problem in unknown coloured background noise is derived. The derivation is a more in-depth extension of [8]. The resulting detector is similar to the ones presented in [23,25] but does not use an independent training data set. The derivation mirrors that of its respective TDS counterpart and is included here for convenience. The setup described in Section 2 and the signal model (2) are adopted (note that the signal model is now channel-specific and applies to each channel). The channel-specific probability density function (pdf) of each observed data matrix $\boldsymbol{X}_{m,n}$ conditioned on the amplitude of the reflected probing signal $\alpha_{m,n}$ is given by [14, p. 121]

$$f(\boldsymbol{X}_{m,n}|\alpha_{m,n}) = \left(\frac{1}{\pi^P|\boldsymbol{C}_{m,n}|}\right)^K \mathrm{etr}\{-\boldsymbol{C}_{m,n}^{-1}\boldsymbol{M}_{m,n}^{\alpha}\} \tag{14}$$

where $\boldsymbol{M}_{m,n}^{\alpha} = \sum_{k=1}^{K}(\boldsymbol{x}_{m,n,k} - \alpha_{m,n}\boldsymbol{s}_{m,n}\boldsymbol{t}_{m,n}(k))(\boldsymbol{x}_{m,n,k} - \alpha_{m,n}\boldsymbol{s}_{m,n}\boldsymbol{t}_{m,n}(k))^H$. It is assumed that the covariance matrices of the background interference $\boldsymbol{C}_{m,n}$ are known for the time being in order to derive the optimal multistatic detector. Here the notation that $|\bullet|$ is the determinant, $\mathrm{etr}(\bullet) = e^{\mathrm{Tr}(\bullet)}$, and $\mathrm{Tr}(\bullet)$ is the trace of the matrix $(\bullet)$ has been adopted. In a MIMO system with sufficient separation between antennas, the background noise processes $\boldsymbol{N}_{m,n}$ are uncorrelated to one another. The joint pdf of the complete set of observations $\mathbb{X} = \{\boldsymbol{X}_{m,n} | m = 1\ldots M, n = 1\ldots N\}$ given the set of amplitudes $\mathbb{\alpha} = \{\alpha_{m,n} | m = 1\ldots M, n = 1\ldots N\}$ can be represented by the product of the individual pdfs given in (14)

$$f(\mathbb{X}|\mathbb{\alpha}) = \prod_{m,n} f(\boldsymbol{X}_{m,n}|\alpha_{m,n}) = \left(\frac{1}{\pi^{MNP}\prod_{m,n}|\boldsymbol{C}_{m,n}|}\right)^K \mathrm{etr}\left\{-\sum_{m,n}\boldsymbol{C}_{m,n}^{-1}\boldsymbol{M}_{m,n}^{\alpha}\right\} \tag{15}$$

Let $\mathbb{\alpha} = \mathbb{0}$ signify the case when every element of the set $\mathbb{\alpha}$ is equal to zero. Therefore, the joint pdf of the set of observation signals $\mathbb{X}$ under the null hypothesis from (2) is given by

$$f_0(\mathbb{X}) = f(\mathbb{X}|\mathbb{\alpha} = \mathbb{0}) = \left(\frac{1}{\pi^{MNP}\prod_{m,n}|\boldsymbol{C}_{m,n}|}\right)^K \mathrm{etr}\left\{-\sum_{m,n}\boldsymbol{C}_{m,n}^{-1}\boldsymbol{M}_{m,n}^{0}\right\} \tag{16}$$

where $\boldsymbol{M}_{m,n}^{0} = \sum_{k=1}^{K}\boldsymbol{x}_{m,n,k}\boldsymbol{x}_{m,n,k}^H$. Under hypothesis H_1 from (2), the joint pdf $f_1(\mathbb{X})$ is simply given by $f(\mathbb{X}|\alpha)$ from Eq. (15). To obtain the ML estimate of the unknown parameters in the set α, the logarithm of (15) is taken and then the partial derivative of the expression with respect to each unknown complex amplitude $\alpha_{m,n}$ individually is formed. The problem thus becomes linearly separable, and the solution is identical to the single channel case presented in [12]

$$\widehat{\alpha}_{m,n} = \frac{\boldsymbol{s}_{m,n}^H\boldsymbol{C}_{m,n}^{-1}\boldsymbol{g}_{m,n}}{\boldsymbol{s}_{m,n}^H\boldsymbol{C}_{m,n}^{-1}\boldsymbol{s}_{m,n}} \tag{17}$$

Note that (17) is identical to the amplitude estimate of the APES filter derived in [35]. Forming the ML ratio of (15) and (16), the multistatic MLED threshold detector for a MIMO system is derived

$$\frac{\max_{\mathbb{\alpha}} f_1}{f_0} = \frac{\mathrm{etr}\{-\sum_{m,n}\boldsymbol{C}_{m,n}^{-1}\widehat{\boldsymbol{M}}_{m,n}^{\alpha}\}}{\mathrm{etr}\{-\sum_{m,n}\boldsymbol{C}_{m,n}^{-1}\boldsymbol{M}_{m,n}^{0}\}} = \mathrm{etr}\left\{-\sum_{m,n}\boldsymbol{C}_{m,n}^{-1}(\widehat{\boldsymbol{M}}_{m,n}^{\alpha} - \boldsymbol{M}_{m,n}^{0})\right\} \tag{18}$$

where $\widehat{\boldsymbol{M}}_{m,n}^{\alpha} = \sum_{k=1}^{K}(\boldsymbol{x}_{m,n,k} - \widehat{\alpha}_{m,n}\boldsymbol{s}_{m,n}\boldsymbol{t}_{m,n}(k))(\boldsymbol{x}_{m,n,k} - \widehat{\alpha}_{m,n}\boldsymbol{s}_{m,n}\boldsymbol{t}_{m,n}(k))^H$, with $\widehat{\alpha}_{m,n}$ being the ML estimate given by (17). The relationship between $\widehat{\boldsymbol{M}}_{m,n}^{\alpha}$ and $\boldsymbol{M}_{m,n}^{0}$ is derived in [14, p. 122] and is provided in Appendix A for convenience

$$\widehat{\boldsymbol{M}}_{m,n}^{\alpha} = \boldsymbol{M}_{m,n}^{0} - K\boldsymbol{g}_{m,n}\boldsymbol{g}_{m,n}^H + K(\boldsymbol{g}_{m,n} - \widehat{\alpha}_{m,n}\boldsymbol{s}_{m,n})(\boldsymbol{g}_{m,n} - \widehat{\alpha}_{m,n}\boldsymbol{s}_{m,n})^H \tag{19}$$

Plugging the relation (19) in (18), taking the logarithm of the expression, and using the identity $\boldsymbol{v}^H\boldsymbol{M}\boldsymbol{v} = \mathrm{Tr}(\boldsymbol{M}\boldsymbol{v}\boldsymbol{v}^H)$ for an arbitrary vector $\boldsymbol{v}$ and matrix $\boldsymbol{M}$, we obtain the ML multistatic threshold detector for the case when the covariance matrices of the background noise and interference $\boldsymbol{C}_{m,n}$ for

all different channels are known

$$T_{MF}=\sum_{m,n}\frac{|\boldsymbol{s}_{m,n}^H\boldsymbol{C}_{m,n}^{-1}\boldsymbol{g}_{m,n}|^2}{\boldsymbol{s}_{m,n}^H\boldsymbol{C}_{m,n}^{-1}\boldsymbol{s}_{m,n}}\underset{H_0}{\overset{H_1}{\gtrless}}\gamma \tag{20}$$

where γ is the decision threshold associated with the combined ML term from all channels. In the current problem, note that T_{MF} in (20) represents the multistatic matched filter-based detector which is an extension to the single-channel one described by (3) and (5). To obtain the multistatic MLED detector, the noise data covariance matrices $\boldsymbol{C}_{m,n}$ are replaced with their SDS APES estimates $\boldsymbol{Q}_{m,n}$ (11)

$$T_M=\sum_{m,n}\frac{|\boldsymbol{s}_{m,n}^H\boldsymbol{Q}_{m,n}^{-1}\boldsymbol{g}_{m,n}|^2}{\boldsymbol{s}_{m,n}^H\boldsymbol{Q}_{m,n}^{-1}\boldsymbol{s}_{m,n}}\underset{H_0}{\overset{H_1}{\gtrless}}\gamma \tag{21}$$

The ML SDS solution (21) to the MIMO case investigated in this work is a summation of the individual single-channel solutions (12) for each path $\{m,n\}$ in the system. The linear separability of the multistatic detector in the sum of the bistatic ones is in accordance with our prior assumption that the individual transmit–receive channels are independent.

4. Multistatic generalised maximum likelihood estimation detector

In this section the multistatic GMLED threshold test algorithm for SDS detection is derived. The derivation is a more in-depth extension of [8]. The resulting detector is similar to the multistatic generalised likelihood ratio test presented in [23–26] but does not require an independent training data set. The derivation is similar to that of its respective TDS counterpart and is included here for convenience. While in the derivation of the MLED the covariance matrices of the noise and interference signals $\boldsymbol{C}_{m,n}$ were assumed to be known, in the GMLED they are kept as unknown parameters from the start. The expression for the pdf of each individual observation signal set $\boldsymbol{X}_{m,n}$, now conditional on both the amplitude $\alpha_{m,n}$ and covariance matrix $\boldsymbol{C}_{m,n}$, is identical to the respective MLED case given by (14). Therefore, the joint pdf in the multistatic extension also remains the same as the one given in (15), this time conditional on the complete set of unknown covariance matrices $\mathbb{C}_\nu=\{\boldsymbol{C}_{m,n}|m=1\ldots M,n=1\ldots N\}$. This is also the expression that provides the relevant likelihood function under the H_1 hypothesis from (2). Under the alternative hypothesis, the likelihood function, now conditional on the parameter set $\mathbb{C}_\nu$, is the same as (16). If the logarithm of this expression is taken, the problem is once again linearly separable. Therefore, the maximum of (16) with respect to all $\boldsymbol{C}_{m,n}$ parameters is equivalent to maximising all the individual likelihoods in (14). As described in [14, p. 122, 12,15] this happens when the matrices $\boldsymbol{C}_{m,n}$ are replaced by their ML estimates $\widehat{\boldsymbol{C}}_{m,n}=K^{-1}\boldsymbol{M}_{m,n}^0$, and the maximised likelihood function is thus

$$\max_{\mathbb{C}_\nu} f_0(\mathbb{X})=\left(\frac{1}{(e\pi K)^{MNP}\prod_{m,n}|\boldsymbol{M}_{m,n}^0|}\right)^K \tag{22}$$

From the same source, the maximisation of the pdf under the alternative hypothesis occurs when $\boldsymbol{C}_{m,n}$ are replaced by $\widehat{\boldsymbol{C}}_{m,n}=K^{-1}\boldsymbol{M}_{m,n}^\alpha$, resulting in the following expression:

$$\max_{\mathbb{C}_\nu} f_1(\mathbb{X}|\mathbb{C}_\nu)=\left(\frac{1}{(e\pi K)^{MNP}\prod_{m,n}|\boldsymbol{M}_{m,n}^\alpha|}\right)^K \tag{23}$$

Noting that once again the conditioned likelihood (23) can be made linearly separable through taking the logarithm, the maximisation of the expression can be achieved when each of the individual terms $|\boldsymbol{M}_{m,n}^\alpha|$ is minimised with respect to $\alpha_{m,n}$. The solution is thus the same as the one provided in the single-channel GMLED derivation and is detailed in Appendix B:

$$\min_{\alpha_{m,n}}|\boldsymbol{M}_{m,n}^\alpha|=K^p|\boldsymbol{Q}_{m,n}|\left(1+\boldsymbol{g}_{m,n}^H\boldsymbol{Q}_{m,n}^{-1}\boldsymbol{g}_{m,n}-\frac{|\boldsymbol{s}_{m,n}^H\boldsymbol{Q}_{m,n}^{-1}\boldsymbol{g}_{m,n}|^2}{\boldsymbol{s}_{m,n}^H\boldsymbol{Q}_{m,n}^{-1}\boldsymbol{s}_{m,n}}\right) \tag{24}$$

$$|\boldsymbol{M}_{m,n}^0|=K^p|\boldsymbol{Q}_{m,n}|(1+\boldsymbol{g}_{m,n}^H\boldsymbol{Q}_{m,n}^{-1}\boldsymbol{g}_{m,n}) \tag{25}$$

Forming the ratio of the maximised likelihoods (23) and (22), the multistatic threshold detector expression can be obtained

$$\frac{\max_{\mathbb{X},\mathbb{C}_\nu} f_1}{\max_{\mathbb{C}_\nu} f_0}=\left(\frac{\prod_{m,n}|\boldsymbol{M}_{m,n}^0|}{\prod_{m,n}\min_{\alpha_{m,n}}|\boldsymbol{M}_{m,n}^\alpha|}\right)^K \tag{26}$$

Plugging in the relevant expressions for the determinants (24) and (25) into (26) and forming the Kth root of the likelihood ratio, the expression for the multistatic GMLED is obtained

$$T_G=\prod_{m,n}\frac{1+\boldsymbol{g}_{m,n}^H\boldsymbol{Q}_{m,n}^{-1}\boldsymbol{g}_{m,n}}{1+\boldsymbol{g}_{m,n}^H\boldsymbol{Q}_{m,n}^{-1}\boldsymbol{g}_{m,n}-\frac{|\boldsymbol{s}_{m,n}^H\boldsymbol{Q}_{m,n}^{-1}\boldsymbol{g}_{m,n}|^2}{\boldsymbol{s}_{m,n}^H\boldsymbol{Q}_{m,n}^{-1}\boldsymbol{s}_{m,n}}}\underset{H_0}{\overset{H_1}{\gtrless}}\nu \tag{27}$$

where ν is the decision threshold associated with the combined ML threshold detector. The multistatic GMLED (27) is a product of the bistatic solutions (13) for each path $\{m,n\}$ in the system expressed in their original form.

5. Analysis

This section provides a statistical analysis of the derived multistatic versions of the MLED and GMLED algorithms. To derive an expression for the probability of false alarm P_{fa} and the probability of detection P_d, the CLT is employed to obtain a Gaussian approximation to both threshold detectors' pdfs for a large number $M\times N$ of transmit–receive pairs.

5.1. Statistical properties of the multistatic MLED

The statistical properties of the bistatic MLED detector are described in [14, pp. 63–65, 12,15]. The detection test for a single bistatic channel shown in (12) is thus equivalent to

$$\frac{\zeta_{m,n}}{L\eta_{m,n}}\underset{H_0}{\overset{H_1}{\gtrless}}\gamma_{m,n} \tag{28}$$

where $L=K-P$. The random variables $\zeta_{m,n}$ and $\eta_{m,n}$ are mutually independent. The random variable $\eta_{m,n}$ follows the type I beta distribution with $L+1$ and $P-1$ degrees of

freedom. The random variable $\zeta_{m,n}$ is distributed according to the non-central F distribution with 2 and $2L$ degrees of freedom and a non-centrality parameter $\lambda_{m,n}$ given by

$$\lambda_{m,n} = 2KP\eta_{m,n}\rho_{m,n} \tag{29}$$

The signal-to-noise ratio (SNR) $\rho_{m,n}$ for each antenna element and pulse in a single channel is derived in [14, p. 17, 12,15]

$$\rho_{m,n} = \frac{1}{P}|\alpha_{m,n}|^2 \boldsymbol{s}_{m,n}^H \boldsymbol{C}_{m,n}^{-1} \boldsymbol{s}_{m,n} \tag{30}$$

In the case where no target is present in the set of observations $\boldsymbol{X}_{m,n}$, the non-centrality parameter $\lambda_{m,n}$ becomes zero, and the random variable $\zeta_{m,n}$ has a central F-distribution with 2 and $2L$ degrees of freedom. Using (21), the multistatic MLED detection test statistics are distributed as

$$\sum_{m,n} \frac{\zeta_{m,n}}{L\eta_{m,n}} \underset{H_0}{\overset{H_1}{\gtrless}} \gamma \tag{31}$$

The test statistics consists of a sum of random terms shown in [12] to be independent of the underlying noise and interference. Therefore, the multistatic MLED is also independent of the statistics of the noise, preserving the CFAR property in the MIMO extension of the algorithm. Due to the complex nature of the random variables involved, obtaining a closed form expression for the pdf of the multistatic MLED detector would be difficult and impractical. Similar conclusions have been reached in both [23,25] where analogical TDS MIMO algorithms for target detection have been proposed. The bistatic approach to the test statistics in (31) is to assume that the random variable η is known, which results in the detection variable having the non-central F-distribution. This pdf can then be integrated to obtain an expression for the probability of detection and the probability of false alarm. In the multistatic case assuming that all variables $\eta_{m,n}$ are known results in the detection variable being a sum of $M \times N$ independent non-identically distributed non-central F-distributed random variables. The pdf of such random variable is not trivial to obtain which makes analysis of the proposed multistatic algorithm difficult. However, if the sum in (31) consists of enough terms, it can be approximated by a normal distribution. This enables the derivation of approximate expressions for the probability of false alarm $P_{Mf}(\gamma)$ and the probability of detection $P_{Md}(\gamma)$ for a given detection threshold γ. The approach and solution can be easily extended to existing TDS detectors [23,25] by using the appropriate parameters and degrees of freedom for those algorithms.

5.2. Gaussian approximation of the multistatic MLED

The multistatic MLED threshold detector consists of a sum of $M \times N$ independent random terms as shown in (31). The CLT dictates that the statistics of the decision variable can be closely approximated by a Gaussian distribution, i.e. $T_M \sim \mathcal{N}(\mu_M, \sigma_M^2)$, provided that $M \times N$ is sufficiently large. Because the terms are not identically distributed, Lindeberg's condition has to be satisfied which is shown in Appendix C. The mean μ_M and variance σ_M^2 are given by the sum of the means and variances of the individual terms in the detector

$$\mu_M = \sum_{m,n} \mu_{M(m,n)} \tag{32}$$

$$\sigma_M^2 = \sum_{m,n} \sigma_{M(m,n)}^2 \tag{33}$$

$$\mu_{M(m,n)} = E\left[\frac{\zeta_{m,n}}{L\eta_{m,n}}\right] \tag{34}$$

$$\sigma_{M(m,n)}^2 = \mathrm{var}\left(\frac{\zeta_{m,n}}{L\eta_{m,n}}\right) \tag{35}$$

Here $E[\bullet]$ signifies the expectation and $\mathrm{var}(\bullet)$ the variance of the random variable or vector $\bullet$. Because the random variables $\zeta_{m,n}$ and $\eta_{m,n}$ are independent, the central moments of their ratios factorise in the following manner [39]:

$$\mu_{M(m,n)} = \frac{1}{L} E[\zeta_{m,n}] E\left[\frac{1}{\eta_{m,n}}\right] \tag{36}$$

$$\sigma_{M(m,n)}^2 = \frac{1}{L^2} E[\zeta_{m,n}^2] E\left[\left(\frac{1}{\eta_{m,n}}\right)^2\right] - \frac{1}{L^2} E[\zeta_{m,n}]^2 E\left[\frac{1}{\eta_{m,n}}\right]^2 \tag{37}$$

Provided that $L > 2$, which can be ensured by collecting enough slow-time samples K at each node, the first two central moments of the F-distributed random variable $\zeta_{m,n}$ are given in statistics literature [40]

$$E[\zeta_{m,n}] = \frac{L}{2}\frac{2+\lambda_{m,n}}{L-1} \tag{38}$$

$$\mathrm{var}(\zeta_{m,n}) = \frac{L^2}{4}\frac{(2+\lambda_{m,n})^2 + 4(1+\lambda_{m,n})(L-1)}{(L-1)^2(L-2)} \tag{39}$$

The first two central moments of $\eta_{m,n}^{-1}$ are obtained by solving the expectation integral of the reciprocal beta-distributed random variable with $L+1$ and $P-1$ degrees of freedom

$$E\left[\frac{1}{\eta_{m,n}}\right] = \frac{K-1}{L} \tag{40}$$

$$\mathrm{var}\left(\frac{1}{\eta_{m,n}}\right) = \frac{(K-1)(P-1)}{L^2(L-1)} \tag{41}$$

Using the fact that $E[\bullet^2] = \mathrm{var}(\bullet) + E[\bullet]^2$, (38)–(41) can be plugged in (34) and (35) to obtain an expression for the mean and variance of the random variable that signifies the bistatic MLED threshold detector

$$\mu_{M(m,n)} = \frac{K-1}{2L}\frac{2+\tilde{\lambda}_{m,n}}{L-1} \tag{42}$$

$$\sigma_{M(m,n)}^2 = \frac{(K-1)(K+P-2)(2+\tilde{\lambda}_{m,n})^2}{4L^2(L-1)^2(L-2)} + \frac{(K-1)(K-2)(1+\tilde{\lambda}_{m,n})}{L(L-1)^2(L-2)} \tag{43}$$

where it has been accounted for the fact that $\lambda_{m,n}$ is a random variable dependent on $\eta_{m,n}$ by replacing it with its expected value $\tilde{\lambda}_{m,n}$ given by

$$\begin{aligned}\tilde{\lambda}_{m,n} &= E[2KP\rho_{m,n}\eta_{m,n}] \\ &= 2P(L+1)\rho_{m,n}\end{aligned} \tag{44}$$

It should be noted that (44) is an additional approximation that is performed for convenience. The CLT holds without replacing the variables $\lambda_{m,n}$ with their first order estimates proposed here. Without this approximation however both the mean (34) and the variance (35) of the normal distribution used to describe the detector statistics are random variables. Integrating over all the $\eta_{m,n}$ variables in the Gaussian pdf is the approach that would be taken in the bistatic detector case, but once again in the multistatic version this is impractical and has no trivial solution which justifies the usage of (44). To obtain the probability of false alarm for a given threshold γ, it is noted that in the absence of target the multistatic MLED threshold detector is approximately distributed as $\mathcal{N}(\mu_{M0}, \sigma^2_{M0})$ where

$$\mu_{M0} = \sum_{m,n} \mu_{m,n}(\tilde{\lambda}_{m,n} = 0) \tag{45}$$

$$\sigma^2_{M0} = \sum_{m,n} \sigma^2_{m,n}(\tilde{\lambda}_{m,n} = 0) \tag{46}$$

Therefore the false alarm probability P_f is approximately

$$P_{Mf}(\gamma) = Q\left(\frac{\gamma - \mu_{M0}}{\sigma_{M0}}\right) \tag{47}$$

where $Q(x)$ is the Q-function associated with the tail probability $\Pr[X > x]$ of the standard normal distribution. The probability of detection is obtained in the case where a target is present in the observations. The multistatic MLED detector variable is then approximately distributed as $\mathcal{N}(\mu_{M1}, \sigma^2_{M1})$, where μ_{M1} and σ^2_{M1} are the same sums as (32) and (33) respectively with the $\tilde{\lambda}_{m,n}$ parameters given by (44). Thus

$$P_{Md}(\gamma) = Q\left(\frac{\gamma - \mu_{M1}}{\sigma_{M1}}\right) \tag{48}$$

Note that the Gaussian approximation to the multistatic MLED proposed here can be easily extended to the multistatic AMF proposed in [23,25]. The approach closely follows the one presented in this work and is thus not provided.

5.3. Statistical properties of the multistatic GMLED

The analysis of the GMLED in [14, pp. 54–63, 12,15] has been performed for the threshold detector expressed in the form given in (13). The multistatic expression (27) requires the return to the original GMLED likelihood ratio expressed as

$$T_{G(m,n)} = \frac{1}{1 - \dfrac{|\boldsymbol{s}^H_{m,n}\boldsymbol{Q}^{-1}_{m,n}\boldsymbol{g}_{m,n}|^2}{\boldsymbol{s}^H_{m,n}\boldsymbol{Q}^{-1}_{m,n}\boldsymbol{s}_{m,n}(1 + \boldsymbol{g}^H_{m,n}\boldsymbol{Q}^{-1}_{m,n}\boldsymbol{g}_{m,n})}} \underset{H_0}{\overset{H_1}{\gtrless}} \nu_{m,n} \tag{49}$$

where $\nu_{m,n} = (1 - \gamma_{m,n})^{-1}$ is the relation between the transformations of the threshold in the bistatic case. The statistical distribution of (49) is thus equivalent to

$$\frac{\zeta_{m,n}}{L} + 1 \underset{H_0}{\overset{H_1}{\gtrless}} \nu_{m,n} \tag{50}$$

where $\zeta_{m,n}$ is the same random variable from the MLED statistics. The multistatic GMLED threshold detector in (27) is therefore distributed as

$$\prod_{m,n}\left(\frac{\zeta_{m,n}}{L} + 1\right) \underset{H_0}{\overset{H_1}{\gtrless}} \nu \tag{51}$$

The test statistics thus consist of a product of random terms that were shown in [14, p. 61, 12,15] to be independent of the underlying noise and clutter distributions. Therefore, the multistatic GMLED threshold detector is, in turn, independent of the statistics of the noise, preserving the CFAR property in the MIMO extension of the algorithm. Similar to the multistatic MLED detector, its generalised extension is difficult to analyse in the statistical sense. In [24,26] statistical analysis of the multistatic TDS detector derived from Kelly's GLRT is provided. However, closed-form expressions for the detection variable pdf exist only for the case when no target is present (hypothesis H_0 here), and thus only the probability of false alarm is derived. A general closed-form expression for the multistatic detector's pdf has not been reached. Therefore, in the next section an approximation to the statistics of the detector in (51) is provided given that a large number of terms take part in the product. As a result it is possible to derive approximate expressions for the probability of false alarm $P_{Gf}(\nu)$ and the probability of detection $P_{Gd}(\nu)$ for a given detection threshold ν. The approach and solution can be easily extended to existing TDS detectors [23–26] by using the appropriate parameters and degrees of freedom for those algorithms.

5.4. Log-normal approximation of the multistatic GMLED

The multistatic GMLED threshold detector consists of a product of $M \times N$ random terms as shown in (51). It would be convenient to take the logarithm of this product to transform it into a sum of random variables

$$\log T_G = \sum_{m,n} \log T_{G(m,n)} \underset{H_0}{\overset{H_1}{\gtrless}} \log \nu \tag{52}$$

The CLT dictates that the statistics of the logarithm of the decision variable given in (52) can be closely approximated by a Gaussian distribution, i.e. $\log T_G \sim \mathcal{N}(\mu_G, \sigma^2_G)$, provided that the number of signal paths $M \times N$ in the system is sufficiently large. Once again the random variables in the sum are not identically distributed so a proof of the validity of Lindeberg's condition for the detector is given in Appendix D. Because the exponential of a normally distributed random variable follows the log-normal distribution with the same parameters, it can be concluded that in a large network $T_G \sim \ln\mathcal{N}(\mu_G, \sigma^2_G)$. To obtain expressions for the parameters of this distribution, the first two moments of the multistatic GMLED random variable have to be obtained. The expectation of the individual terms in the product (27) can be obtained from (50) by using the expectation of an F-distributed random variable given in (38)

$$E[T_{G(m,n)}] = \frac{2L + \lambda_{m,n}}{2(L-1)} \tag{53}$$

Because it is assumed that the random variables coming from the different channels $T_{G(m,n)}$ are independent, the expectation of their product factorises into a product of

their expectations. Therefore, the first moment of the multistatic GMLED random variable is given by

$$E[T_G] = \prod_{m,n} \frac{2L+\lambda_{m,n}}{2(L-1)} \tag{54}$$

The second moment of the individual product terms $T_{G(m,n)}$ is obtained from the variance of the F-distributed random variable given in (39) and the derived first moment (53).

$$E\left[T_{G(m,n)}^2\right] = \frac{(\lambda_{m,n}+2L)^2-4L}{4(L-1)(L-2)} \tag{55}$$

The second moment of the multistatic GMLED detection variable is the product of the second moments of the statistically independent individual terms $T_{G(m,n)}$

$$E\left[T_G^2\right] = \prod_{m,n} \frac{(\lambda_{m,n}+2L)^2-4L}{4(L-1)(L-2)} \tag{56}$$

From statistics literature, the first and second moments of a random variable T_G following the log-normal distribution with parameters μ_G and σ_G^2 are given by

$$E[T_G] = e^{\mu_G + \sigma_G^2/2} \tag{57}$$

$$E[T_G^2] = e^{2\mu_G + 2\sigma_G^2} \tag{58}$$

The derived expectations (54) and (56) and the parametric expressions (57) and (58) form a system of two equations. Solving the system for the parameters of the approximating distribution μ_G and σ_G^2 results in

$$\mu_G = \frac{1}{2}\sum_{m,n} \log\left(\frac{(\tilde{\lambda}_{m,n}+2L)^4(L-2)}{4((\tilde{\lambda}_{m,n}+2L)^2-4L)(L-1)^3}\right) \tag{59}$$

$$\sigma_G^2 = \sum_{m,n} \log\left(\frac{((\tilde{\lambda}_{m,n}+2L)^2-4L)(L-1)}{(\tilde{\lambda}_{m,n}+2L)^2(L-2)}\right) \tag{60}$$

where once again the random variables $\lambda_{m,n}$ have been replaced with their expected values $\tilde{\lambda}_{m,n}$ given by (44). In the absence of target the threshold detector is distributed as $\ln \mathcal{N}(\mu_{G0}, \sigma_{G0}^2)$ where μ_{G0} and σ_{G0}^2 no longer need to be approximated. Their exact values can be computed due to the fact that for $\lambda_{m,n}=0$ the non-central F distribution becomes a central F distribution with 2 and $2L$ degrees of freedom, and the pdf of the distribution simplifies to

$$f_{2,2L}(x) = \frac{1}{\left(1+\frac{x}{L}\right)^{L+1}} \tag{61}$$

Thus the integral expression for the first and second central moments of the logarithm of the bistatic GMLED random variable becomes solvable and yields the following results for the multistatic one which are no longer approximations:

$$\mu_{G0} = \frac{MN}{L} \tag{62}$$

$$\sigma_{G0}^2 = \frac{MN}{L^2} \tag{63}$$

The probability of false alarm for a certain threshold ν is

$$P_{Gf}(\nu) = Q\left(\frac{\log \nu - \mu_{G0}}{\sigma_{G0}}\right) \tag{64}$$

When a target is present the detector statistics are distributed as $\ln \mathcal{N}(\mu_{G1}, \sigma_{G1}^2)$ where μ_{G1} and σ_{G1}^2 are given by (59) and (60) respectively. The probability of detection is thus

$$P_{Gd}(\nu) = Q\left(\frac{\log \nu - \mu_{G1}}{\sigma_{G1}}\right) \tag{65}$$

Note that the log-normal approximation to the multistatic GMLED proposed here can be easily extended to the multistatic GLRT proposed in [23–26]. The approach closely follows the one presented in this work and is thus not provided.

6. Simulations

The multistatic MLED and GMLED algorithms were simulated in order to show the viability of the theoretical models and approximations presented in this work. Three approaches to the performance analysis of the models have been used. The first approach is a numerical Monte Carlo simulation of the proposed algorithms in (21) and (27). The results from these runs are labelled as "simulated" in the presented figures. The second simulation approach that is undertaken is based on the theoretical analysis of the multistatic MLED and GMLED algorithms. A closed-form expression for the test statistics of the detectors was never obtained. Therefore, the theoretical simulation results have been obtained through drawing samples from the random variables (31) and (51) presented in the analysis of the two algorithms. Instead of doing a Monte Carlo simulation to generate the $\lambda_{m,n}$ random variables, the first order approximation in (44) was used. These sets of results are labelled as "theoretical" in the provided figures. The third implemented approach aims to show the viability of the normal and log-normal approximations developed in this paper. These results are labelled as "approximation" on the figures.

The operational parameters of the transmitted pilots are the same as the ones in [18]. A pulse repetition frequency of 500 Hz, carrier frequency of 1 GHz, and target velocity of 30 m/s are set. It is also assumed that the direction of movement of the target is known which means that the exact velocity $\boldsymbol{v} = [v_x, v_y]^T$ in the (x,y)-direction is known given 2-dimensional motion. A number of experiments have been done with a smaller setup of $M=N=10$ transmitters and receivers and a larger one of $M=N=20$. The geometry of the MIMO setup consists of random placement of transmitters and receive ULAs. The amplitudes of the returned pilots $\alpha_{m,n}$ are also chosen at random from a complex normal distribution $\mathcal{CN}(0,1)$. The exact formula for obtaining the Doppler frequencies of the returned pilots in the sense of MIMO radar can be found in [18,41]. The receiver ULA has $P_T=5$ elements that collect $K_T=40$ and $K_T=120$ pulses per CPI. These slow-time observations have been rearranged into data snapshots of size $P=10$, where the number of snapshots is $K=20$ and $K=60$. To generate the clutter in each channel, the general clutter model presented in [31] has been used. The spectrum of the clutter exhibits low-pass behaviour and is also roughly shaped in accordance to the realistic model discussed in [42, pp. 293–322]. The simulations consist of 10^6 Monte Carlo runs of each system for different SNR

values and depict the average probability of detection for each case when the probability of false alarm has been fixed to 2×10^{-2}. The SNR follows the definition in (30) and is assumed to be the same for all channels in the system.

Fig. 3 shows the obtained results for the smaller network of 10 transmitters and 10 receivers and $K = 20$ snapshots. As expected, the GMLED algorithm performs slightly better than the MLED one for a small K, exhibiting the same probability of detection at approximately 1 dB less SNR. The results show that the simulated detector curves based on (21) and (27) match the theoretical models describing their statistics shown in (31) and (51) respectively. Moreover, the fact that the approximation to the $\lambda_{m,n}$ variables was used in the theoretical curves proves the viability and justifies the usage of (44). The Gaussian approximations to the multistatic detectors given in (47), (48), (64) and (65) are also close to the simulated and theoretical curves. The small offset comes from the fact that approximation based on the first two moments of the multistatic MLED and GMLED threshold detector random variables is performed. Moreover, the convergence of sums of non-identically distributed random variables to the CLT is usually slower than the iid counterparts. As it will be show, the approximations become much better as the number of transmitters and receivers in the system increases.

Fig. 4 shows the simulation results under the same conditions as Fig. 3 except the number of snapshots is now $K = 60$. It can be seen that both the multistatic MLED and GMLED are significantly affected by the temporal frame size, having the same detection rate at approximately 6 dB lower SNR value. This can be explained by the improvement of the SDS covariance matrix estimate (11) through the addition of more data samples. It should be noted that as the temporary frame size increases, the multistatic MLED and GMLED algorithms' performance becomes almost identical. This is evident in the simulations as well and reflects the behaviour of the MLED and GMLED bistatic algorithms presented in [12,14,15].

Fig. 5 aims to simulate the performance of a larger radar network. The number of transmitters and receivers doubles. Compared to Fig. 4, the curve of the probability of detection shifts by a further 3 dB to the left. This reflects the improvement in the performance of the multistatic MLED and GMLED detectors due to the increased spatial diversity in the system. The accuracies of the proposed Gaussian and log-normal approximations to the multistatic MLED and GMLED respectively are also greatly enhanced. This is because the number of terms in the summations (31) and (52) increases which, according to the CLT, brings the distribution of the sums closer to the Gaussian curve. In a hypothetical radar network of infinite size this approximation will become exact.

Fig. 6 presents an investigation into the relative approximation error of the detection probability provided by the Gaussian models proposed in this work. As expected, the approximation is poor for a small number of channels in the multistatic system. This is due to the fact that there are not enough random variables coming from the different

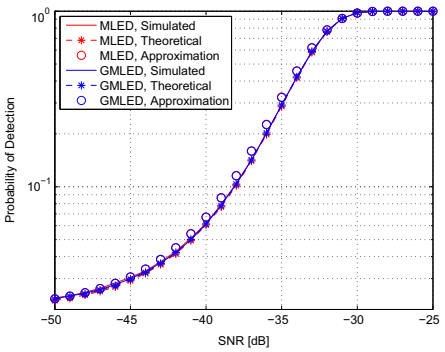

Fig. 4. Probability of detection vs SNR of the multistatic MLED and GMLED detectors for $P_{Mf} = 2 \times 10^{-2}$ and $P_{Gf} = 2 \times 10^{-2}$, K=60, $M = N = 10$.

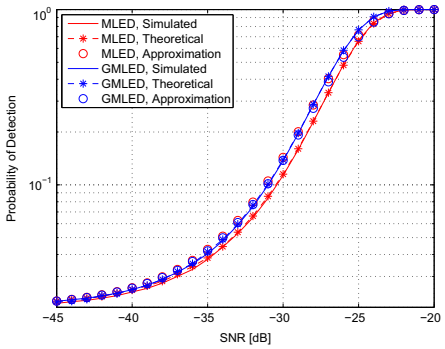

Fig. 3. Probability of detection vs SNR of the multistatic MLED and GMLED detectors for $P_{Mf} = 2 \times 10^{-2}$ and $P_{Gf} = 2 \times 10^{-2}$, K=20, $M = N = 10$.

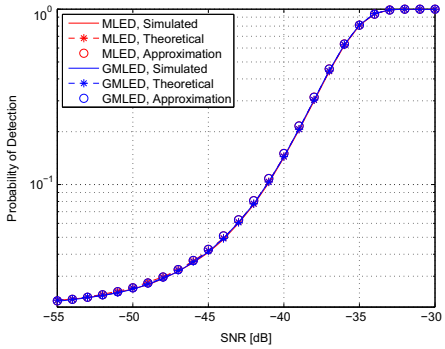

Fig. 5. Probability of detection vs SNR of the multistatic MLED and GMLED detectors for $P_{Mf} = 2 \times 10^{-2}$ and $P_{Gf} = 2 \times 10^{-2}$, K=60, $M = N = 20$.

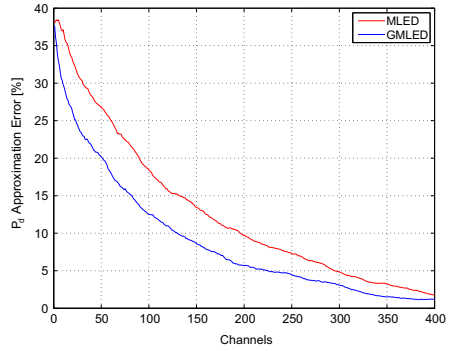

Fig. 6. Relative error of estimation of P_{Md} and P_{Gd} for $P_{Mf} = 2 \times 10^{-2}$ and $P_{Gf} = 2 \times 10^{-2}$, K=20.

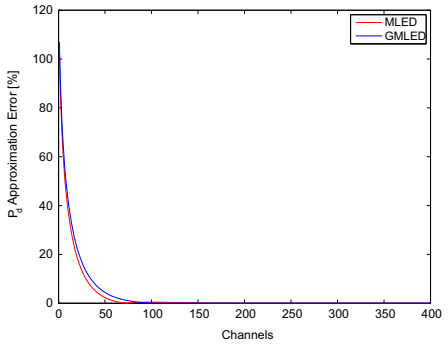

Fig. 7. Relative error of estimation of P_{Md} and P_{Gd} for $P_{Mf} = 2 \times 10^{-2}$ and $P_{Gf} = 2 \times 10^{-2}$, K=60.

channels to provide reliable convergence of the CLT. As more channels are added to the system, the approximation continues to get asymptotically closer to the real value of the detection probability.

Another factor that influences the approximation error is the number of iid snapshots in the system K. Fig. 7 shows the relative approximation error of the detection probability as a function of the number of channels for $K = 60$ snapshots. It is clear that the convergence of the combination of bistatic random variables to the CLT is much quicker. The reason for this phenomenon is found in the higher moments of the underlying central and non-central F distributions present in the statistical analysis of the MLED and GMLED algorithms. As K increases, the higher moments of these distributions get smaller [40]. Thus the distributions become more and more Gaussian-like, which inherently speeds up the convergence rate to an actual bell-shaped curve after multiple convolutions.

7. Conclusion

This work proposes two SDS multistatic STAP algorithms for the detection of signals of known template in coloured Gaussian interference. The performance of the multistatic algorithms in a MIMO radar target detection scheme has been analysed. It has been shown that the algorithms exhibit the CFAR property. In order to analyse the system, simplified Gaussian approximation models for the statistics of the detectors have been proposed. Through these models the theoretical probabilities of detection and false alarm have been derived. The validity of the theoretical models as well as the simplified Gaussian approximations has been verified through numerical simulations. The performance gains of the multistatic detectors over their bistatic counterparts have been shown.

Acknowledgements

This work was supported by the Institute for Digital Communications at the University of Edinburgh, Selex ES and EPSRC (EP/J015180/1).

Appendix A. Detailed derivation of Eq. (19)

This appendix contains a detailed description of the steps required to obtain Eq. (19). The steps are originally found in [14, p. 122] and are provided here for convenience. All references to the index $\{m, n\}$ indicating the path between the mth transmitter and the nth receiver are omitted in this proof. The matrices $\boldsymbol{M}^0$ and $\boldsymbol{M}^{\alpha}$ introduced earlier are defined as

$$\boldsymbol{M}^0 = \sum_{k=1}^{K} \boldsymbol{x}_k \boldsymbol{x}_k^H \tag{A.1}$$

$$\widehat{\boldsymbol{M}^{\alpha}} = \sum_{k=1}^{K} (\boldsymbol{x}_k - \hat{\alpha}\boldsymbol{s}\boldsymbol{t}(k))(\boldsymbol{x}_k - \hat{\alpha}\boldsymbol{s}\boldsymbol{t}(k))^H \tag{A.2}$$

Expanding (A.2), the connection with (A.1) can be made

$$\begin{aligned}\widehat{\boldsymbol{M}^{\alpha}} &= \sum_{k=1}^{K} \boldsymbol{x}_k \boldsymbol{x}_k^H - \sum_{k=1}^{K} \hat{\alpha}^* \boldsymbol{x}_k \boldsymbol{t}^*(k) \boldsymbol{s}^H \\ &\quad - \sum_{k=1}^{K} \hat{\alpha}\boldsymbol{s}\boldsymbol{t}^T(k)\boldsymbol{x}_k^H + \sum_{k=1}^{K} |\hat{\alpha}|^2 |\boldsymbol{t}(k)|^2 \boldsymbol{s}\boldsymbol{s}^H \\ &= \boldsymbol{M}^0 - K\hat{\alpha}^* \boldsymbol{g}\boldsymbol{s}^H - K\hat{\alpha}\boldsymbol{s}\boldsymbol{g}^H + K|\hat{\alpha}|^2 \boldsymbol{s}\boldsymbol{s}^H \end{aligned} \tag{A.3}$$

where the substitution for $\boldsymbol{g}$ from (4) has been made, and the fact that in this work $|\boldsymbol{t}|^2 = K$ has been used. Adding and subtracting the term $K\boldsymbol{g}\boldsymbol{g}^H$ to (A.3) and grouping the factors, the desired results in (19) are obtained. The factor K comes from the normalisation of the power of the temporary steering vector which is arbitrary. In some works it is set to unity and is therefore omitted. In this work the factor is simply included into the threshold γ of the target detector.

Appendix B. Detailed derivation of Eqs. (24) and (25)

This appendix contains a detailed description of the steps required to obtain Eqs. (24) and (25). Some of the steps are originally found in [14, p. 123] and are provided here for convenience. All references to the index $\{m,n\}$ indicating the path between the mth transmitter and the nth receiver are omitted in this proof.

Note that (19) can be written in terms of the SDS covariance estimation matrix $\boldsymbol{Q}$ that directly follows from its definition in (11) and the fact that $\widehat{\boldsymbol{R}}$ is defined as a scaled version of $\boldsymbol{M}^0$

$$\boldsymbol{M}^{\alpha} = K\boldsymbol{Q} + K(\boldsymbol{g}-\alpha\boldsymbol{s})(\boldsymbol{g}-\alpha\boldsymbol{s})^H \tag{B.1}$$

Using the generalisation of Sylvester's identity for matrix determinants [43] it can be shown that, following from (B.1)

$$|\boldsymbol{M}^{\alpha}| = K^P|\boldsymbol{Q}|(1+(\boldsymbol{g}-\alpha\boldsymbol{s})^H\boldsymbol{Q}^{-1}(\boldsymbol{g}-\alpha\boldsymbol{s})) \tag{B.2}$$

Eq. (24) is obtained after minimising (B.2) with respect to the unknown return amplitude α by solving the partial derivative

$$\begin{aligned}\frac{\partial}{\partial\alpha^*}|\boldsymbol{M}^{\alpha}| &= \frac{\partial}{\partial\alpha^*}K^P|\boldsymbol{Q}|\left(1+(\boldsymbol{g}-\alpha\boldsymbol{s})^H\boldsymbol{Q}^{-1}(\boldsymbol{g}-\alpha\boldsymbol{s})\right)\\ &= -K^P|\boldsymbol{Q}|\boldsymbol{s}^H\boldsymbol{Q}^{-1}(\boldsymbol{g}-\alpha\boldsymbol{s})\\ &= \alpha K^P|\boldsymbol{Q}|\boldsymbol{s}^H\boldsymbol{Q}^{-1}\boldsymbol{s} - K^P|\boldsymbol{Q}|\boldsymbol{s}^H\boldsymbol{Q}^{-1}\boldsymbol{g}\end{aligned} \tag{B.3}$$

It is clear that the solution to (B.3) for α is the same as the one for the MLED case in (17) but directly adapted to the SDS detection scenario

$$\widehat{\alpha} = \frac{\boldsymbol{s}^H\boldsymbol{Q}^{-1}\boldsymbol{g}}{\boldsymbol{s}^H\boldsymbol{Q}^{-1}\boldsymbol{s}} \tag{B.4}$$

When this solution (B.4) is plugged into (B.2), the resulting equation is the same as (24). When there is no target in the radar detection scenario, the amplitude of the returned waveform is $\alpha = 0$. Plugging this into (B.2) results in Eq. (25).

Appendix C. Proof of Lindeberg's condition for the multistatic MLED approximation

In terms of the notation used in this paper, Lindeberg's condition takes the following form:

$$\lim_{MN\to\infty}\frac{1}{\sigma_M^2}\sum_{k=0}^{MN}\int_{|T_{M(k)}-\mu_{M(k)}|>\epsilon\sigma_M}(T_{M(k)}-\mu_{M(k)})^2 f_k(T_{M(k)})\,dT_{M(k)} = 0 \tag{C.1}$$

where the subscript (m,n) indicating the path between the mth transmitter and the nth receiver has been replaced with the generic subscript k for convenience. The term $T_{M(k)}$ represents the kth component in the sum (21). The probability density function $f_k(T_{M(k)})$ is associated with the bistatic MLED random variable (28). If (C.1) holds for any constant $\epsilon > 0$, then the condition is sufficient to claim that the multistatic MLED random variable (31) will converge to a Gaussian distribution as the number of transmit–receive pairs $M \times N$ goes to infinity. Chebyshev's inequality for the variance of the bistatic MLED detector states that

$$P\left(\left|T_{M(k)}-\mu_{M(k)}\right| \geq \epsilon\sigma_M\right) \leq \frac{\sigma_{M(k)}^2}{\epsilon^2\sigma_M^2} \tag{C.2}$$

Note that the mean $\mu_{M(k)}$ given in (42) and the variance $\sigma_{M(k)}^2$ from (43), considering a realistic system with finite time samples K and receive sensors P, both exist and are finite. This is due to the assumption that $\lambda_{m,n}$ is finite because the SNR $\rho_{m,n}$ is practically finite. The term σ_M^2 can be written in the form

$$\sigma_M^2 = \sum_{m,n}a_{m,n}\lambda_{m,n}^2 + \sum_{m,n}b_{m,n}\lambda_{m,n} + cMN \tag{C.3}$$

where $a_{m,n}, b_{m,n}, c \in \mathbb{R}$. The sum in (C.3) goes to infinity as $M \times N \to \infty$. Therefore, the right-hand side of Chebyshev's inequality (C.2) goes to 0 since $\epsilon \neq 0$ is a constant. Therefore the left-hand side probability in the inequality is bounded by 0, which translates to

$$\lim_{M\times N\to\infty}\int_{|T_{M(k)}-\mu_{M(k)}|>\epsilon\sigma_M} f_k(T_{M(k)})\,dT_{M(k)} = 0 \tag{C.4}$$

Combined with the fact that the mean $\mu_{M(k)}$ is finite, this proves that each term in the sum (C.1) converges to 0 in the limit. Therefore the whole sum converges to 0 and Lindeberg's condition is satisfied, which justifies the Gaussian approximation of the multistatic MLED threshold detector.

Appendix D. Proof of Lindeberg's condition for the multistatic GMLED approximation

The expectation and second moment of the bistatic GMLED threshold detector given in (53) and (55) respectively are finite due to the assumptions that the parameters K, P, and $\lambda_{m,n}$ are practically finite (see Appendix C). In this proof the following logarithmic inequality will be used:

$$\log x \leq x - 1 \tag{D.1}$$

From (D.1) an upper bound for the expectation of the logarithm of the bistatic GMLED threshold detector can be obtained

$$E[\log T_{G(m,n)}] \leq E[T_{G(m,n)} - 1] \tag{D.2}$$

where the right-hand side of (D.2) is finite. Moreover, due to the nature of the random variables involved, it can be concluded that the expectation in the same equation is bounded from below by the case when the non-centrality parameter of the F-distribution becomes zero, or $\lambda_{m,n} = 0$

$$\frac{1}{L} \leq E\left[\log T_{G(m,n)}\right] \tag{D.3}$$

where the left-hand side of (D.2) is obtained from the expectation in (62). In a similar manner boundaries for the second moment of the logarithm of the bistatic GMLED threshold detector can be derived:

$$\frac{1}{L^2} \leq E\left[(\log T_{G(m,n)})^2\right] \leq E\left[(T_{G(m,n)}-1)^2\right] \tag{D.4}$$

The upper boundary in (D.4) comes from (D.1), while the lower one is derived from the fact that $E[x^2] \geq E[x]^2$. Combining (D.3), (D.2), and (D.4), it can be concluded that the variance of the logarithm of the bistatic GMLED detector is also bounded from below and above by certain finite bounds. The exact values of these bounds are not essential for the current proof and will therefore not be

calculated

$$\sigma_{lb}^2 \le \sigma_{G(m,n)}^2 \le \sigma_{ub}^2 \tag{D.5}$$

The bounds in (D.5) are enough to conclude that for any arbitrary constant $\epsilon > 0$

$$\lim_{M\times N\to\infty} \frac{\sigma_{G(m,n)}^2}{\epsilon^2 \sigma_G^2} = 0 \tag{D.6}$$

since the lower bounds on the total multistatic variance σ_G^2 tend to infinity as the number of transmitter–receiver pairs in the system tends to infinity. At this point the analogical Chebyshev bound to (C.2) for the GMLED becomes zero which, similar to Appendix C, proves the validity of Lindeberg's condition.

Appendix E. Supplementary data

Supplementary data associated with this paper can be found in the online version at http://dx.doi.org/10.1016/j.sigpro.2015.04.001.

References

[1] D. Bliss, K. Forsythe, Multiple-input multiple-output (MIMO) radar and imaging: degrees of freedom and resolution, in: Conference Record of the Thirty-Seventh Asilomar Conference on Signals, Systems and Computers, vol. 1, 2003, pp. 54–59. http://dx.doi.org/10.1109/ACSSC.2003.1291865.

[2] E. Fishler, A. Haimovich, R. Blum, D. Chizhik, L. Cimini, R. Valenzuela, MIMO radar: an idea whose time has come, in: Radar Conference, Proceedings of the IEEE, 2004, pp. 71–78. http://dx.doi.org/10.1109/NRC.2004.1316398.

[3] E. Fishler, A. Haimovich, R. Blum, R. Cimini, D. Chizhik, R. Valenzuela, Performance of MIMO radar systems: advantages of angular diversity, in: Conference Record of the Thirty-Eighth Asilomar Conference on Signals, Systems and Computers, vol. 1, 2004, pp. 305–309. http://dx.doi.org/10.1109/ACSSC.2004.1399142.

[4] E. Fishler, A. Haimovich, R. Blum, L.J. Cimini, D. Chizhik, R. Valenzuela, Spatial diversity in radars-models and detection performance, IEEE Trans. Signal Process. 54 (3) (2006) 823–838. http://dx.doi.org/10.1109/TSP.2005.862813.

[5] N. Goodman, D. Bruyere, Optimum and decentralized detection for multistatic airborne radar, IEEE Trans. Aerosp. Electron. Syst. 43 (2) (2007) 806–813, http://dx.doi.org/10.1109/TAES.2007.4285374.

[6] A. Haimovich, R. Blum, L. Cimini, MIMO radar with widely separated antennas, IEEE Signal Process. Mag. 25 (1) (2008) 116–129, http://dx.doi.org/10.1109/MSP.2008.4408448.

[7] H. Godrich, A. Haimovich, R. Blum, Target localization accuracy gain in MIMO radar-based systems, IEEE Trans. Inf. Theory 56 (6) (2010) 2783–2803, http://dx.doi.org/10.1109/TIT.2010.2046246.

[8] B. Shtarkalev, B. Mulgrew, Multistatic single data set target detection in unknown coloured Gaussian interference, in: Radar Conference (RADAR), 2013 IEEE, 2013, pp. 1–5. http://dx.doi.org/10.1109/RADAR.2013.6585997.

[9] Y. Abramovich, G.J. Frazer, Bounds on the volume and height distributions for the MIMO radar ambiguity function, IEEE Signal Process. Lett. 15 (2008) 505–508, http://dx.doi.org/10.1109/LSP.2008.922514.

[10] G. Frazer, Y. Abramovich, B. Johnson, MIMO radar limitations in clutter, in: Radar Conference, IEEE, 2009, pp. 1–5. http://dx.doi.org/10.1109/RADAR.2009.4976946.

[11] R. Adve, T. Hale, M. Wicks, Practical joint domain localised adaptive processing in homogeneous and nonhomogeneous environments. 2. Nonhomogeneous environments, IEE Proc. Radar Sonar Navig. 147 (2) (2000) 66–74, http://dx.doi.org/10.1049/ip-rsn:20000085.

[12] E. Aboutanios, B. Mulgrew, A STAP algorithm for radar target detection in heterogeneous environments, in: IEEE/SP 13th Workshop on Statistical Signal Processing, 2005, pp. 966–971. http://dx.doi.org/10.1109/SSP.2005.1628734.

[13] C.-H. Lim, B. Mulgrew, E. Aboutanios, Bistatic JDL-STAP for ground moving target detection, in: IET International Conference on Radar Systems, 2007, pp. 1 –5.

[14] C.-H. Lim, Bistatic space–time adaptive processing for ground moving target indication (Ph.D. thesis), Engineering, The University of Edinburgh, URL: ⟨http://hdl.handle.net/1842/6373⟩, October 2006.

[15] C. Lim, E. Aboutanios, B. Mulgrew, Training strategies for joint domain localised-space–time adaptive processing in a bistatic environment, IEE Proc. Radar Sonar Navig. 153 (6) (2006) 516–524, http://dx.doi.org/10.1049/ip-rsn:20050121.

[16] E. Aboutanios, B. Mulgrew, Hybrid detection approach for STAP in heterogeneous clutter, IEEE Trans. Aerosp. Electron. Syst. 46 (3) (2010) 1021–1033, http://dx.doi.org/10.1109/TAES.2010.5545171.

[17] P. Wang, H. Li, B. Himed, A new parametric GLRT for multichannel adaptive signal detection, IEEE Trans. Signal Process. 58 (1) (2010) 317–325, http://dx.doi.org/10.1109/TSP.2009.2030835.

[18] P. Wang, H. Li, B. Himed, Moving target detection using distributed MIMO radar in clutter with nonhomogeneous power, IEEE Trans. Signal Process. 59 (10) (2011) 4809–4820, http://dx.doi.org/10.1109/TSP.2011.2160861.

[19] P. Wang, H. Li, B. Himed, Parametric Rao tests for multichannel adaptive detection in partially homogeneous environment, IEEE Trans. Aerosp. Electron. Syst. 47 (3) (2011) 1850–1862, http://dx.doi.org/10.1109/TAES.2011.5937269.

[20] P. Wang, H. Li, B. Himed, A parametric moving target detector for distributed MIMO radar in non-homogeneous environment, IEEE Trans. Signal Process. 61 (9) (2013) 2282–2294, http://dx.doi.org/10.1109/TSP.2013.2245323.

[21] J.-F. Degurse, S. Marcos, L. Savy, Subspace-based and single dataset methods for STAP in heterogeneous environments, in: IET International Conference on Radar Systems (Radar 2012), 2012, pp. 1–6. http://dx.doi.org/10.1049/cp.2012.1693.

[22] J.-F. Degurse, L. Savy, S. Marcos, J.-P. Molinié, Deterministic aided STAP for target detection in heterogeneous situations, vol. 2013, 2013, p. 10. URL: ⟨http://dx.doi.org/10.1155/2013/826935⟩.

[23] D. Bruyere, N. Goodman, Adaptive detection and diversity order in multistatic radar, IEEE Trans. Aerosp. Electron. Syst. 44 (4) (2008) 1615–1623, http://dx.doi.org/10.1109/TAES.2008.4667736.

[24] C.Y. Chong, F. Pascal, J. Ovarlez, M. Lesturgie, MIMO radar detection in non-Gaussian and heterogeneous clutter, IEEE J. Sel. Top. Signal Process. 4 (1) (2010) 115–126, http://dx.doi.org/10.1109/JSTSP.2009.2038980.

[25] L. Kong, M. Yang, B. Zhao, Adaptive detection for shared-spectrum multistatic radar in Gaussian clutter, in: Radar Conference (RADAR), 2012 IEEE, 2012, pp. 0309 –0313. http://dx.doi.org/10.1109/RADAR.2012.6212156.

[26] J. Liu, Z.-J. Zhang, Y. Cao, S. Yang, A closed-form expression for false alarm rate of adaptive MIMO-GLRT detector with distributed MIMO radar, Signal Process. 93 (9) (2013) 2771–2776. doi:http://dx.doi.org/10.1016/j.sigpro.2013.03.001 URL: ⟨http://www.sciencedirect.com/science/article/pii/S0165168413000753⟩.

[27] W. Melvin, A STAP overview, IEEE Aerosp. Electron. Syst. Mag. 19 (1) (2004) 19–35, http://dx.doi.org/10.1109/MAES.2004.1263229.

[28] R. Ash, C. Doléans-Dade, Probability and Measure Theory, Harcourt/Academic Press, Burlington, MA, 2000 URL: ⟨http://books.google.co.uk/books?id=GkqQoRpCO2QC⟩.

[29] D. Bliss, K. Forsythe, S. Davis, G. Fawcett, D. Rabideau, L. Horowitz, S. Kraut, GMTI MIMO radar, in: Waveform Diversity and Design Conference, International, 2009, pp. 118 –122. http://dx.doi.org/10.1109/WDDC.2009.4800327.

[30] J. Kantor, D. Bliss, Clutter covariance matrices for GMTI MIMO radar, in: Conference Record of the Forty Fourth Asilomar Conference on Signals, Systems and Computers (ASILOMAR), 2010, pp. 1821 –1826. http://dx.doi.org/10.1109/ACSSC.2010.5757856.

[31] J. Ward, Space–time Adaptive Processing for Airborne Radar, Technical Report, MIT Lincoln Labs, December 1994. URL: ⟨http://handle.dtic.mil/100.2/ADA293032⟩.

[32] B. Shtarkalev, B. Mulgrew, Effects of FDMA/TDMA orthogonality on the Gaussian pulse train MIMO ambiguity function, IEEE Signal Process. Lett. 22 (2) (2015) 153–157, http://dx.doi.org/10.1109/LSP.2014.2351256.

[33] W. Melvin, R. Hancock, M. Rangaswamy, J. Parker, Adaptive distributed radar, in: Radar Conference – Surveillance for a Safer World, 2009, RADAR, International, 2009, pp. 1–6.

[34] L. Brennan, L. Reed, Theory of adaptive radar, IEEE Trans. Aerosp. Electron. Syst. AES-9 (2) (1973) 237–252, http://dx.doi.org/10.1109/TAES.1973.309792.

[35] P. Stoica, H. Li, J. Li, A new derivation of the APES filter, IEEE Signal Process. Lett. 6 (8) (1999) 205–206, http://dx.doi.org/10.1109/97.774866.

[36] F. Robey, D. Fuhrmann, E. Kelly, R. Nitzberg, A CFAR adaptive matched filter detector, IEEE Trans. Aerosp. Electron. Syst. 28 (1) (1992) 208–216, http://dx.doi.org/10.1109/7.135446.
[37] E. Kelly, An adaptive detection algorithm, IEEE Trans. Aerosp. Electron. Syst. AES-22 (2) (1986) 115–127, http://dx.doi.org/10.1109/TAES.1986.310745.
[38] A. Robinson, B. Mulgrew, A comparison of contemporary space–time adaptive processing techniques for GMTI, in: IET International Conference on Radar Systems (Radar 2012), 2012, pp. 1–5. http://dx.doi.org/10.1049/cp.2012.1691.
[39] F. Frishman, On the arithmetic means and variances of products and ratios of random variables, in: G. Patil, S. Kotz, J. Ord (Eds.), Statistical Distributions in Scientific Work, vol. 1, D. Reidel Publishing Company, Dordrecht-Holland, 1975, pp. 401–406.
[40] P. Patnaik, The non-central χ^2 and F-distributions and their applications, Biometrika 36 (1–2) (1949) 202–232.
[41] N.J. Willis, Bistatic Radar, 2nd ed. SciTech Publishing, Raleigh, NC, 2005 URL: ⟨http://books.google.co.uk/books?id=U0XG5WB-vY8C⟩.
[42] G.W. Stimson, Introduction to Airborne Radar, 2nd ed. SciTech Publishing, Inc., Raleigh, NC, 1998.
[43] G. Mhlbach, M. Gasca, A generalization of Sylvester's identity on determinants and some applications, Linear Algebra Appl. 66 (1985) 221–234. http://dx.doi.org/10.1016/0024-3795(85)90134-X URL: ⟨http://www.sciencedirect.com/science/article/pii/002437958590134X⟩.

References

[1] R. Watson, *Radar Origins Worldwide: History of Its Evolution in 13 Nations Through World War II*. Trafford Publishing, 2009.

[2] M. Skolnik, *Introduction to Radar Systems*. Electrical engineering series, McGraw Hill, 2001.

[3] M. Skolnik, *Radar Handbook, Third Edition*. Electronics electrical engineering, McGraw-Hill Education, 2008.

[4] N. J. Willis, *Bistatic Radar*. SciTech Publishing, 2nd ed., 2005.

[5] J. Li, J. Li, and P. Stoica, *MIMO Radar Signal Processing*. Wiley, 2009.

[6] G. Moore, "Cramming more components onto integrated circuits," *Proceedings of the IEEE*, vol. 86, pp. 82–85, Jan 1998.

[7] J. Guerci, *Space-time Adaptive Processing for Radar*. Artech House radar library, Artech House, 2003.

[8] G. W. Stimson, *Introduction to Airborne Radar*. SciTech Publishing, Inc., second ed., 1998.

[9] E. Kelly, "An adaptive detection algorithm," *Aerospace and Electronic Systems, IEEE Transactions on*, vol. AES-22, pp. 115 –127, march 1986.

[10] F. Robey, D. Fuhrmann, E. Kelly, and R. Nitzberg, "A CFAR adaptive matched filter detector," *Aerospace and Electronic Systems, IEEE Transactions on*, vol. 28, pp. 208 –216, jan 1992.

[11] L. Brennan and L. Reed, "Theory of adaptive radar," *Aerospace and Electronic Systems, IEEE Transactions on*, vol. AES-9, pp. 237 –252, march 1973.

[12] P. Wang, H. Li, and B. Himed, "Moving target detection using distributed MIMO radar in clutter with nonhomogeneous power," *Signal Processing, IEEE Transactions on*, vol. 59, pp. 4809 –4820, oct. 2011.

[13] P. Wang, H. Li, and B. Himed, "Recursive moving target detection with distributed MIMO radar in clutter with non-homogeneous power," in *Radar Conference (RADAR), 2012 IEEE*, pp. 0504 –0509, may 2012.

[14] P. Wang, H. Li, and B. Himed, "A parametric moving target detector for distributed MIMO radar in non-homogeneous environment," *Signal Processing, IEEE Transactions on*, vol. 61, no. 9, pp. 2282–2294, 2013.

[15] W. Melvin, "Space-time adaptive radar performance in heterogeneous clutter," *Aerospace and Electronic Systems, IEEE Transactions on*, vol. 36, pp. 621–633, Apr 2000.

[16] K. Gerlach and M. Steiner, "Adaptive detection of range distributed targets," *Signal Processing, IEEE Transactions on*, vol. 47, pp. 1844–1851, Jul 1999.

[17] E. Aboutanios and B. Mulgrew, "A STAP algorithm for radar target detection in heterogeneous environments," in *Statistical Signal Processing, 2005 IEEE/SP 13th Workshop on*, pp. 966–971, July 2005.

[18] C.-H. Lim, *Bistatic Space-Time Adaptive Processing for Ground Moving Target Indication*. PhD thesis, Engineering, The University of Edinburgh, Oct 2006. Available: http://hdl.handle.net/1842/6373.

[19] E. Aboutanios and B. Mulgrew, "Hybrid detection approach for STAP in heterogeneous clutter," *Aerospace and Electronic Systems, IEEE Transactions on*, vol. 46, pp. 1021 –1033, July 2010.

[20] J.-F. Degurse, S. Marcos, and L. Savy, "Subspace-based and single dataset methods for STAP in heterogeneous environments," in *Radar Systems (Radar 2012), IET International Conference on*, pp. 1–6, 2012.

[21] J.-F. Degurse, L. Savy, and S. Marcos, "Reduced-rank STAP for target detection in heterogeneous environments," *Aerospace and Electronic Systems, IEEE Transactions on*, vol. 50, pp. 1153–1162, April 2014.

[22] G. H. Knittel, "Phase 2 Netted radar demonstration," *NASA STI/Recon Technical Report N*, vol. 81, p. 33380, Oct. 1980.

[23] F. Folster and H. Rohling, "Data association and tracking for automotive radar networks," *Intelligent Transportation Systems, IEEE Transactions on*, vol. 6, pp. 370–377, Dec 2005.

[24] T. Derham, S. Doughty, K. Woodbridge, and C. Baker, "Design and evaluation of a low-cost multistatic netted radar system," *Radar, Sonar Navigation, IET*, vol. 1, pp. 362–368, October 2007.

[25] H. Godrich and A. Haimovich, "Localization performance of coherent MIMO radar systems subject to phase synchronization errors," in *Communications, Control and Signal Processing (ISCCSP), 2010 4th International Symposium on*, pp. 1–5, March 2010.

[26] Q. He, R. Blum, and Z. He, "Noncoherent versus coherent MIMO radar for joint target position and velocity estimation," in *Radar (Radar), 2011 IEEE CIE International Conference on*, vol. 1, pp. 108–111, Oct 2011.

[27] E. Fishler, A. Haimovich, R. Blum, D. Chizhik, L. Cimini, and R. Valenzuela, "MIMO radar: an idea whose time has come," in *Radar Conference, 2004. Proceedings of the IEEE*, pp. 71 – 78, april 2004.

[28] E. Fishler, A. Haimovich, R. Blum, R. Cimini, D. Chizhik, and R. Valenzuela, "Performance of MIMO radar systems: advantages of angular diversity," in *Signals, Systems and Computers, 2004. Conference Record of the Thirty-Eighth Asilomar Conference on*, vol. 1, pp. 305 – 309 Vol.1, nov. 2004.

[29] E. Fishler, A. Haimovich, R. Blum, J. Cimini, L.J., D. Chizhik, and R. Valenzuela, "Spatial diversity in radars-models and detection performance," *Signal Processing, IEEE Transactions on*, vol. 54, pp. 823 – 838, march 2006.

[30] A. Haimovich, R. Blum, and L. Cimini, "MIMO radar with widely separated antennas," *Signal Processing Magazine, IEEE*, vol. 25, no. 1, pp. 116 –129, 2008.

[31] H. Godrich, A. Haimovich, and R. Blum, "Target localization accuracy gain in MIMO radar-based systems," *Information Theory, IEEE Transactions on*, vol. 56, pp. 2783 – 2803, june 2010.

[32] N. Goodman and D. Bruyere, "Optimum and decentralized detection for multistatic airborne radar," *Aerospace and Electronic Systems, IEEE Transactions on*, vol. 43, pp. 806–813, April 2007.

[33] Q. He, N. H. Lehmann, R. S. Blum, and A. M. Haimovich, "MIMO radar moving target detection in homogeneous clutter," *Aerospace and Electronic Systems, IEEE Transactions on*, vol. 46, pp. 1290 –1301, july 2010.

[34] Q. He, R. Blum, and A. Haimovich, "Noncoherent MIMO radar for location and velocity estimation: More antennas means better performance," *Signal Processing, IEEE Transactions on*, vol. 58, pp. 3661–3680, July 2010.

[35] Q. He, R. Blum, H. Godrich, and A. Haimovich, "Target velocity estimation and antenna placement for MIMO radar with widely separated antennas," *Selected Topics in Signal Processing, IEEE Journal of*, vol. 4, pp. 79–100, Feb 2010.

[36] A. Hassanein, S. Vorobyov, A. Gershman, and M. Rubsamen, "Estimating the parameters of a moving target in MIMO radar with widely separated antennas," in *Sensor Array and Multichannel Signal Processing Workshop (SAM), 2010 IEEE*, pp. 57–60, Oct 2010.

[37] A. Mrstik, "Multistatic-radar binomial detection," *Aerospace and Electronic Systems, IEEE Transactions on*, vol. AES-14, pp. 103–108, Jan 1978.

[38] M. Barkat and P. Varshney, "Decentralized CFAR signal detection," *Aerospace and Electronic Systems, IEEE Transactions on*, vol. 25, pp. 141–149, March 1989.

[39] R. Srinivasan, "Designing distributed detection systems," *Radar and Signal Processing, IEE Proceedings F*, vol. 140, pp. 191–197, Jun 1993.

[40] R. Viswanathan and P. Varshney, "Distributed detection with multiple sensors I. Fundamentals," *Proceedings of the IEEE*, vol. 85, pp. 54–63, Jan 1997.

[41] R. Blum, S. Kassam, and H. Poor, "Distributed detection with multiple sensors II. Advanced topics," *Proceedings of the IEEE*, vol. 85, pp. 64–79, Jan 1997.

[42] L. Neng-Jing, "Radar ECCMs new area: anti-stealth and anti-ARM," *Aerospace and Electronic Systems, IEEE Transactions on*, vol. 31, pp. 1120–1127, Jul 1995.

[43] C. Baker, "An introduction to multistatic radar," *NATO SET-136 Lecture Series Multistatic Surveillance and Reconnaissance: Sensor, Signals and Data Fusion*, 2009.

[44] W. Melvin, R. Hancock, M. Rangaswamy, and J. Parker, "Adaptive distributed radar," in *Radar Conference - Surveillance for a Safer World, 2009. RADAR. International*, pp. 1–6, Oct 2009.

[45] Y. Abramovich and G. J. Frazer, "Bounds on the volume and height distributions for the MIMO radar ambiguity function," *Signal Processing Letters, IEEE*, vol. 15, pp. 505–508, 2008.

[46] G. Frazer, Y. Abramovich, and B. Johnson, "MIMO radar limitations in clutter," in *Radar Conference, 2009 IEEE*, pp. 1–5, 2009.

[47] B. Shtarkalev and B. Mulgrew, "Effects of FDMA/TDMA orthogonality on the Gaussian pulse train MIMO ambiguity function," *Signal Processing Letters, IEEE*, vol. 22, pp. 153–157, Feb 2015.

[48] D. V. Dranidis, "Shipboard phased-array radars: Requirements, technology and operational systems," *Waypoint Magazine*, vol. 1, February 2003.

[49] J. Ward, "Space-time adaptive processing for airborne radar," tech. rep., MIT Lincoln Labs, Dec. 1994.

[50] S. Blunt, K. Gerlach, and M. Rangaswamy, "STAP using knowledge-aided covariance estimation and the fracta algorithm," *Aerospace and Electronic Systems, IEEE Transactions on*, vol. 42, pp. 1043–1057, July 2006.

[51] E. Aboutanios and B. Mulgrew, "Regularisation methods for covariance matrix estimation in low sample support STAP," in *Radar Systems, 2007 IET International Conference on*, pp. 1–5, Oct 2007.

[52] Y. Abramovich, B. Johnson, and N. Spencer, "Multivariate spectral reconstruction of STAP covariance matrices: Toeplitz-block solution," in *Sensor Array and Multichannel Signal Processing Workshop, 2008. SAM 2008. 5th IEEE*, pp. 229–233, July 2008.

[53] W. Melvin, "A STAP overview," *Aerospace and Electronic Systems Magazine, IEEE*, vol. 19, pp. 19 –35, jan. 2004.

[54] C. Lim, E. Aboutanios, and B. Mulgrew, "Bistatic STAP training without navigation data," in *NATO, RTO SET-095 Specialist Meeting (SM), Bi-/Multistatic Radar and Sonar-Systems*, 2006. Available: http://www.see.ed.ac.uk/ bernie/Conference_Papers/Lim2006a.pdf.

[55] E. Aboutanios and B. Mulgrew, "Evaluation of the single and two data set STAP detection algorithms using measured data," in *Geoscience and Remote Sensing Symposium, 2007. IGARSS 2007. IEEE International*, pp. 494–498, July 2007.

[56] B. Shtarkalev and B. Mulgrew, "Multistatic single data set target detection in unknown coloured Gaussian interference," in *Radar Conference (RADAR), 2013 IEEE*, pp. 1–5, 2013.

[57] P. Wang, H. Li, and B. Himed, "Centralized and distributed tests for moving target detection with MIMO radars in clutter of non-homogeneous power," in *Signals, Systems and Computers (ASILOMAR), 2011 Conference Record of the Forty Fifth Asilomar Conference on*, pp. 878 –882, nov. 2011.

[58] T. Ali, A. Sadeque, M. Saquib, and M. Ali, "MIMO radar for target detection and localization in sensor networks," *Systems Journal, IEEE*, vol. 8, pp. 75–82, March 2014.

[59] C. Capraro, G. Capraro, D. Weiner, M. Wicks, and W. Baldygo, "Improved STAP performance using knowledge-aided secondary data selection," in *Radar Conference, 2004. Proceedings of the IEEE*, pp. 361–365, April 2004.

[60] M. Wicks, W. Melvin, and P. Chen, "An efficient architecture for nonhomogeneity detection in space-time adaptive processing airborne early warning radar," in *Radar 97 (Conf. Publ. No. 449)*, pp. 295–299, Oct 1997.

[61] P. Stoica, H. Li, and J. Li, "A new derivation of the APES filter," *Signal Processing Letters, IEEE*, vol. 6, pp. 205–206, Aug 1999.

[62] A. Haimovich, "The eigencanceler: adaptive radar by eigenanalysis methods," *Aerospace and Electronic Systems, IEEE Transactions on*, vol. 32, no. 2, pp. 532–542, 1996.

[63] D. Bliss and K. Forsythe, "Multiple-input multiple-output (MIMO) radar and imaging: degrees of freedom and resolution," in *Signals, Systems and Computers, 2003. Conference Record of the Thirty-Seventh Asilomar Conference on*, vol. 1, pp. 54 – 59 Vol.1, nov. 2003.

[64] N. Levanon, *Radar principles*. A Wiley Interscience publication, Wiley, 1988.

[65] D. Bruyere and N. Goodman, "Adaptive detection and diversity order in multistatic radar," *Aerospace and Electronic Systems, IEEE Transactions on*, vol. 44, pp. 1615 – 1623, oct. 2008.

[66] R. Daher and R. Adve, "A notion of diversity order in distributed radar networks," *Aerospace and Electronic Systems, IEEE Transactions on*, vol. 46, pp. 818–831, April 2010.

[67] L. Kong, M. Yang, and B. Zhao, "Adaptive detection for shared-spectrum multistatic radar in Gaussian clutter," in *Radar Conference (RADAR), 2012 IEEE*, pp. 0309 –0313, may 2012.

[68] P. M. Woodward, "Radar ambiguity analysis," tech. rep., DTIC Document, 1967.

[69] H. Burchardt, N. Serafimovski, D. Tsonev, S. Videv, and H. Haas, "VLC: Beyond point-to-point communication," *Communications Magazine, IEEE*, vol. 52, pp. 98–105, July 2014.

[70] D. Swick, "A review of narrowband ambiguity functions," tech. rep., DTIC Document, 1970.

[71] P. Woodward, *Probability and Information Theory, with Applications to Radar*. Radar Library, Artech House, 1980.

[72] R. Price and E. Hofstetter, "Bounds on the volume and height distributions of the ambiguity function," *Information Theory, IEEE Transactions on*, vol. 11, no. 2, pp. 207–214, 1965.

[73] I. Glover and P. Grant, *Digital Communications*. Pearson Prentice Hall, 3rd ed., 2010.

[74] H. Deng, "Orthogonal netted radar systems," *Aerospace and Electronic Systems Magazine, IEEE*, vol. 27, pp. 28–35, May 2012.

[75] B. Shtarkalev and B. Mulgrew, "Multistatic moving target detection in unknown coloured Gaussian interference," *Signal Processing*, vol. 115, no. 0, pp. 130 – 143, 2015.

[76] P. Wang, H. Li, and B. Himed, "A new parametric GLRT for multichannel adaptive signal detection," *Signal Processing, IEEE Transactions on*, vol. 58, no. 1, pp. 317–325, 2010.

[77] P. Wang, H. Li, and B. Himed, "Parametric Rao tests for multichannel adaptive detection in partially homogeneous environment," *Aerospace and Electronic Systems, IEEE Transactions on*, vol. 47, no. 3, pp. 1850–1862, 2011.

[78] R. Ash and C. Doléans-Dade, *Probability and Measure Theory*. Harcourt/Academic Press, 2000.

[79] J. Neyman and E. S. Pearson, "On the problem of the most efficient tests of statistical hypotheses," *Philosophical Transactions of the Royal Society of London. Series A, Containing Papers of a Mathematical or Physical Character*, vol. 231, pp. pp. 289–337, 1933.

[80] J. Magnus and H. Neudecker, *Matrix differential calculus with applications in statistics and econometrics*. Wiley Series in Probability and Statistics - Applied Probability and Statistics Section, Wiley, 3rd. ed., 2007.

[81] N. R. Goodman, "Statistical analysis based on a certain multivariate complex Gaussian distribution (an introduction)," *The Annals of Mathematical Statistics*, vol. 34, pp. 152–177, 03 1963.

[82] G. Mhlbach and M. Gasca, "A generalization of Sylvester's identity on determinants and some applications," *Linear Algebra and its Applications*, vol. 66, no. 0, pp. 221 – 234, 1985.

[83] F. Frishman, "On the arithmetic means and variances of products and ratios of random variables," in *Statistical Distributions in Scientific Work* (G. Patil, S. Kotz, and J. Ord, eds.), vol. 1, (Dordrecht-Holland), pp. 401 –406, D. Reidel Publishing Company, 1975.

[84] P. Patnaik, "The non-central χ^2 and F-distributions and their applications," *Biometrika*, vol. 36(1-2), pp. 202–232, 1949.

[85] N. Balakrishnan and C. Lai, *Continuous Bivariate Distributions*. Springer, 2009.

[86] J. Liu, Z.-J. Zhang, Y. Cao, and S. Yang, "A closed-form expression for false alarm rate of adaptive MIMO-GLRT detector with distributed MIMO radar," *Signal Processing*, vol. 93, no. 9, pp. 2771 – 2776, 2013.

[87] A. C. Berry, "The accuracy of the Gaussian approximation to the sum of independent variates," *Transactions of the American Mathematical Society*, vol. 49, no. 1, pp. pp. 122–136, 1941.

[88] H. Wang and L. Cai, "On adaptive spatial-temporal processing for airborne surveillance radar systems," *Aerospace and Electronic Systems, IEEE Transactions on*, vol. 30, pp. 660–670, Jul 1994.

[89] J. S. Bergin and P. M. Techau, "Multiresolution signal processing techniques for ground moving target detection using airborne radar," *EURASIP Journal on Advances in Signal Processing*, vol. 2006, no. 1, p. 047534, 2006.

[90] C. Rago, P. Willett, and Y. Bar-Shalom, "Censoring sensors: a low-communication-rate scheme for distributed detection," *Aerospace and Electronic Systems, IEEE Transactions on*, vol. 32, pp. 554–568, April 1996.

[91] S. Appadwedula, V. Veeravalli, and D. Jones, "Energy-efficient detection in sensor networks," *Selected Areas in Communications, IEEE Journal on*, vol. 23, pp. 693–702, April 2005.

[92] S. Appadwedula, V. Veeravalli, and D. Jones, "Decentralized detection with censoring sensors," *Signal Processing, IEEE Transactions on*, vol. 56, pp. 1362–1373, April 2008.

[93] S. Marano, V. Matta, P. Willett, and L. Tong, "Cross-layer design of sequential detectors in sensor networks," *Signal Processing, IEEE Transactions on*, vol. 54, pp. 4105–4117, Nov 2006.

[94] R. Blum and B. Sadler, "Energy efficient signal detection in sensor networks using ordered transmissions," *Signal Processing, IEEE Transactions on*, vol. 56, pp. 3229–3235, July 2008.

[95] Q. He, R. Blum, and Z. Rawas, "Ordering for energy efficient communications for noncoherent MIMO radar networks," in *Acoustics, Speech and Signal Processing (ICASSP), 2012 IEEE International Conference on*, pp. 5189–5192, March 2012.

[96] J.-F. Degurse, L. Savy, R. Perenon, and S. Marcos, "An extended formulation of the maximum likelihood estimation algorithm. application to space-time adaptive processing," in *Radar Symposium (IRS), 2011 Proceedings International*, pp. 763–768, Sept 2011.

[97] R. Strichartz, *A guide to distribution theory and Fourier transforms*. Studies in advanced mathematics, CRC Press, 1994.

[98] A. P. Dawid, "Conditional independence for statistical operations," *The Annals of Statistics*, vol. 8, no. 3, pp. pp. 598–617, 1980.

[99] A. Swinfen, *Foundations of Galois Theory*. Dover books on mathematics, Dover Publications, 2004.

[100] C. Poynton, *Digital Video and HDTV: Algorithms and Interfaces*. Electronics & Electrical, Morgan Kaufmann Publishers, 2003.

[101] B. W. Jung, R. Adve, and J. Chun, "Frequency diversity in multistatic radars," in *Radar Conference, 2008. RADAR '08. IEEE*, pp. 1–6, May 2008.

[102] R. Beerends, *Fourier and Laplace Transforms*. Fourier and Laplace Transforms, Cambridge University Press, 2003.

[103] K. Hoffman, *Banach Spaces of Analytic Functions*. Dover Publications, 2014.

[104] P. A. Bromiley, "Products and convolutions of Gaussian distributions," Internal Report Tina Memo No. 2003-003, Imaging Science and Biomedical Engineering Division Medical School, University of Manchester, Nov 2003.

[105] K. Mardia, J. Kent, and J. Bibby, *Multivariate analysis*. Probability and mathematical statistics, Academic Press, 1979.

[106] S. L. Zabell, "Alan Turing and the central limit theorem," *The American Mathematical Monthly*, vol. 102, no. 6, pp. pp. 483–494, 1995.